Measuring Muon-Neutrino Charged-Current Differential Cross Sections with a Liquid Argon Time Projection Chamber

A Dissertation
Presented to the Faculty of the Graduate School
of
Yale University
in Candidacy for the Degree of
Doctor of Philosophy

by
Joshua B. Spitz

Dissertation Director: Bonnie T. Fleming

December 2011

Abstract

Measuring Muon-Neutrino Charged-Current Differential Cross Sections with a Liquid Argon Time Projection Chamber

Joshua B. Spitz

2011

More than 80 years after its proposed existence, the neutrino remains largely mysterious and elusive. Precision measurements of the neutrino's properties are just now beginning to take place. Such measurements are required in order to determine the mass of the neutrino, how many neutrinos there are, if neutrinos are different than anti-neutrinos, and more.

Muon-neutrino charged-current differential cross sections on an argon target in terms of the outgoing muon momentum and angle are presented. The measurements have been taken with the ArgoNeuT Liquid Argon Time Projection Chamber (LArTPC) experiment. ArgoNeuT is the first LArTPC to ever take data in a low energy neutrino beam, having collected thousands of neutrino and anti-neutrino events in the NuMI beamline at Fermilab. The results are relevant for long baseline neutrino oscillation experiments searching for non-zero θ_{13}, CP-violation in the lepton sector, and the sign of the neutrino mass hierarchy, among other things. Furthermore, the differential cross sections are important for understanding the nature of the neutrino-nucleus interaction in general. These measurements represent a significant step forward for LArTPC technology as they are among the first neutrino physics results with such a device.

© 2011 by Joshua B. Spitz
All rights reserved.

Dedicated to my parents and Lindsey

Acknowledgements

Any success I've had in graduate school can largely be attributed to surrounding myself with an extraordinary group of people. I wish to thank those people here.

-Sam Zeller, for knowing so much about the neutrino cross section and being incredibly approachable. You exemplify everything that I love about Fermilab.

-Carl Bromberg, for many fruitful discussions and your fervent interest in ArgoNeuT.

-Costas Andreopolous, for helping me understand the neutrino-nucleus interaction and how the GENIE neutrino software handles it.

-Ornella, Maddalena, and Flavio, for being fun to work with and teaching me about neutrino interactions.

-Tingjun Yang, Adam Patch, Ellen Klein, and Saima Farooq, for help with my analysis.

-Teppei Katori, for enlightening physics discussions. Although you are an incredible physicist, you are best known for your contagious love of life. I admire you for both.

-Taritree Wongjirad, for teaching me a lot about hardware and playing golf with me.

-Stephen Pordes, for being a consistent source of liquid argon knowledge and general physics wisdom.

-Andrew Lathrop, for being one of ArgoNeuT's greatest resources and a good friend.

-Moshe Gai, for introducing me to many experimental physics techniques and providing your house for proposing to my wife.

-Kinga Partyka, for being a good friend, help with my analysis, and many hilarious physics discussions.

-Brian Page, for many useful discussions. Working on reconstructing neutrino events with you has been a lot of fun.

-Brian Rebel, for being an incredibly helpful top-notch programmer and physicist. Thank you for always having an open door for me.
-Eric Church, for help with my analysis and software in general.
-Andrzej Szelc and Roxanne Guenette, for teaching me about dark matter and astrophysics, respectively.
-Rashid Mehdiyev and Robert Hatcher, for going out of your way to provide an enormous amount of knowledge about the MINOS detector and software.
-Georgia Karagiorgi and Kendall Mahn, for teaching me about MiniBooNE.
-Bob Nelson, Mike Wilking, Keith Ulmer, Rune Niclasen, and Hugh Lippincott, for being role models to me. You influenced me much more than you know.
-Jim Hirschauer, for teaching me a lot about physics and life. You have been a role model to me as a physicist and as a father.
-Joe Grange and Ranjan Dharmapalan, for being great friends and colleagues. I had a great time learning neutrino physics with you.
-Joe Walding, Jason St. John, and Arati Prakash for many terrific conversations over lunch.
-The MINOS collaboration, for providing an integral piece of my analysis.
-The ArgoNeuT collaboration, for a very successful and fun experiment.
-Fermilab, for providing me access to the world's particle physics experts.
-Eric Zimmerman, for introducing me to neutrino physics and research in general. You are the main reason that I entered graduate school and your influence on me has been enormous.
-Colin Bruzewicz and Matt Phillips, for friendship and help with graduate school homework.
-Brent Kelsall and Micah Friedman, for providing non-physics intellectual stimulation.
-Marilyn, Mom, and Dad, for unlimited support and love.
-Lindsey, for always being there for me. I love you lots.
-Abby, for being a most welcome distraction. I love you lots.
-Janet Conrad, for being a rich source of original ideas and insights. It has been an incredible pleasure to think outside the box with you. You have made me a better and broader physicist.
-Mitch Soderberg, for teaching me almost everything I know about hardware and much of what I know about software. You have been like an "official" adviser to me. Thanks for letting me be your apprentice. Rediscovering the neutrino with you was my favorite part of graduate school.

-Bonnie Fleming, for being an amazing adviser and mentor. I consider joining your group one of the best decisions I have ever made. You set the standard as a physicist, leader, and person in so many ways. Thank you for everything.

Contents

List of Figures

List of Tables

Part I

Knowledge of the Neutrino

1 The Neutrino

The history of the proposed existence, discovery, and description of the neutrino represents a beautiful interplay between theory and experiment in physics. A brief overview of progress in understanding the neutrino is provided below.

1.1 Missing Energy, Found

1.1.1 The idea of the neutrino

Conservation is the cornerstone of physics. The neutrino was envisaged by Pauli in 1930 in order to maintain the basic physical concepts of conservation of energy and conservation of momentum (linear and angular), concepts which much of physics and science in general rely. The nuclear beta decay process could not simply be explained by the emission of an electron by a parent nucleus ($A \longrightarrow e^- A'$, with A and A' as the parent and daughter nuclei, and e^- an electron). The decay is readily observed as it is quite common for unstable nuclei. Examples include ${}^{40}_{19}\mathrm{K} \rightarrow {}^{40}_{20}\mathrm{Ca}$ and ${}^{3}_{1}\mathrm{H} \rightarrow {}^{3}_{2}\mathrm{He}$. The energy of the electron in a two-body decay with the parent nucleus at rest is given by:

$$E = (\frac{m_A^2 - m_{A'}^2 + m_{e^-}^2}{2m_A})c^2 \ , \tag{1.1}$$

where m is mass. Given the three masses, E is single-valued, monoenergetic in the equation above. Experimentally, however, the energy of these decay electrons was found to be continuous, with the two-body decay equation setting the endpoint of the observed electron energy distribution. As unobserved secondary interactions with the material surrounding the decaying nucleus were ruled out as a source of the continuous spectrum, the conservation rules governing the momentum and energy of the initial and final particles

were thought to have been broken. Pauli proposed that an unseen third particle was being emitted in beta decay, accounting for the anomalous energy spectrum of the emitted electron. The neutrino was born. The idea of the neutrino was considered tenuous for a few years until Fermi put forward a theory of beta decay in 1934 [1], explaining the experimental observations successfully.

1.1.2 The detection of the neutrino

The neutrino was not detected until 1956 when Cowan, Reines, and colleagues observed neutrinos (really anti-neutrinos) created via beta decay inside a nuclear reactor [2]. They measured the $\overline{\nu}_e + p \longrightarrow n + e^+$ interaction in a tank of water and $CdCl_2$. Although the concept of neutrino flavor had not yet been developed, the particles that they had detected were anti-electron-neutrinos. The positron created in this process annihilates with a nearby electron to produce two gamma rays. These gamma rays were detected by a scintillator and photomultiplier tube combination carefully positioned in the water tank. The product neutron was also detected with the neutron capture interaction $n + {}^{108}\mathrm{Cd} \longrightarrow {}^{109}\mathrm{Cd} + \gamma$. The gamma ray from the nuclear de-excitation was detected approximately 5 μs after the positron annihilation's gamma rays. Reactor-on and reactor-off configurations were compared and the neutrino was experimentally discovered. Furthermore, the $\sim$3/events/hour neutrino interaction rate was found to be fairly consistent with the predicted cross section [3].

1.2 Description of the Neutrino

With the neutrino unambiguously detected, physicists have sought to measure its properties in more detail. We now know that the neutrino is a spin-$\frac{1}{2}$ particle that interacts only weakly and is paired in doublets with the three charged leptons. The neutrino can only interact via an exchange of a $W^{\pm}$ boson (charged-current) or a Z^0 boson (neutral-current), rendering its interaction cross section very small. In the past 10 years or so, the neutrino has been found to carry a non-zero mass. These discoveries are discussed below.

1.2.1 Helicity

Mirror reflection symmetry, or parity, was predicted to be violated in weak interactions theoretically in 1956 [4] and observed experimentally in 1957 [5]. Following up their the-

oretical discovery of parity violation in weak decays, Lee and Yang devised a theory in which the half-integer spin neutrino (which is only created via the weak interaction) has a definite helicity, or orientation of a particle's momentum with respect to its spin. This can be compared to other particles which have two possible helicities, a spin that is in the same direction as its momentum and a spin that is in the opposite direction as its momentum. The actual helicity of the neutrino was found a few years later to be "left-handed", meaning that the spin and momentum are anti-parallel [6]. The anti-neutrino is known as "right-handed" with its spin and momentum vectors parallel to each other. The V-A theory of the weak interaction was soon formulated. It described $W^{\pm}$ bosons coupling to left-handed particles and right-handed anti-particles as the solution to the observed maximal violation of parity [7].

1.2.2 Charged-current interactions and flavor

The muon neutrino was discovered in 1962 with a particle-accelerator-based neutrino beam [8] of significantly higher energy ($\sim$1 GeV) than any previous neutrino experiment. This type of neutrino, created via a high energy proton collision, pion creation, and then subsequent pion decay into a muon and neutrino, was found to create a muon rather than an electron when it interacted (via the charged-current, $\nu_{\mu} + N \longrightarrow N^{'} + \mu$, where $N^{(')}$ is a nucleon). The idea of neutrino flavor was born. In an interaction featuring a charged lepton final state, an (anti-) electron neutrino interacts to create a (positron) electron and a (anti-) muon neutrino interacts to create a (anti-) muon. The third charged lepton was discovered in 1975 [9] and its partner neutrino in 2000 [10].

1.2.3 Neutral-current interactions

Neutrino interactions with a neutrino in the final state ($\nu + X \longrightarrow \nu + Y$) were observed at CERN in 1973 [11]. These interactions were revealed to be neutral-current interactions which proceeded by the exchange of a Z^0 boson, rather than a $W^{\pm}$ boson as in the case of a charged-current interaction. The gauge theory of electroweak interactions describing these particles and their relation to the force carrier of electromagnetism (the photon) was put forth in the years 1961-1968 [12–14]. The actual weak interaction mediating bosons ($W^{\pm}$ and Z^0) were discovered in 1983 [15, 16].

1.2.4 Mass and Mixing

Until recently, the neutrino was thought to be massless. The observation of neutrino oscillations, discussed in the next section, has convincingly demonstrated that neutrinos mix between flavors and have mass.

2 Neutrino Oscillation

2.1 Neutrino Oscillation Theory

Experimental observations have shown that there are multiple flavors of neutrino and that one neutrino can change into another one after traveling a distance. The observation of this "neutrino oscillation" has occurred at many different length and energy scales. Neutrinos created in the sun, atmosphere, nuclear reactors, and particle accelerators have all been found to exhibit flavor transformation. The theoretical concept of neutrino mixing was theorized by Pontecorvo who imagined that a massive neutrino could oscillate in time/distance into its own anti-particle [17]. This description was similar to that which was developed for the neutral kaon oscillation $K^0 \longrightarrow \overline{K}^0$. Soon after and with the advent of flavor, the idea of oscillation between flavors was proposed [18].

The implications of neutrino oscillation and the phenomenon's mathematical description are described below, followed by the experimental evidence of neutrino oscillations.

2.1.1 From flavor eigenstate to mass eigenstate and back

The W^+ leptonic decay produces a charged lepton l^+_α (α is the lepton's flavor with $\alpha = e, \mu, \tau$) and a neutrino ν_i (i is the neutrino mass eigenstate with $i = 1,\ 2,\ 3, ...$). The amplitude for the decay $W^+ \longrightarrow l^+ + \nu_i$ is $U^*_{\alpha i}$, where U are elements of the flavor mixing matrix. The neutrino flavor eigenstate can therefore be written as a linear superposition of mass eigenstates,

$$\mid \nu_\alpha >= \sum_i U^*_{\alpha i} \mid \nu_i > \ , \tag{2.1}$$

where $\mid \nu_\alpha >$ is a neutrino of a given flavor, $U^*_{\alpha i}$ are elements of the flavor mixing matrix more specifically defined by subscripts, $\alpha = e$, μ, τ are the flavor indices, $i = 1, 2, 3$ are the indices of the mass eigenstates, and $\mid \nu_i >$ are the mass eigenstates of the neutrino. The PMNS or flavor mixing matrix in the three neutrino case is written as

$$U = \begin{bmatrix} U_{e1} & U_{e2} & U_{e3} \\ U_{\mu 1} & U_{\mu 2} & U_{\mu 3} \\ U_{\tau 1} & U_{\tau 2} & U_{\tau 3} \end{bmatrix} \tag{2.2}$$

This matrix can be thought of as the leptonic mixing analogy to the CKM quark mixing matrix.

All mass eigenstates have a characteristic phase that goes as

$$\exp[-i(Et - pL] \ , \tag{2.3}$$

where E is energy, t is time, p is momentum, L is the distance traveled, and $\hbar = c = 1$. A neutrino in an initial $\mid \nu_\alpha >$ state evolves in time as

$$\mid \nu_\alpha(\tau) >= \sum_i U^*_{\alpha i} e^{-i m_i \tau_i} \mid \nu_i(0) > \ \ , \tag{2.4}$$

where τ is the neutrino's proper time and m is mass. In the laboratory frame, the state evolves as

$$\mid \nu_\alpha(t) >= \sum_i U^*_{\alpha i} e^{-i(E_i t - p_i L)} \mid \nu_i(0) > \tag{2.5}$$

If the neutrino momentum is much larger than its mass, then $E_i = \sqrt{p^2 + m_i^2} \approx p + \frac{m_i^2}{2p}$. Also, as neutrinos are very relativistic, $t \approx L$. Our characteristic phase is now $e^{-i(E_i t - p_i L)} \approx e^{-i(m_i^2/2E)L}$ and the neutrino time evolution equation becomes

$$\mid \nu_\alpha(L) >= \sum_i U^*_{\alpha i} e^{-i(m_i^2/2E)L} \mid \nu_i > \tag{2.6}$$

As time does not change for massless particles, the above equation implies that neutrinos, in the case that their state evolves in time, cannot be massless. Since the mass eigenstates have different masses, they will have different frequencies. With different frequencies, the superpositioned eigenstates will interfere to produce different ratios of mass functions and a superposition of flavor. Once a neutrino of a given flavor propagates, it can be detected as a different flavor. In other words, a neutrino with initial flavor α can

oscillate into a neutrino of flavor β after traveling a distance L with a non-zero probability of $\alpha \neq \beta$:

$$\mid \nu_\alpha(L) > \approx \sum_\beta \Big[\sum_i U^*_{\alpha i} e^{-i(m_i^2/2E)L} U_{\beta i} \Big] \mid \nu_\beta > \tag{2.7}$$

The probability of an oscillation from flavor α to β is

$$P(\nu_\alpha \longrightarrow \nu_\beta) = \mid < \nu_\beta \mid \nu_\alpha(L) > \mid^2 = \mid \sum_i U^*_{\alpha i} e^{-i(m_i^2/2E)L} U_{\beta i} \mid^2 \tag{2.8}$$

Expanding the equation yields

$$\begin{aligned} P(\nu_\alpha \longrightarrow \nu_\beta) = \delta_{\alpha\beta} \quad &- \quad 4 \sum_{i>j} \mathrm{Re}(U^*_{\alpha i} U_{\beta i} U_{\alpha j} U^*_{\beta j}) \sin^2(\tfrac{(m_i^2 - m_j^2)L}{4E}) \\ &+ \quad 2 \sum_{i>j} \mathrm{Im}(U^*_{\alpha i} U_{\beta i} U_{\alpha j} U^*_{\beta j}) \sin(\tfrac{(m_i^2 - m_j^2)L}{2E}) \end{aligned} \tag{2.9}$$

The third term $[2 \sum_{i>j} \mathrm{Im}(...)]$ is the CP violating term. The "CP" operation refers to the combination of charge-conjugation (C), the transformation of a particle into its anti-particle, and the parity operation (P), which generates the mirror image of a physical coordinate system. CP violation refers to a fundamental difference between a particle and its parity-transformed anti-particle. It is worth noting here that the predominance of matter over anti-matter in the universe today requires CP violation. Although CP violation has been observed in the quark sector, its magnitude cannot account for the observed universal baryon asymmetry. CP violation in the lepton sector may be responsible for some of the discrepancy. A heavy Majorana lepton N (arising from the seesaw mechanism discussed later) produced in the Big Bang may have led to the inequality [19]:

$$\Gamma(N_i \longrightarrow l^+ + ...) \neq \Gamma(N_i \longrightarrow l^- + ...) \tag{2.10}$$

The resulting lepton (l) asymmetry in conjunction with known Standard Model processes may have produced this eventual dominance of matter over anti-matter [20–22]. Probing CP violation with the related observed light neutrinos could elucidate this mechanism.

The oscillation probability for anti-neutrinos is arrived at after replacing U in Equation 2.9 with its complex conjugate. This operation leads to a minus sign instead of a plus sign just in front of the third term. Therefore, in the case that neutrinos exhibit CP violation, the probability of a neutrino of flavor α to oscillate into a neutrino of flavor β

would be different than the probability of an anti-neutrino of flavor α to oscillate into an anti-neutrino of flavor β [i.e. $P(\nu_\alpha \longrightarrow \nu_\beta) \neq P(\bar{\nu}_\alpha \longrightarrow \bar{\nu}_\beta]$. Note that Eq. 2.9 implies that disappearance experiments with sensitivity to $P(\nu_\alpha \longrightarrow \nu_\alpha)$ are not sensitive to CP violation as $\mathrm{Im}(U^*_{\alpha i} U_{\beta i} U_{\alpha j} U^*_{\beta j}) = 0$ when $\alpha = \beta$.

Including the missing $\hbar$ and c constants, specifying units, and setting $m_i^2 - m_j^2 = \Delta m_{ij}^2$ gives

$$\frac{\Delta m_{ij}^2 \, c^3 \, L}{4\hbar E} \approx 1.27 \times \frac{\Delta m_{ij}^2}{\mathrm{eV}^2} \frac{L}{\mathrm{km}} \frac{\mathrm{GeV}}{E} \ , \tag{2.11}$$

and the oscillation equation becomes

$$\begin{aligned} P(\nu_\alpha \longrightarrow \nu_\beta) = \delta_{\alpha\beta} \quad &- \quad 4 \sum_{i>j} \mathrm{Re}(U^*_{\alpha i} U_{\beta i} U_{\alpha j} U^*_{\beta j}) \sin^2(\tfrac{1.27 \Delta m_{ij}^2 L}{E}) \\ &+ \quad 2 \sum_{i>j} \mathrm{Im}(U^*_{\alpha i} U_{\beta i} U_{\alpha j} U^*_{\beta j}) \sin(\tfrac{2.54 \Delta m_{ij}^2 L}{E}) \end{aligned} \tag{2.12}$$

2.1.2 Two neutrino mixing

In an oscillation scenario with two neutrinos, the mixing matrix takes the form

$$U = \begin{bmatrix} \cos\theta & \sin\theta \\ -\sin\theta & \cos\theta \end{bmatrix} \ , \tag{2.13}$$

where θ represents a mixing angle. U is entirely real in this case. The relationship between neutrino mass eigenstate and flavor is therefore

$$\begin{bmatrix} \nu_\alpha \\ \nu_\beta \end{bmatrix} = \begin{bmatrix} \cos\theta & \sin\theta \\ -\sin\theta & \cos\theta \end{bmatrix} \begin{bmatrix} \nu_1 \\ \nu_2 \end{bmatrix} \ , \tag{2.14}$$

with the oscillation probability

$$P(\nu_\alpha \longrightarrow \nu_\beta) = \delta_{\alpha\beta} - 4 |U^*_{\alpha 2} U_{\beta 2} U_{\alpha 1} U^*_{\beta 1}| \sin^2(\frac{1.27 \Delta m^2 L}{E}) \tag{2.15}$$

After inserting the matrices into the oscillation probability equation, we arrive at

$$P(\nu_\alpha \longrightarrow \nu_\beta) = \delta_{\alpha\beta} - \sin^2 2\theta \sin^2(\frac{1.27 \Delta m^2 L}{E}) \ , \tag{2.16}$$

where Δm^2, L and E remain in eV^2, km and GeV, respectively.

The probability of neutrino disappearance ($\nu_\alpha \longrightarrow \nu_\alpha$) and appearance ($\nu_\alpha \longrightarrow \nu_\beta$) are given by the equation above. No oscillation takes place when $\theta = 0$.

2.1.3 Three neutrino mixing and complications

In the experimentally established three neutrino mixing scheme, the two neutrino mixing probability equation is often applicable as is discussed later. This is fortunate as the full three neutrino oscillation probability equation is complicated, carrying six parameters: three mixing angles, two mass squared differences, and a phase. Note that since $\Delta m^2_{12} + \Delta m^2_{23} + \Delta m^2_{31} = 0$, there are only two independent mass squared terms. The three neutrino mixing matrix can be written in terms of three component 3x3 matrices:

$$U = \begin{bmatrix} U_{e1} & U_{e2} & U_{e3} \\ U_{\mu 1} & U_{\mu 2} & U_{\mu 3} \\ U_{\tau 1} & U_{\tau 2} & U_{\tau 3} \end{bmatrix} \tag{2.17}$$

$$= \begin{bmatrix} 1 & 0 & 0 \\ 0 & c_{23} & s_{23} \\ 0 & -s_{23} & c_{23} \end{bmatrix} \begin{bmatrix} c_{13} & 0 & s_{13}e^{-i\delta} \\ 0 & 1 & 0 \\ -s_{13}e^{i\delta} & 0 & c_{13} \end{bmatrix} \begin{bmatrix} c_{12} & s_{12} & 0 \\ -s_{12} & c_{12} & 0 \\ 0 & 0 & 1 \end{bmatrix} \begin{bmatrix} e^{i\alpha_1/2} & 0 & 0 \\ 0 & e^{i\alpha_2/2} & 0 \\ 0 & 0 & 1 \end{bmatrix}$$

$$= \begin{bmatrix} c_{12}c_{13} & s_{12}c_{13} & s_{13}e^{-i\delta} \\ -s_{12}c_{23} - c_{12}s_{23}s_{13}e^{i\delta} & c_{12}c_{23} - s_{12}s_{23}s_{13}e^{i\delta} & s_{23}c_{13} \\ s_{12}s_{23} - c_{12}c_{23}s_{13}e^{i\delta} & -c_{12}s_{23} - s_{12}c_{23}s_{13}e^{i\delta} & c_{23}c_{13} \end{bmatrix} \begin{bmatrix} e^{i\alpha_1/2} & 0 & 0 \\ 0 & e^{i\alpha_2/2} & 0 \\ 0 & 0 & 1 \end{bmatrix},$$

where $c_{ij} = \cos\theta_{ij}$ and $s_{ij} = \sin\theta_{ij}$. The variables δ and $\alpha_{1,2}$ are phases associated with CP violation. $\alpha_{1,2}$ are non-zero only if neutrinos are their own anti-particles and do not appear in the equation(s) governing oscillation probability regardless. However, these phases do affect neutrinoless double beta decay significantly. Neutrinos are there own anti-particles if there is just one neutrino object, with two (left-handed and right-handed) possible helicity states. In this case, the left-handed neutrino and right-handed neutrino, although still the same particle, would interact and behave differently based on the helicity differences alone. It is not currently known whether neutrinos are their own anti-particles.

Although the various observations of neutrino oscillation are discussed later, we now mention the three neutrino mixing parameters with specific reference to electron-neutrinos, muon-neutrinos, and tau-neutrinos. Experimentally, the muon-neutrino to tau-neutrino transition, as seen by long baseline and atmospheric experiments discussed below, does not feature a significant electron-neutrino contribution and largely follows a two-neutrino mixing probability governed by θ_{23} and Δm^2_{23}. The electron-neutrino contribution to this

mixing (expressed as the mixing angle θ_{13} or $\sin^2\theta_{13}$) has not been observed but is at least known to be small. Notably, the experimentally observable effect of CP violation depends on the value of θ_{13}, as $\sin(\theta_{13})$ is a factor in front of each $e^{i\delta}$ term in Eq. 2.17. The unfortunate case of $\theta_{13} = 0$ renders CP violation in the neutrino sector unobservable.

Just like in the atmospheric case, the solar neutrino oscillation transition $\nu_e \longrightarrow \nu_x$, where x is a superposition of e, μ and τ, can be described well by the two neutrino mixing equation with θ_{12} and Δm^2_{12} as the relevant parameters governing oscillation. That is, three neutrino mixing can usually be described in terms of two neutrinos. This is due to the following experimental facts: 1) θ_{13} is small and 2) two of the mass eigenstates have similar values, as compared to the third (i.e. $|\Delta m^2_{31}| \approx |\Delta m^2_{32}|$). For example, the ν_μ disappearance probability reduces to

$$P(\nu_\mu \longrightarrow \nu_\mu) = 1 - \sin^2(2\theta_{23})\sin^2(\frac{1.27\Delta m^2_{13}L}{4E}) + \text{sub-leading terms} \tag{2.18}$$

To date, atmospheric and accelerator-based neutrino oscillation experiments have little sensitivity to the sub-leading terms in the above equation. As a result, the sign of Δm^2_{13} is unknown. The mass hierarchy is said to be "normal" when ν_3 is more massive than ν_1 and is said to be "inverted" when ν_1 is more massive than ν_3. What is understood about the neutrino mass hierarchy can be seen in Figure 2.1. Although the above equation is symmetric under the $\Delta m^2 \longrightarrow -\Delta m^2$ exchange, so-called "matter effects" [23, 24] can alter the two-neutrino oscillation probability equation in such a way as to observe a difference between the two possible mass hierarchy orientations. Matter effects arise due to the fact that the electron-neutrino has a different "index of refraction" than muon- and tau-neutrinos as it travels through matter. Although each flavor encounters the same neutral-current interaction probability in normal matter, the electron-neutrino specifically can interact with matter via the charged-current. The muon- and tau-neutrinos cannot. This effect alters the oscillation probability equations in matter (as compared to vacuum) for neutrinos traveling large enough distances through the media.

2.1.4 Acquisition of Mass

Neutrino mass was not originally conceived to be part of the Standard Model due to the left (right) handed nature of neutrinos (anti-neutrinos). The Lagrangian density for a spin-$\frac{1}{2}$

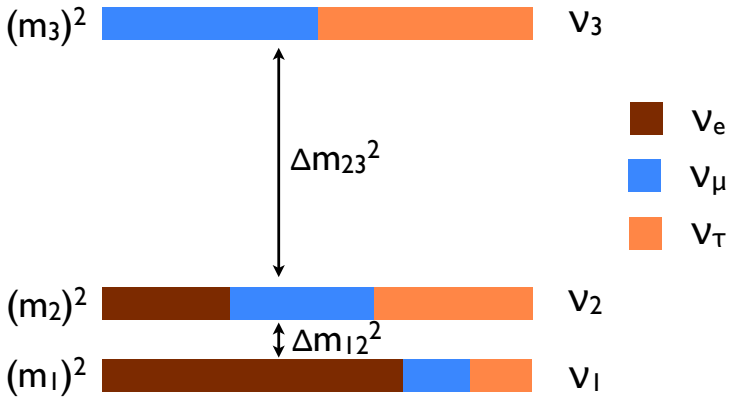

Figure 2.1: The neutrino mass hierarchy. The ν_e contribution to ν_3 is known to be small but remains unmeasured and the sign of Δm^2_{13} ($\Delta m^2_{13} > 0$ or $\Delta m^2_{13} < 0$) is unknown.

field Ψ is

$$\mathcal{L} = i\bar{\Psi}\gamma_\mu\partial_\mu\Psi - m\bar{\Psi}\Psi \ , \tag{2.19}$$

where $\bar{\Psi} = \Psi^\dagger\gamma^0$ and $\hbar = c = 1$. Note that applying the Euler-Lagrange equation to the above gives the Dirac equation for a massive spin-$\frac{1}{2}$ particle:

$$i\gamma_\mu\partial_\mu\Psi - m\Psi = 0 \tag{2.20}$$

The Lagrangian's mass term in each neutrino generation $\mathcal{L}_{\text{mass}} = m\bar{\nu}\nu$ can be written with the left and right-handed projections as

$$-\mathcal{L}_{\text{Dirac}} = m_D(\bar{\nu}_R\nu_L + \bar{\nu}_L\nu_R) \tag{2.21}$$

Since the mass term involves right-handed neutrinos and left-handed anti-neutrinos and these states have never been seen, the neutrino was thought to be massless for many years. In fact, the neutrino is massive and Eq. 2.21, describing the Dirac mass term in the Lagrangian, represents the neutrino coupling to the Higgs field and acquiring mass. This is in analogy to the Standard Model fermion acquisition of mass through the Higgs coupling and assumes that neutrinos are "Dirac particles" with ν_R and ν_L independent. In the case that neutrinos are Dirac particles, it is unclear why the coupling to the Higgs field yields such small masses for the neutrinos as compared to their generational counterparts, the charged

leptons. Another scenario exists for the origin of neutrino mass, however. That is, it is possible that there are more mass terms in the Lagrangian.

In the case that the neutrino is a "Majorana particle", ν_R and ν_L are not independent and $\nu_L = (\nu_R^C)$, $\nu_R = (\nu_L^C)$, where C stands for the charge conjugation operator ($\nu^C = C\overline{\nu}^T$) [25]. It follows that

$$\nu^C = (\nu_L + \nu_R)^C = (\nu_L)^C + (\nu_R)^C = \nu_R + \nu_L = \nu \tag{2.22}$$

In other words, a neutrino is described by two components, left-handed and right-handed, and $\nu = \nu^C$.

Majorana mass terms are made with only left-handed neutrinos, only right-handed neutrinos, or a combination. A left-handed Majorana mass in the Lagrangian looks like this:

$$-\mathcal{L}_{\text{Majorana}} = \frac{1}{2}(\overline{\nu_R^C + (\nu_R)}) = \frac{1}{2}\overline{\nu_R^C} M_R(\nu_R) + h.c.\ , \tag{2.23}$$

where $h.c.$ is the hermitian conjugate and M_R (which has units of mass) is a free parameter. Adding this term alongside the Dirac mass term in the Lagrangian, we get

$$-\mathcal{L}_{\text{mass}} = \bar{\nu}_L m_D \nu_R + \frac{1}{2}\overline{\nu_R^C} M_R \nu_R \ + \ h.c. = \frac{1}{2}\begin{bmatrix}\overline{\nu_L} & \overline{\nu_R^C}\end{bmatrix}\begin{bmatrix}0 & m_D \\ m_D & M_R\end{bmatrix}\begin{bmatrix}\nu_L^C \\ \nu_R\end{bmatrix} \ + \ h.c. \tag{2.24}$$

Diagonalizing the above equation ($\frac{1}{2}\overline{\Psi}\mathcal{M}\Psi^C + h.c.$) yields the eigenvalues of the matrix $\mathcal{M}$ ($= \begin{bmatrix}0 & m_D \\ m_D & M_R\end{bmatrix}$):

$$\lambda_\pm = \frac{M_R \pm \sqrt{M_R^2 + 4m_D^2}}{2} \tag{2.25}$$

We see that $\lambda_+ \approx M_R$ and $\lambda_- \approx \frac{-m_D^2}{M_R}$. The former corresponds to a heavy neutrino and the latter corresponds to a light neutrino. This "seesaw" (type-I) mechanism [26–28], so called because as one mass gets heavier the other one gets lighter, may explain why the known, measured neutrino masses are so tiny. The heavier mass may correspond to an as yet unseen heavy neutral lepton with mass comparable to the GUT scale ($\sim 10^{16}$ GeV). The potentially enormous difference in mass between light neutrinos (known to have mass from 0.001-0.1 eV) and heavy neutrinos could represent evidence for grand unification and help to explain the wide range of elementary particle masses.

2.2 The Evidence

A few of the most important neutrino oscillation results are discussed below. It should be noted that a multitude of experiments have probed the $(\Delta m^2, \theta)$ phase space with many turning up null (consistent with no oscillation) results. It is perhaps unfortunate that even a well performed neutrino oscillation experiment can see no evidence of oscillation if the $\frac{L}{E}$ is not chosen "correctly". Many of the non-null oscillation results are discussed below.

2.2.1 Solar neutrino oscillations

The proton-proton fusion chain reaction (with a small contribution from the CNO cycle) turns hydrogen into helium and powers the sun. The reactions that make up these processes produce a multitude of neutrinos. The "Standard Solar Model" [29] describes this convoluted spectrum in great detail in terms of each reaction (there are nine separate neutrino-creating reactions, including electron-capture) and predicts the neutrino flux we should expect at Earth.

About $6.5\times\ 10^{10}$ solar neutrinos travel through each square centimeter of Earth every second. The vast majority of solar neutrinos actually come from the first step in the proton-proton chain. However, with an energy less that 0.43 MeV, these "pp" interactions are extremely difficult to detect as their interaction cross section is comparatively low and interaction signature weak. Most of the solar neutrinos detected on Earth have come from ^{8}B neutrinos, produced in the proton-proton chain, which go up to about 15 MeV.

The Homestake experiment was the first to observe solar/cosmic neutrinos. Ray Davis and collaborators located a 100,000 gallon tank of dry-cleaning fluid (C_2Cl_4) 4850 feet underground at the Homestake Mine in Lead, South Dakota. By counting the number of argon isotopes inside the detector, created as a result of solar neutrino interactions with the fluid's chlorine ($\nu_e\ +\ ^{37}\mathrm{Cl}\ \longrightarrow\ ^{37}\mathrm{Ar}\ +\ e^-$, with a threshold of 0.8 MeV), Davis and colleagues were able to establish the solar neutrino rate/flux at the Earth. The Homestake experiment found that about one-third of the number of neutrinos expected from the Standard Solar Model were being detected [30]. Either something was happening to the neutrinos in between their creation inside the sun and their detection on Earth or the Standard Solar Model was wrong. The SAGE [31] and GALLEX [32] experiments also observed a significant neutrino flux deficit while searching for the reaction $\nu_e + {}^{71}\mathrm{Ga} \longrightarrow {}^{71}\mathrm{Ge} + e^-$.

The Kamioka Nucleon Decay Experiment (KamiokaNDE) started taking "production

data" in 1987. In addition to its primary goal of searching for proton decay, KamiokaNDE made important contributions to the understanding of solar and atmospheric neutrinos. The experiment was based on Cerenkov light detection with light-collecting photomultiplier tubes in a tank of 3,000 tons of water. Cerenkov light is created when a (neutrino-induced, in this case) charged particle moves faster than the speed of light in a medium. KamiokaNDE observed a significant solar neutrino deficit [33] in detecting the elastic-scattering interaction ($\nu_x + e^- \longrightarrow \nu_x + e^-$, where $x = e, \mu, \tau$). Note that this reaction is more sensitive to ν_e than ν_μ or ν_τ as the cross section for electron-neutrino scattering is about six times higher than either muon-neutrinos or tau-neutrinos. KamiokaNDE's ability to reconstruct the directionality of neutrinos confirmed that neutrinos were in fact being emitted by the sun [34] and their observation of a solar neutrino deficit further compounded the solar neutrino problem. Along with their solar measurements, KamiokaNDE observed that the ratio of atmospheric electron-flavor neutrinos to muon-flavor neutrinos was much smaller than that which was expected from theory [35]. This result came to be known as the "atmospheric neutrino problem" and is discussed below.

A Cerenkov-based detector deep underground called the Sudbury Neutrino Observatory (SNO) unambiguously solved the solar neutrino puzzle in 2001. SNO employed a detector design with 1,000 tons of heavy water surrounded by photomultiplier tubes that was capable of detecting the following reactions independently [36]:

$$\begin{aligned} \nu_e + d &\longrightarrow p + p + e^- \\ \nu_{e,\mu,\tau} + d &\longrightarrow p + n + \nu_{e,\mu,\tau} \end{aligned} \tag{2.26}$$

where p is a proton, n is a neutron, and d is a deuteron.

The first interaction is a charged-current interaction. As the solar neutrino energies (<18 MeV) are too low to produce a massive muon or tau (with rest masses of 106 MeV and 1780 MeV, respectively), the reaction only proceeds with electron-neutrinos. That is, the first interaction measures the electron-neutrino rate/flux. The second reaction is flavor-blind and measures the total, all-flavor neutrino rate/flux. SNO found that the total neutrino flux from the sun is three times greater than the electron-neutrino flux alone, confirming the Standard Solar Model and the results of the Homestake experiment. Neutrinos don't disappear, they transform into one another. Of course, the word "disappearance" is still used in neutrino oscillation to describe $\nu_x \longrightarrow \nu_y$, where ν_x interactions are identifiable and

create a charged lepton above detection threshold and ν_y interactions are not identifiable or do not create a charged lepton above detection threshold.

2.2.2 Atmospheric neutrino oscillations

Cosmic ray interactions with Earth's upper atmosphere are another source of neutrinos, most commonly through pion creation (e.g. $p + X \longrightarrow \pi^{\pm} + Y$, where X is an atmospheric molecule and Y are the other interaction products) and the subsequent decay chain ($\pi^{\pm} \longrightarrow \mu + \nu_{\mu}$, $\mu \longrightarrow e + \nu_{\mu} + \nu_e$). Although the flux of atmospheric neutrinos is much smaller than that of solar neutrinos, atmospheric neutrinos have a higher energy and therefore a larger interaction cross section than their solar counterparts.

The Super-Kamiokande experiment was created in order to definitively solve the solar and atmospheric neutrino problems. Basically a larger version of the original KamiokaNDE detector, Super-Kamiokande is made of 50 kilotons of pure water surrounded by 11,200 photomultiplier tubes. The experiment observed a zenith angle dependence of the flux of atmospheric muon-neutrinos. That is, muon neutrinos that were coming from above seemed to be more prevalent than muon-neutrinos coming from below. Something was happening to the muon-neutrinos in between their creation in the atmosphere on the other side of the Earth and their detection in Super-Kamiokande. That "something" was not happening to the muon-neutrinos that were created in the atmosphere above the detector. The muon-neutrinos were disappearing as a function of the distance they traveled. Note that this cannot be attributed to the apparent opacity of Earth as the minuscule neutrino interaction cross section makes the Earth basically transparent to neutrinos; the flux of neutrinos is not measurably diminished after traveling through the Earth. Electron-neutrinos created in the atmosphere, also detectable by Super-Kamiokande, did not exhibit the same disappearance behavior as muon-neutrinos. This observation, announced in 1998, marked the first evidence of neutrino oscillation and non-zero neutrino mass [37]. Note that the Super-Kamiokande experiment has since precisely measured atmospheric muon-neutrino oscillation (disappearance) [38] and even claims a modest tau-neutrino-like appearance signal [39], presumably coming from the atmospheric muon-neutrino to tau-neutrino transition.

The solar and atmospheric observations discussed so far indicate that electron-neutrinos of solar energies oscillate on a Sun-Earth distance scale or less and muon-neutrinos of atmospheric energies oscillate over diameter-of-the-Earth distance scales or less.

2.2.3 Reactor neutrino oscillations

Since the work of Cowan and Reines, many different oscillation experiments have used neutrinos produced at nuclear reactors as their neutrino sources. Here, the most recent of these to publish results, the Kamioka Liquid Scintillator Antineutrino Detector (KamLAND) experiment is described. KamLAND has used the neutrinos created in reactor fission product decays at 55 different Japanese reactors to search for neutrino oscillations. The detector employs about 1 kiloton of ultra-pure liquid scintillator in a transparent nylon balloon which is a flux weighted average distance of 180 km from an array of Japanese reactors. The inner detector is instrumented with 1,900 photomultiplier tubes which detect the inverse beta decay reaction ($\overline{\nu}_e + p \longrightarrow n + e^+$). The positron creates a prompt scintillation signal in the liquid, providing a measure of the anti-neutrino energy. The neutron capture, $\sim$200 μs later, provides the second part of the double coincidence signal used to tag neutrino events and differentiate them from background. KamLAND has measured the energies of the reactor neutrinos in the 1-8 MeV range, a range that overlaps with the solar neutrino energy spectrum. The experiment has observed almost two complete anti-electron-neutrino oscillation cycles with $\frac{L}{E}$ from about 20-100 km/MeV [40] (see Figure 2.2). This observation of a sinusoidal oscillation probability is consistent with the oscillation parameters as measured with solar neutrinos and rules out other non-sinusoidal neutrino damping hypotheses such as neutrino decoherence and decay [41–44]. KamLAND is distinguished from solar experiments in that it measures the total number of neutrinos in the detector as well as their precise energy spectrum. With the latter unique ability, KamLAND has very good sensitivity to the oscillation frequency. However, the amplitude of the oscillation effect is better measured by the solar neutrino experiments.

2.2.4 Accelerator neutrino oscillations

Accelerator-based experiments produce neutrino beams in much the same way neutrinos are made in the upper atmosphere; by taking advantage of a high energy proton collision to produce unstable pions which decay into neutrinos and muons (which themselves decay into neutrinos). These beams can be used to probe the $\frac{L}{E}$ region where atmospheric oscillations are observed as well as the higher Δm^2 region. The KEK to Kamioka (K2K) long baseline neutrino oscillation experiment has used neutrinos produced by a particle accelerator to measure their oscillation/disappearance behavior. The standard method for

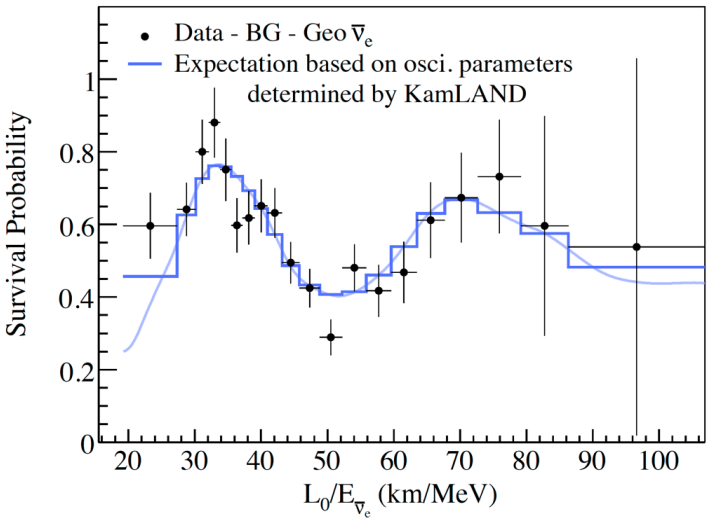

Figure 2.2: The KamLAND result, a striking confirmation of neutrino oscillation (taken from Ref [40]). Two distinct oscillation signals are observed.

creating an accelerator-based muon-neutrino beam is discussed at length in Chapter 4. K2K has searched for the disappearance of muon-neutrinos in a pure ∼1-2 GeV muon-neutrino beam using two sets of detectors at different distances from the neutrino creation point. Comparing the number of neutrinos as a function of flavor, energy, and distance traveled at the "near" detector to those expected at the "far" detector, given a nominal $1/r^2$ flux dependence, provides sensitivity to neutrino oscillation. Expecting about 158 events in the absence of oscillation based on observations at the 1 km baseline near detector, K2K observed 58 muon-neutrino-like events at the Super-Kamiokande far detector, 250 km away from the neutrino creation point [45]. This result is inconsistent with the no-oscillation hypothesis at 4.3σ and consistent with the atmospheric $\frac{L}{E}$ oscillatory behavior discussed above.

The Main Injector Neutrino Oscillation Search (MINOS), also a long baseline neutrino oscillation experiment, has both confirmed the K2K result and made precision measurements of the relevant oscillation parameters, θ_{23} and Δm^2_{23}, for neutrinos and anti-neutrinos [46, 47]. The experiment utilizes a magnetized (for differentiating the products of neutrino and anti-neutrino interactions) near-far detector configuration with a baseline of 735 km and a pure muon-neutrino. The polarization of the magnets used to focus the secondary mesons created in the proton interaction (eventually decaying into neutrinos) can be reversed in order to create a predominantly anti-muon-neutrino beam. Although primarily

a muon-neutrino and anti-muon-neutrino disappearance experiment, MINOS does feature some sensitivity to electron-neutrino [48, 49] and tau-neutrino appearance.

The Oscillation Project with Emulsion-tRacking Apparatus (OPERA) experiment studies neutrino oscillations at long baseline as well. The OPERA detector is located at Gran Sasso National Laboratory in Italy, 730 km away from the beam source at CERN. OPERA's goal is to detect (for the first time) tau-neutrinos in an initially muon-neutrino beam. In other words, OPERA is attempting to directly observe the oscillation of muon-neutrinos to tau-neutrinos rather than just the disappearance of muon-neutrinos. The average muon-neutrino energy in the beam is about 17 GeV/c, well above the ∼3.5 GeV/c required for a tau-neutrino (oscillated from muon-neutrino) to produce a detectable charged tau lepton in the final state. OPERA utilizes 150,000 "bricks" as its detection medium with a series of scintillators and spectrometers which provide the vertex location of the neutrino interaction in real time. Each brick is composed of photographic emulsion film interleaved with lead pieces. If a brick is identified as having a neutrino candidate of interest, the brick is extracted from the detector and the photograph is developed and analyzed. The film provides sub-mm resolution, necessary for identifying a charged-current tau-neutrino interaction. Specifically, the fine-grained detector is designed to identify the short-lived (sub-mm distance in the relevant tens-of-GeV energy range) tau decay kink. As of this writing, the OPERA experiment has observed a single tau-neutrino-like candidate event. The result is consistent with a tau-neutrino charged-current interaction with a significance of 2.4σ above background [50]. The collaboration does not yet claim that this observation is muon-neutrino to tau-neutrino oscillation.

2.2.5 Unconfirmed oscillations

A number of experiments have observed neutrino oscillation behavior from various sources that cannot be easily explained within the well established three neutrino mixing model. These results can be considered unconfirmed. Selected experiments and results are briefly described below.

LSND and MiniBooNE

The Liquid Scintillator Neutrino Detector (LSND) neutrino experiment searched for anti-muon-neutrino to anti-electron-neutrino oscillation at Los Alamos National Laboratory.

The experiment found a 3.8σ excess above background of anti-electron-neutrino events. LSND utilized a largely decay-at-rest source of neutrinos. The source was created with an intense 800 MeV proton on water-target collision. Approximately 95% of the π^+ ($\pi^+ \longrightarrow \mu^+ + \nu_\mu$) and daughter μ^+ ($\mu^+ \longrightarrow e^+ + \overline{\nu}_\mu + \nu_e$) created in the proton on target collision decayed at rest inside a copper beam stop adjacent to the proton target. The remaining 5% of π^+ decayed in flight. The LSND detector, featuring a cylindrical tank filled with 170 tons of liquid scintillator and surrounded by photomultiplier tubes for scintillation and Cerenkov light collection, was located about 30 m away from the beam stop. In the search for anti-muon-neutrino to anti-electron neutrino oscillations (with $\frac{L}{E} \sim 0.4 - 1.2\ \frac{\mathrm{m}}{\mathrm{MeV}}$), LSND detected anti-electron neutrino interactions via the positron from inverse beta decay ($\overline{\nu}_e + p \longrightarrow n + e^+$) followed by detection of the product neutron's capture on a free proton and subsequent nuclear de-excitation photon. The double coincidence signal of the positron (scintillation and Cerenkov) with energy up to 52 MeV and a 2.2 MeV photon $\sim$200 μs later allowed a precise determination of the anti-electron-neutrino flux at the detector with a small background contamination. The anti-electron-neutrino excess above background was measured to be 87.9$\pm$22.4$\pm$6.0 events consistent with $\overline{\nu}_e + p \longrightarrow n + e^+$ [51]. This measurement seems to indicate that neutrino oscillation occurs in the Δm^2 =0.2-10 $\frac{\mathrm{eV}^2}{\mathrm{c}^4}$ and that the neutrino mass is greater than 0.4 $\frac{\mathrm{eV}}{\mathrm{c}^2}$.

The Δm^2 measured by LSND is inconsistent with observations from the atmospheric/long-baseline and reactor/solar observations (assuming a three neutrino model), whose Δm^2's are 10^{-3} eV^2 and 10^{-5} eV^2, respectively. With only two independent Δm^2's, the LSND result is in conflict with these measurements in a three neutrino hypothesis. One solution to explain the LSND result is to envision a "sterile" neutrino. Such a sterile neutrino, if it (or they) exists, is believed to either not couple to the weak force or not decay to the Z boson because of its large mass. The well measured Z-boson decay width indicates that the Z decays/couples to three flavors of neutrino [52, 53]. With a single sterile neutrino, the neutrino flavor state would become

$$\mid \nu_\alpha >= \sum_i^4 U^*_{\alpha i} \mid \nu_i > \tag{2.27}$$

The neutrino state would then be composed of four distinct mass eigenstates with one of them sterile. The most common models employed in an attempt to explain the LSND result usually involve a 3+1 (one sterile neutrino) or 3+2 (two sterile neutrinos) oscillation picture.

The MiniBooNE accelerator-based neutrino oscillation experiment was conceived in order to confirm or refute the LSND claim of anti-muon-neutrino to anti-electron-neutrino oscillation at Δm^2 =0.2-10 $\frac{\mathrm{eV}^2}{\mathrm{c}^4}$. The MiniBooNE experiment uses an intense 8 GeV proton beam from Fermilab's Booster Accelerator complex (see Section 4 for a description of how the Booster accelerator operates). The beam impinges on a beryllium target to eventually create a predominantly muon-neutrino beam. Note that MiniBooNE's horn current can be reversed in order to create an anti-muon-neutrino beam as well.

The MiniBooNE detector, a 12 m diameter spherical ball filled with pure mineral oil and surrounded by ∼1300 photomultiplier tubes, detects the scintillation and Cerenkov light produced in the ∼1 GeV neutrino interactions. Muon- and electron-neutrino charged-current interactions are identified by their characteristic Cerenkov ring patterns as seen by the detector. In 2007, MiniBooNE published its neutrino-mode result, a search for muon-neutrino to electron-neutrino oscillations in a two neutrino model. MiniBooNE excluded the oscillation hypothesis at the 98% confidence level [54]. Notably, however, the MiniBooNE experiment performed this initial search in neutrino-mode; the LSND results are for anti-neutrinos.

Since their initial result, MiniBooNE has switched to anti-neutrino mode. The latest MiniBooNE anti-neutrino oscillation result is consistent with anti-muon-neutrino to anti-electron-neutrino oscillations in the Δm^2 =0.1-1.0 $\frac{\mathrm{eV}^2}{\mathrm{c}^4}$ range and seems to be consistent with the LSND result [55]. The MiniBooNE excess of events in the 475< E_ν <1250 MeV energy range (L is fixed at 541 m) has a 0.5% probability of being due to the expected background. The LSND and MiniBooNE results can be seen together in Figure 2.3. MiniBooNE is still running in anti-neutrino-mode and hopes to improve the statistics-limited anti-neutrino result with final measurements expected to be published in the next few years.

2.2.6 Neutrino oscillation summary

The world's neutrino oscillation results in terms of mixing angle and squared mass splitting difference can be seen in Figure 2.4. The confirmed mixing parameters are measured to be (best fit value):

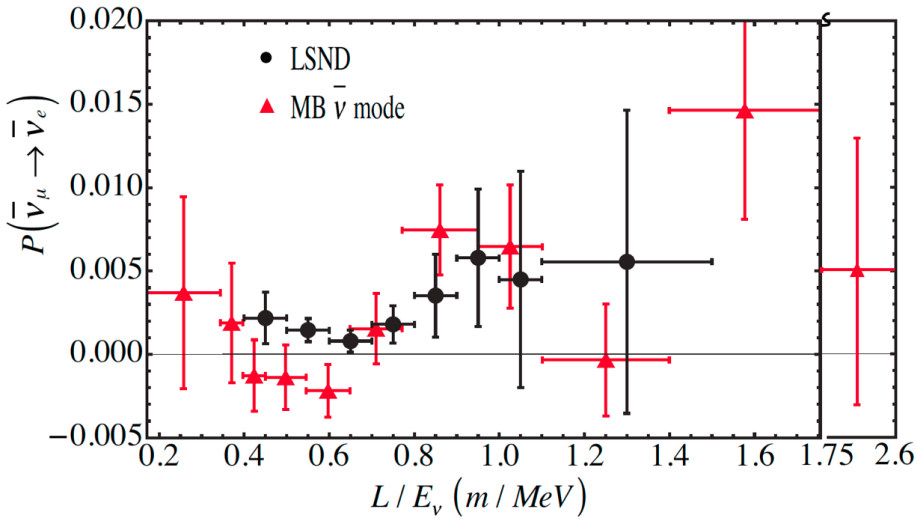

Figure 2.3: The LSND and MiniBooNE anti-muon-neutrino to anti-electron-neutrino oscillation results superimposed (from Reference [55]). The oscillatory behavior seen by both experiments is intriguing but remains unconfirmed.

$\lvert\Delta m^2_{31}\rvert$	$(2.30 - 2.56) \times 10^{-3}$ eV^2 ($\pm 1\ \sigma$)
$\lvert\Delta m^2_{21}\rvert$	$(7.7 - 8.4) \times 10^{-5}$ eV^2 ($\pm 1\ \sigma$)
θ_{23}	$36.8° - 53.2°$ (90% C.L.)
θ_{12}	$32.3° - 35.5°$ ($\pm 1\ \sigma$)
θ_{13}	$0° - 11.4°$ (90% C.L.)

There is currently no information available about the value of δ_{CP}, sign(Δm^2_{13}), and the "Dirac versus Majorana" nature of neutrinos. It is not yet known if there are more than three neutrinos. Note also that there is only an upper limit on the value of θ_{13}. Examining the kinematics of tritium nuclear beta decay has yielded the upper limit on the "effective mass" of the electron-neutrino, $m_{\nu_e} < 2.2$ eV (95% C.L.) [57, 58], where m_{ν_e} is defined as

$$m^2_{\nu_e} = \sum_i |U_{ei}|^2 m_i^2 \tag{2.28}$$

Note that this effective mass is dependent on the actual orientation of the mass hierarchy.

2.3 Selected Future Neutrino Oscillation Experiments

Future neutrino oscillation experiments seek to:

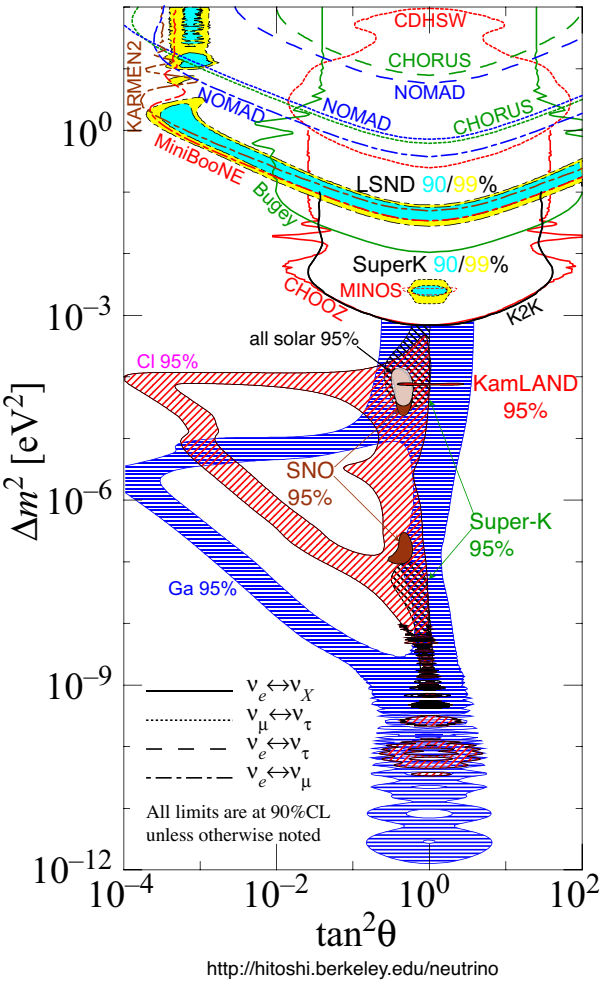

Figure 2.4: The world's neutrino oscillation data as of 2010, from Reference [56].

- Measure the "last" three-neutrino mixing parameter, θ_{13}.
- Precisely measure the other three-neutrino mixing parameters and confirm/disconfirm the three-neutrino mixing hypothesis.
- Understand the difference between neutrinos and anti-neutrinos.
- Determine the orientation of the mass hierarchy.
- Probe the entire relevant (Δm^2, θ) parameter space.
- Keep an eye out for the unexpected.

Understanding the Dirac/Majorana nature of the neutrino, measuring the absolute neutrino mass, fully characterizing solar neutrinos, detecting supernova diffuse neutrinos and

big bang neutrinos, measuring and understanding the oscillatory behavior of burst supernova neutrinos, and more, are all important, related subjects as well.

A few selected future neutrino oscillation experiments are described below.

2.3.1 T2K

The Tokai to Kamioka (T2K) project at the Japan Proton Accelerator Research Center (JPARC) is a long-baseline neutrino oscillation experiment in Japan [59]. The experimental concept is very similar to the aforementioned K2K and MINOS experiments with a near detector at Tokai 280 m from the neutrino source and a far detector (Super-Kamiokande) 295 km away from the source. T2K uses an off-axis beam [60] to produce a neutrino flux which is more monoenergetic than an on-axis beam and peaked in the interesting oscillation energy region (with fixed baseline, L). Notably, the T2K near detector features a magnetized segmented detector for neutrino and anti-neutrino differentiation. T2K will more precisely measure the atmospheric neutrino mixing parameters (θ_{23} and Δm^2_{23}) and will search for the unmeasured mixing angle θ_{13} via muon-neutrino to electron-neutrino appearance. Recently, the experiment has reported a hint of non-zero θ_{13} at the 2.5σ level [61]. The electron-neutrino events observed are consistent with $0.03(0.04) < \sin^2 2\theta_{13} < 0.28(0.34)$ for $\delta_{CP} = 0$ and a normal (inverted) mass hierarchy [61]. Future upgrades to the beam and/or (near/far) detectors could offer T2K sensitivity to as yet unseen CP violation in the lepton sector [e.g. $P(\nu_\mu \longrightarrow \nu_e) \neq P(\bar{\nu}_\mu \longrightarrow \bar{\nu}_e)$].

2.3.2 Double CHOOZ

A number of reactor-based experiments are set to probe lower and lower values of θ_{13} in the next few years [62, 63]. As of 2010, the CHOOZ reactor-based experiment boasted the most stringent limit for this parameter, $\sin^2(2\theta_{13}) < 0.15$ with 90% confidence level for $\Delta m^2_{13} = 2.5 \times 10^{-3}$ eV^2 [64]. The successor to CHOOZ, Double CHOOZ [65] is designed with two identical detectors at different distances from a nuclear reactor that detect and classify the neutrinos created in the decay of fission products there. Comparing the anti-neutrino rates at the near detector, at a distance of 400 m, and the far detector, at a distance of 1.05 km, provides sensitivity to θ_{13}. The detection concept is very similar to that used by KamLAND and LSND discussed above. Anti-electron-neutrinos are detected inside a 10 m^3 Gd-doped liquid scintillator target via a double coincidence signal featuring

prompt scintillation and neutron capture 30 μs later. The light signals are collected by 390 photomultipliers inside a non-scintillating mineral oil buffer that acts as a natural radioactivity shield. With the two detectors running together, Double CHOOZ expects to reach a sensitivity of $\sin^2(2\theta_{13}) > 0.03$ within 3 years.

2.3.3 NOνA

The accelerator-based NOνA [66] experiment is very similar to the MINOS experiment described earlier. It will utilize an upgraded version of the same beamline as MINOS, NuMI, although it will be exposed to an off-axis component of the beam. The purely (anti-)muon-neutrino beam will be about twice as intense as the present-day version of NuMI. The NuMI beamline is described at length in Section 4. NOνA will employ a near-far detector configuration 1 km and 810 km from the neutrino source, respectively, and will have the ability to run in either neutrino- or anti-neutrino-mode. Each detector will be composed of PVC extrusions filled with mineral oil and liquid scintillator. The light created in interactions of charged particles with these media will be routed out of the detector via wavelength shifting fibers and directed to a series of photodetectors for neutrino event analysis.

Just like T2K, NOνA will be measuring the atmospheric neutrino mixing parameters precisely, attempting to measure the last unmeasured mixing angle θ_{13}, and searching for CP violation in the lepton sector. Furthermore, with its comparatively long baseline (810 km), NOνA will be sensitive to matter effects on the electron-neutrino part of the oscillated neutrino beam. Depending on the true orientation of the mass hierarchy, matter effects can increase the electron-neutrino appearance rate with a normal hierarchy as compared to an inverted hierarchy. The converse is true for anti-neutrinos and the anti-electron neutrino appearance rate. Although NOνA may have sensitivity to determining the orientation of the mass hierarchy, these effects may be difficult to disentangle from possible CP violating effects, however.

2.3.4 Neutrino detection with Liquid Argon Time Projection Chamber techniques and the future

Neutrino physics has come a long way since Pauli's "desperate remedy" was introduced in 1930. Despite this, there exist many open questions in neutrino physics, all relevant for

cosmology and our understanding of the universe in general. The key to answering many of these questions is a precision neutrino detector. The ArgoNeuT Liquid Argon Time Projection Chamber (LArTPC) based experiment represents an important step towards the realization of a large-scale precision detector for neutrino oscillation and a multitude of other physics topics. As well as performing relevant physics measurements, ArgoNeuT has fulfilled important research and technology development towards building an ultra-large, kiloton-scale LArTPC. As a far detector in a long baseline neutrino oscillation experiment, such a device could search for non-zero θ_{13} and δ_{CP} as well as determine the orientation of the mass hierarchy, among other physics measurements.

Part II

Measuring Neutrino Properties

3 Neutrino Detection and the Liquid Argon Time Projection Chamber

A neutrino detector (or detectors) is the first of two ingredients required for an accelerator-based neutrino experiment. It is worth noting that some neutrino experiments require only a single (paid) ingredient, a detector, as their neutrino source is free. Examples include solar-, geo-, reactor-, and astrophysical-source-based neutrino experiments. An accelerator-based experiment detector's purpose is to reconstruct those particles that are created in a neutrino interaction in order to infer the energy and flavor (in the case of a charged-current interaction) of the neutrino in question. In an accelerator-based experiment, other parameters such as the initial neutrino direction and the distance the neutrino has traveled are largely known. A good choice for such a detector would be one that detects neutrinos with high efficiency and sufficient statistics, measures the flavor of the neutrinos with high purity, and reconstructs their energy precisely and accurately. As an added bonus, such detectors can be used for studying atmospheric/solar/geo neutrinos, proton decay, and supernova burst/diffuse neutrinos, among other things.

3.1 The LArTPC Concept

The goal of any detector in a neutrino experiment is to measure the properties, like flavor and energy, of the neutrinos in question. LArTPC technology is able to efficiently reconstruct neutrino flavor and energy with low background and systematics. Despite its detection power, the LArTPC concept is a simple one. A neutrino interacts with an argon atom inside the detector. The products of the interaction, the reconstruction of which is

required to determine the neutrino's properties, quickly traverse the liquid argon inside the volume. When the particles pass through, they leave a trail of ion-electron pairs in their wake. As argon is a noble element, this ionization is free to drift across the medium. An electric field is imposed in the TPC, the ions and electrons are pulled apart, and the electron ionization trails are drifted toward sensing wire planes that are oriented with respect to one another at an angle. The resulting wire signal pulses are then read out and analyzed. The ionization induces a current on the "induction" plane(s) and is collected by the "collection" plane. It is worth noting here that the induction signal is bipolar. Nearby electrons induce a current on the wire as they approach and as they recede, each case inducing the opposite sign current of the other. The collection signal is unipolar as charge approaches the wire and is collected.

Combining the information from both planes and detecting the events in time allows a three-dimensional image of the event to be obtained. That is, the wire plane orientation provides a two dimensional projection of the event as each wire crossing corresponds to a two dimensional point in space. Timing information fron the charge induced and collected in time allows the third (drift/time) coordinate to be obtained. Also, calorimetric information is acquired as the charge induced/collected is proportional to the amount of energy the particle deposited in the detector. Scintillation light (128 nm) is also produced in the interaction. Although some LArTPC-based experiments do not employ photomultiplier tubes to detect this light, future LArTPCs may use this information to measure t_0, the time of the initial neutrino interaction, more precisely. Accelerator-based experiments like ArgoNeuT obtain t_0 (and a trigger) from beam timing information. Light detection can also prove valuable in reducing the detector's minimum reconstructable energy threshold as well as providing a trigger for non-beam-related physics like supernova diffuse/burst neutrino detection and proton decay. In general, knowledge of the fast scintillation light complements the wire signals for efficient reconstruction of all types of interesting events.

A schematic depicting the LArTPC concept for neutrino detection can be seen in Figure 3.1. Similar designs have been employed and envisioned for use in the direct detection of WIMP dark matter. In fact, the world's most stringent limit on spin-independent WIMP interactions is currently owned by a LXeTPC-based experiment [67]. Argon, with a comparatively large density, short radiation length, and high scintillation yield (see Figure 3.2), is ideal for neutrino detection and event containment. Krypton and Xenon, although attractive for the same reasons in principle, are far less abundant in the atmosphere and

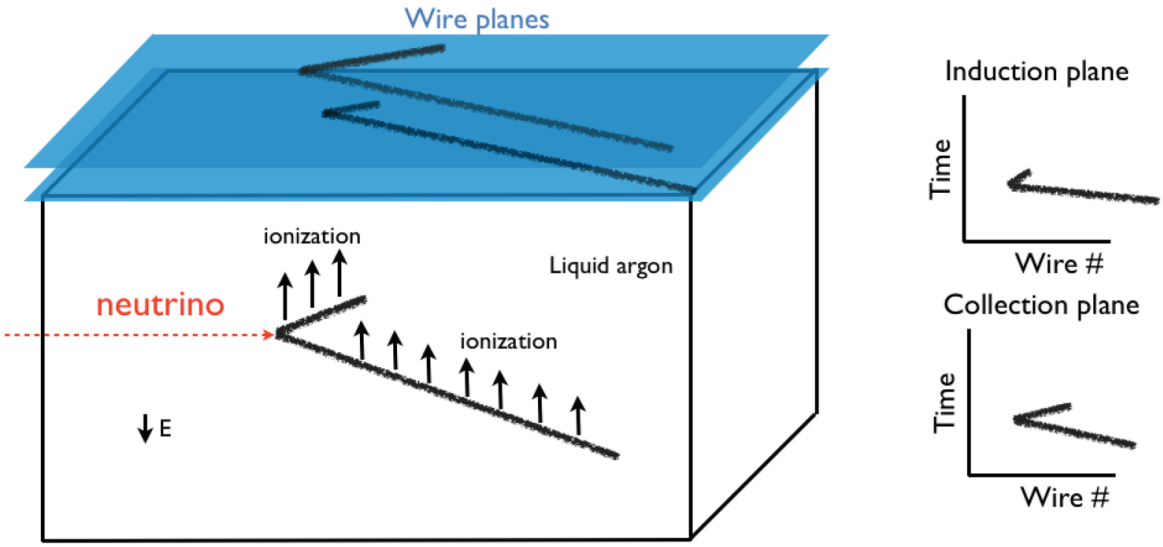

Figure 3.1: The LArTPC concept for neutrino detection. (Left) A neutrino comes in from the left, strikes an argon nucleus, and produces some particles. The ionization created along the charged particles' travels through the liquid argon is drifted to sensing wire planes via an applied electric field. (Right) Each wire plane measures the event in terms of time of detection and wire number. Knowledge of the wire orientation and position along with timing from both planes provides a three dimensional image of the event with complete calorimetric information.

therefore very expensive. Liquid, rather than gas, is used because of a larger target density leading to a higher interaction rate, higher ionization density for ease of detection, lower electron transport diffusion for better track reconstruction resolution, and dielectric properties accommodating of the TPC's high voltage requirements.

3.1.1 LArTPC specifications

A neutrino event as seen by the ArgoNeuT LArTPC's collection plane is shown in Figure 3.3. The event is seen in the (wire,time) view with the colors representing the collection plane wires' signal heights. Also visible is a single collection plane wire's signals in time.

A delicate balance of electric fields in the space between the drift region and the induction wire plane and then again in the space in between the induction and the collection wire planes is required for minimal signal attenuation. That is, for an electron to drift from space 1 to space 2, separated by a wire grid, the ratio of electric fields E_1 and E_2 needs to be carefully chosen to allow for maximum grid electron transparency. The transparency

	He	Ne	Ar	Kr	Xe
Boiling Point [K] @ 1atm	4.2	27.1	87.3	120.0	165.0
Density [g/cm^3]	0.125	1.2	1.4	2.4	3.0
Radiation Length [cm]	755.2	24.0	14.0	4.9	2.8
Scintillation [γ /MeV]	19,000	30,000	40,000	25,000	42,000
dE/dx [MeV/cm]	0.24	1.4	2.1	3.0	3.8
Scintillation λ [nm]	80	78	128	150	175

Figure 3.2: The most relevant (for use in particle detection and characterization) properties of the stable noble elements. Among the noble elements, argon represents a compromise between optimal neutrino detection properties and price per mass.

condition [68] requires that

$$\frac{E_2}{E_1} > \frac{1+\rho}{1-\rho} \ , \tag{3.1}$$

where $\rho = \frac{2\pi r}{a}$ and r and a are the wire radius and the space between the wires, respectively. This equation can be employed for more than just two adjacent wire planes. LArTPCs can employ a"shield" plane separating the induction and collections planes from the larger drift region. The shield plane acts to prevent the other planes from having a charge induced on them before the ionization enters the wire plane region. That is, the induction and collection planes are largely immune to induced charge from drifting ionization as long as the shield plane satisfies the following equation:

$$\frac{a}{2\pi s}\ln(\frac{a}{2\pi r}) \sim 1 \ , \tag{3.2}$$

where s is the distance between the shield plane and the adjacent plane (the induction plane in our example). The shield plane also acts to help shape the field in the region near the wire planes and can be instrumented in the case that a third "view" of the event is deemed necessary. This extra view can aid in the positional and calorimetric reconstruction of neutrino events. Figure 3.4 shows the three relevant drift regions for LArTPCs with two instrumented planes and a shield plane. In the figure, the fields E_1, E_2, and E_3 are chosen

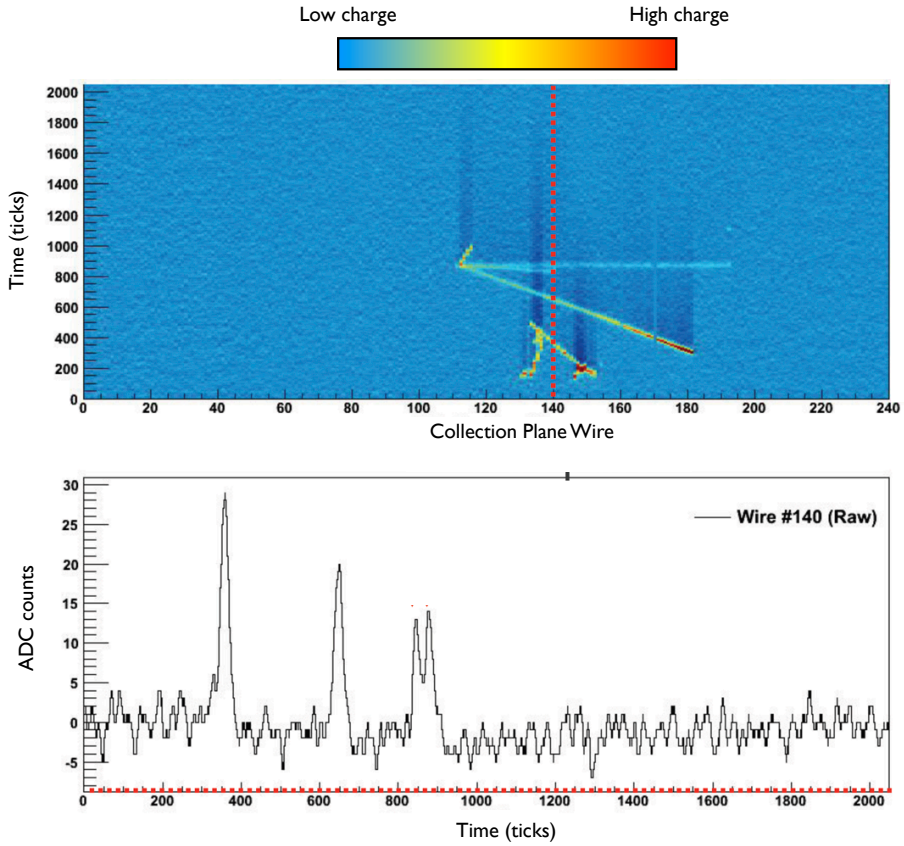

Figure 3.3: (Top) A neutrino event in ArgoNeuT as seen in the collection plane's (wire, time) view. The colors are indicative of the amount of charge collected on the wire, with blue<yellow<red. (Bottom) The wire view in raw ADC counts as a function of time for Wire #140. Notice that the four separate wire bump signals correspond to the four distinct tracks as seen in the collection plane view.

to satisfy Eq. 3.1, given a wire diameter and spacing, and the plane separation is chosen to satisfy Eq. 3.2. Note also that the collection plane needs to carry a positive voltage and the cathode must carry a negative voltage for the ionization to be properly drifted and detected. A common TPC drift field (E_1) chosen for LArTPCs is 500 V/cm, in consideration of high voltage practicality, electron drift velocity (1.5-1.6 mm/μs at 500 V/cm), and sampling rate.

3.1.2 Calorimetry

From charge to energy

The charge detected by the wire planes is proportional to the amount of energy deposited by the corresponding particle on its travels in the liquid argon. Along with gaining knowledge

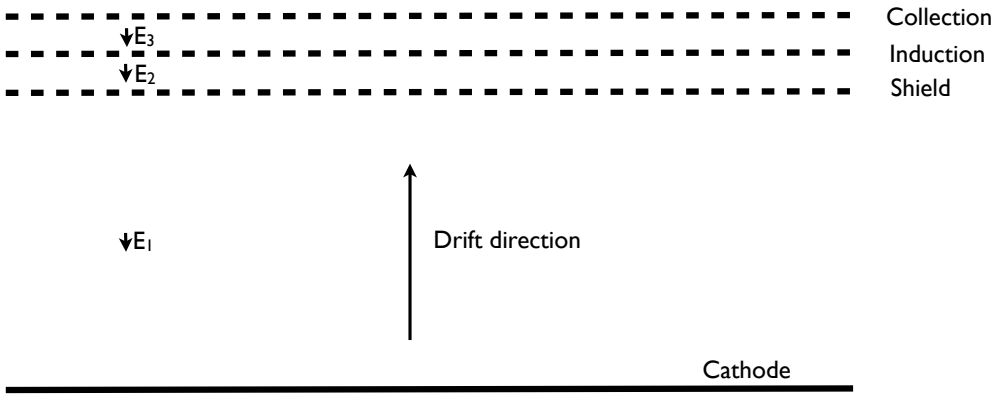

Figure 3.4: A LArTPC's wire planes and drift regions. ArgoNeuT instruments the induction and collection plane. MicroBooNE will instrument the shield, induction, and collection planes.

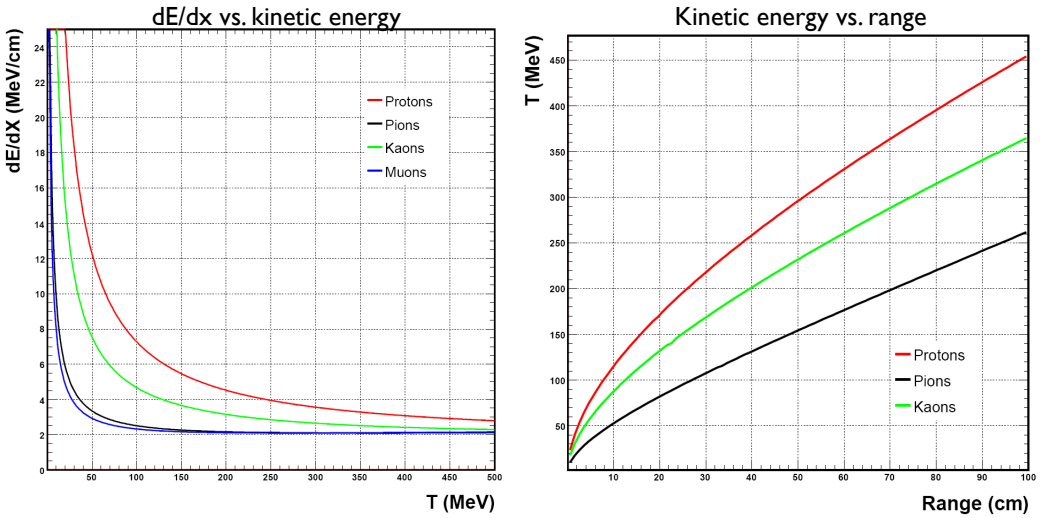

Figure 3.5: (Left) $\frac{dE}{dx}$ versus kinetic energy and (right) kinetic energy versus range for a variety of relevant particles. These plots are taken from Reference [69].

of the amount of energy deposited along a stopping track and hence the kinetic energy of the initial particle, calorimetry is useful for identifying particles. The energy deposited along the track per unit length, $\frac{dE}{dx}$, often used in conjunction with track range in the case that the particle stops, can be utilized to differentiate one particle from another (see Figure 3.5).

Separating gammas from electrons is vital to the success of future LArTPCs used as detectors in long baseline electron-neutrino appearance searches. As one example, neutral-current π^0 ($\nu_l N \longrightarrow l^{\pm} N \pi^0$, with N a nucleon and $l^{\pm}$ a charged lepton) events are a

dominant background for signal electron-neutrino events. Note that there are other cases in which a non-electron-neutrino event can mimic the signal process such as neutral-current resonant events featuring a radiative delta decay ($\Delta \longrightarrow N\gamma$, where Δ is the resonance).

A discrimination method using $\frac{dE}{dx}$ can be employed in order to differentiate gamma-induced electromagnetic showers from electron-induced ones. The $\frac{dE}{dx}$ of a gamma-induced electron-positron pair track is approximately twice as large as that of a single electron track. Taking advantage of this fact and determining $\frac{dE}{dx}$ can provide a particle identification tag before the electromagnetic shower of the track begins and the track becomes difficult to characterize, usually in the first few centimeters of track.

Neutral-current π^0 and charged-current electron-neutrino events are generally separated by the following:

- (1) A shower with a displaced vertex is an indication of a gamma conversion.
- (2) A charged-current, electron-neutrino event generally features a single shower. A neutral-current, neutral pion event generally features two showers.
- (3) An electron from a charged-current, electron-neutrino event is close to minimum ionizing at the beginning of its track, before the shower begins. A converted gamma, converting into an electron-positron pair, is close to doubly minimum ionizing at the beginning of its track, before the shower begins. Measuring the amount of energy lost per unit length ($\frac{dE}{dx}$) in the first few centimeters of track can assist in differentiating the two classes of events in case ambiguity is left after considering items 1 and 2 above.

The conversion from charge collected to $\frac{dE}{dx}$ requires knowledge of the preamplifier/electronics calibration factor (which turns ADC counts into charge), the amount of ionization-attenuating impurities in the medium, the effect of ionization-attenuating recombination of electrons with argon ions, the efficiency of charge collection, and track orientation. The ionization-attenuating impurities in the medium refers to electronegative impurities (e.g. H_2O) which can prevent the ionization electrons from reaching the sensing wire planes. This is discussed in detail in Section 5.4. The ionization-attenuating recombination of electrons with ions refers to the possibility for a liberated ionization electron to be immediately recaptured on an argon ion after creation via electrostatic pull. This effect is a function of the energy density of the charge and the applied electric field, which can more easily pull the electron

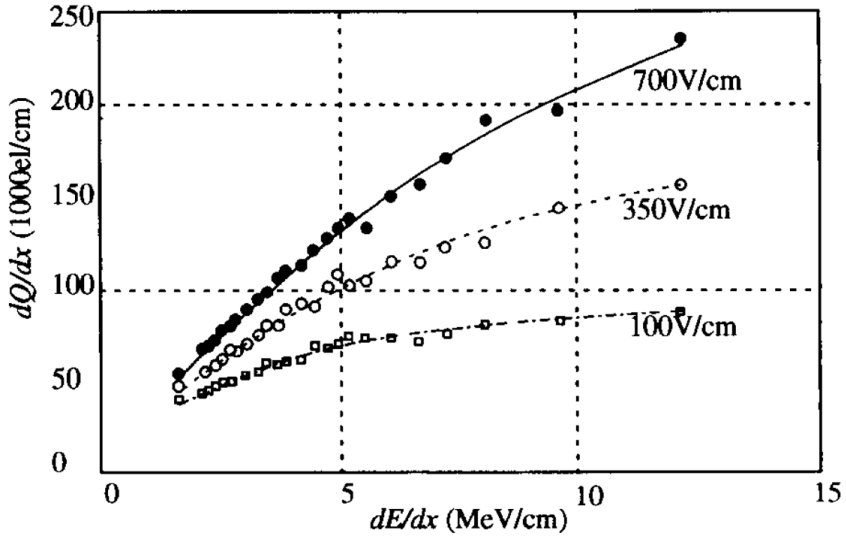

Figure 3.6: The effect of recombination in converting charge deposited into energy deposited. The <dQ/dx> dependence on <dE/dx> is shown for a few electric field values. This plot has been taken from Reference [71].

and ion apart at higher values. In consideration of the recombination effect only:

$$\frac{dQ_{\text{cor}}}{dx} = A\frac{(dE/dx)}{1 + K_B(dE/dx)}, \tag{3.3}$$

where Q_{cor} is the corrected charge and A and K_B are measured constants (constant in a given electric field). This semi-empirical equation is generally referred to as Birk's law [70]. The constants A and K_B have been measured by Reference [71] at a number of different voltages typical of LArTPC-based experiments. Figure 3.6 shows the effect of recombination at different voltages. Notice that the strength of recombination can be quite substantial and that special care needs to be taken when converting between charge and energy for particles that have low kinetic energy and are close to stopping. As $\frac{dE}{dx}$ is rapidly changing for such particles, the charge-energy conversion factor is rapidly changing as well.

Energy determination with multiple scattering

Analyzing a track in terms of range-out distance is the main method in determining a particle's initial energy in a LArTPC. Other techniques exist, however, and can be used together with simply adding up all the charge deposited along the track path in order to more precisely measure its energy. A magnetic field inside a LArTPC has been demonstrated [72] and opens up the possibility for future LArTPCs to measure a track's momentum via the

curvature of the track in a magnetic field. However, not all future LArTPC proposals call for this feature. The ICARUS collaboration has demonstrated that muon momentum can be determined (even in the absence of both track range out and magnetic field) based on Coulomb multiple scattering along the particle's path as long as the muon in question travels >1 m and has energy less than ∼10 GeV [73]. The Kalman filter technique [74] employed to determine a track's energy characterizes the amount of multiple scattering along a track segment, a variable that is dependent on the particle's energy. As multiple scattering is not discernible with standard millimeter-scale LArTPC position resolution for particle tracks of >10 GeV, the technique is only applicable to muons with energy below that threshold. ICARUS finds that a 3 GeV muon's momentum can be determined to ∼25% after traveling 100 cm, with the momentum resolution improving as track length increases and as energy decreases. The muon momentum determination using multiple scattering is an important result for those experiments that cannot hope to contain the majority of their GeV-scale neutrino-induced muons and do not feature a magnetic field.

3.2 A Look Towards the Future of LArTPCs

3.2.1 MicroBooNE

MicroBooNE is a LArTPC-based experiment set to start taking data in the Booster Neutrino Beam (BNB) at Fermilab in 2013. The MicroBooNE experiment's goals are threefold: understand the MiniBooNE low energy anomaly [54, 75], measure neutrino cross sections in the ∼1 GeV energy range, and perform research and development for future LArTPC detectors. The MicroBooNE detector specifications are shown in Table 3.1.

Cryostat volume	170 tons
Active TPC volume	90 tons
# Electronic channels	∼8300 over 3 planes
Wire spacing	3 mm
Electronics style (temperature)	CMOS (87 K)
Max. drift length (time)	2.5 m (∼1.6 ms)
Light collection	30 8" Hamamatsu PMTs

Table 3.1: MicroBooNE detector specifications.

In their search for two neutrino appearance (muon-neutrino to electron-neutrino) oscillations, MiniBooNE excluded the LSND oscillation hypothesis [51] at the 98% confidence level [54]. However, a $>3\sigma$ low energy excess (statistical and systematic errors included) of electron/gamma-like events remained at low neutrino energy (200-475 MeV). Notably, the MiniBooNE experiment cannot differentiate electron tracks/showers from gamma-induced tracks/showers (e.g. arising from neutral-current π^0 events). The excess, 96±19(stat.)±21(syst.) events from 300-475 MeV and 91±19(stat.)±25(syst.) events from 200-300 MeV suggest an unpredicted background or new physics [76–83]. Another interesting possible explanation of the excess is that the intrinsic electron-neutrino content of the beam is actually disappearing and creating a deficit of electron-like events at high energy [84]. This idea seems to fit well with the reactor antineutrino anomaly [85] and a 3+1 sterile neutrino model, although Reference [86] notes that LSND [87] and KARMEN [88] severely restrict electron-neutrino disappearance as an explanation for the low-energy excess. In whatever new physics or background scenario, this excess must be understood. MicroBooNE will have the ability to differentiate electrons from gammas with high purity and efficiency using $\frac{dE}{dx}$ and event topology. The experiment will be sensitive to the MiniBooNE low energy anomaly at the 4-5σ level depending on the actual (electron-like or gamma-like) nature of the signal.

MicroBooNE will also measure neutrino cross sections in the ∼1 GeV range. All of these measurements will be interesting in their own right and relevant for long baseline oscillation searches as well. Figure 3.7 shows the expected fraction of each event class in MicroBooNE in the BNB at Fermilab. There are about 100,000 (130,000) expected BNB muon-neutrino charged-current (charged-current plus neutral-current) interactions in MicroBooNE in a two year neutrino-mode run with 6×10^{20} protons on target (POT). Note that MicroBooNE will also be exposed to the NuMI off-axis beam, a potentially rich source for neutrino cross section physics measurements, among other things.

Along with its physics goals, MicroBooNE has the following LArTPC research and development goals:

- Create a simulation framework, automated reconstruction, and analysis tools for neutrino measurements with LArTPCs.
- Understand cosmic ray backgrounds in a surface detector.
- Gain experience with cold electronics.

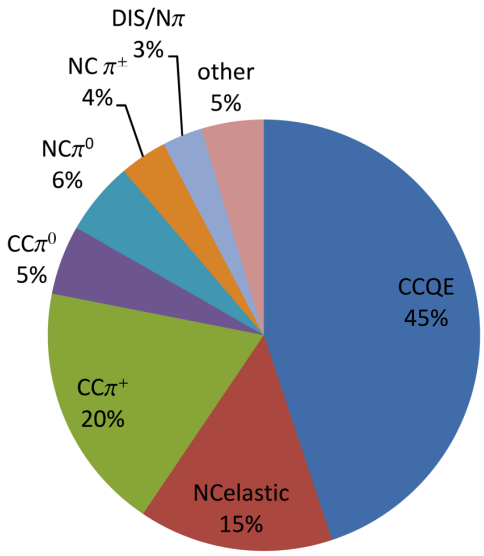

Figure 3.7: The expected fraction of various event classes in MicroBooNE exposed to the BNB. The total number of expected events is about 130,000 in two years of running (6×10^{20} POT). The definitions of each channel can be seen with Table 6.1

- Test the effectiveness of a gaseous argon purge in a large, instrumented vessel for achieving/maintaining purity. This technique may be effective for the pre-fill removal of impurities in non-evacuable vessels.
- Build and install the TPC, wire planes, purity monitors, photomultiplier tubes, etc.
- Refine physics and reconstruction sensitivity/efficiency estimates for future LArTPC-based detectors.

3.2.2 ICARUS

The ICARUS collaboration has pioneered the use of the LArTPC for neutrino detection. The culmination of this work is the successful commissioning and running of the ICARUS-T600 [89, 90] LArTPC exposed to the on-axis CNGS beam, 732 km away from the source. The experiment began operations in 2010. The ICARUS-T600 is the largest LArTPC ever built, with a total active mass of about 476 tons. The detector utilizes a dual module design with two separate drift regions, instrumented with about 54,000 wires. Along with being a major step towards the realization of a multi-kiloton LArTPC, the experiment expects to collect about 1200 muon-neutrino charged-current events and 10 electron-neutrino events per year. In addition to cross section measurements and the refinement of the LArTPC

technique, the ICARUS T600 will search for tau-neutrino appearance in the primarily muon-neutrino CNGS beam and sterile neutrinos as suggested by the LSND result [51].

The ICARUS collaboration has recently put forward the idea of re-using the T600 as a far detector in a short baseline neutrino oscillation experiment [91]. The near and far LArTPC-based detectors would be at 127 m and 850 m, respectively, and would employ the CERN-PS in order to explore the LSND, MiniBooNE, and reactor anomalies previously mentioned [92].

3.2.3 Kiloton-scale LArTPCs

The focus of this LArTPC introduction has largely been on detectors for long baseline neutrino oscillation electron-neutrino appearance searches. Along with the standard accelerator-based physics opportunities (precise atmospheric oscillation parameter determination, searching for non-zero θ_{13} and δ_{CP}, searching for tau-neutrino appearance, determining the orientation of the mass hierarchy, and the always requisite "looking for the unexpected"), there are a number of other physics measurements possible with a large precision detector. A comprehensive physics program will require a massive device deep underground. The technologies under consideration for such a detector or detectors are water Cerenkov and LArTPC. A few non-accelerator-based physics opportunities are mentioned briefly here.

Other uses: Proton decay

LArTPC-based detectors with a significant mass are sensitive to proton decay. The latest Super-Kamiokande (a water Cerenkov detector) results [93] provide lower limits on the proton half life of $\sim 1 \times 10^{33}$ years by searching for (among other decay modes) the $p \longrightarrow e^{+}\pi^{0}$ decay. While Cerenkov-based detectors are most sensitive to this channel, they are inefficient at detecting proton decay modes with daughter particles produced below Cerenkov threshold. With low background, high efficiency, and the ability to "see" particles below Cerenkov threshold, LArTPCs can offer more sensitivity than a similar mass water-based detector in most other channels, especially those involving kaons in the final state [94]. By searching for the $p \longrightarrow K^{+}\overline{\nu}$ channel, a 100 kiloton LArTPC could reach a $\sim 1 \times 10^{35}$ year sensitivity with a ten year run [95]. Of course, the two technologies could be complementary, with a large water detector providing extra sensitivity in the positron decay mode and a large LArTPC providing extra sensitivity in the kaon and single gamma decay modes.

Other uses: Atmospheric neutrinos

Exploring and more precisely measuring the atmospheric neutrino oscillation mixing parameters are obvious goals for any large neutrino detector. A LArTPC, however, can also search for tau-neutrino appearance from originally-muon-flavored atmospheric neutrinos [96, 97]. An observation of tau-neutrino appearance would be a confirmation of the three neutrino mixing model and the muon-neutrino to tau-neutrino transition, in general. Furthermore, a precise cross section measurement of the least well understood observed Standard Model particle (the tau-neutrino) would be an interesting probe of the Standard Model. To date, only ten tau-neutrino events have ever been directly observed [10, 50].

Other uses: Burst and diffuse supernova neutrinos

The detection of solar neutrinos discussed above marked the beginning of neutrino astronomy. The field of extragalactic neutrino astronomy was initiated when neutrinos were detected from Supernova 1987A by the Kamiokande II [98], IMB [99], and Baksan [100] experiments. The experiments detected 11, 8, and 5 neutrinos, respectively, in a burst that lasted <13 seconds. A star's gravitational core collapse leading to a (type-II) supernova provides an enormous amount of neutrinos. A 50 kiloton LArTPC could detect about 5,000 neutrino events from a supernova at 10 kpc from the Earth. This can be compared to the ∼20 total neutrinos that were seen from the SN1987a burst. Such a large sample could provide sensitivity to θ_{13} and the orientation of the mass hierarchy along with knowledge of supernova evolution and a probe of beyond the Standard Model physics [101, 102]. Just like for most of the mentioned physics possibilities, water and argon detectors could be quite complementary in discerning the flavor composition and oscillatory properties of neutrinos from a supernova burst.

Supernova diffuse (also called relic) neutrinos are the neutrinos that are left over from all of the type-II supernovae that have ever occurred in the universe. No definitive signal for these particles has been seen. Detecting and characterizing the diffuse neutrino background could help us understand the type-II supernova rate and could shed light on the supernova mechanism itself. The former is proportional to the star formation rate for stars with mass greater than eight times that of the sun, an important cosmological parameter [103]. Although the sensitivity prediction is highly dependent on the diffuse neutrino flux, it is estimated that a 100 kiloton LArTPC could observe the supernova relic neutrinos at the

4σ level with five years of data taking [103].

3.2.4 The technical challenges of a large LArTPC

The ArgoNeuT experiment is one of the first steps in the phased US program towards a kilton-scale LArTPC. This thesis would be incomplete without mentioning that ArgoNeuT is largely a research and development venture towards such a detector. Much of the work in this thesis has been and will be applied to MicroBooNE and future LArTPCs.

There are a number of technical challenges associated with LArTPC-based designs. Many of these challenges become enhanced with an increasing size detector but all of the issues listed apply to almost all sizes of LArTPC. It should be noted that the signal processing, automated reconstruction, and analysis tasks necessary for physics with LArTPC neutrino experiments also present rather significant challenges. These topics are discussed at length in Chapter 7.

Safety

Kilotons of liquid argon in a confined space represents an obvious potential safety hazard. Although argon is inert and not a direct (loosely defined) danger to humans, argon gas can push away oxygen from the breathing pathway and render a human oxygen-less. The expansion ratio, or volume of gas at room temperature divided by volume of liquid at the boiling point, is about 850. Therefore, a catastrophic spill of even just a few tons of liquid argon could become a dangerous situation quite quickly, especially in a confined area. Implementing measures to avoid and possibly contain such a spill deep underground is a challenge. Filling the detector (along with filling it in a safe way) is another closely related issue facing future large LArTPCs underground. Gas relief lines from each isolated argon container/pipe, oxygen deficiency alarms, slow control monitoring with pressure/temperature feedback loops, fast volume exchange rate of ambient air, spill containment vessel(s), etc. are just some of the measures that need to be employed for safe running underground.

Purity

The liquid argon medium must be thousands of times more pure than is commercially available for electron ionization to be readily detected by the sensing wire planes given a standard drift length of $\sim$100s of centimeters in a large LArTPC. This topic and methods

for achieving pure liquid argon are discussed at length in Section 5.4. It would seem that an open volume 20 kiloton detector with a reasonable number of wires would necessarily have a maximum electron drift of >10 m from cathode to the wire planes. Such a long drift is an incredible challenge. A modularized design, featuring a segmented TPC design (i.e. multiple drift regions), can mitigate this potential problem and push the drift distance to a more manageable ∼2-3 m. Of course, this design comes at the expense of more wires and readout channels.

Building a ship (in a bottle)

Building the detector components of a large LArTPC will be challenging, especially underground. The construction logistics and infrastructure requirement challenges for assembling a multi-kiloton cryogenic detector hundreds of feet underground are immense. Directing high voltage inside the detector, purity monitoring, maintaining a uniform field over a large volume, stringing wires at constant tension over long distances, cryostat pressure issues, temperature and pressure gradients, maintaing liquid argon purity, insulation and removing heat loads, keeping the argon cold, ability to evacuate (or not), are just some of the issues associated with such a device.

Light collection

As mentioned earlier, liquid argon is a good scintillator and the light created by charged particle tracks can be readily detected. The light generated in an interaction can be used to assist in the reconstruction of charged particle tracks, especially in the case of short, low energy tracks, and/or can be used as a trigger as previously mentioned. Such a triggering system would be especially important for non-beam-related (i.e. no natural trigger available) physics with a LArTPC such as a proton decay search, atmospheric neutrino oscillation characterization, and supernova burst and diffuse neutrino detection. Although the standard wire signals themselves can be used as a trigger at some level, the absolute drift/time coordinate of the track in question cannot be determined well in the case of a wire trigger. Ideas exist, however, to take advantage of the charge induced on the first wire plane as soon as the track arrives in the detector and determine the absolute drift/time coordinate of the track in that way. Unfortunately, this determination can be confused by the presence of other, non-interesting (e.g. cosmic ray) tracks within the drift time window.

A method for light detection, with nanosecond-scale timing resolution and sensitivity to low energy tracks, is a welcome addition to a beam-based LArTPC experiment and seemingly a necessity for those LArTPC experiments wishing to accomplish non-beam-based physics as well.

Scintillation in liquid argon is dominated by two main processes:

$$\mathrm{Ar}^{*} + \mathrm{Ar} \longrightarrow \mathrm{Ar}_2^{*} \longrightarrow 2\mathrm{Ar} + \gamma$$

$$\mathrm{Ar}^{+} + \mathrm{Ar} \longrightarrow \mathrm{Ar}_2^{+} + e^{-} \longrightarrow \mathrm{Ar}^{**} + \mathrm{Ar} \longrightarrow \mathrm{Ar}_2^{*} \longrightarrow 2\mathrm{Ar} + \gamma$$

The first process, referred to as self trapped exciton luminescence, results in the neutrino interaction's charged-particle-induced argon excitation creating a molecular pair with a neighbor argon atom and then de-exciting. The latter process, referred to as recombination luminescence, results in the neutrino interaction's charged-particle-induced argon ion recombining with a neighbor argon atom to form a molecular ion. This ion subsequently breaks apart and de-excites by releasing a photon. Both processes mentioned result in a single 128 nm photon emission. The timing of the emission of these light signals depends on the ionization density and is made up of a single and triplet state with 6 ns and 1.6 μs decay constants. Such light is very difficult to detect with conventional photomultiplier tubes as glass has a low transmittance at these wavelengths. A high transmittance light detection glass alternative can be utilized. More common, however, is a wavelength shifter used in conjunction with glass-based photomultiplier tubes to shift the light into the visible spectrum and make it detectable.

Part III

The ArgoNeuT Experiment

4 The NuMI Neutrino Beam

A neutrino beam is the next ingredient required for an accelerator-based neutrino experiment. The most important aspects of a neutrino beam are intensity, flavor purity, energy profile, and knowledge of each. The beam should be intense, as neutrino experiments are usually statistics limited, especially at a far detector in a long baseline experiment. The beam should also be pure. That is, searching for $\nu_\mu \longrightarrow \nu_e$ oscillations is best done in a purely ν_μ beam with little or no intrinsic ν_e content. In the case that the detectors' energy resolution is weak, the energy spectrum should be as close to monoenergetic (at an energy conducive to oscillation, given a baseline length) as possible. A wide-band beam can be used in the case that the energy resolution is strong and/or in the case that multiple oscillation probability maxima/minima are being searched for. Knowledge of the intensity, flavor composition, and energy spectrum (shape and absolute normalization) is also essential to a good neutrino oscillation experiment, especially in the absence of a near detector. Measuring (e.g.) $\nu_\mu \longrightarrow \nu_e$ oscillation as a function of energy (really $\frac{L}{E}$) is difficult if the ν_μ/ν_e composition as a function of energy of the beam is poorly understood.

The ArgoNeuT experiment was located at a near location in the Neutrinos at the Main Injector (NuMI) beam, about 1 km from the neutrino production target. The production of the beam and its characteristics are described below.

4.1 From a Gas Bottle to a Neutrino Beam

The Fermilab accelerator complex creates the NuMI neutrino beam with 120 GeV protons from the Main Injector. The entire process begins with a simple and common cylinder of compressed hydrogen gas, H_2. The atoms are turned into H^- ions by a magnetron-

created plasma that confers an extra electron onto the hydrogen in a small container. The ions are then accelerated by a 750 kV DC voltage source supplied by a Cockroft-Walton generator and exit their container at 750 keV kinetic energy. The ions are then accelerated to 400 MeV and bunched 5 ns apart by an Alvarez-type linear accelerator before being injected into the Booster ring. As the typical pulse length, or sum of all bunches, is 20 ms coming off the linear accelerator and the circumference of the Booster is only 2.2 ms, the linear accelerator pulse encircles the Booster a number of revolutions ("turns"). Before the multi-turn injection, the H^- ions are necessarily stripped of both of their electrons by a thin carbon foil, becoming a single proton–H^+. This ensures that the proton pulse already wrapped around the Booster is not knocked out by any injected negative ions. The Booster 15 Hz (currently operated at ∼7 Hz) synchrotron accelerates the 400 MeV protons to 8 GeV over about 16,000 revolutions. The Booster employs 17 RF cavities with frequency increasing from 37.8 MHz during the linear accelerator injection to 52.8 MHz during extraction to the Main Injector. A Booster "batch", or the sum of the (typically 10) turns inside the Booster at a time, yields about 5×10^{12} protons. The Booster injects a maximum of 11 batches of protons into the Main Injector in about 0.7 s.

The Main Injector synchrotron accelerates protons to either 120 GeV, for use in the creation of anti-protons to be injected into the Tevatron for collider experiments or NuMI, or 150 GeV, for injection into the Tevatron for collider experiments. There are seven booster batches that can nominally fit in the circumference of the Main Injector, with each batch end-to-end. Note that six of the slots are used as one is left open for the injection kicker to have time to ramp down. "Slip stacking" involves injecting two Booster batches of slightly different energy end-to-end into the Main Injector. With a differing rotational frequency around the accelerator ring, the batches "slip" in next to each other before eventually coalescing and taking up the space of only a single batch in the nominally seven batch circumference Main Injector ring. The currently used multi-batch slip stacking program involves 5 initial batches injected into the Main Injector followed by 6 batches that are slip stacked with the initial ones. Of these 11 batches, normally 9 go to NuMI and 2 go to the Tevatron. The actual number of protons received at NuMI is dependent on the number of turns in the Booster that make it into the Main Injector.

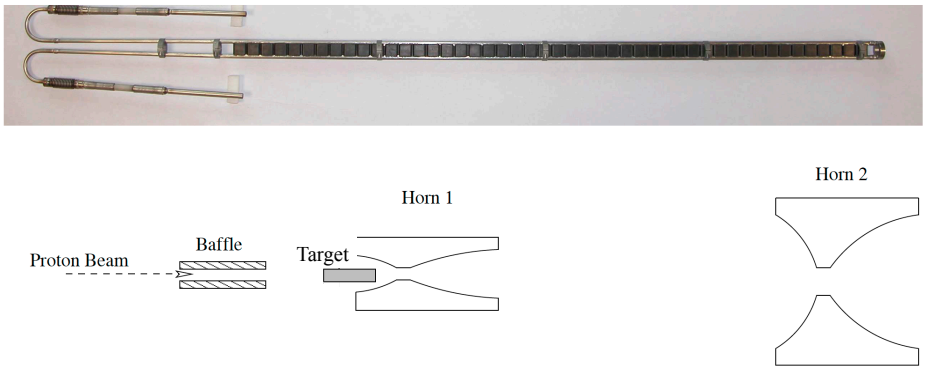

Figure 4.1: (Top) The NuMI target. (Bottom) The arrangement of the target and magnetic focusing horns in the NuMI beamline.

4.2 The NuMI Beamline

Main Injector protons intended for NuMI are extracted with kicker magnets, bent downward at 3.3° towards the site of the on-axis MINOS far detector in Soudan, Minnesota, and delivered 350 m to the NuMI target. The batches are normally extracted every 1.9 s (although this time can increase) with an 8.6 μs "spill", or beam window. The beam window can increase to about 10 μs when all of the Main Injector's protons are sent to NuMI. The protons impinge on a 94 cm long water-cooled graphite target. The 94 cm corresponds to 1.9 interactions lengths, allowing ≈85% of protons to interact with the target. The target is made of 47 rectangular graphite segments lined up end-to-end, with a cross sectional area of 6.4×18 mm^2 (see Figure 4.1). The geometry and composition of the target were chosen in consideration of maximizing pion creation, minimizing pion absorption, and maintaining tolerable thermal expansion properties. The beam profile at the target is circular with an RMS width of ∼1 mm. The stability of the beam on the target is ±0.25 mm and ±60 μrad.

The target is partially enveloped by the first "horn" of a two horn magnetic focusing system [104]. The system is designed to focus the right-sign mesons, positively charged in the case of neutrino-mode, into the decay region and down the beamline. The target is inserted ∼50 cm into this first horn which itself is 3.3 m long. A second horn is located about 10 m downstream of the first and is 3.58 m long. The target and horn configuration can be seen in Figure 4.1. A graphite baffle situated just upstream of the target is used to protect the target and horns from wayward protons in the primary beam.

An array of mesons at many different angles and energies is created in the high energy

proton on target collision. A set of two magnetic focusing horns is used to corral the wayward mesons of the right sign into the beamline. The horns can be made to focus the positive mesons and defocus the negative mesons (in neutrino mode, as $\pi^+ \longrightarrow \mu^+ + \nu_\mu$) and vice versa (in anti-neutrino mode, as $\pi^- \longrightarrow \mu^- + \overline{\nu}_\mu$). The horn's toroidal magnetic field ($B \sim 1/r$) is created in the space between two coaxial conductors. The basic idea behind the shape of a magnetic horn (see Figure 4.1) is to strongly focus the wayward positive pions into the beamline and only slightly focus the positive pions that are just barely off the beamline in neutrino-mode. The magnetic horns are not perfect meson collimators as there are many mesons coming through the magnetic volume at different angles and momenta. Also of note, the horn's conductor along with everything else in the beamline contributes to the unwanted scattering and absorption of pions. Not all π^+ (in the case of neutrino-mode running) will be focused correctly and some π^+ can even be over focused if they go through too much magnetic field. For example, if a positive pion is moving parallel to the beam axis as prescribed and interacts with a magnetic volume, then it can be over-focused off the beam axis. This undesirable over-focusing is made even more likely if the pion has a low momentum. The horns are therefore designed with less magnetic volume close to the beam axis and more magnetic volume far from the axis. Figures 4.2 and 4.3 show the T2K long baseline neutrino oscillation experiment's neutrino beamline. T2K and NuMI use similar target and horn configurations to create their intense neutrino beams and the concept of meson focusing displayed in the figures applies to both experiments. Note that T2K employs three horns, each symmetric along the beam axis.

All remaining hadrons after the horn system enter a 675 m long, 2 m diameter helium-filled decay pipe. Almost all of the unstable hadrons quickly decay into neutrinos. All of the non-leptonic particles that make it through to the end of the decay pipe are measured by a dedicated set of ionization chambers known as the hadron monitor and eventually stopped by an aluminum/steel/concrete absorber. Any remaining muons in the beam are stopped by the ∼240 m of rock in between the absorber and the MINOS near detector hall and only neutrinos are left in the beam. The muon flux and spatial distribution are measured by a series of three parallel-plate, helium-based, ionization chamber muon monitors, one just after the absorber, one 12 m past the absorber, and one 30 m past the absorber. With different amounts of rock needed to pass through and reach the detector, each monitor measures muons above a certain energy threshold. That is, the three muon monitors measure three energy bins worth of muon flux. Such a coarse grained measurement

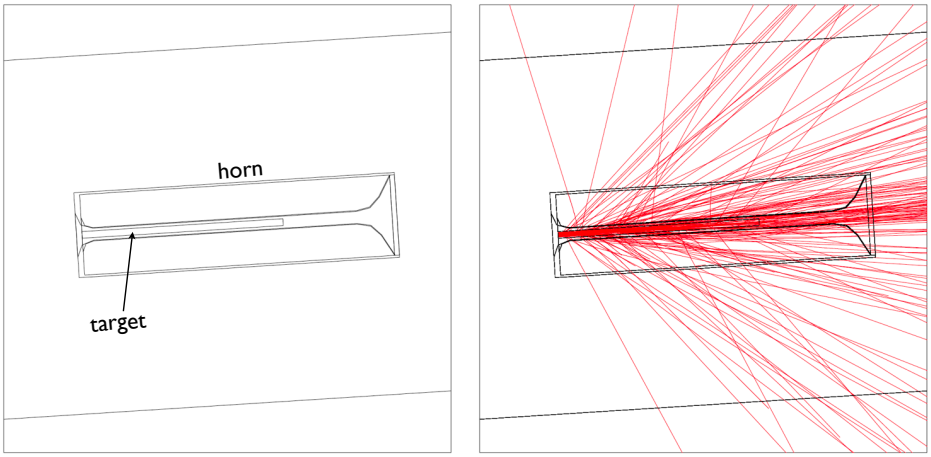

Figure 4.2: (Left) An early version of the T2K target inside a magnetic horn. (Right) Simulated pions being created in the proton on target collision and their focusing by the horn. The π^+ mesons are shown by the red lines and the beam is incident from the left. The drawings are taken from the author's undergraduate thesis [105].

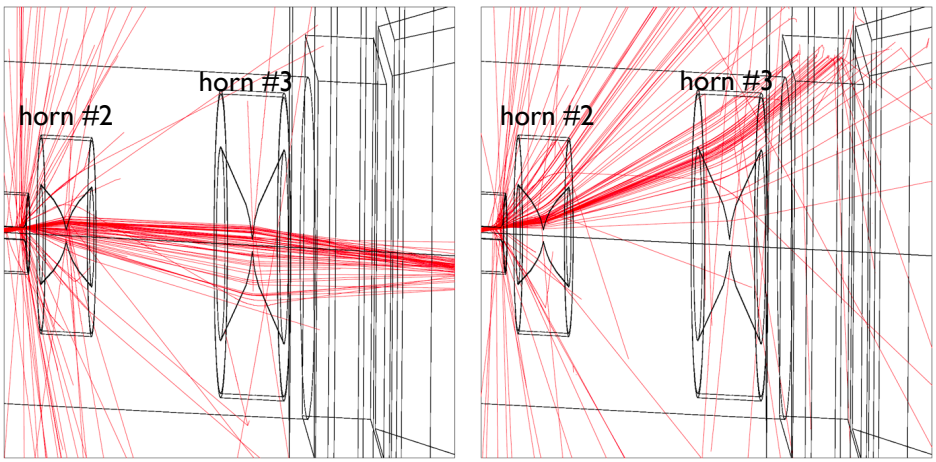

Figure 4.3: (Left) A simulation of π^+ focusing and (right) π^- defocusing by the horns in the T2K experiment's [59, 106] beamline in neutrino-mode. The π^+ mesons are shown by the red lines and the beam is incident from the left. Note that the aspect ratio is incorrect–the image has been squeezed horizontally for clarity. The drawings are taken from the author's undergraduate thesis [105].

would naively be useless to a neutrino experiment with hundreds of bins of energy across the same range. However, studying these muons in different beamline configurations has provided kinematic constraints on the parent mesons that produce detectable neutrinos.

Each horn's current, and therefore magnetic field, is adjustable. The target's position inside the horn is also adjustable. These two effects by themselves or in combination

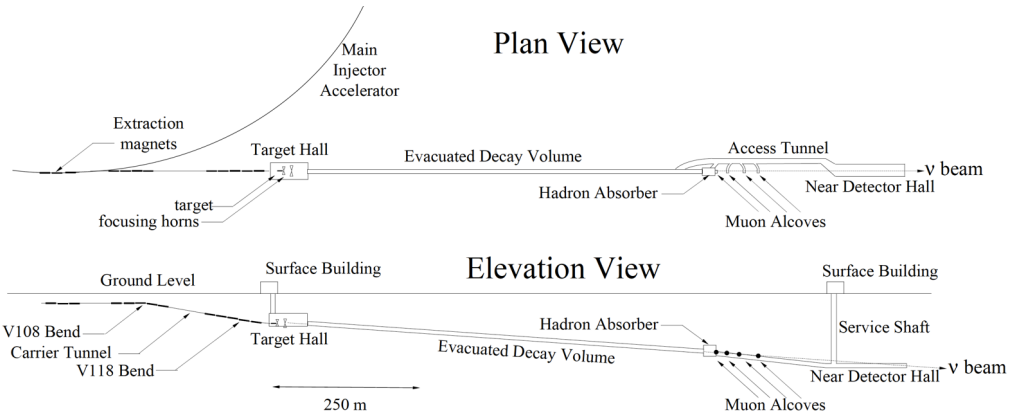

Figure 4.4: A bird's eye and elevation view of the beginning of the NuMI beamline. ArgoNeuT was located in the "near detector hall" and was accessed via the "service shaft".

alter the energy spectrum of the beam significantly. Studying these effects with the muon monitors can constrain (x_F, p_T) of the parent mesons that produce detectable neutrinos. Note that $x_F = 2p_L/\sqrt{s}$ is the Feynman scaling variable, where p_L is the longitudinal momentum and $\sqrt{s}$ is the total energy in the center of momentum frame, and p_T is the transverse momentum. The pre-target and post-target beamline up to the site of ArgoNeuT and the MINOS near detector, 1.04 km away from the target in the "near detector hall", can be seen in Figure 4.4.

4.2.1 The neutrino beam composition

The mesons created in the proton on target collision produce the neutrino beam. The following decays contribute to the muon neutrino spectrum:

$$\begin{aligned} \pi^{\pm} &\longrightarrow \mu + \nu_\mu \\ K^{\pm} &\longrightarrow \mu + \nu_\mu \\ K^0_L &\longrightarrow \pi + \mu + \nu_\mu \\ \mu &\longrightarrow e + \nu_e + \nu_\mu \end{aligned} \tag{4.1}$$

The first three decays above have lifetimes on the order of tens of nanoseconds. The fourth, a muon decay, has a much longer lifetime at 2.2 μs; the muon almost always stops before decaying. The isotropic muon decay contributes only a few percent to the total ν_μ flux at the MINOS near and ArgoNeuT detectors. Although muons are not a significant

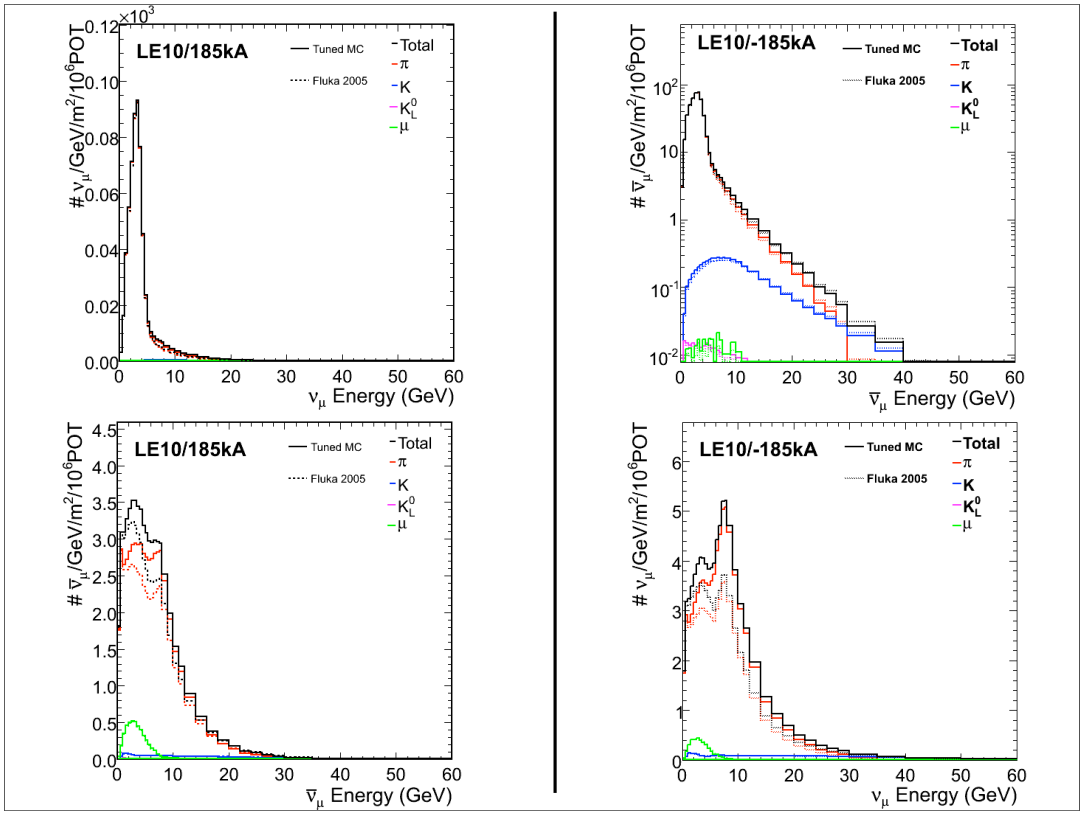

Figure 4.5: (Left) The ν_μ and $\overline{\nu}_\mu$ flux, top to bottom, in neutrino-mode. (Right) The $\overline{\nu}_\mu$ and ν_μ flux, top to bottom, in anti-neutrino-mode. The contributions from each parent meson are shown. The entire ArgoNeuT physics run (neutrino- and anti-neutrino-mode) was in the "LE-10" horn/target configuration. "LE" refers to the low energy NuMI beam configuration and "10" refers to the downstream end of the target begin placed 10 cm from the first focusing horn's neck. These plots are from Reference [107].

source of ν_μ in the beam relative to the other parent mesons, they are a significant source of ν_e relative to the other parents ($K^0_L \longrightarrow \pi + e + \nu_e$ and $K^\pm \longrightarrow \pi^0 + e + \nu_e$). The intrinsic ν_e contamination in the ν_μ beam is relevant for the MINOS ν_e appearance search. The neutrino- and anti-neutrino-mode fluxes at the ArgoNeuT location are shown in Figure 4.5. A thorough discussion of the flux used for the analysis presented here can be found in Section 8.4.

5 ArgoNeuT Hardware

5.1 The Physics Run

ArgoNeuT, a NSF/DOE project at Fermilab, is the first LArTPC to go in a low-energy neutrino beam and just the second LArTPC to go in a neutrino beam ever [108]. In this case, "low-energy" means that the neutrino energy is in the 0.5-10.0 GeV range. These energies are most relevant for long baseline neutrino oscillation searches as the oscillation probability is maximal in the few GeV region, assuming typical values of $\theta_{13} \sim 5^{\circ}$, $\theta_{23} \sim 45^{\circ}$, $\Delta m^2_{13} \sim 2.4 \times 10^{-3}$ eV^2, and a baseline of about 1000 km.

The ArgoNeuT experiment's operations began with a cosmic ray commissioning run on the surface in Summer 2008 and a cosmic ray and beam-induced neutrino commissioning run underground in Spring 2009. The surface run took place at the Proton Assembly Building at Fermilab and the underground runs, commissioning and physics were in the MINOS near detector hall. The commissioning runs served to debug various aspects of the experiment: a faulty high voltage feedthrough, dead/noisy wires, low purity, poor recirculation rate, inaccurate temperature readings, etc. The first neutrino candidate was taken on May 27, 2009.

With sufficient purity, ease of operation, and remote monitoring abilities in place, the ArgoNeuT physics run was initiated. The physics run began in September 2009 as the Fermilab accelerator complex ended a summer shutdown. During this time, ArgoNeuT was located about 1.5 m upstream of the MINOS near detector [109], about 26 cm below both the center of the NuMI on-axis beam and the center of the MINOS near detector's fiducial volume. A rendering and pictures of ArgoNeuT's location in the MINOS near detector hall can be seen in Figures 5.1 and 5.2. The main ArgoNeuT detector specifications can be

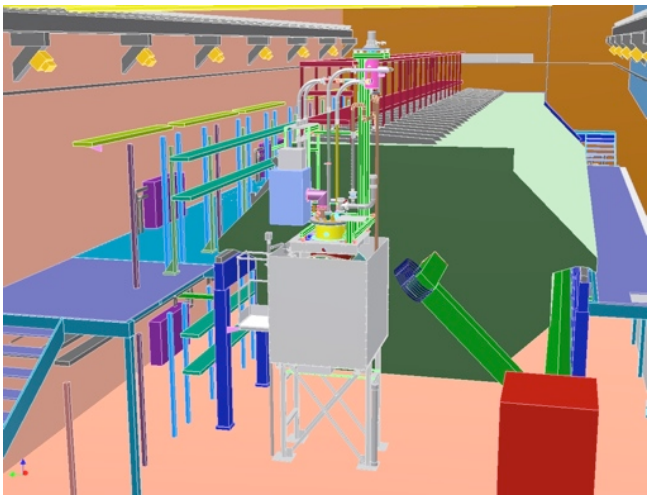

Figure 5.1: A rendering of the MINOS near detector hall. ArgoNeuT, inside the gray box, can be seen just upstream of the MINOS near detector. ArgoNeuT's position corresponds approximately to the center of the NuMI beam.

seen in Table 5.1. It is worth noting that the MINERνA experiment [110] was installed over a period of months during the ArgoNeuT physics run, in a location just upstream of ArgoNeuT.

The ArgoNeuT physics run lasted until late February 2010 and consisted of about two weeks of neutrino-mode running and four-and-a-half months of anti-neutrino mode running. The experiment collected about 1.35×10^{20} POT total with the "low-energy" NuMI configuration ($\sim0.1\times10^{20}$ in neutrino mode and $\sim1.25\times10^{20}$ in anti-neutrino mode). Run operations were largely stable and shift-free over the >5 month time period. The experiment saw an uptime in terms of "POT delivered" of about 86%, including a two-week downtime in October 2009 due to a commercial cryocooler failure (see Figure 5.3). Without including the cryocooler failure, the uptime was about 95% for the entire physics run. A plot of the electron lifetime as a function of date during neutrino-mode can be seen in Figure 7.26. The electron lifetime during the two weeks in neutrino-mode was about 750 μs, which resulted in an attenuation of the ionization signal for maximally drifting tracks, created at the cathode, of $\sim$36%. This level of attenuation is acceptable for physics analyses, in consideration of the signal-to-noise observed.

A number of neutrino events taken in ArgoNeuT's neutrino-mode run are shown in Figures 5.4, 5.5, 5.6, and 5.7.

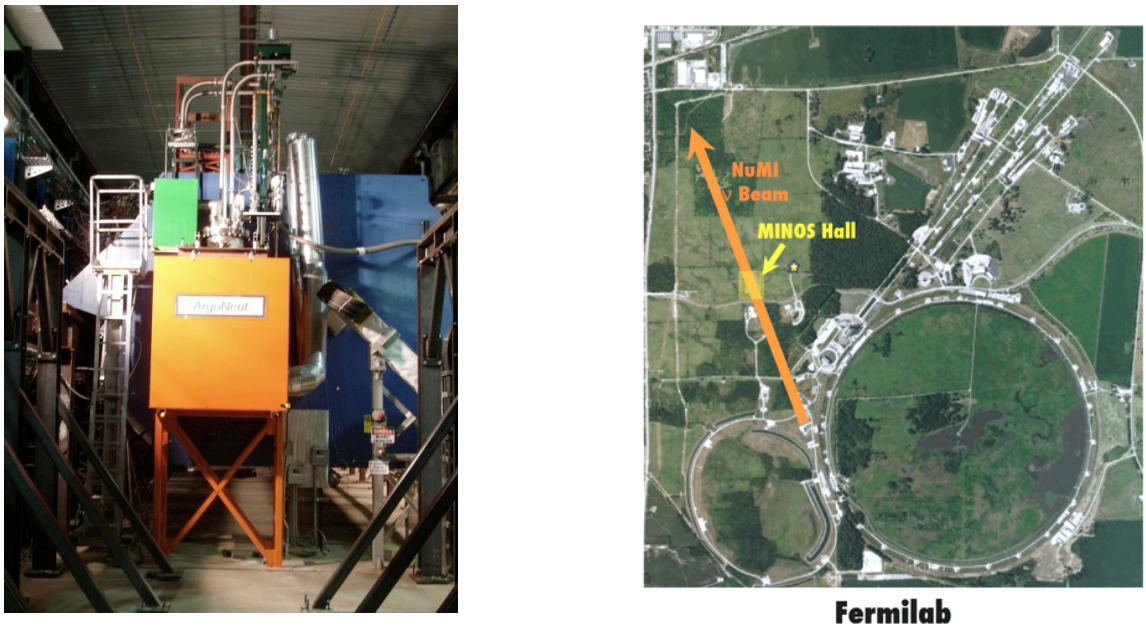

Figure 5.2: (Left) The fully instrumented ArgoNeuT detector in the beamline. The man-lift to the left of ArgoNeuT was used to access ArgoNeuT. The orange box was meant to contain spilled liquid argon in the case of an accident. (Right) An aerial view of Fermilab. The "MINOS Hall" is located about 1 km away from the NuMI target station which utilized a beam created by the Main Injector ring. The Main Injector can be seen in the bottom left of the image, adjacent to the larger Tevatron ring.

Cryostat volume	550 liters
TPC volume	175 liters
# Electronic channels	480 (240/plane)
Wire spacing	4 mm
Electronics style (temperature)	JFET (293 K)
Max. drift length (time)	47 cm (~330 μs)
Light collection?	No

Table 5.1: ArgoNeuT detector specifications.

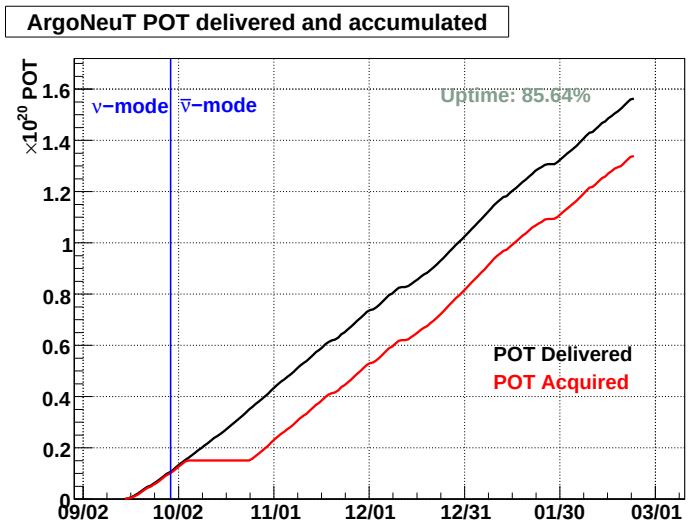

Figure 5.3: The ArgoNeuT physics run in terms of delivered/acquired protons on target (POT) as a function of date, spanning 2009/2010. The ∼2 week downtime in October was due to a cryocooler failure.

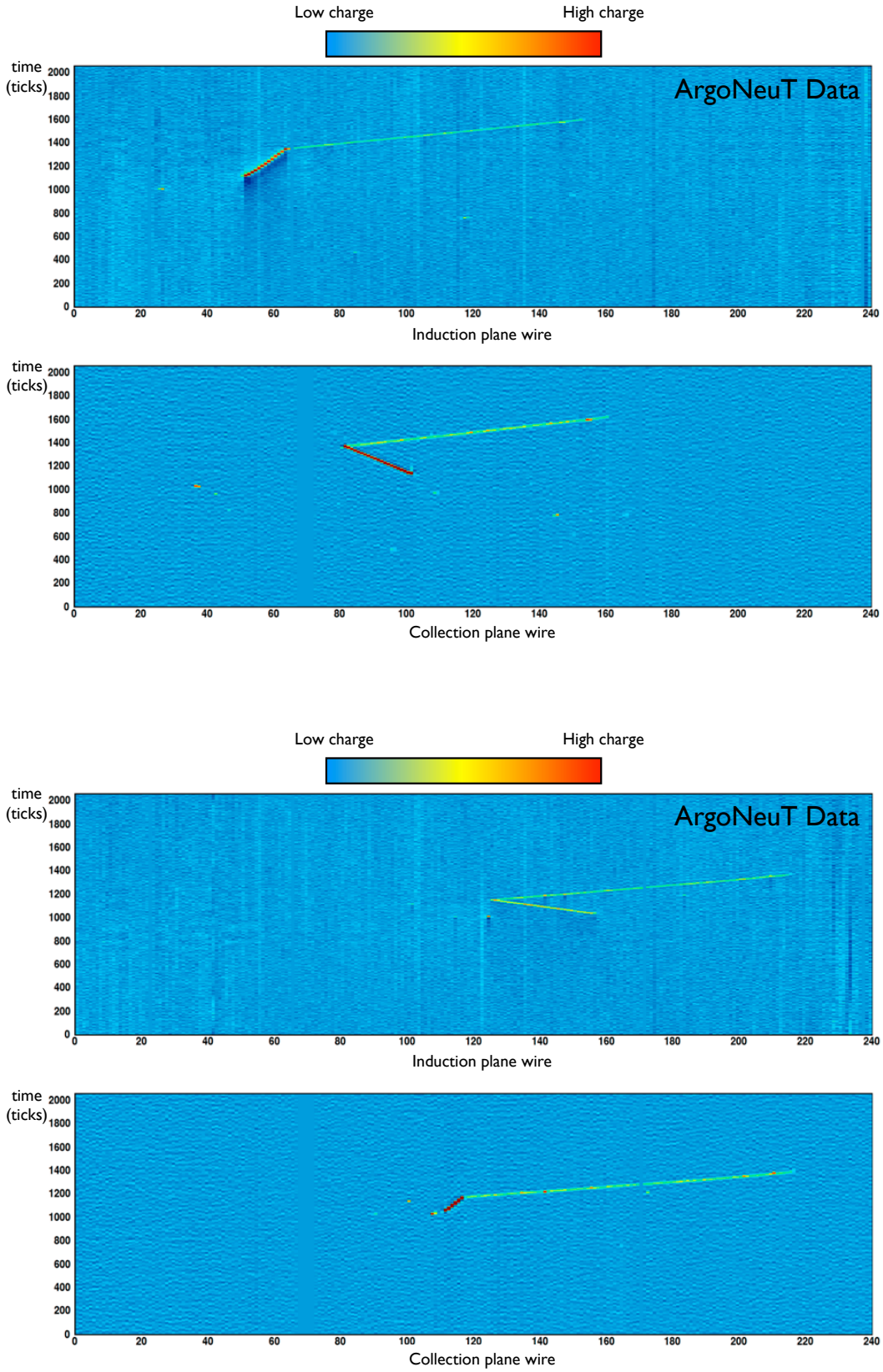

Figure 5.4: Neutrino events acquired during the ArgoNeuT neutrino-mode physics run.

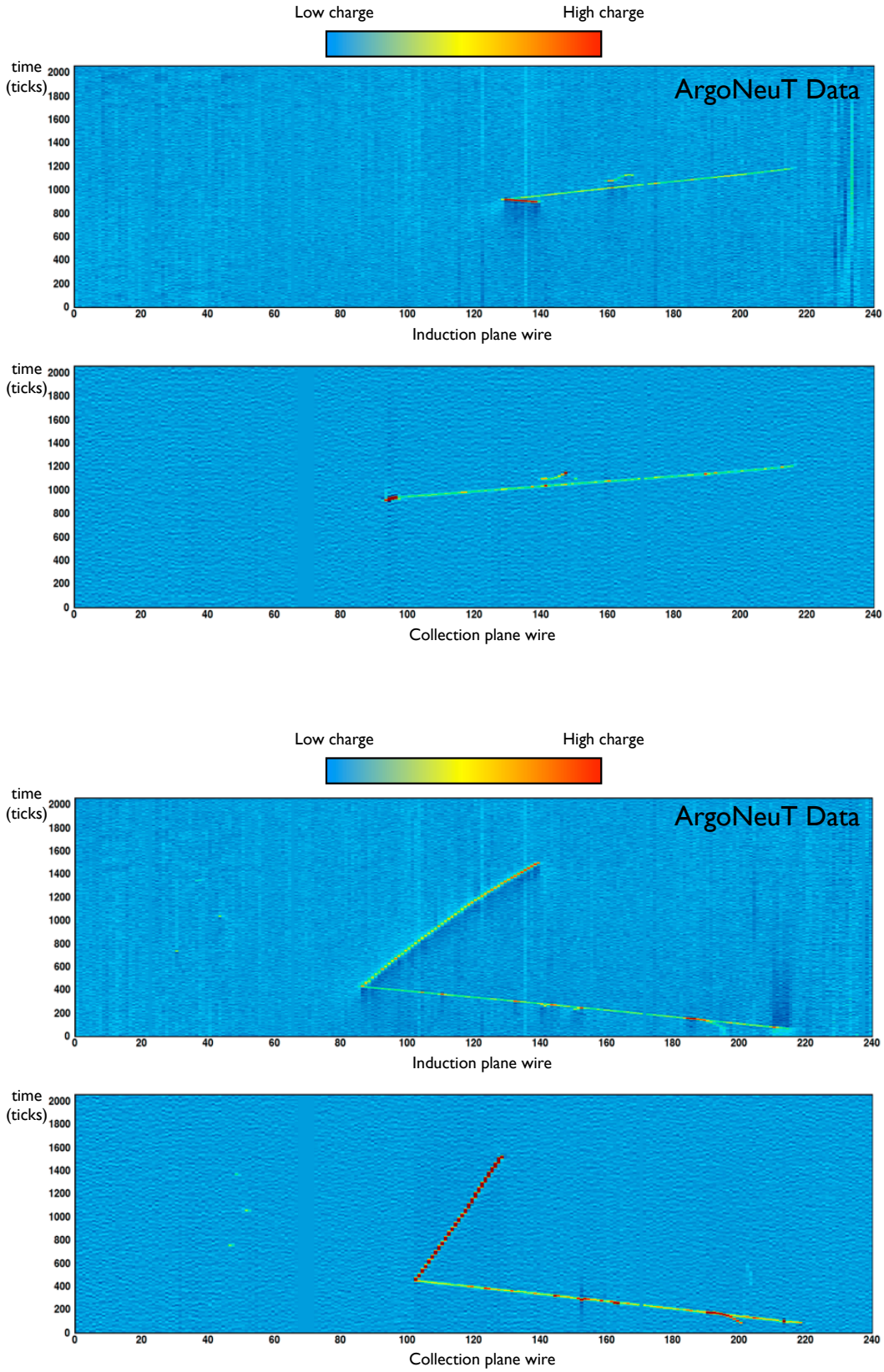

Figure 5.5: Neutrino events acquired during the ArgoNeuT neutrino-mode physics run.

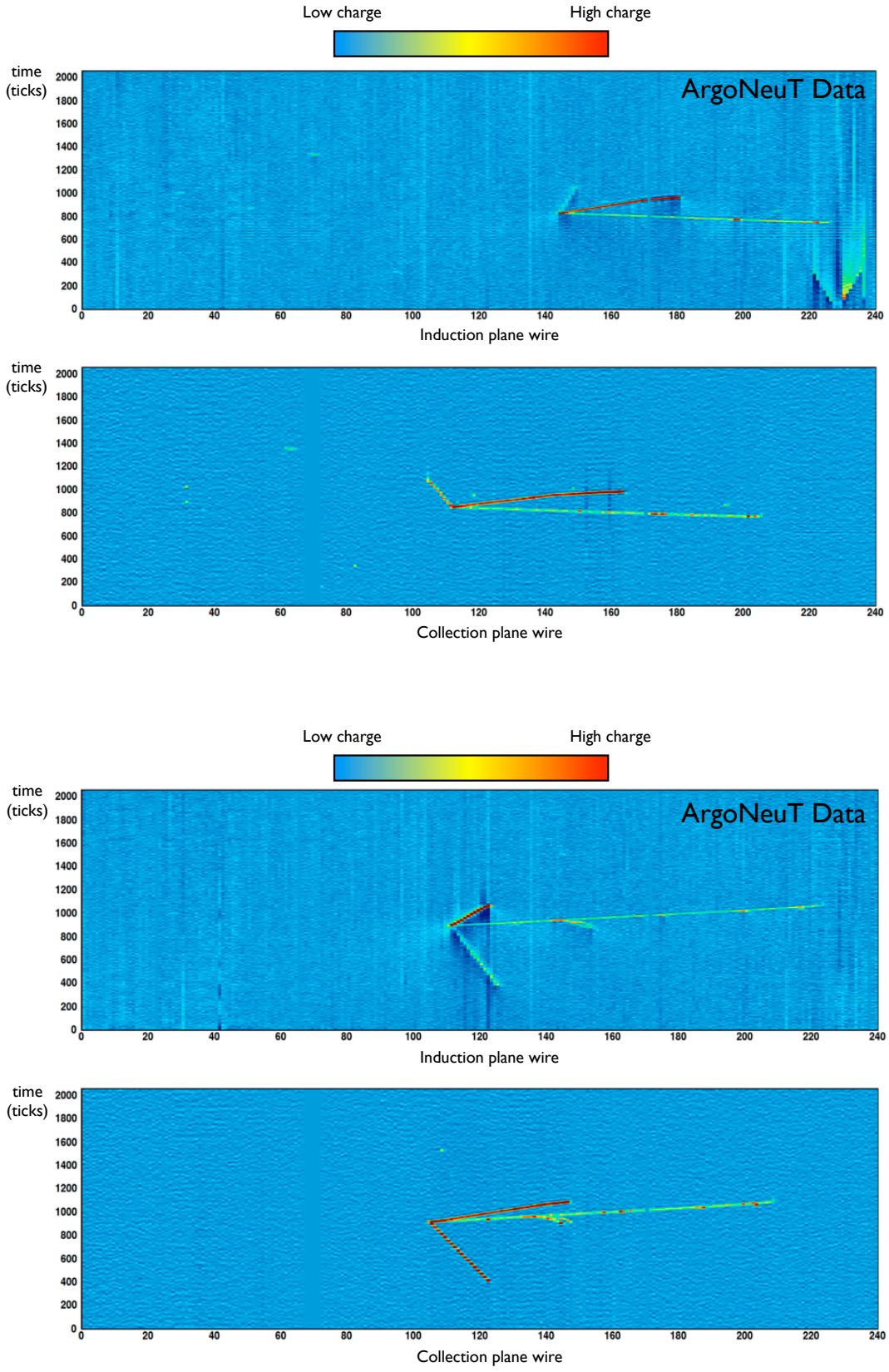

Figure 5.6: Neutrino events acquired during the ArgoNeuT neutrino-mode physics run.

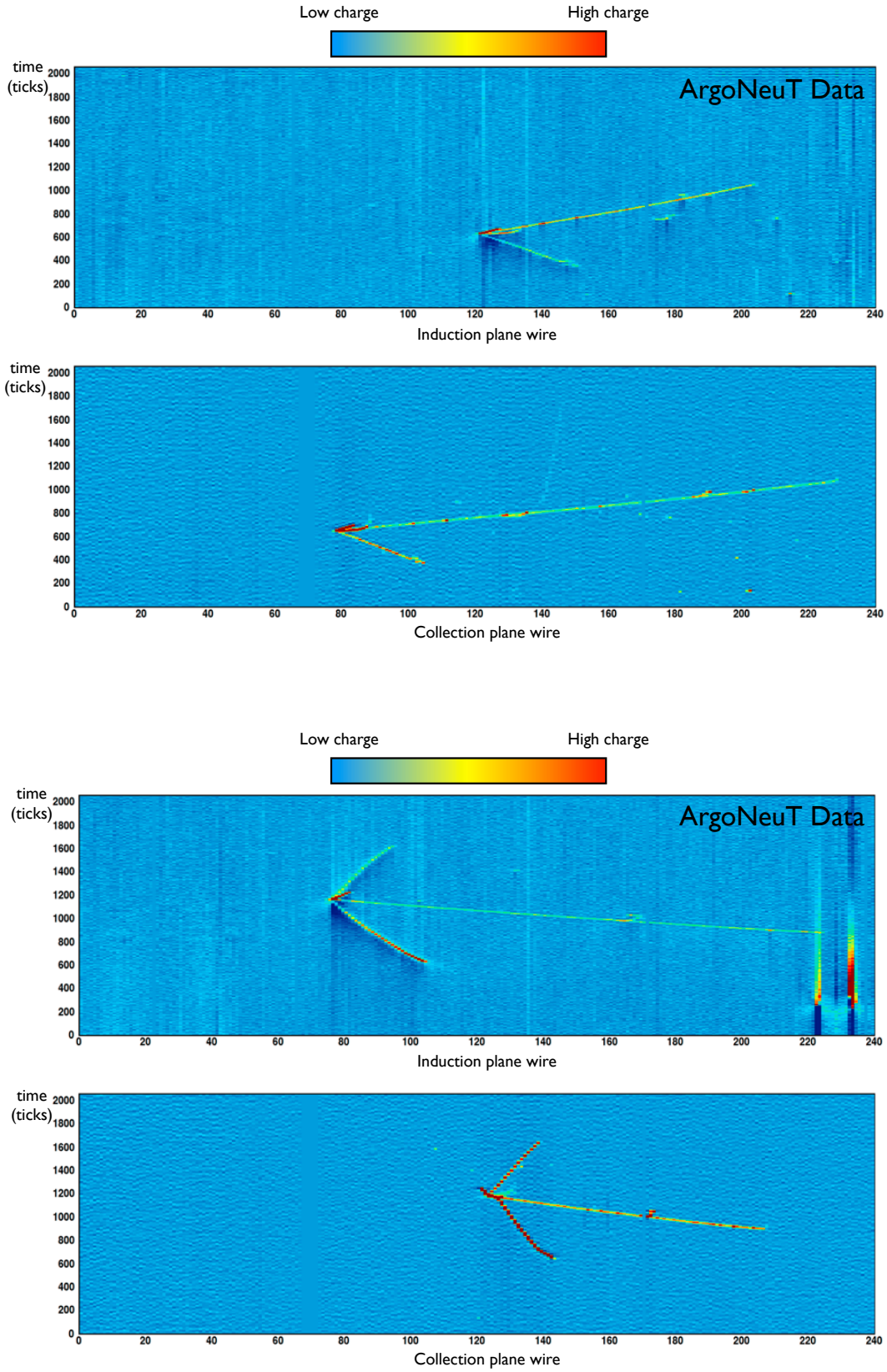

Figure 5.7: Neutrino events acquired during the ArgoNeuT neutrino-mode physics run.

5.2 Cryostat and Cryocooler

ArgoNeuT's liquid argon was contained by a stainless steel cryostat vessel, referred to as the "inner cryostat". The majority of the 550 liter inner cryostat was surrounded by a thick layer of vacuum insulation created in the space between an outer cryostat and the inner one. The vacuum jacket was kept at a pressure of about 10^{-3}-10^{-4} torr for the length of the physics run. A 300 W Gifford-McMahon cryocooler in combination with a copper heat exchanger and helium-based compressor kept the liquid argon inside the cryostat cold. Boil off argon gas coming up from the surface of the liquid volume was re-condensed by the cryocooler, about 3 m above the cryostat. The resulting liquid argon was then forced through one of three pipe pathways in its return trip back to the liquid volume at the bottom of the cryostat. Two of the three pathways were through argon filters and one of them was through a bypass pipe. Liquid was directed through the bypass pipe only on rare occasions. The filters and pathways were vacuum insulated. Just before re-entering the main liquid argon volume, the liquid was directed through a sintered metal cap (see Figure 5.8). Passing liquid through such a cap has been known to improve the purity of the liquid argon. Initially, it was thought that this was due to the discharge of any electron-ionization-attenuating ions in the liquid through the cap. However, Reference [111] suggests that the impurities present in the liquid before the cap can adsorb onto the cold metal surface and therefore be removed from the active detection volume. The outfitted ArgoNeuT cryostat and a schematic of the recirculation system can be seen in Figure 5.9 and the cryocooler apparatus and containment can be seen in Figure 5.10.

The inner and outer cryostat, cryocooler, and filters were instrumented with a number of temperature and pressure sensors. These sensors, in combination with heaters throughout the volume, made up a feedback loop. Slow control software controlled this loop and maintained a constant pressure/temperature system with a consistent recirculation rate. A screenshot of the remotely controllable software at work on the running ArgoNeuT experiment can be seen in Figure 5.11. A set of heaters in the liquid at the bottom of the inner cryostat were employed in order to promote recirculation, given the excess cooling power available. A constant pressure of 2.0 PSIG was maintained in the gas above the cryostat. If the pressure dipped below 2.0 PSIG, heaters attached to the cryocooler would kick on and the cooling power of the device would be reduced. If the pressure increased above this value, the heaters were automatically dialed down and the cooling allowed to increase. As

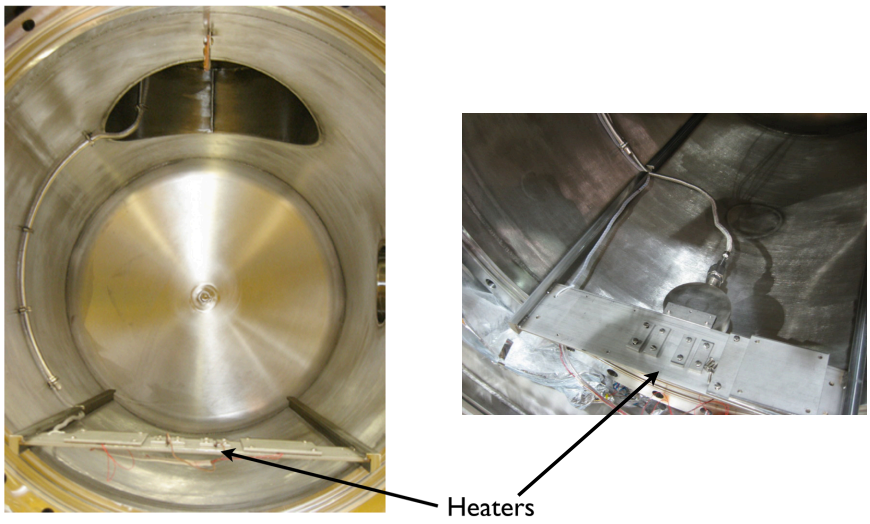

Figure 5.8: (Left) The inner cryostat. The liquid argon return line can be seen on the left of the picture along with a set of heaters at the bottom. (Right) The heaters at the bottom of the inner cryostat from a different vantage point. The sintered metal cap at the end of the return line can now be seen.

there was an excess of cryocooling power above the heat load on the system, the heaters on the cryocooler were usually on and the system consistently stable.

Relief lines were placed on any liquid argon containment volume in order to allow the argon to expand and escape the volume safely in case of boiling. All of the relief lines led to a common vent pipe that was routed up to the surface and out of the building. The outer cryostat and surrounding containment vessel (the orange box in Figure 5.2) were to act as containers for any spilled liquid in the case of a major accident or failure. The containment vessel also contained oxygen deficiency sensors and fans.

5.3 Time Projection Chamber

The ArgoNeuT Time Projection Chamber (TPC) is a $40\times47\times90$ cm^3 ($\sim$175 liter) rectangular box that sits inside of the inner cryostat. The box itself is composed of G10 and all of the conductors inside are copper. The TPC is oriented so that the longest dimension is approximately parallel to the beam and the drift direction is perpendicular to the beam. The maximum drift length is 47 cm from the negatively charged (-25 kV) cathode to the grounded first wire plane. ArgoNeuT employs three wire planes. The first plane, closest to the cathode, has 225 wires that are vertically oriented with respect to the ground, perpen-

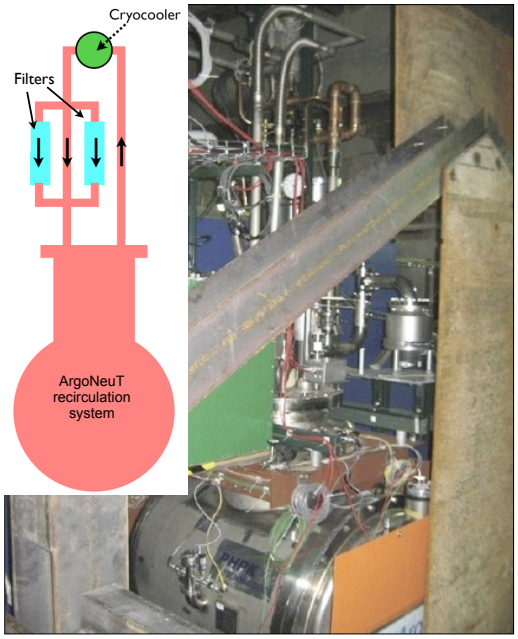

Figure 5.9: The ArgoNeuT experiment during the physics run. Part of the MINERνA shield plane, the first piece of the MINERνA experiment's installation underground, is visible in the foreground. (Inset) A drawing of the fully contained ArgoNeuT recirculation system featuring a cryocooler and two liquid argon filters. Argon gas goes up to the cryocooler and liquid argon comes back down through the filters before returning to the cryostat.

dicular to the beam axis. This plane is not instrumented for readout purposes but serves to shape the electric field near the wire planes and shield the outer, instrumented planes from drifting ionization. That is, the "shield plane" reduces the possibility of current being induced on the other planes as the ionization is drifted through the TPC. The second plane, often called the "induction plane" or "second induction plane" (a charge is induced on the shield, or "first induction", plane as well), consists of 240 wires which are oriented at $+60°$ relative to the beam axis. The third plane, often called the "collection plane", is made up of 240 wires and is oriented at $-60°$ relative to the beam axis. The wire spacing is 4 mm in all planes and the planes are themselves spaced 4 mm apart. The wire plane orientation can be seen in Figure 5.12 (left).

The electric field throughout the drift region is operated at 500 V/cm. Aside from the cathode and wire planes, there are also 23 1 cm wide copper field rings (the "rings" are rectangular and follow the edge of the TPC frame) spaced at 1 cm all the way up the TPC from the cathode to the first wire plane. A resistor chain from the -25 kV cathode through

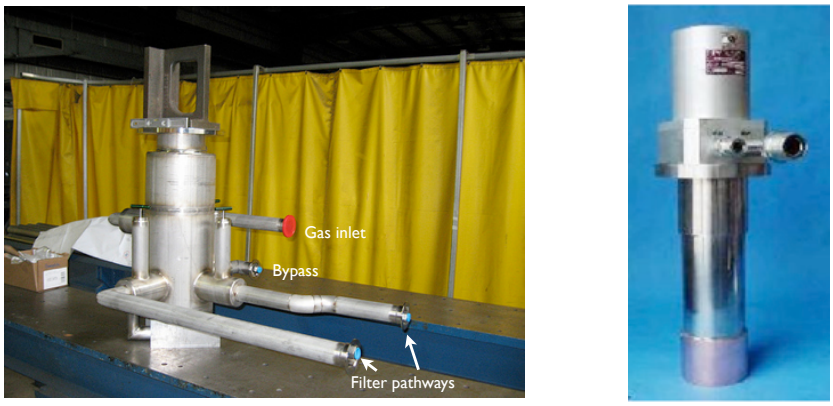

Figure 5.10: (Left) The cryocooler containment vessel, inlet, and outlets. Boil off argon gas enters the "Gas inlet", re-condenses on the cryocooler, and returns to the cryostat via the "Bypass" or one of two "Filter pathways". (Right) The 300 W Gifford-McMahon cryocooler employed in ArgoNeuT. This device is located inside the vacuum-insulated cryocooler containment vessel. The compressed helium gas entrance and return ports can be seen.

each field ring ensures a uniform electric field throughout the TPC. The entire TPC is visible in Figure 5.12 (right) and the inside of the TPC can be seen in Figure 5.13.

5.4 Liquid Argon Purification

The liquid argon inside the detector vessel is required to be at the level of parts-per-trillion (ppt) pure in order for the drifting ionization to reach the wire planes, given a reasonable drift distance. The electron drift velocity in a typical LArTPC operated at 500 V/cm is about 1.5-1.6 mm/μs [112]. With a 47 cm maximum drift, as in ArgoNeuT, the electron lifetime needs to be >450 μs for <50% attenuation along a drift originating from a track at the cathode. A <10% attenuation over the same length would require a lifetime of >3 ms. An electron lifetime of 450 μs (3 ms) corresponds to an oxygen-equivalent impurity of about 650 ppt (100 ppt). For comparison and to demonstrate the challenge of liquid argon purification, commercially available "ultra-pure" liquid argon arrives at a few parts-per-million (ppm) oxygen-equivalent concentration. Despite these difficulties, ICARUS [113] and FNAL [114] have routinely demonstrated electron lifetimes in excess of 10 ms after employing argon filtration methods.

The argon filtration used by ArgoNeuT is based on a technique developed and pioneered by the ICARUS collaboration [115]. The first utilization of the method was with

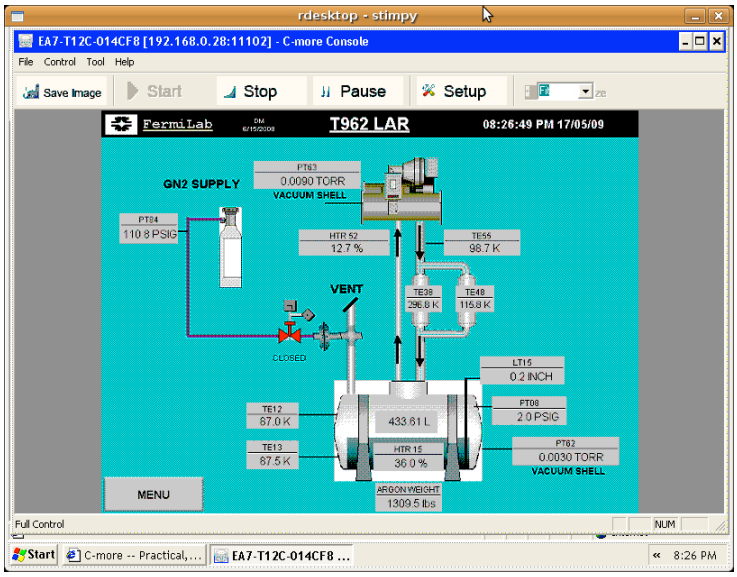

Figure 5.11: A screenshot of the remotely controllable cryosystem monitoring software applet. Feedback loops keeping track of temperature and pressure and adjusting heater outputs kept the recirculation/purification system running and the argon cold.

the ICARUS 3 ton LArTPC [71, 116] and the first use with a LArTPC in an accelerator-based neutrino beam was with the ICARUS 50 L LArTPC [117]. A full description of the ArgoNeuT filter technique using a non-proprietary and regenerable design can be found in Reference [114]. The ArgoNeuT filters are made of activated-copper-coated alumina granules [118] inside of a conflat flange cylindrical nipple with sinterized steel caps on each end. The caps serve to keep the granules inside the filter while letting liquid argon flow through. Each cylindrical filter has a 2.5 inch diameter and is 24 inches long. The three filters used during the ArgoNeuT physics run were each wrapped in about 8 inches of fiberglass for insulation. While in the recirculation system, the filters were further insulated by a weak vacuum of 100-200 Torr. After the initial filter assembly, the filters were regenerated (see Section 5.4.1) and installed in ArgoNeuT's closed loop recirculation system, just downstream of the cryocooler. That is, liquid coming out of the cryocooler was forced by gravity and pressure through one of two filters. After the liquid flowed through the filter, the outlet returned the purified liquid argon back to the bottom of the cryostat. The recirculation system provided a full volume (∼550 liters) exchange every 4-5 days.

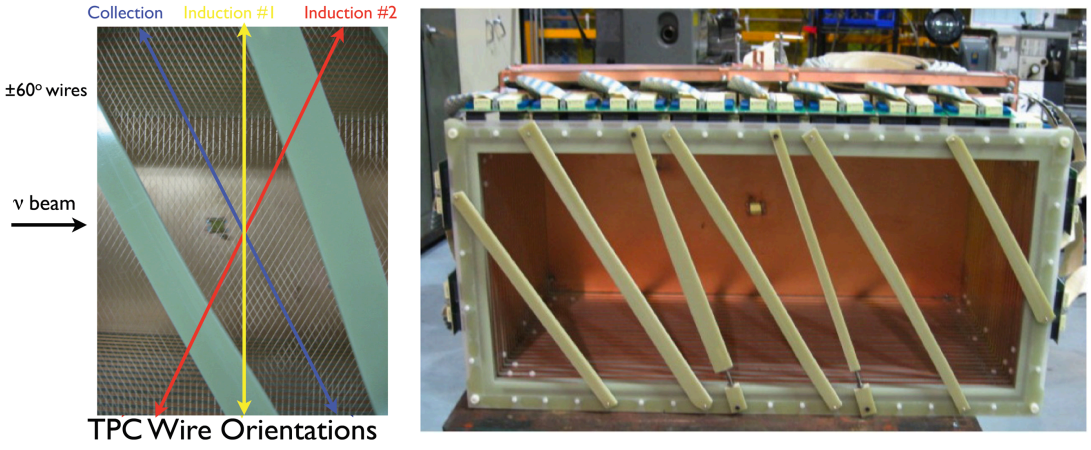

Figure 5.12: (Left) The orientation of the ArgoNeuT TPC's wire planes. Note that only the "Induction #2" and "Collection" plane are instrumented. (Right) The fully assembled TPC. Looking into the TPC, the wire planes are in the foreground and the copper cathode is in the background. The bias voltage distribution cards are seen on top of the TPC. The nearly-parallel G10 bars, used to reduce wire sag and stabilize the TPC frame, are also visible in the foreground.

Figure 5.13: A look inside the TPC. The solid copper sheet is the cathode plane and the copper strips lining the TPC are the field cage rings. The TPC frame (i.e. what the copper is attached to) is composed of G10.

5.4.1 Filter regeneration

A filter's effectiveness degrades over time as electronegative impurities accumulate inside, saturating the copper-based filtering agent. The ArgoNeuT filters needed to be regenerated every three weeks on average. The need for regeneration was spurred by the electron lifetime improvement rate, as measured by the purity monitor, noticeably slowing down

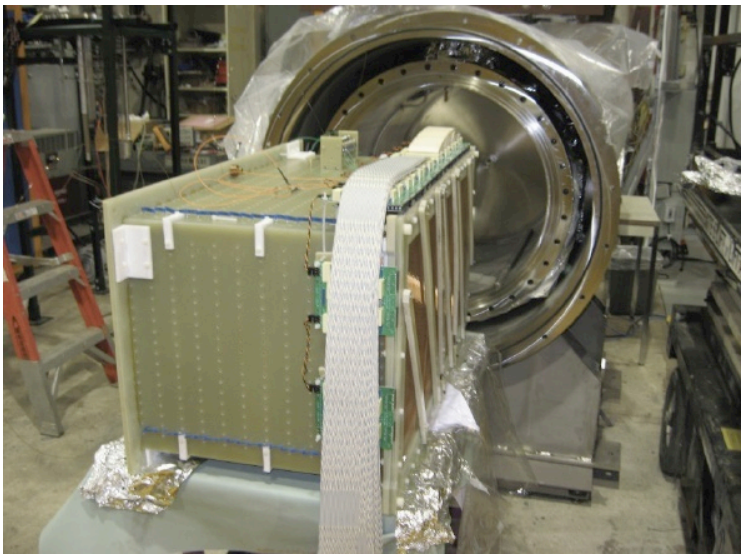

Figure 5.14: The fully instrumented TPC being inserted into the ArgoNeuT inner cryostat. As can be seen, the cryostat is composed of an inner, liquid argon layer and an outer, vacuum-jacket layer.

or even stopping in some cases. The filters were regenerated following the manufacturer's instructions [118]. After pumping out any remaining argon, the filter was brought up to $\sim 250°C$ via heating tape surrounding and in contact with the stainless steel filter container. Thermocouples near the heating tape and in the center of the filter, along with a feedback loop controlling the current through the heating tape, ensured that the filter material was at the specified temperature. These thermocouples also served to monitor the temperature of the filter in the closed loop recirculation system and provided a measure of the liquid's ability to flow through the filters against a potential heat load. After the filters were brought up to temperature for regeneration, a 95%/5% mixture of Ar/H_2 gas was flowed through the filter at 5 ft^3/hour for 24-36 hours. A dew point monitor at the outlet of the filter was used to monitor the water vapor concentration of the gas exiting the filter. The water vapor concentration was an effective regeneration status indicator. Figure 5.16 shows a typical water vapor concentration curve in time for a full ArgoNeuT filter regeneration. The water vapor concentration rises quite quickly at the beginning of the regeneration due to the initial reduction reactions on the copper granules, reaches a steady state, and then falls asymptotically as the impurity concentration exiting the filter drops. The regeneration is considered complete when the water vapor concentration curve is observed to level out, usually about 24-36 hours after the beginning of regeneration. The gas flow is turned off

Figure 5.15: The ArgoNeuT filter cartridges used to purify the argon in liquid form coming out of the cryocooler before returning to the cryostat. The cryocooler containment vessel, although difficult to see, is just above and behind the filter manifold. Liquid argon flow could be diverted to either of the filters at any time, depending on whether the filter(s) were exhausted or newly regenerated. The liquid enters through the top and comes out the bottom in its return back to the cryostat.

and the filters are cooled, evacuated with a vacuum pump, and then purged with argon gas before being reinstalled in the fully contained ArgoNeuT recirculation system. The bare filters just downstream of the cryocooler can be seen in Figure 5.15. The stability of the pressure and temperature of the system was fairly consistent during filter installation and replacement.

5.4.2 Filling ArgoNeuT with pure liquid argon

In installing the detector components and TPC, the inner cryostat was kept as clean as possible. Before the fill, the cryostat was evacuated to about 10^{-5} torr, purged with argon gas, and evacuated again. The cycle was repeated three separate times. As previously discussed, commercial-grade "ultra-pure" liquid argon, has an unacceptably high amount of impurities by about four orders of magnitude. A newly regenerated set of two filters was used during the fill. The filters were oriented in series just downstream of the argon dewar. The warm lines and filters were cooled with an initial stream of cold gas from the dewar. With a positive pressure inside the vessel and a significant amount of cooling required before

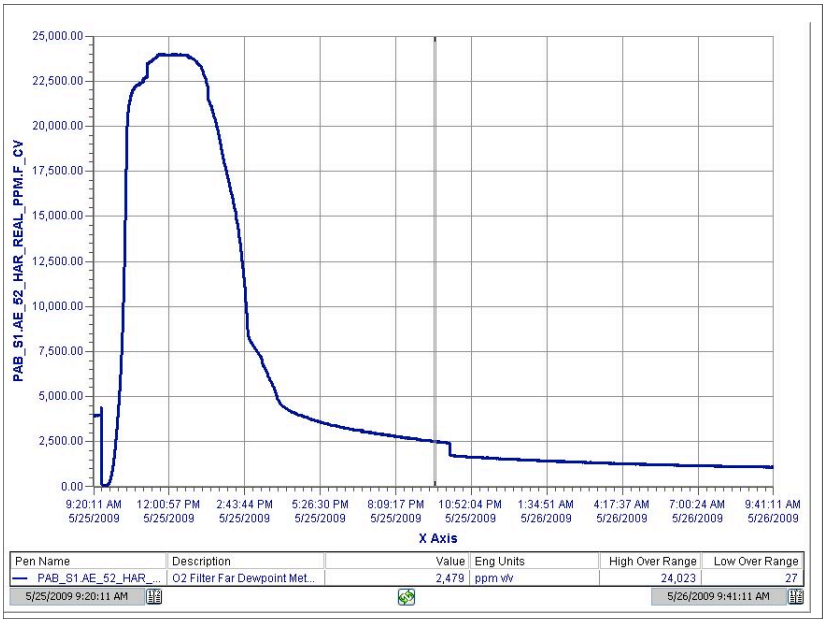

Figure 5.16: The water vapor concentration at the outlet of the filter during regeneration as a function of time. The water concentration is seen to increase rapidly after the regeneration process begins, peak, and then asymptotically decrease until further regeneration becomes ineffective.

liquid began to deposit itself at the bottom of the inner cryostat, gas was allowed to vent out of the detector during the fill. A positive pressure inside the volume meant that no impure air could enter the cryostat during the fill. The entire 500 L cryostat was filled in about 12 hours with 6-7 dewars of liquid argon. The fill was made intentionally slow so as to allow the argon sufficient exposure to the inline filters in order to remove the impurities inherent to the commercial product. There are advantages to a fast fill, however. Warm detector components, like the TPC's G10 frame, outgas impurities into the gas volume above the liquid at a significant rate. Such impurities can diffuse into the liquid and significantly affect purity. The idea of a fast fill would be to quickly "freeze-out" this outgassing, as materials at 87 K have been found to have a low outgassing rate [111]. However, even with an ArgoNeuT cryostat completely filled with liquid argon for physics operations, there is still a significant gas ullage above the liquid with many kilograms worth of warm G10 in it. Therefore, any benefit of a fast fill in terms of freezing-out the TPC's G10 from outgassing would be quickly erased by the G10 in the warm gas in the area above the TPC. The following non-metal (i.e. possible sources of significant impurity outgassing) inside the ArgoNeuT gas volume included: G10 radiation baffles, a G10 cable tray which routed the readout wires to the signal feedthrough, polyolefin readout wire insulation, quartz optical

fibers, epoxy from the optical fiber feedthrough, stycast insulation for the high voltage feedthrough, and the mostly G10 (with a trace of nylon) electronics feedthrough board.

The cryocooler was in operation during the fill and the liquid argon coming off the cryocooler was directed through the filter manifold beginning just after the fill completed. The fill was considered complete when the capacitive liquid level meter, placed about a foot above the TPC, was nearly covered with liquid. After the fill, the system took a few hours to reach an equilibrium state as the liquid containers lowered in temperature and the cryocooler began re-condensing the boil off gas effectively. Liquid was forced through the filter manifold and the recirculation/purification process was considered stable after this brief post-fill cooling period.

5.5 Purity Monitor

The ArgoNeuT purity monitor, located right on top of the TPC inside the inner cryostat, was used to almost instantaneously determine the purity of the liquid argon. Although the absolute measurement of the electron lifetime via the purity monitor is subject to sizable systematic uncertainty as discussed in Section 7.7, consecutive purity monitor measurements over a number of hours/days can effectively determine the rate and direction of purity increase/decrease. Such measurements can also help to diagnose recirculation system and filter issues as well as assist in determining if an initial liquid argon fill was successful. Also, in the absence of the more precise measurement via the reconstruction of long tracks at varying drift times/distances as discussed in Section 7.7, the purity monitor can provide the electron lifetime attenuation factor, in the case of a measurably finite lifetime, required for the calorimetric reconstruction of particle tracks.

The purity monitor is based on the design described in [119] and works as follows. Light from a xenon flash lamp outside the cryostat is directed via a set of redundant solarization-resistant optical fibers [120] inside the cryostat. The fibers point towards a gold photocathode at the negatively charged base/cathode of the purity monitor. The photon-gold interaction produces photoelectrons. The photoelectrons are drifted through the $\sim$100V/cm purity monitor field cage and are detected 10 cm ($\sim$200 μs) later on the anode. The cathode and anode signals are then compared in order to determine the level of ionization attenuation across the drift distance/time. A drawing of the purity monitor concept can be seen in Figure 5.17. The ArgoNeuT purity monitor and the results of an

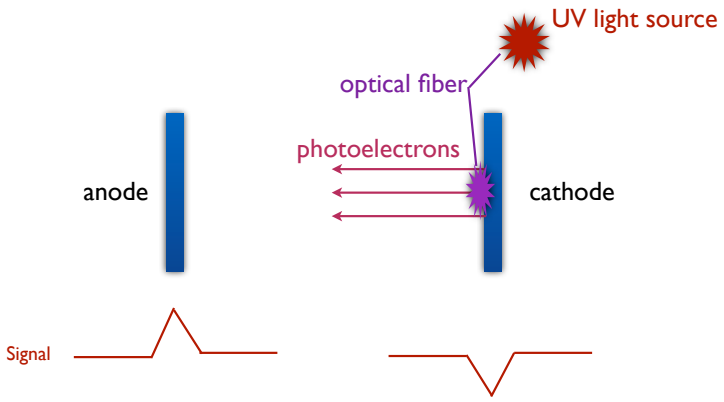

Figure 5.17: The purity monitor concept. The cathode and anode signals, separated in time, are compared in order to determine the electron lifetime, a measure of purity, of the liquid argon.

electric field and electron drift simulation with the purity monitor geometry can be seen in Figure 5.18. Note that slight field distortions are apparent on the edges of the purity monitor. An oscilloscope is employed in order to compare the signal induced on the cathode to the signal collected by the anode after drifting a time, t. In the case of an infinite electron lifetime (i.e. infinite purity), the cathode and anode signal amplitudes would appear equal and opposite, after accounting for the slightly different responses of the cathode and anode electronics readouts.

The electron drift lifetime, τ_{lifetime}, is determined with

$$\frac{Q_{\text{anode}}}{Q_{\text{cathode}}} = e^{-t/\tau_{\text{lifetime}}} \ , \tag{5.1}$$

where Q_{anode} and Q_{cathode} are proportional to the anode and cathode pulse heights, respectively. A purity monitor oscilloscope trace acquisition system was developed in order to automatically determine the electron lifetime from an average of 500 traces. The program employs peak-finding techniques to measure the cathode and anode signal amplitudes and then fits the exponential decay from each in order to account for the electronics signal response and ultimately extract the electron lifetime, given a drift time in between the signals. An example of one of these measurements is shown in Figure 5.19.

The electronegative impurity concentration inside the liquid argon can be obtained with (from Reference [121])

$$\frac{d[e]}{dt} = -k_s[S][e] \ , \tag{5.2}$$

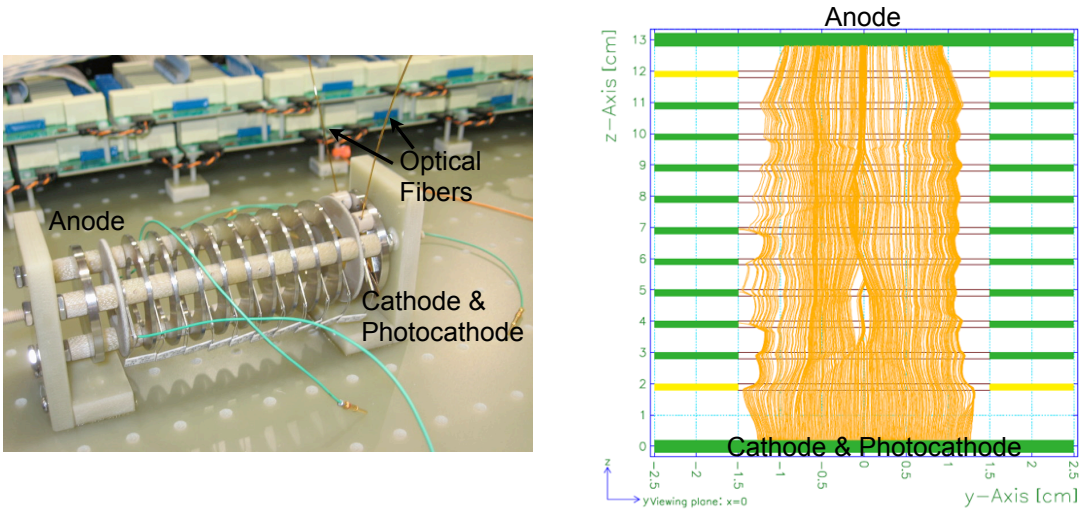

Figure 5.18: (Left) The purity monitor attached to the top of the TPC. A few bias voltage distribution cards can be seen in the background. (Right) An electric field and electron drift simulation of the purity monitor. The bottom is the cathode and photocathode where the photoelectrons originate, the top is is the anode, and the field cage is in between.

where $[e]$ is the electron concentration, t is time, $[S]$ is the electronegative impurity concentration, and k_s is the electron attachment rate constant ($\approx 10^{11}\mathrm{M}^{-1}\mathrm{s}^{1}$ at 100 V/cm for oxygen). Recombination with positive ions is ignored.

A solution to Equation 5.2 is

$$[e(t)] = [e_0]e^{-k_s[S]t} \ , \tag{5.3}$$

or, equivalently,

$$\frac{Q_{\mathrm{anode}}}{Q_{\mathrm{cathode}}} = e^{-k_s[S]t} \ , \tag{5.4}$$

where Q_{anode} and Q_{cathode} correspond to $[e_0]$ and $[e_t]$ after accounting for a few conversion factors. Now, with the help of Equations 5.1 and 5.3, we can write the relation between electron drift lifetime and electronegative impurity

$$[S] = \frac{1}{(35 \times k_s \times \tau_{\mathrm{lifetime}})} \ , \tag{5.5}$$

with the molar volume of liquid argon (35 mol/L) required to get $[S]$ (nominally in units of mol/L) in terms of a molar fraction (e.g. ppt), and the units of τ_{lifetime} in seconds. An

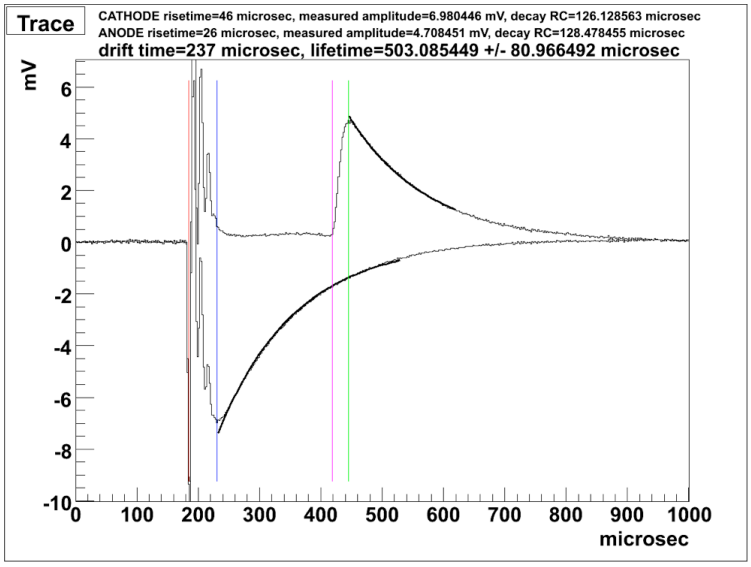

Figure 5.19: An average of 500 purity monitor oscilloscope traces taken in quick succession. The negative cathode signal can be seen on the left and the positive anode signal can be seen on the right. The time in between the signals is the drift time.

electron drift lifetime of 750 μs (typical of ArgoNeuT's neutrino-mode physics run) is found to be equivalent to an oxygen-equivalent electronegative impurity concentration of 400 ppt.

5.6 Electronics Readout

There are 706 wires that make up the wire planes of the ArgoNeuT TPC, 240 wires on each of the instrumented induction and collection planes and 226 wires on the uninstrumented shield plane. Each wire is 0.006 inches in diameter and is made of Beryllium-Copper Alloy #125. Bias voltage is applied to the wire planes by a Lecroy DC power supply and is distributed to the wires with 100 MΩ resistors. A DC blocking capacitor is placed in series with the signal in order to decouple the DC bias voltage from the AC signal ($\sim$150 kHz) output. The resistor and capacitor have little effect on the signal shape. The bias voltage distribution cards (see Figure 5.20) inside the cryostat and surrounding the TPC provide bias voltage, filtering, the resistor distribution, and DC blocking on the signal output wires. A single bias voltage distribution card is responsible for 24 wires and connects to the wire frame with two 12 pin connections. Voltages of -298 V, -18 V, and +338 V were provided to the shield, induction, and collection planes, respectively.

Ribbon cables with 24 signal+ground pairs of wires each bring the signal from the

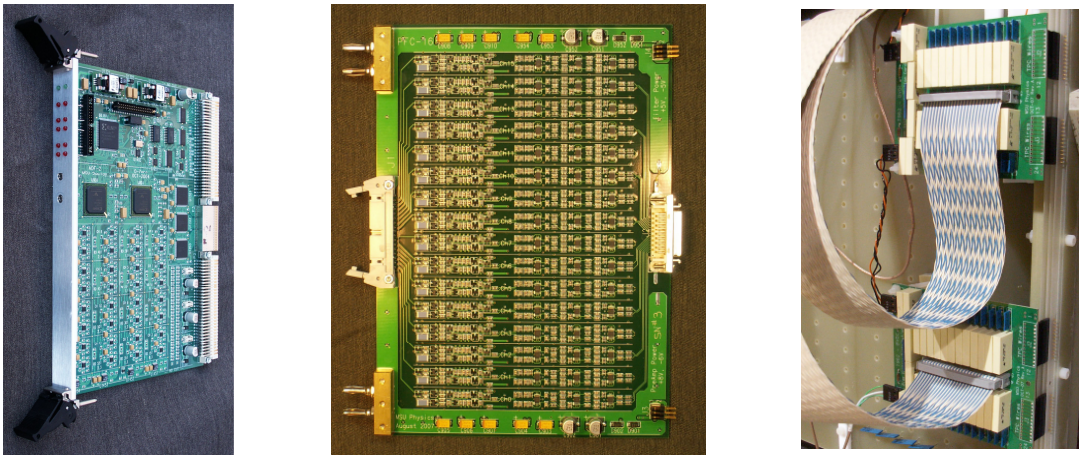

Figure 5.20: (Left) An ADF2 digitizer card, which samples at 5 MHz (2048 samples/channel). (Middle) The FET preamplifier and filters. (Right) A set of bias voltage distribution cards.

bias voltage distribution cards to the signal feedthrough about 9 feet away. Note that each bias voltage distribution card is in the liquid argon, right on top of the TPC, and the signal feedthrough is in the argon gas in the upper part of the cryostat. The signal feedthrough bridges the gap between the vacuum tight cryostat and the outside of the cryostat. After exiting the feedthrough, the signals arrive at a dual FET charge integrating preamplifier. The gain of the preamplifier provides 0.5 mV/fC output with a time constant of 200 μs. The signal output is then sent through a series of high and low pass filters. The feedthrough, 16-channel preamplifier cards, and pulse shaping filters are enclosed in a double RF shielded cage mounted on the outside of the cryostat. The cage features a remote duct cooling system. The outside of the feedthrough, shielding cage, remote ducts, custom filter/preamplifier power supply, and preamplifier card slots can be seen in Figure 5.21. After amplification and filtering, the signal is routed along 25 feet of cable and then digitized by a set of 32 channel ADF-2 modules. Each module features a 10 bit analog-to-digital converter. FPGAs in the ADF-2 modules sample every 198 ns and record the digital information on a circular buffer with 2048 positions. The digital signals are then read out by a computer and saved in binary format, one file for each event/trigger. The ADF2 digitizer and preamplifier/filter modules can be seen in Figure 5.20.

Nominally, the ArgoNeuT data acquisition system begins to read out an event after a trigger in time with the NuMI beam spill. Successive beam spills are about 1.9 s apart

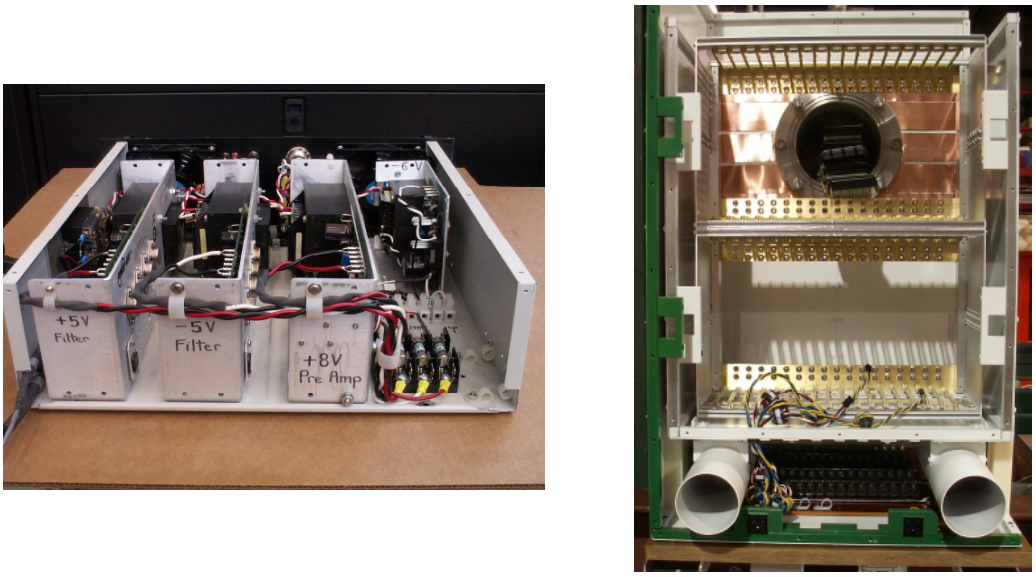

Figure 5.21: (Left) The ArgoNeuT electronics custom power supply. (Right) The RF shielding cage used to minimize noise on the feedthrough and preamplifiers. Also shown is the preamplifier cooling mechanism (with remote ducts).

and the total readout period is about 400 μs (2048 samples $\times$ 198 ns/sample). Note that this time window is larger than the maximum drift time of $\sim$333 μs from the cathode to the wire planes. The extra time allowed the events to be pre- and post-sampled–a useful background elimination and debugging tool. A thorough description of the ArgoNeuT electronics readout configuration can be found at Reference [122].

5.7 A Brief Introduction to the MINOS Near Detector

A description of the MINOS near detector, an essential component in ArgoNeuT's neutrino event reconstruction, follows. Although the MINOS experiment uses a near-far detector configuration, only the near detector is described here. Unless otherwise specified, "MINOS" will refer to the MINOS near detector henceforth.

The 0.98 kiloton MINOS detector utilizes a sandwich design with interleaved layers of magnetized steel and plastic scintillator. The sandwich is formed with a 1 cm thick scintillator affixed to a 2.54 cm thick slab of steel. Each scintillator-steel plane combination is separated from adjacent planes by 2.54 cm of air. Adjacent scintillator planes are oriented with respect to one another by 90° and $\pm$45° with respect to vertical in order to provide a

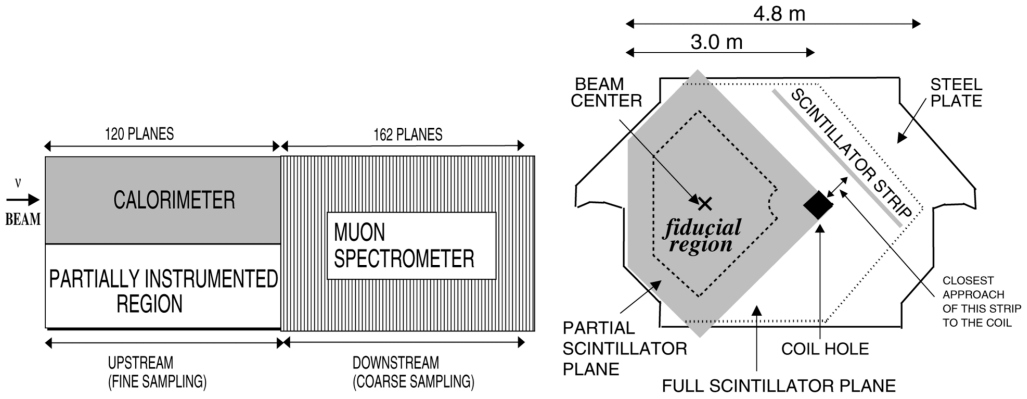

Figure 5.22: (Left) The regions of the MINOS near detector, as used by the MINOS experiment. The "partially instrumented" region has a full coverage plane every fifth plane. (Right) The MINOS plane configurations. The beam and fiducial volume are centered around the middle of the partially instrumented planes, left of the coil. Each plane provides a two dimensional view and adjacent planes are combined to form a three dimensional image of the event. The plots were taken from Reference [123].

three dimensional view of the event. There are 282 planes that make up the 16.6 m long near detector with 153 of those planes active. The planes are octagonally shaped with a 4.8 m width and 3.8 m height. Notably, the beam (and 1 m radius fiducial region) is off-center from the detector (see Figure 5.22). The most upstream 120 planes are all instrumented with every fifth plane being given full coverage and the other four receiving coverage on the beam centered side of the detector, in the fiducial volume. The remaining 162 planes downstream are instrumented every fifth plane with full coverage. The upstream and downstream ends are instrumented to provide a fine grained "target" region and a coarsely grained "muon spectrometer" region, respectively. The idea is that neutrinos that interact in the upstream target region create a muon (in the case of a charged-current muon-neutrino interaction) which ranges out and is fully reconstructed in the downstream muon spectrometer region. ArgoNeuT employs all available instrumented planes for muon reconstruction. The MINOS detector regions, plane configurations, and fiducial volume with respect to the beam can be seen in Figure 5.22.

Plastic scintillator is the active detector component in MINOS. Wavelength shifting fibers of 1.2 mm diameter run through each extruded scintillator and carry the >470 nm light produced in charged particle interactions in the scintillator to multi-anode photomultiplier tubes and readout electronics. The fiber layout and concept can be seen in Figure 5.23.

Light from a charged particle interaction with the scintillator is reflected multiple times by the reflecting walls surrounding the scintillator bars. The light that is eventually absorbed by the wavelength shifting fiber is re-emitted isotropically. The light that is emitted at an angle of incidence above the "critical angle" is internally reflected in the fiber and routed out of the detector for collection. The MINOS readout electronics digitize the photomultiplier tube signals with a dead-time-free sampling window (the sample rate is 19 ns/sample) during the entire beam spill. Cosmic ray physics and calibration data is taken in between beam spills.

Along with a stopping cosmic ray muon based calibration, a light injection system acts to calibrate the detector after measuring the detector response to a known light input. These calibration techniques are used to turn the raw photomultiplier tube signals into deposited energy [109]. MINOS features a <1.3 T> magnetic field created by a current-carrying coil which runs down the length of the detector near its center and then comes back along the outside of the detector. The 40 kA-turns coil provides a toroidal magnetic field. Knowledge of the field's spatial dependence comes from *in-situ* induced current loop measurements and precise steel and geometry modeling.

The MINOS detector is employed in this analysis for completely reconstructing neutrino-induced muons that originate inside of ArgoNeuT. Above 1 GeV, the muon energy measurement resolution ($\Delta E_\mu / E_\mu$) shifts smoothly from about 6% to 13% at higher energies [124]. Muons at typical neutrino-induced energies in the low-energy configuration of the NuMI beam ($\sim$2 GeV/c) lose about 30 MeV in each plane of steel until the end of the muon track when ionization increases rapidly. A 1.8 GeV muon travels through approximately 3 m of the MINOS detector before stopping, without considering the curvature due to the magnetic field. Therefore, the vast majority of neutrino-induced muons range out in the detector and are precisely calorimetrically reconstructed with $\sim$6% energy resolution. Those muons that do not range out in the detector and escape can be calorimetrically reconstructed by their curvature in the magnetic field. The energy resolution for exiting 10 GeV/c muons is about 13%.

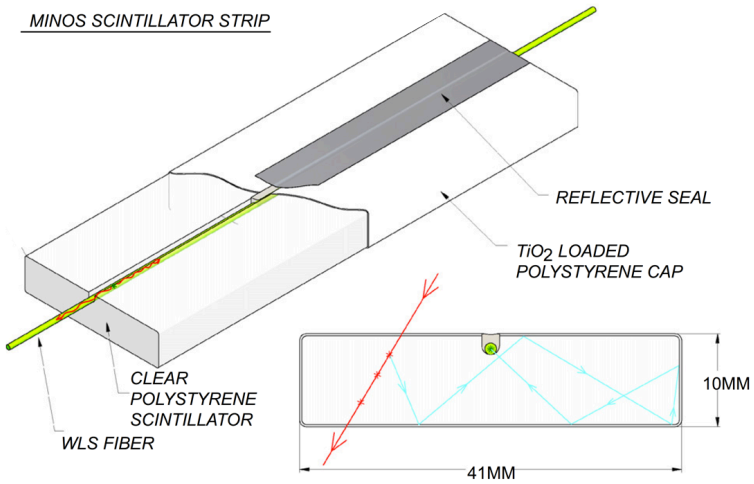

Figure 5.23: The composition of and concept behind a MINOS scintillator strip. This plot has been adapted from Reference [109].

6 ArgoNeuT Software: Simulation

The ArgoNeuT simulation includes neutrino event generation, propagation of the neutrino-induced particles through a detailed detector model, drift and diffusion of the resulting ionization, creation of signals on the wires of the TPC, and a model of the electronics response to those signals. Furthermore, the simulation propagates those particles that leave the TPC volume and, when applicable, onto the front face of the MINOS near detector. Just like in the case of data, simulated particle trajectories as seen by the ArgoNeuT wires and MINOS are reconstructed. The simulation is necessary in order to understand the detection/reconstruction efficiency and measurement resolution in a multitude of neutrino event and kinematic scenarios. The software is also useful in the determination of selection cuts, reconstruction algorithm tuning, and comparison to data, among other things.

6.1 Neutrino Event Generation

Simulating neutrino-nucleus/nucleon events is a difficult challenge. First, the neutrino can interact in many different ways with a nucleus/nucleon and the cross section for each exclusive process with $E_\nu \lesssim 25$ GeV is usually only known to $\sim$25%. Second, free-nucleon- and bound-nucleon-target neutrino cross sections are not the same and different nuclei carry unique characteristic cross sections and outgoing neutrino-product particle kinematics. Even in the case of a target with only bound nucleons, nucleon binding energy, Fermi momentum, Pauli blocking, Fermi shadowing, and more can change the cross section depending on the target nucleus. These effects represent the scattering probability and outgoing kinematic contributions from the momentum of the struck nucleon as well as the properties of the struck nucleon's environment. Third, hadrons created in a neutrino in-

teraction often re-interact in the nucleus. The cross sections and angular distributions of these interactions are not well measured, especially for high-A targets. Some of these issues are discussed below in the context of comparing two commonly used neutrino event generators and simulating neutrino interactions on argon. Exclusive neutrino interaction channels, including neutral-current ones, are discussed in order to more readily discern differences between the generators. The main subject of this thesis, the muon-neutrino charged-current inclusive interaction, is discussed at length in Section 8.1. The following discussion on neutrino event generation, exclusive neutrino interaction channels, and final state interactions is relevant to this analysis, however. The event generator discussion leads to the GENIE program [125] being adopted for neutrino simulation in the analysis presented here and provides some insight into the various models that are used for simulating neutrino interactions. The neutrino interaction channel discussion serves to help understand the exclusive components of the inclusive cross section. The final state interaction and exclusive channel definition sections demonstrate some of the complications associated with making a cross section measurement and definitively identifying a neutrino event of a particular channel. Along with being valuable in the treatment of the subtleties of neutrino event generation, these topics exemplify the importance of precisely measuring and understanding the standard candle of neutrino interactions, the charged-current inclusive interaction.

6.1.1 Comparing the Nuance and GENIE Event Generators

Without a universal standard for event generation, the neutrino community is often forced to consult more than one neutrino generator for a given experiment. The Nuance and GENIE neutrino event generators have been studied for use with liquid argon and more specifically, the ArgoNeuT experiment.

The Nuance (v3) and GENIE (v2.6) programs are two of the most widely used neutrino generators at GeV-scale energies. In the following study, each generator takes the NuMI all-flavor neutrino-mode flux at ArgoNeuT as an input and produces events with a random spatial distribution in the ArgoNeuT TPC. The output primary particles are then directed to Geant4 and tracked through the argon medium of the TPC.

6.1.2 LAr-specific modifications to GENIE and Nuance

The GENIE software is billed as a "Universal Neutrino Generator" and has been treated as such. Apart from specifying argon as the interaction medium at run time, nothing has been changed in GENIE with regard to neutrino interaction simulation. Performing a direct comparison to Nuance did require some code additions, however. The lead developer of GENIE confirms that argon is simulated correctly in GENIE but should benefit from an upgraded nuclear model based on fully validated spectral functions in the future [126]. The spectral function of a given nucleus $P(\vec{p}, E)$ is the probability distribution describing the chance to find a nucleon with momentum $\vec{p}$ and removal energy E. Note that there is a single recent paper on argon spectral functions [127]. The GENIE documentation notes that "(GENIE) encompasses and supersedes a host of successful Fortran neutrino MC generators, such as GENEVE, NEUT, NeuGEN, and NUX that have been used extensively in the design and exploitation of many previous and current neutrino experiments" [125, 128–131].

Nuance was originally created for simulating neutrino interactions in a water Cerenkov detector. The MiniBooNE collaboration [132] has edited the Nuance code extensively in order for it to simulate neutrino interactions on carbon (CH_2). Taking these code changes as a template, the Nuance source code has been edited to simulate neutrino interactions on (liquid) argon.

6.1.3 Cross sections

Even with the help of the downstream MINOS detector, ArgoNeuT can rarely fully reconstruct single pion resonant (e.g. $\nu_\mu p \longrightarrow \mu^- p \pi^+$) and deep inelastic (e.g. $\nu_\mu N \longrightarrow \mu^- X$) events as the hadronic components of such events usually escape the active detection region. However, demonstrating the ability to identify these events as a background to signal processes with unprecedented efficiency using $\frac{dE}{dx}$ and topology near the event vertex is of great interest to the neutrino community and vital for future experiments. Therefore, all relevant processes at NuMI energies are discussed. A table of the most relevant GeV-scale exclusive neutrino interactions is shown in Figure 6.1.

CCQE ($\nu_\mu n \longrightarrow \mu^- p$)

With only an outgoing muon and proton, a CCQE event (see Figure 6.2) is perhaps the easiest neutrino interaction to identify and reconstruct. Also, the cross section is compara-

Type	Reaction
Quasi-elastic (QE)	$\nu_\mu n \longrightarrow \mu^- p$
Resonant pion (RES)	$\nu_\mu p \longrightarrow \mu^- p\pi^+$
	$\nu_\mu n \longrightarrow \mu^- p\pi^0$
	$\nu_\mu n \longrightarrow \mu^- n\pi^+$
Neutral-current (NC)	$\nu_\mu p \longrightarrow \nu_\mu p\pi^0$
	$\nu_\mu p \longrightarrow \nu_\mu n\pi^+$
	$\nu_\mu n \longrightarrow \nu_\mu n\pi^0$
	$\nu_\mu n \longrightarrow \nu_\mu p\pi^-$
Deep inelastic (DIS)	$\nu_\mu N \longrightarrow \mu^- X$
	$\nu_\mu N \longrightarrow \nu_\mu X$

Figure 6.1: A table of common muon-neutrino interactions at GeV-scale energies. Note that the products of the neutrino interactions in this table have not yet been subject to final state interactions in the nucleus. All hadrons produced in a neutrino-argon interaction are subject to final state interactions. That is, the produced hadrons have to navigate through the dense nucleus before they are able to be detected and reconstructed. The hadrons are subject to pion/nucleon absorption (e.g. $\pi N \longrightarrow NN$), pion charge exchange (e.g. $\pi^+ X \longrightarrow \pi^0 Y$), pion production (e.g. $\pi X \longrightarrow \pi\pi Y$), and inelastic and elastic scattering (e.g. $hX \longrightarrow hY$ and $hX \longrightarrow hX$). One can imagine how such reactions confuse exclusive channel classification of neutrino events.

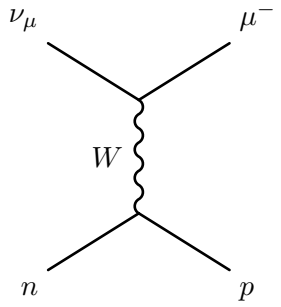

Figure 6.2: A CCQE interaction.

tively high at energies typical of neutrino oscillation experiments (E_ν=0-10 GeV). GENIE handles CCQE interactions with an implementation of the Llewellyn-Smith model [133] and Nuance uses Smith and Moniz [134]. Both generators use the Fermi gas model to simulate Pauli blocking. Pauli blocking is the reduction of the phase space for a nucleon transition (e.g. neutron-to-proton) due to occupation of the nucleon momentum states within the Fermi gas volume. The free nucleon cross section for a given axial vector mass (M_A) value is well known, so any disagreement between the generators would largely come from different nuclear suppression factors (a function of Q^2) in the Fermi gas model. Note that the CCQE cross section is nearly linearly dependent on M_A and the default value of M_A=0.990 GeV used in GENIE and Nuance is low compared to the recent measurements of K2K [135]

and MiniBooNE [136, 137]. However, M_A can only be considered in the context of a form factor model as different models require different M_A values in order to get the same agreement with data. M_A and other parameters can be changed easily in both generators. By default, Nuance uses the Bosted [138] quasi-elastic vector form-factor model and GENIE the BBA2005 [139, 140] model. Both generators allow other form-factor models to be used. The CCQE cross section on argon according to each generator can be seen in Figure 6.3. An example of the CCQE outgoing particle kinematics with each generator can been seen in Figure 6.4.

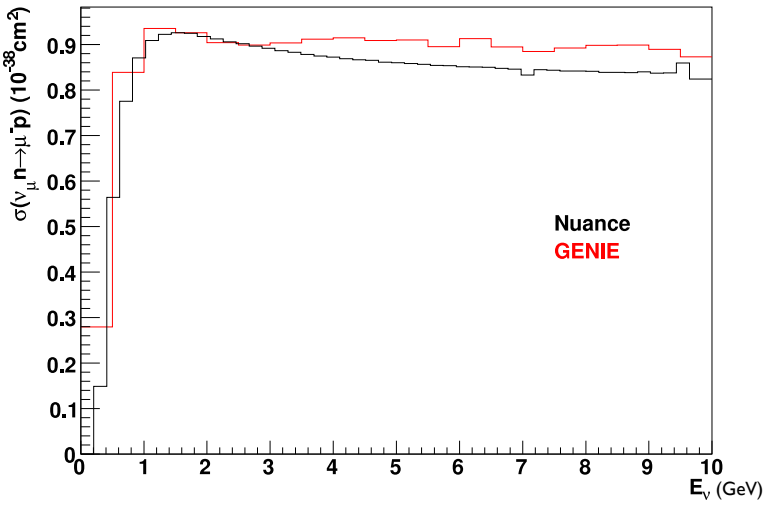

Figure 6.3: The CCQE cross section on argon (M_A=0.990 GeV) in Nuance and GENIE.

Neutral-current elastic ($\nu_\mu N \longrightarrow \nu_\mu N$)

With the ability to reconstruct and identify low energy particle tracks, LArTPCs are optimal for studying the neutral-current elastic channel (see Figure 6.5). The outgoing proton (in the case of $\nu p \longrightarrow \nu p$) is usually invisible to Cerenkov-based detectors and there are few measurements of this process available. Also, tagging neutron events may be possible if more than one track due to a neutron interaction is seen in the TPC. The neutral-current elastic proton to CCQE ratio ($\frac{\nu p \longrightarrow \nu p}{\nu_\mu n \longrightarrow \mu^- p}$) may also allow a measurement of Δ_s, the strange spin component of the nucleon. This measurement can benefit greatly from a LArTPC's high event identification efficiency utilizing $\frac{dE}{dx}$, topology, and the ability to distinguish protons from neutrons, if the neutron identification requirement is met. The neutral-current elastic

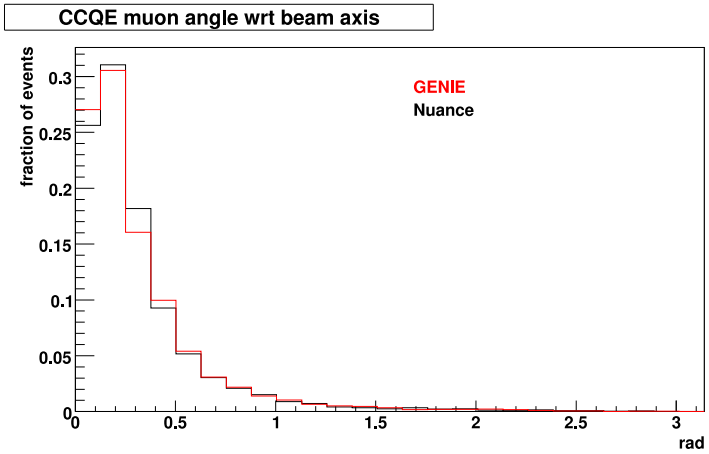

Figure 6.4: The muon angle with respect to the incoming neutrino for simulated CCQE events on argon.

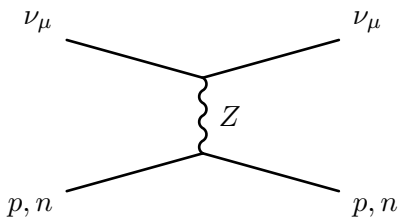

Figure 6.5: A neutral-current elastic interaction.

cross sections for both the proton and neutron channels according to each generator can be seen in Figure 6.6. Disagreement between the generators may be due to the fact that few $\frac{d\sigma}{dQ^2}$ measurements are available (for neutral-current elastic interactions, $Q^2 = 2M_N T$, where M_N is the mass of the struck nucleon and T is the kinetic energy of the nucleon). However, Reference [141] is the main resource for this channel and both generators seem to use this paper for their cross section modeling. Note that MiniBooNE has recently published a measurement of the neutral-current elastic cross section [142].

Single pion resonant ($\nu_\mu N \longrightarrow l N^{(\prime)} \pi$)

Although fully reconstructing a single pion resonant event (see Figure 6.7) will prove to be a challenge with ArgoNeuT, a cross section measurement of a high rate resonant channel like "CCpi+" ($\nu_\mu N \longrightarrow \mu^- N \pi^+$) may be possible. Furthermore, demonstrating the event identification power of a LArTPC with CCpi+ and other resonant channels is impor-

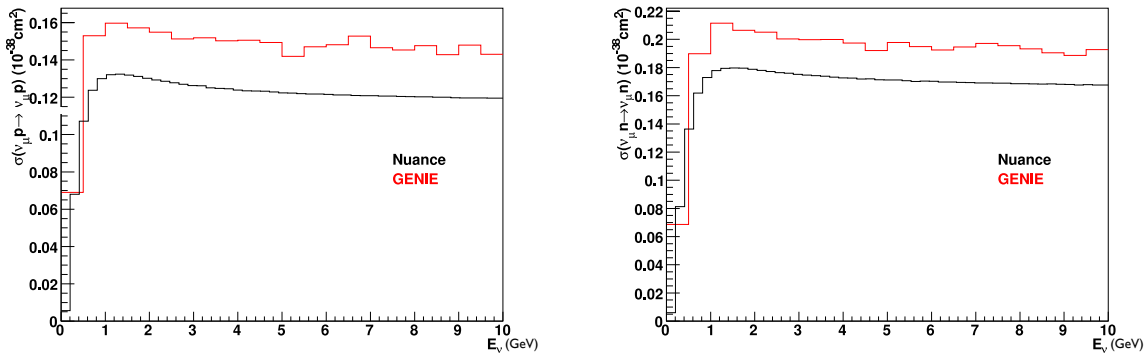

Figure 6.6: The proton (left) and neutron (right) neutral-current elastic cross section on argon in Nuance and GENIE.

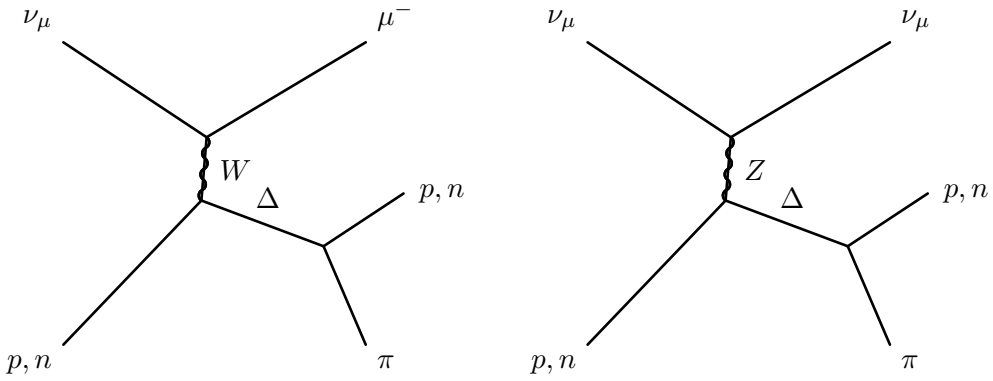

Figure 6.7: Single pion resonant interactions (charged-curent on left, neutral-current on right).

tant. Notably, the MiniBooNE experiment has recently published a number of total and differential cross section results on exclusive final state resonant interactions [143–146].

GENIE and Nuance use the Rein-Sehgal model [147] for neutral-current and charged-current resonant interactions. The model employs the relativistic harmonic oscillator model [148] for calculating the matrix elements of the nucleon-to-resonance excitation process. GENIE neglects interference between resonances with equal isospin while Nuance's single pion channels interfere coherently (with the other channels interfering incoherently). The axial vector mass, essentially the main parameter in the Rein-Sehgal model, has been made the same in Nuance and GENIE. However, the generators define non-resonant background in different ways as discussed in Section 6.1.7. Aside from small width and mass differences, the implementation of Rein-Sehgal is also slightly different due to the fact that Nuance uses 18

resonances while GENIE counts 16 resonances "that are listed as unambiguous in the latest PDG baryon tables" [125].

Note that the single pion cross section plots that follow show the resonant plus non-resonant cross section and have been made after altering GENIE's DIS definition. The GENIE DIS definition has been made to relatively coincide with Nuance's by requiring that to be considered DIS, the invariant mass W must be greater than 1.7 GeV. GENIE's integrity remains as the cuts were made after event generation and do not affect the source code. A DIS event in GENIE with W<1.7 GeV is considered "non-resonant" background in the single pion resonant cross section plots below and is added onto the resonant part to give the total cross section for a given channel.

As GENIE handles such events differently than Nuance, it is worth explicitly stating what goes into a particular channel. As an example, we arbitrarily consider the $\nu_\mu n \longrightarrow \mu^- p \pi^0$ channel in GENIE. The resonant part requires an incoming muon neutrino interacting with a neutron via the charged-current, W less than 1.7 GeV, resonance creation, one primary (before intra-nuclear scattering) proton, zero primary neutrons, one primary π^0, zero primary π^+s, and zero primary π^-s. The non-resonant part includes events originally defined as charged-current DIS events with an incoming muon neutrino interacting with a neutron via the charged-current, W less than 1.7 GeV, one primary proton, zero primary neutrons, one primary π^0, zero primary π^+s, and zero primary π^-s.

The transition region ambiguities (discussed below) aside, the correct way to place a non-resonant event in a particular channel is unclear. The primary state should obviously include a π^0. But, should the cut exclude events with more than one primary π^0? Should the cut exclude events with π^+ and/or π^-? Should the cut require a final state π^0 and what about pion re-absorption?

In summary, the concept of "channel" is ambiguous in two ways:

1. There are three different processes (resonant, normal DIS, transition DIS) that can contribute to the same hadronic system before intra-nuclear scattering.

2. Intra-nuclear scattering affects the final-state topology of an event. For example, a topology with $X\pi^0$ in the final state may have come from a $Y\pi^-$ initial hadronic system with the π^- undergoing a charge exchange process ($\pi^- Y \longrightarrow \pi^0 X$).

Luckily, GENIE's channel scheme is not set in stone and the above questions can be answered in different ways by the experimentalist. The CCpi+ cross section according to

the generators can be seen in Figure 6.8. The cross sections for the other relevant resonant channels can be seen in Figure 6.9.

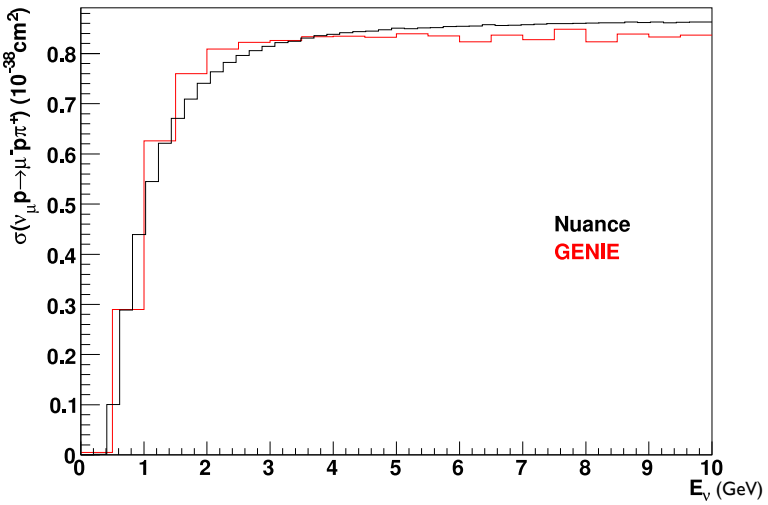

Figure 6.8: The single pion resonant CCpi+ cross section on argon in Nuance and GENIE.

Deep Inelastic Scattering ($\nu_\mu N \longrightarrow lX$)

Deep inelastic scattering (see Figure 6.10) cross sections are computed using the modified leading order QCD-based Bodek-Yang (BY) model (Reference [149] in Nuance and Reference [150] in GENIE). However, GENIE includes nuclear effects (shadowing, anti-shadowing) and longitudinal structure functions (with the Whitlow R parametrization [151]) while Nuance does not. The DIS cross section plots below use a consistent definition of DIS (requiring W>1.7 GeV), as discussed above. GENIE and Nuance both use a combination of KNO-based and tuned LUND-based models [152, 153] for hadronization and hadron multiplicity. The model was tuned with the NOMAD experiment, in the context of the NUX generator [131]. The Nuance documentation notes that "deep-inelastic scattering is undoubtedly the regime where Nuance currently lags behind the state-of-the-art in other generators dedicated to high-energy neutrino physics" [154]. The DIS cross sections according to each generator can be seen in Figure 6.11.

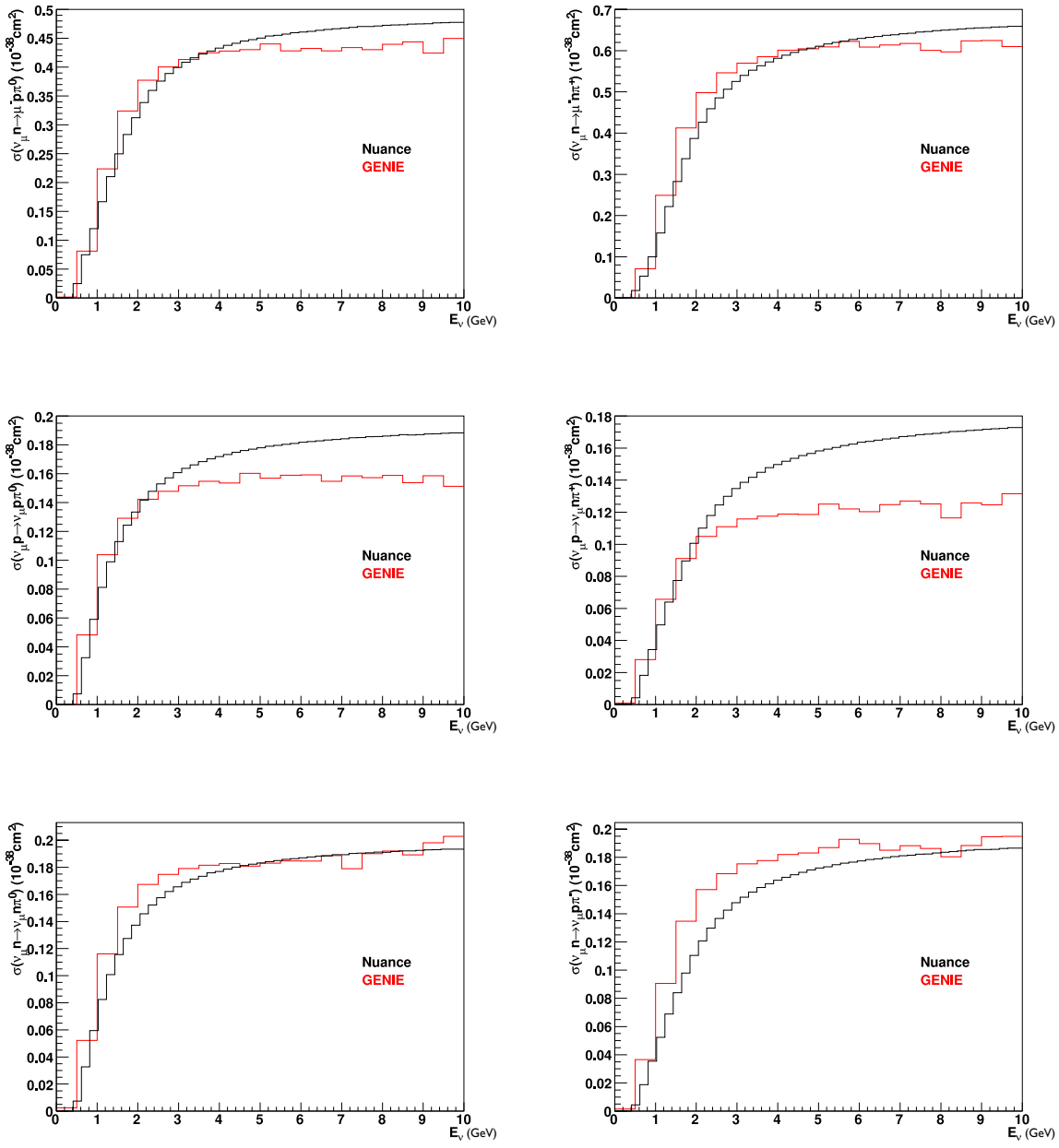

Figure 6.9: The single pion resonant cross sections on argon in Nuance and GENIE.

Coherent ($\nu_\mu A \longrightarrow l A \pi^{+,0}$)

The coherent neutrino pion production interaction (see Figure 6.12), where a neutrino scatters from the whole of the nucleus to produce a pion, is perhaps the least well understood exclusive channel for 0-10 GeV-scale neutrino energies. Although both channels can contribute a >10% increase to total neutrino-induced pion production, the neutral-current

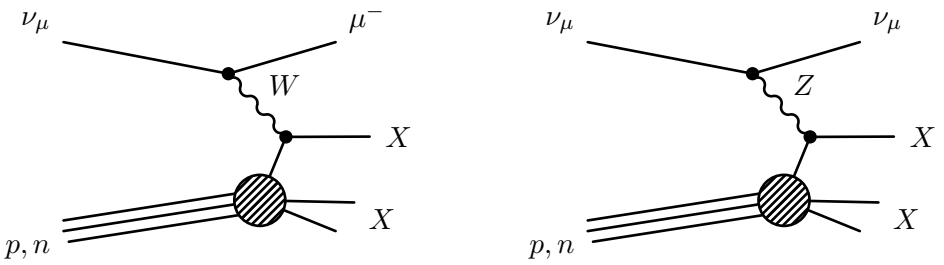

Figure 6.10: DIS interactions (charged-current on left, neutral-current on right).

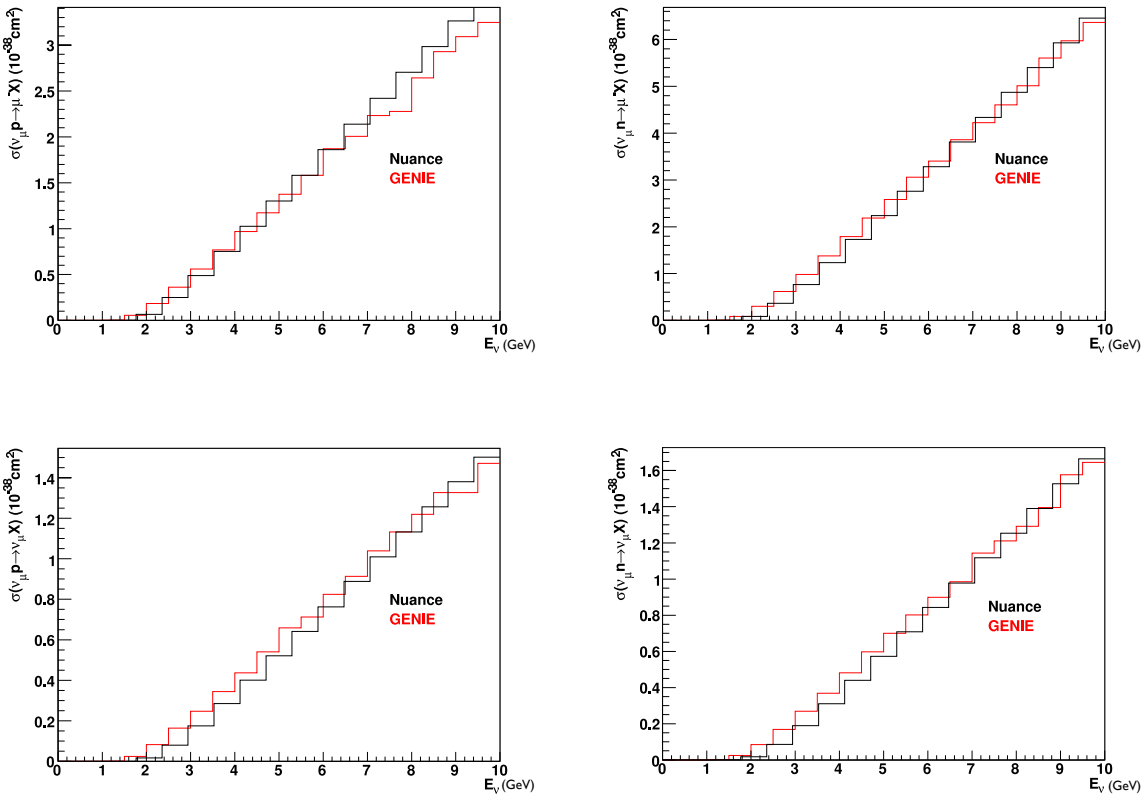

Figure 6.11: The DIS cross sections on argon in Nuance and GENIE.

mode is especially important for long baseline neutrino oscillation experiments as it is a background for the signal charged-current electron-neutrino process. Nuance and GENIE both use the Rein and Sehgal cross section calculation [155] for coherent scattering. However, GENIE uses the updated Rein version [156] with the modified PCAC formula, including destructive interference between some terms for charged-current interactions. There is more than 100% uncertainty on the cross section for the neutral-current coherent π^0 channel at relevant energies. Also, pion absorption in coherent interactions is poorly understood

and can lead to a factor of two difference in coherent rate [154]. MiniBooNE has recently published a coherent π^0 to single π^0 resonant fraction of $(19.5 \pm 2.7)\%$ at $<E_\nu>\approx$1.1 GeV, 35% lower than the Rein-Sehgal prediction [157, 158]. SciBooNE reports the ratio of coherent π^0 to total CC cross section of (0.007±0.004) based on the Rein Sehgal model at $<E_\nu>\approx$1.1 GeV with a Monte Carlo prediction of the ratio equal to 0.0121 [159]. The K2K collaboration has shown data consistent with no charged-current coherent π^+ production at $<E_\nu>\approx$1.3 GeV [160]. Similar behavior is seen from SciBooNE [161]. These results are inconsistent with the original Rein-Sehgal paper as the model, assuming $\sigma \sim A^{\frac{1}{3}}$ in order to compare different targets, predicts $\sigma_{\rm CC}=2\sigma_{\rm NC}$. However, the updated Rein paper predicts a suppression of coherent π^+ production in the $Q^2<0.1$ GeV^2 region of a factor of ≈0.77 [156]. Other coherent production models are difficult to test and do not provide pion kinematics [160]. The MINERνA experiment [110], taking data in the NuMI beamline since 2009, may shed some light on coherent scattering as it is poised to measure 85,000 charged-current coherent π^+ and 37,000 neutral-current coherent π^0 on different targets (He, C, Fe, Pb). Measuring the dependence of the coherent cross section on atomic number is a priority for the experiment.

The coherent cross sections according to each generator can be seen in Figure 6.13. Figures 6.14 and 6.15 show the Q^2 (left) and π^+ angle with respect to the incoming neutrino direction distributions in single pion resonant and coherent events. The coherent event signature, a forward-scattered pion, may be difficult to discern with low event containment and low statistics in ArgoNeuT. However, ArgoNeuT and future LArTPCs will benefit from being able to identify as background those single pion events with a clear proton/neutron track or a significant energy deposition at the vertex, indicative of a resonant event.

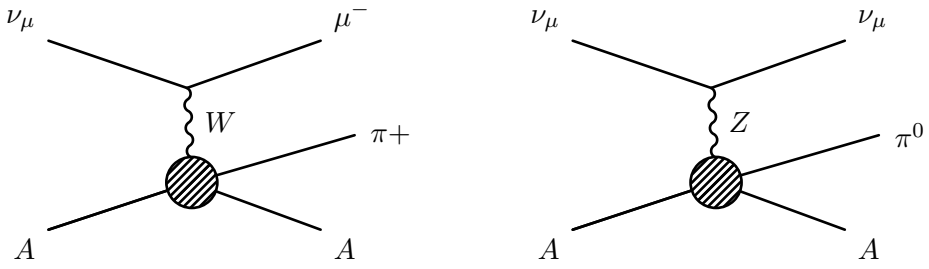

Figure 6.12: Coherent interactions (charged-current on left, neutral-current on right).

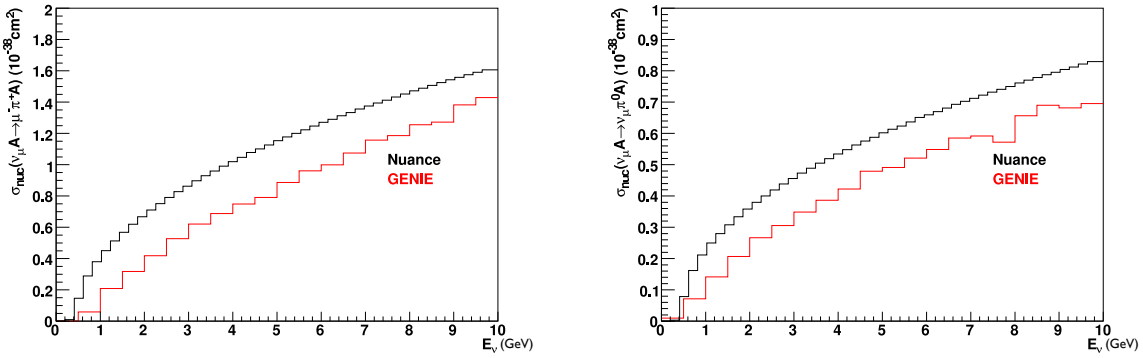

Figure 6.13: Charged-current coherent π^+ (left) and coherent neutral-current π^0 (right) cross section on argon in Nuance and GENIE.

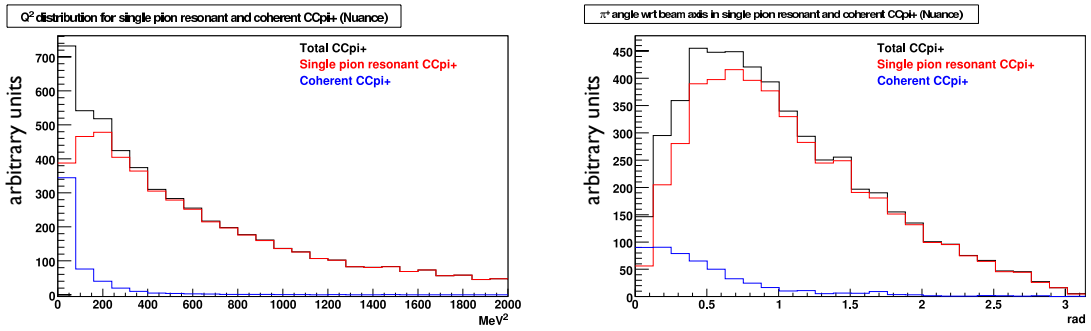

Figure 6.14: Single pion resonant CCpi+ ($\nu_\mu p \longrightarrow \mu^- p\pi^+$ and $\nu_\mu n \longrightarrow \mu^- n\pi^+$) and coherent CCpi+ Q^2 (left) and π^+ angle with respect to the incoming neutrino direction (right) in Nuance. Notice the low-Q^2 and π^+ forward scattering for coherent CCpi+.

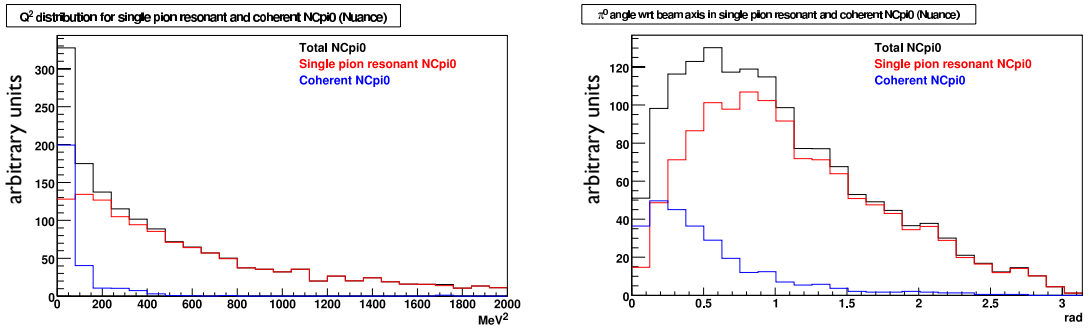

Figure 6.15: Single pion resonant NCpi0 ($\nu_\mu p \longrightarrow \nu_\mu p\pi^0$ and $\nu_\mu n \longrightarrow \nu_\mu n\pi^0$) and coherent NCpi0 Q^2 (left) and π^0 angle with respect to the incoming neutrino direction (right) in Nuance. Notice the low-Q^2 and π^0 forward scattering for coherent NCpi0.

6.1.4 Kinematics

The Nuance and GENIE neutrino event generators largely agree on exclusive channel cross sections considering that precise cross section data from 10 MeV to 10 GeV is usually lacking and a 20% "disagreement" in a particular channel is often not unexpected. Furthermore, models like Rein-Sehgal (resonant, single pion), and Bodek-Yang (DIS) are universally accepted for parameterizing neutrino cross sections. Nuclear effects like Pauli blocking and Fermi momentum can alter the functions (along with different and non-trivial model implementation) but the free-nucleon cross sections should be fairly similar between generators.

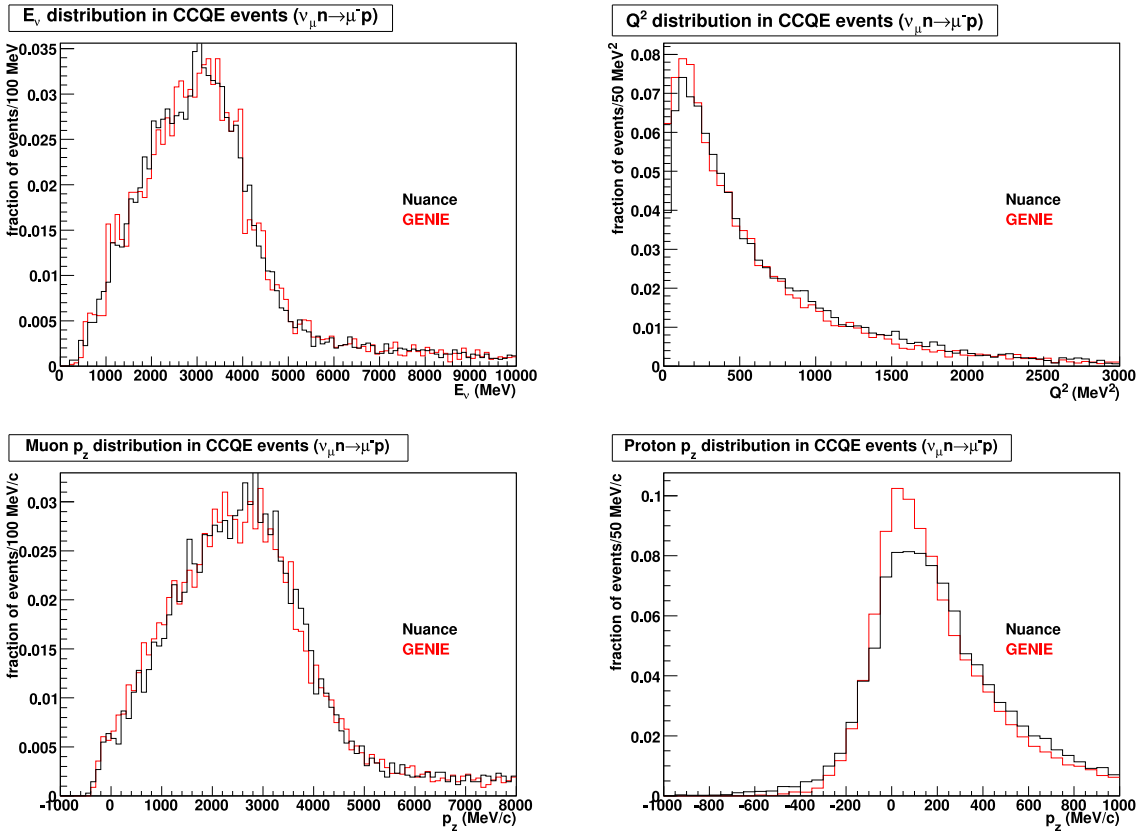

Figure 6.16: CCQE kinematics in ArgoNeuT.

Particle multiplicity and kinematics, largely based on the final state interaction model being used, are what really separate one generator from another. As final state interactions are not observable and observable processes do not necessarily correspond to their theoretically conjectured and often poorly modeled unobservable past, we can expect that there

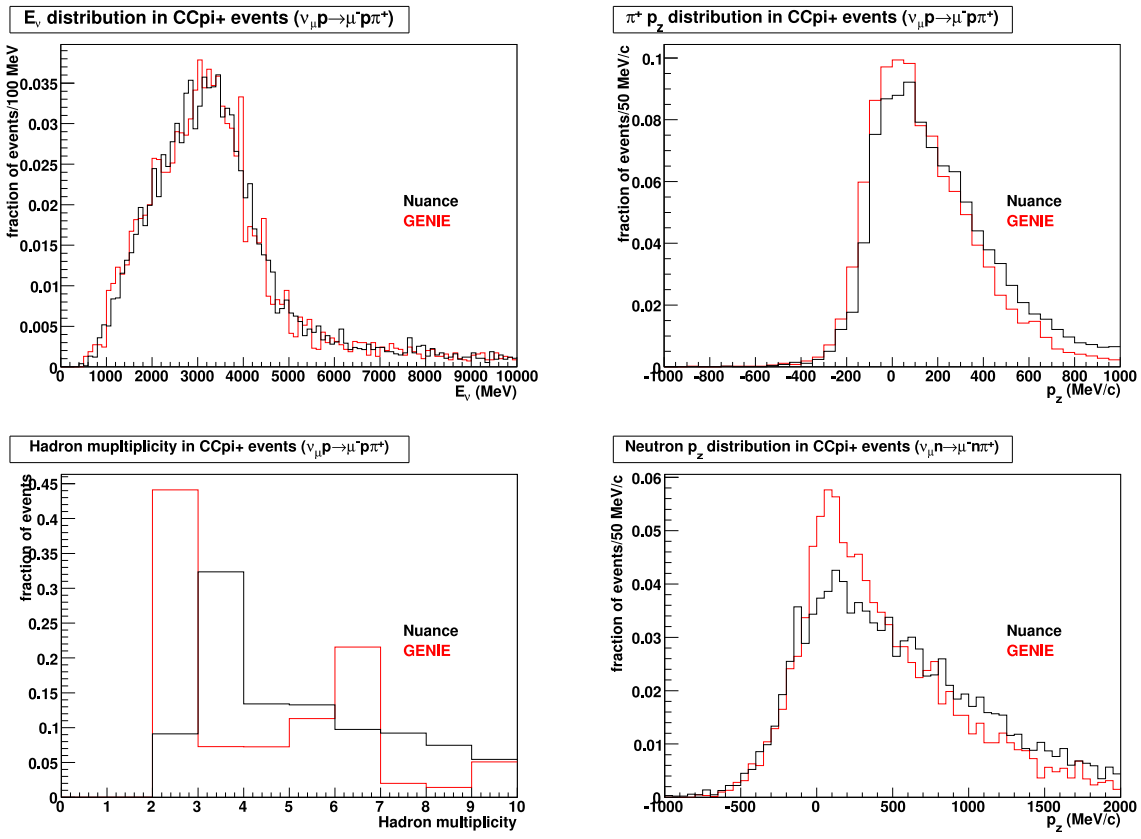

Figure 6.17: CCpi+ kinematics in ArgoNeuT.

will be some disagreement between models. Without mentioning the cross section of such interactions, modeling the energy and angular distribution of the products of intra-nuclear collisions is difficult as there are many types of interactions and little data. The kinematics of intra-nuclear pion absorption is an interesting example. An absorbed pion can drastically affect the reconstructed neutrino energy as the pion's energy is often distributed to a large number (>2) of nucleons [162, 163]. These nucleons may have kinetic energy below that which is detectable and can therefore lead to a reconstructed neutrino energy that is too low. In Nuance, an absorbed pion's energy gets distributed in a 2-nucleon final state ($\pi N \longrightarrow NN$) [164]. GENIE's INTRANUKE goes a step further and distributes the pion's energy according to phase space in one of the following channels: $\pi N \longrightarrow np$, $\pi N \longrightarrow pp$, $\pi N \longrightarrow npp$, $\pi N \longrightarrow nnp$, $\pi N \longrightarrow nnpp$, and $\pi N \longrightarrow n\pi^+\pi^0$.

Much work has been done in Nuance and GENIE to match the meson-nucleon/nucleus and nucleon-nucleon/nucleus cross section and angular distribution models to data. One

can compare the generator results against data by running the simulation in reverse by starting a pion, kaon, or nucleon and impinging it on the outside of a nucleus. Data is available for ^{16}O, ^{16}C, ^{56}Fe and others. A study comparing Nuance to GENIE in this regard has not been completed by the author, although it is possible to perform such a study with both generators. Furthermore, a full study on a LArTPC's sensitivity to final state interactions has not been completed. A sense of the effects of different intra-nuclear models can be gathered from the kinematics plots shown in Figures 6.16 and 6.17. Notice that although the neutrino energy and muon p_z distributions are quite similar between the generators, the final-state-hadron multiplicity and p_z distributions can differ significantly.

It is worth briefly summarizing the different approaches to the complicated process of intra-nuclear scattering (also referred to as "final state interactions") here.

6.1.5 Nuclear processes in Nuance

In Nuance, a neutrino-nucleon interaction is given a starting position based on the Woods-Saxon nuclear density distribution $\rho(r) = \frac{\rho_0}{1+e^{(r-c)/z1}}$. The time it takes for a quark to hadronize in a "formation zone", during which the quark interacts with very low probability, is taken into account. The hadron formation time is 2.0 fm/c in Nuance. After creation, the hadron is then tracked through the nucleus in 0.3 fm steps after being given a 1.0 fm "free" (of interactions) first step. The hadron is stepped through the nucleus until it interacts with a nucleon or leaves the nucleus. The interaction probability is taken from pion-nucleon and nucleon-nucleon cross sections and angular distributions. A free step is given after every interaction. After an interaction, the hadron continues to step though the nucleus. Any interaction products follow the same stepping procedure. The nucleus is considered as an isoscalar sphere of effective radius $R = R_0 A^{1/3}$ (with $R_0 = 1.01$ fm) with nuclear density and Fermi momentum radially dependent. Note that the differential nuclear density's affect on cross section is simulated. That is, Nuance takes into account the changing nuclear density as nucleons are pushed out of the nucleus. The pion-nucleon and nucleon-nucleon cross sections and angular distributions are based on HERA data [165] and have been tuned using the reverse-simulation method mentioned above with ^{16}O. Any data-less interaction cross section is treated with respect to isospin symmetry. Pion/nucleon absorption (e.g. $\pi N \longrightarrow NN$), pion charge exchange (e.g. $\pi^+ X \longrightarrow \pi^0 Y$), pion production (e.g. $\pi X \longrightarrow \pi\pi Y$), inelastic and elastic scattering (e.g. $hX \longrightarrow hY$ and $hX \longrightarrow hX$), and

nuclear de-excitation are simulated in Nuance. Further details can be found in the Nuance documentation previously cited.

6.1.6 Nuclear processes in GENIE

GENIE uses a C++ adaptation of NeuGEN's [130] updated INTRANUKE package for intra-nuclear hadron transport. A formation zone is also treated in GENIE with the SKAT model [166], which has formation time (of 0.52 fm/c) as the only free parameter. The incident neutrino is made to interact on the outside of the nucleus with interaction probability based on a modified Woods-Saxon model of the density distribution. The hadron scatters according to the hadron-nucleon cross section and the matter density at radius r, given a mean free path $\lambda = \frac{1}{\rho(r)\ \sigma_{hN}(E)}$ that is calculated as the hadron moves through the nucleus of radius $R = R_0 A^{1/3}$ (with $R_0 = 1.4$ fm). The hadrons that are directly produced by the incoming neutrino are allowed to re-interact in the nucleus only once. After an interaction, the resultant particles are placed outside the nucleus and considered "final-state". Inelastic processes like pion absorption and inelastic scattering are well matched to data in this semi-classical model. However, the model ignores quantum mechanical wave-effects which are important for hadron-nucleus elastic scattering [167]. A modification to the c parameter in $\rho(r)$ fixes this to increase the nuclear size and thereby increase the model's hadron-nucleus cross section to fit data (π^+ on ^{16}C and ^{56}Fe). This modification to $\rho(r)$ is only valid for hadron re-scattering in the nucleus and not for the initial neutrino-nucleus vertex.

The hadron-nucleus cross sections in GENIE come from a complicated hybridization of the world's data [168–176] and the CEM03 calculations [177, 178] for pion and nucleon interactions on iron (with re-weighting for other nuclei). Pion/nucleon absorption, pion charge exchange, pion production, inelastic and elastic scattering, nuclear breakup, and nuclear de-excitation are simulated in INTRANUKE until $r = 3R$. Note that the probabilities for each channel do not come from hadron-nucleon cross sections. Instead, they come from existing hadron-nucleus data, making the current version of INTRANUKE a simplified intra-nuclear cascade model. It should be emphasized that this is not a bad thing as 1) the simplified hadron-nucleus model is well matched to data, 2) there isn't data available for all possible hadron-nucleon cross sections and kinematics, and 3) the model is simple enough as to easily study systematics. The GENIE developers are currently working on an updated full cascade model which derives all interaction probabilities from hadron-nucleon cross

sections. Further details can be found in the GENIE and INTRANUKE documentation previously cited.

6.1.7 The transition region

Nuance employs a convenient neutrino channel numbering scheme in order to differentiate one type of event from another. For example, CCQE events ($\nu_\mu n \longrightarrow \mu^- p$) are given channel number 1, CCpi+ events ($\nu_\mu p \longrightarrow \mu^- p \pi^+$) are channel number 3, neutral-current DIS events ($\nu_\mu N \longrightarrow \nu_\mu X$) are channel number 91, etc. The exclusive channels refer to the neutrino-nucleus interactions themselves and are therefore defined before final state interactions. This scheme works well for an experiment like MiniBooNE with E_ν ~1 GeV. Problems arise, however, if the neutrino energy is higher than the DIS threshold and the transition region (between resonant and deep inelastic scattering) becomes relevant. Resonant and inelastic, non-resonant events can give similar final state particles in this region. In reality, the transition between scattering off of nucleons and scattering off of quarks is a smooth one and there is no hard cutoff between resonant and DIS interactions [154]. Assigning an event to a particular channel can become ambiguous in this region and beyond. Performing a direct comparison between generators on a channel-by-channel basis is complicated by the fact that there is no single standard for parametrizing the transition region and defining DIS.

The transition region and definition of RES/DIS are nominally different between the generators. By default, Nuance cuts off resonant interactions above 1.7 GeV and parametrizes the turn-on of DIS in the following way:

$$\sigma_{DIS} = \sigma_{BY} * F(W) \qquad\qquad W_{high}(= 1.7 \text{ GeV by default})$$

$$\begin{aligned} &F(W) = 0 \ \text{ if } \ W < W_{high} \\ &F(W) = .38 * \frac{(W - W_{high})}{2GeV - W_{high}} \ \text{ if } \ W_{high} < W < 2 \text{ GeV} \\ &F(W) = 1.0 \ \text{ if } \ W > 2 \text{ GeV} \end{aligned} \tag{6.1}$$

A non-resonant event producing a μ^-, π^+, and proton (with possibly more nuclear fragments) in the 1.7<W<2.0 GeV range will fall with some non-zero probability into the CCpi+ channel 3 and with some non-zero probability into the charged-current DIS channel

92. Nuance makes the distinction between resonant and non-resonant background within a single channel–although the experimentalist is not afforded this luxury.

GENIE cuts off resonant interactions above 1.7 GeV and uses:

$$W_{high}(= 1.7 \text{ GeV by default})$$

$$\begin{aligned} \frac{d^2\sigma}{dW dQ^2}_{DIS} &= \frac{d^2\sigma}{dW dQ^2}_{BY} \sum_m R_m * P_m^{had} \quad \text{if} \quad W < W_{high} \\ \frac{d^2\sigma}{dW dQ^2}_{DIS} &= \frac{d^2\sigma}{dW dQ^2}_{BY} \quad \text{if} \quad W > W_{high} \end{aligned} \tag{6.2}$$

where R_m is a tunable parameter and P_m^{had} is the hadronization model probability that the DIS final state multiplicity is equal to m. The subscript BY refers to the previously mentioned Bodek-Yang DIS cross section model. The R_m factors are very much data-driven and are tuned to give agreement between the total cross section and the world's 1-pion and 2-pion cross section data [125]. The numerical values of the 16 [one per channel, corresponding to $2(\nu/\overline{\nu})\times 2$(hit neutron/proton)$\times 2(CC/NC)\times 2$(1 pion/2 pion final state)=16] free R_m parameters can be found in the GENIE documentation [125]. The invariant mass distribution of a simulated set of events in GENIE can be seen in Figure 6.18. Note that W refers to the invariant mass selected by GENIE during event generation. This means that it is computed with complete kinematic knowledge including Fermi momentum. There is another "smeared W" variable that neglects the unobservable Fermi momentum and can go above 1.7 GeV.

A hard cut or parametrization type for the transition region and definition of DIS need to be chosen and explicitly stated for those neutrino experiments which see a significant number of DIS events and wish to perform a resonant or DIS exclusive cross section measurement. The advantages and disadvantages of each parametrization/definition as well as the experimentalist's responsibility to maintain "smoothness" in the transition region are unclear.

6.1.8 Parameters

Table 6.1 shows some important parameters that go into neutrino event generation in liquid argon. These parameters are employed for the neutrino event generation in the analysis

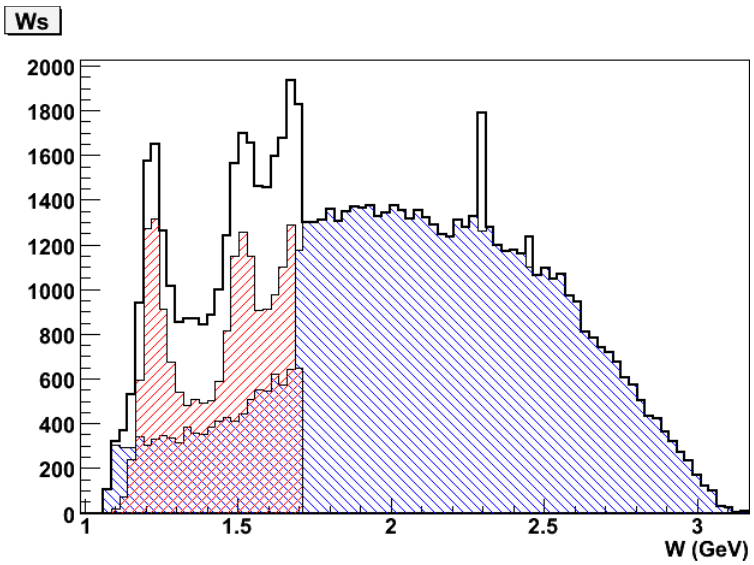

Figure 6.18: Invariant mass (W) of a sample of E_ν=5 GeV neutrino-neutron interactions in GENIE showing the resonance region and above. The red area is resonant and the blue area is DIS. The ambiguous "resonant/DIS" below W=1.7 GeV is sometimes referred to as non-resonance inelastic background in the resonance region [126].

described later. The parameters have been made to match in Nuance and GENIE (with a bias towards GENIE's more up-to-date values) in the event generator comparison. The LAr-specific Woods-Saxon parameters have been taken from Reference [179]. A subjective attempt to maintain generator integrity has been made and of course, not all parameters/models are reconciled. The GENIE-specific Bodek-Yang parameters used in the simulation of deep inelastic scattering neutrino events in this analysis are given in Table 6.2.

6.1.9 GENIE or Nuance?

GENIE is fully supported, updated as new results become available, and continually enhanced and upgraded. Nuance is not supported and has not been updated since 2004. Along with new nuclear process parameterizations, cross section data and models, and Particle Data Group parameters since then, Nuance does not include such important processes as anomaly-mediated gamma [82] and pion re-interactions to produce new resonances. GENIE simulates all of the above (with anomaly-mediated gammas to 0-th order). Although MiniBooNE has added or is in the process of adding all of the aforementioned processes to Nuance, the code is not publicly available. Even if acquired, the updated Nuance code will quickly become obsolete and it may not be worth updating the Nuance code further

LAr	Nucleon binding energy= 29.5 MeV Fermi Momentum (p)= 242 MeV Fermi Momentum (n)= 259 MeV Density=1.396 g/cm^3
LAr nuclear density $\rho(r) = \frac{\rho_0}{1+e^{(r-c)/z1}}$	c=3.53 fm z1=0.542 fm
CCQE	M_A=0.990 GeV M_V=0.840 GeV $F_A(Q^2 = 0)$=-1.2670
Neutral-current elastic	M_A=0.990 GeV M_V=0.840 GeV
Single pion resonant	M_A=1.120 GeV M_V=0.840 GeV Ω_{FKR}=1.05
Coherent	M_A=1.00 GeV

Table 6.1: The common parameters that were set in the GENIE-Nuance neutrino event generator Monte Carlo comparison.

DIS (Bodek-Yang Parameters)	A_{ht}=0.538 B_{ht}=0.305 C_{v1u}=0.291 C_{v2u}=0.189 C_{v1d}=0.202 C_{v2d}=0.255 C_{sd}=0.621 C_{su}=0.363

Table 6.2: The Bodek-Yang parameters for simulating deep inelastic scattering employed in GENIE.

with an up-to-date GENIE already in hand. It is not worth disregarding Nuance entirely, however. As has been shown, Nuance provides a wonderful comparison and sanity check tool to GENIE. Nuance's treatment of the transition region, definition of DIS, neutrino channel organization, intra-nuclear model, etc. have been and will continue to be valuable in optimizing and validating GENIE.

The GENIE (v2.6) neutrino event generator is used for simulating neutrino and anti-neutrino interactions in ArgoNeuT for this analysis.

6.2 ArgoNeuT Detector Geometry and Particle Propagation with Geant4

The Geant4 software package takes the neutrino interaction particles produced by GENIE, after the neutrino scatter itself and final state interactions, and propagates them through

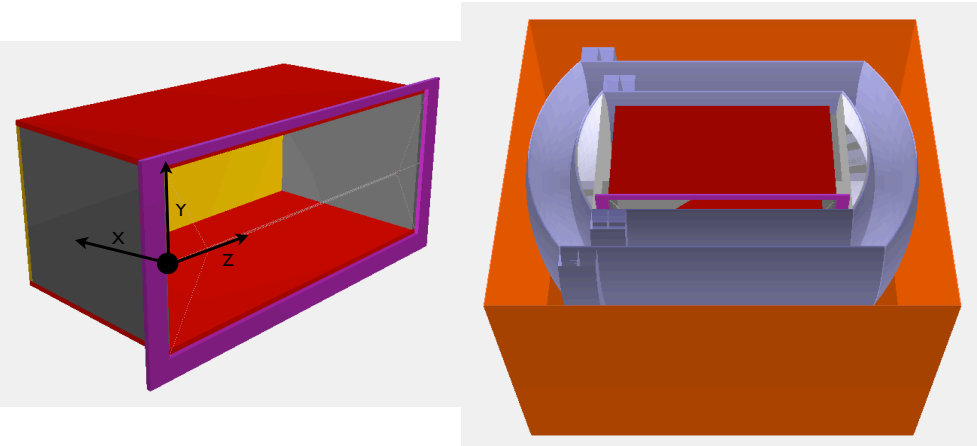

Figure 6.19: (Left) The ArgoNeuT TPC in Geant4 with the cathode in the background and the wire planes in the foreground. The orientation of the wire planes can be seen. The origin of the ArgoNeuT coordinate system is marked with the black dot. (Right) The TPC and inner/outer cryostat as simulated in Geant4. The beam is incident from the left in the drawing. The detailed TPC, inner cryostat, outer cryostat, and containment vessel geometry and composition are all modeled. The first MINOS plane (not shown) is also part of the simulation.

the liquid argon medium and the other detector materials. The entire argon volume is simulated along with the inner cryostat, outer cryostat, chimney, containment vessel, and the first plane of the MINOS near detector. Figure 6.19 shows the ArgoNeuT geometry as seen in the Geant4-based simulation. The particles are stepped through the simulation automatically and the most relevant physical processes are modeled. The energetic particles are propagated through the media until they reach 100 keV in kinetic energy, at which time their final energy is recorded. For energy deposition and propagation in the liquid argon active volume, three dimensional voxels (pixels in three dimensions) keep track of the ionization product electron clouds to be drifted to the readout wire planes. A $0.03 \times 0.03 \times 0.03$ cm^3 voxel size is employed in the ArgoNeuT simulation, dimensions safely below the 4 mm wire spacing (and time sampling) detection resolution.

6.3 Electron Drift and Wire Signal Simulation

After all of the charged particles' energy depositions in each voxel are recorded, the software drifts the ionization electron cloud associated with each voxel towards the readout wire planes. The number of electrons drifted and the $\frac{dE}{dx}$ used to obtain the correct recombination factor (see Equation 3.3) come from the energy deposition and track orientation

of the particle that traverses the voxels. Longitudinal and transverse diffusion constants of 6.2×10^{-9} cm^2/ns and 16.3×10^{-9} cm^2/ns, respectively, are used when drifting the electrons to the wire planes. Of course, the diffusion is dependent on the drift time of these electrons, a function of the electric field in the TPC and the drift distance. Recombination is also simulated with the constants A=0.8 and K_B=0.097 $\frac{\text{g}}{\text{MeV}\times\text{cm}^2}$ (see Equation 3.3) [71]. The number of electrons that reach a wire is tabulated with the final, post-diffusion location of the electron cloud at the drift position of the wire plane(s) and assigned to the relevant wires. Attenuation due to the relevant electron-lifetime is accounted for with an appropriate correction to the wire signal amplitudes as a function of drift distance.

After the electron clouds have been assigned to their wires, they are turned into a charge and associated with a range of time ticks. The induction and collection response shapes (see Section 7.1) are then convoluted with the charge in order to create raw digit ADC counts. Along with the signals, a realistic random noise is injected onto the wires, completing the electron drift and wire signal simulation. Wires that are considered noisy or dead in reality are given a flat signal equivalent to zero ADC counts for all time samples in both data and simulation. Note that an electron drift velocity of 1.56×10^{-4} cm/ns in the active TPC volume is assumed throughout the simulation.

6.4 Through-going Muon Simulation

A through-going muon that enters ArgoNeuT, usually from the upstream end, can enter the signal sample if its entrance position/vertex is misreconstructed. This can occur due to a reconstruction software failure or if the muon multiple scatters enough for the vertex finder to identify the scatter point as a vertex. An *in-situ* background measurement is applied in order to estimate the level of this contamination. The properties (position/kinematics) of every reconstructed charged muon that entered the front face of MINOS during the ArgoNeuT neutrino-mode run are tabulated. Then, these charged muons are injected into the Geant4 simulation with their same reconstructed properties 1.5 m upstream of the ArgoNeuT detector. The through-going muons are then propagated through the fully simulated ArgoNeuT geometry and reconstructed. Those muons that enter the final sample after selection cuts are considered a background for the charged-current muon-neutrino inclusive analysis presented later.

7 ArgoNeuT Software: Reconstruction

LArTPC detectors, featuring fine grained spatial resolution and precise calorimetric reconstruction capabilities, provide an enormous amount of information for characterizing neutrino events. However, all of this information makes reconstructing neutrino events an immense challenge. The ArgoNeuT reconstruction software described below is a work in progress. The software has been created from scratch and remains in the early stages of development.

ArgoNeuT's automated software reconstruction chain for the charged-current muon-neutrino differential cross section analysis proceeds as follows:

- Signal hits are formed from the raw data information.
- Proximal hits are grouped together to form two dimensional [in (wire,time) or (wire, X coordinate)] clusters of hits.
- Line-like objects are searched for on a cluster-by-cluster basis. The lines are simultaneously found and fitted. Hits that are not a part of the previously found clusters are ignored.
- Parallel or near-parallel lines that feature shared endpoints are merged together.
- Two dimensional vertices are searched for after considering the longest line-like objects on each plane. The three dimensional vertex is formed from each plane view's two dimensional vertex with a common drift time.
- Three dimensional tracks and space-points are formed from the line-like objects in each plane.

- The three dimensional tracks are matched with reconstructed (by MINOS) events in the MINOS near detector.

The current version of the ArgoNeuT software also features calorimetry, shower finding, and multiple vertex finding packages, among other tools. These algorithms are not discussed as they are not employed in the analysis presented here. The relevant reconstruction software is described in detail in the following sections.

7.1 Raw Data Deconvolution

A simple threshold-above-noise requirement by itself is insufficient to identify hits in a LArTPC. Overlapping hit signals that are close in time can drastically change each other's signal heights, especially in the case of overlapping bipolar (induction plane) pulses. The processing of the digital signals that are acquired from the DAQ electronics seeks to make hit finding and subsequent event reconstruction as simple as possible while maintaining the integrity of the pulses. A deconvolution step is required to mitigate a few inconvenient features present in LArTPCs in general and the ArgoNeuT electronics specifically.

A LArTPC's induction signal is naturally bipolar. Overlapping hits in time on a single induction (and to a lesser extent, collection) wire can appear as one. Identifying and separating bipolar hits for calorimetric purposes is an inherent challenge for LArTPC-based detectors. Another inconvenience involves the capacitive coupling of ArgoNeuT's digitizer inputs, which was originally designed for signals about 100 times shorter. For a collection plane signal, the DAQ provides a positive unipolar pulse followed by a negative overshoot in the return to baseline and a subsequent exponential return to the true baseline. A Fast Fourier Transform (FFT)-based raw data deconvolution is used to ensure that a simple hit threshold is unbiased to all signals. The raw data deconvolution renders the induction signal unipolar, removes the baseline shift apparent in the collection plane, increases signal-to-noise, and improves adjacent hit separation in both planes.

The FFT approach assumes that all raw wire signals can be resolved into elements that basically have the same signal shape in time. The representative shapes are normally found via measuring the electronics response to a known input pulse. The response function can then be used to extract the signal while minimizing any electronics affects on it. For the ArgoNeuT deconvolution, the base signal shapes for each individual wire/channel have been produced empirically after analyzing thousands of long muon tracks that were nearly

parallel to both wire planes. This technique accounts for the affects of the electron drift in addition to the electronics response. Muon-induced delta rays were avoided in generating the base shapes so as not to bias the pulses towards a wider shape. The narrowest signal in these tracks was considered analogous to a delta function input pulse. Deconvolution based on these signal shapes has been found to be a good first order approximation, especially for the collection plane in which the majority of the signal comes from charge converging on the wire. The induction plane signals arise from charge that is close to the wire itself as well as charge that is closer to neighboring wires. This distant charge can alter the signal shape from that which is naively expected on the induction plane. However, the base signal shape is an acceptable approximation as the shape differences are largely negated by the electronic shaping circuits' frequency response.

The base signal shapes employed for each plane can be seen in Figure 7.1. It is worth noting that, in the case that a track's angle with respect to the wire plane and particle identification (from e.g. ionization deposition expected per unit length) are known, a better approximation of the base signal shape can be determined. Such a scheme is not yet employed by ArgoNeuT. Figure 7.2 demonstrates the raw signal deconvolution at work on a set of three adjacent and overlapping hits associated with two tracks in the induction plane. The raw data and deconvoluted data can be seen for each wire in time. The deconvolution can be seen to separately increase signal and reduce noise, smooth signal and noise, change the natural bipolar induction signal into a unipolar one, separate hits that are close in time, and account for the second hit's baseline shift (due to the first hit's return to baseline).

A frequency filter is also employed in the deconvolution process. The filter ensemble is a bit different for each plane although both planes utilize a high frequency filter to remove high frequency noise components that have been amplified by the FFT. The induction plane filter uses an analytic function to remove the high frequency components and the collection plane filter is based on the power spectrum of the base signal and thus accepts low frequencies due to the slowly changing baseline shift.

7.2 Hit Finding

ArgoNeuT's hit finding is performed on a wire-by-wire basis. Perhaps one can consider taking into account nearby wires with a future, more sophisticated algorithm in order to better separate overlapping hits in time. If a region is flagged as possibly containing a set of

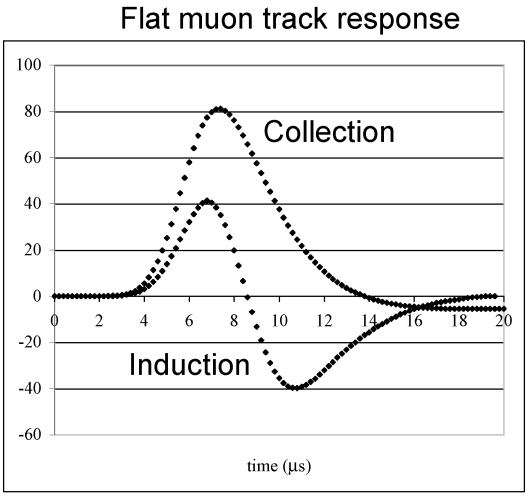

Figure 7.1: The base signal shapes for the induction and collection plane as determined by an analysis of a large sample of "horizontal" muons.

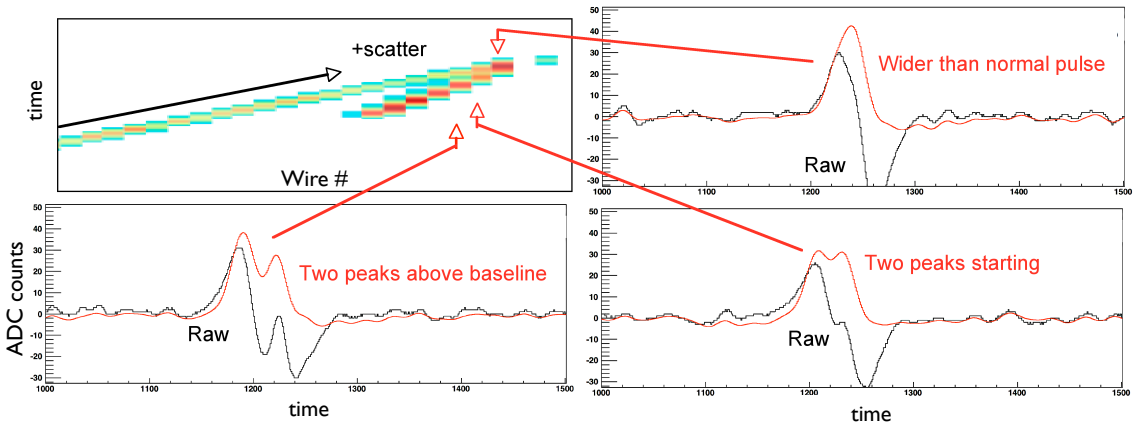

Figure 7.2: (Upper left) Two deconvoluted tracks as seen on a few wires in the induction plane. Part of the tracks are overlapping in time. (Upper right, lower left, lower right) The wire signals in time in raw (black) and deconvoluted (red) form on three successive wires with overlapping hits.

overlapping hits, such a program could ask whether two distinct hits are seen on a neighbor wire within a similar time region. The decision to consider the region as one or multiple hits could be guided by this extra information.

The hit finding algorithm is provided with the smooth and unipolar deconvoluted signals on each plane. The algorithm begins with a search for local minima in the (time, ADC) space of a single wire. Once a minimum is found, nearby time bins are followed in increasing time until a local maximum is found. The pulse is considered a hit in the case that the

local maximum is above a characteristic threshold. The full time width of the hit is then determined by scanning in increasing time until a local minimum is found. The region in between the local minima is considered the hit region. In the case that the local maximum is below the set threshold, the region is rejected as a hit. The process repeats itself until all time regions on a wire have been considered and accounted for.

With the hit regions identified, the algorithm employs a fit or fits to precisely describe the characteristics of the hit(s) within each region. A multiple hit finding technique is used in the case of overlapping hits where n Gaussians are fit to n consecutive candidate hits in the overall waveform. Each fit requires a set of seed parameters from which the fit starts and the parameters need to be well chosen for the fit to converge. The seeded hit width parameter is derived from a typical hit width, with different characteristic values given for the induction and collection planes. The seeded time position of the hit is set equal to the time of the local maximum. With the width and time of the pulse determined through the fit, the signal amplitude is all that remains to be found. In the case of a single hit within the hit region, the signal amplitude is set as the local maximum. For multiple, overlapping hits, a more sophisticated procedure is needed to determine the signal amplitudes. A hit's amplitude is set equal to its height plus any contribution from its neighbors through a linear approximation. An approximation of the true height is:

$$O_i = \sum A_j f(t_j - t_i; w) \tag{7.1}$$

where O_i and A_j are the observed and true amplitudes of the hits and $f(t_j - t_i; w)$ is a function representing a normalized model pulse. The indices i and j represent the hit being considered and the adjacent hits, respectively, and w is the width of the hit. The function f basically evaluates the model pulse for each hit at the position of adjacent hits to determine how much the adjacent hit (or hits) has influenced the amplitude of the hit in question. To find the true amplitude, A_j, a singular value decomposition is used after considering the above equation as $\vec{O} = M\vec{A}$, with M taken from the values of f evaluated at each point.

Each unique hit is described in terms of signal amplitude, integrated ADC counts above and below the baseline, central time, start and end time, width, and a multi-hit flag indicating that the hit in question is considered close in time to another hit. These variables are passed along to subsequent reconstruction steps.

7.3 Density-based Cluster Finding

Automated reconstruction of neutrino events in LArTPCs can be partially accomplished using digital image analysis techniques. Shape recognition is a common problem in digital image analysis and there are many algorithms available for describing and characterizing an image. Grouping similar and/or close objects together is an important problem in the field of computer vision. The goal is to be able to efficiently recognize arbitrarily shaped families of proximal hits over large data samples. ArgoNeuT has employed a technique popular in the computer vision community to establish clusters in each event. After hits are found in each plane, the grouping of proximal hits, based on position and extent, takes place. Note that this procedure is done separately for each plane; hit clustering is done in two [(wire, time)], rather than three, dimensions. Hit grouping is accomplished through a process based on "Density-Based Spatial Clustering of Applications with Noise" (DBSCAN) [180]. Whilst clustering neighboring hits, the algorithm concurrently identifies noise hits, as such hits are rarely associated with any neighbors. That is, noise hits can be considered those clusters that are composed of a single hit. Such noise hits/clusters are ignored in the analysis presented here and the DBSCAN-based algorithm acts to identify and remove noise hits for the purposes of more effectively identifying line-like tracks (described in the next section).

DBSCAN identifies clusters based on the idea of "density reachability". A point (or hit in the case of ArgoNeuT's clustering, after accounting for hit width in time) q is "directly density-reachable" to a point p if the points are within a set distance ϵ of each other and point p is proximal to a certain number of other points. A sequence of points $p_1, ..., p_n$ with $p_1 = p$ and $p_n = q$ with each $p_i + 1$ directly density-reachable from p_1 is required for q to be "density-reachable" from p. It is important to note that, with these definitions, q may be directly density-reachable from p but p may not be directly density-reachable from q. This asymmetry occurs in the case that p is not surrounded by the required number of points but q is. Since p's relationship to q is different than q's relationship to p, a distinct definition is needed. Two points, p and q are considered "density-connected" if there exists a point s in between q and p such that s and p and s and q are both density-reachable. Figure 7.3 provides specific examples of each definition: directly density-reachable, density-reachable, and density-connected. With these definitions, clusters are formed. All points inside a cluster are density connected and all points that are density reachable from any point inside a cluster are part of the cluster as well. The cluster finding algorithm starts with an

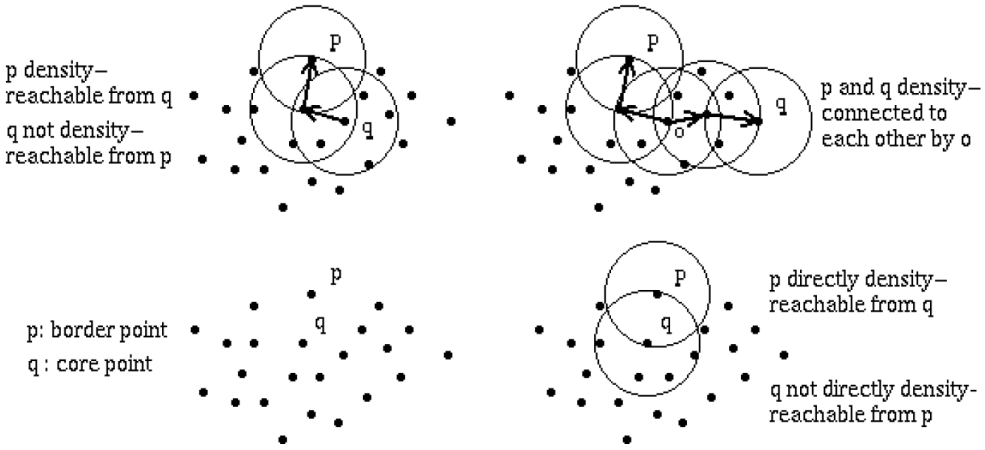

Figure 7.3: DBSCAN definitions (adapted from Reference [180]).

arbitrary point k and searches for all of k's density-reachable points to create the cluster. The notion of "core" and "border" points is introduced with core points (i.e those having density-reachable points) inside a cluster and border points (i.e those not having density-reachable points) on the edge of a cluster. Once a cluster is formed and completed, the algorithm moves on to the other remaining points in the image and the process is iterated on until each point has been considered and described. Figure 7.4 shows an example of the DBSCAN algorithm at work on a neutrino event in ArgoNeuT's collection plane.

A few modifications to the above procedure are necessary for the ArgoNeuT-specific two dimensional clustering. For ArgoNeuT, the "points" considered above are hits in (wire,time) with varying extent as each hit has a unique width in the time direction. Furthermore, in (wire,time) space, the notion of an ϵ neighborhood is modified slightly in order to account for the different resolutions in the wire and time directions. An elliptically shaped neighborhood is employed with two parameters (the semi-minor and semi-major axes of the ellipse, ϵ_1 and ϵ_2).

7.4 Line Finding

A simple fit to a known shape can be complicated by blurring, noisy and dead pixels, low resolution, non-standard shapes, and more. LArTPC neutrino events are subject to such challenges. Dead and noisy wires, random noise, electromagnetic showers, multiple-

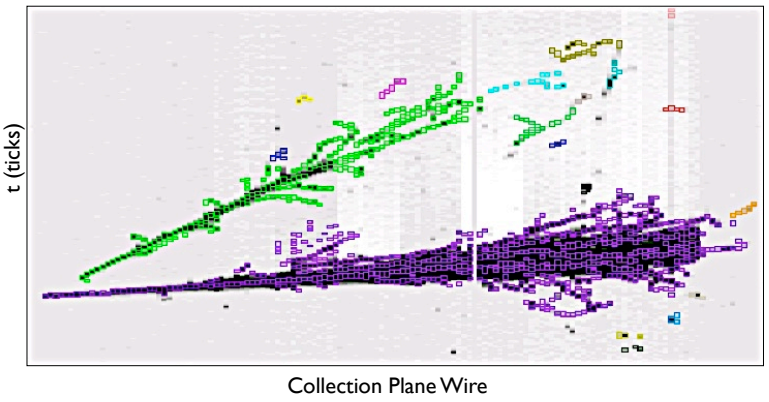

Figure 7.4: The DBCSCAN hit clustering algorithm at work on a neutrino event. The event's raw data is shown in grey and the colors show the distinct clusters found with the algorithm.

scattering, E-field non-uniformities, etc. are just some of the effects that can lead to non-simple patterns and make track recognition and fitting difficult.

As neutrino events in a magnetic-field-free detector largely feature line-like tracks, a line recognition/fitting algorithm has been implemented into the software for LArTPC neutrino reconstruction. A linear regression algorithm is limited in the sense that it can only find a single best fit line to a set of data points. This is unacceptable for images that contain more than a single line and/or significant noise. A more clever technique is necessary to simultaneously fit all the points in an image to multiple lines. Such a technique needs to be able to not only fit imperfect data points to a single line, but also to have room for the possibility of multiple lines and multiple fits. The Hough Transform [181] is employed to find and fit line-like objects in a two dimensional image. Originally designed to find line-like objects in an image, the Hough Transform is capable of finding any arbitrary shape.

The Hough Transform creates a parameter space filled according to the image's pixel locations and weights. The filling of the parameter space can be thought of as a voting procedure, with the parameters that describe the image's objects best gaining the most votes. The local maxima, usually found with a peak finding algorithm after the parameter space has been filled, correspond to object-of-interest candidates.

A line can be parameterized by $r = xcos(\theta) + ysin(\theta)$. This equation represents a sinusoidal curve in the (r, θ) plane that is unique to each (x, y) point. If the curves corresponding to two points are overlaid, the (r, θ) crossing point corresponds to the line that

passes through both points (see Figure 7.5). The Hough Transform takes advantage of this fact. Each (x, y) point in an event is parameterized and placed in a "Hough Accumulator" (r, θ) space, composed of discretized cells of finite dimension. After all of the image points have been parameterized and placed in the Hough Accumulator, the cells with weight above some threshold are selected as line candidates.

7.4.1 The Hough Transform applied to LArTPC events

Deconvolution of the raw data and hit finding is performed before the Hough Transform line-finding algorithm. The DBSCAN cluster finder algorithm can also optionally be run before the line-finding algorithm, as is the case for the charged-current inclusive analysis described here. The advantages and disadvantages of running DBSCAN first are discussed below.

The Hough Transform based algorithm forms an image from hits in wire and time and finds line-like objects within the image. In other words, (wire,time) is used in place of (x, y) in the example above. All of the hits in a plane, in the case that DBSCAN is not run before line finding, or all of the hits in a cluster, in the case that DBSCAN is run before line finding, go into forming the Hough Accumulator. Cells with no curves passing through them are given a weight of zero. The Hough Accumulator's r and θ are discretized in the form of cells of finite height and width. The number of Hough Accumulator cells in r and θ determine the algorithm's resolution. A small number of cells can lead to poor resolution while a large number of cells can lead to line candidate ambiguity. As the number of cells decreases, the number of possible (r, θ) values, and therefore resolution, decreases. As the number of cells in an imperfect image's Hough Accumulator approaches infinity, a cell corresponding to a true line will lose weight (as its neighbors fill up) and eventually become hard to distinguish. The signal-to-noise ratio, or largest cell weight divided by noise cell weight, in the accumulator should usually be greater than ten. The number of cells is chosen in consideration of resolution, processing time, and signal-to-noise ratio in the accumulator. The number of r bins need not equal the number of θ bins in the Hough accumulator.

After all of the hits have been added to the Hough Accumulator, the cell with the largest weight/curve-crossings is found. The center-of-mass of the 3x3 cell window with the weightiest cell at center corresponds to a candidate line. The center-of-mass of the 9-cell

system is used to form the candidate line instead of the actual central cell coordinate so that the extracted line parameters are not limited by the central cell coordinate's discreteness. Some algorithms employ a two dimensional Gaussian fit to the weightiest cell and its nearest neighbors to extract the parameters best corresponding to the line candidate. The process is iterated on, considering only hits that have not yet been associated with a line, until the "minimum weight to be considered a line" (threshold) or "maximum number of lines to be found" has been reached. Each line-like object/cluster is given a unique identification.

7.4.2 The endpoints of a track

The Hough transform finds the slope and intercept of a line-like track. However, it does not by itself find the endpoints of a track. A separate algorithm, featuring two simple requirements, has been developed to define the endpoints of a line-like object. The most upstream wire with a hit is considered an endpoint if 1) the cluster's line falls some time inside a specified wire/time window centered around the wire number and crossing time of the hit and 2) the hit is "adjacent" to other hits that fall along the line. A hit is considered adjacent to another hit if they are separated by at most one wire. Dead and noisy wires are ignored (bridged) when considering whether a hit is adjacent to another hit. The other endpoint considers the most downstream wire.

Figure 7.6 shows a through-going muon as seen in ArgoNeuT's collection plane and the Hough Accumulator corresponding to the hits in the event. The hits can be seen in the red boxes and the Hough line can be seen in white in the event display. Note that noise hits (i.e. hits that are not associated with a cluster) are included in the Hough Accumulator image for clarity. However, such hits/curves would normally not enter the accumulator as the accumulator is normally only filled with those hits that are associated with clusters featuring more than one hit. The parameters of the best-fit line can easily be seen on the Hough Accumulator image as the point at which most of the curves converge. Figure 7.7 shows a slightly more complicated event in the form of a neutrino candidate as seen in the collection plane view. There are a few notable features in this event. Three Hough lines are found in the collection plane. The uppermost two lines clearly correspond to the same track and probably will need to be merged in the downstream reconstruction. The bottom-most track has successfully been fitted and identified as a single line-like object. The small blob of hits just below and to the right of the interaction vertex is not line-like and is not

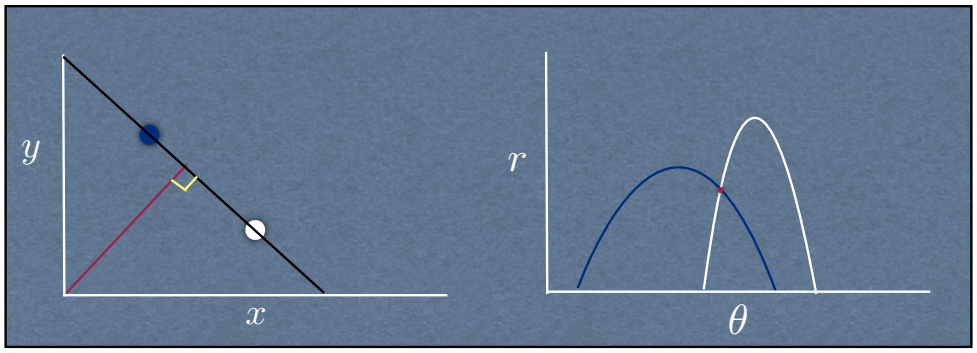

Figure 7.5: (Left) Two points in the (x, y) plane. (Right) The two points parameterized in the (r, θ) plane. The curve crossing in (r, θ) corresponds to the line that passes through both points in (x, y).

fitted with the Hough line finding algorithm. The algorithm is seen to reconstruct the most prominent and relevant features of the event. However, it is limited in the sense that it is only able to find line-like objects and is sensitive to errors in upstream reconstruction steps.

7.4.3 Limitations

The main limitation of the Hough line finding algorithm is the inability to find non-line-like tracks. Extended electromagnetic showers, curved delta rays, large multiple scatters, etc. are largely ignored by the algorithm. Such tracks are most efficiently found, and perhaps characterized by, the DBSCAN-based cluster finder. The algorithm is further limited by the fact that it takes hits directly from either the hit finding algorithm or the DBSCAN clustering algorithm. The Hough line finding algorithm cannot be made to know about missed hits or hits that may have merged together to form a single hit and is therefore extremely dependent on the efficiencies of the upstream reconstruction algorithms. A number of other limitations associated with the algorithm are discussed below.

The concept of "hit-weight" has not yet been implemented. That is, every hit is given equal weight in the Hough Accumulator, without regard for (e.g.) hit amplitude. One can

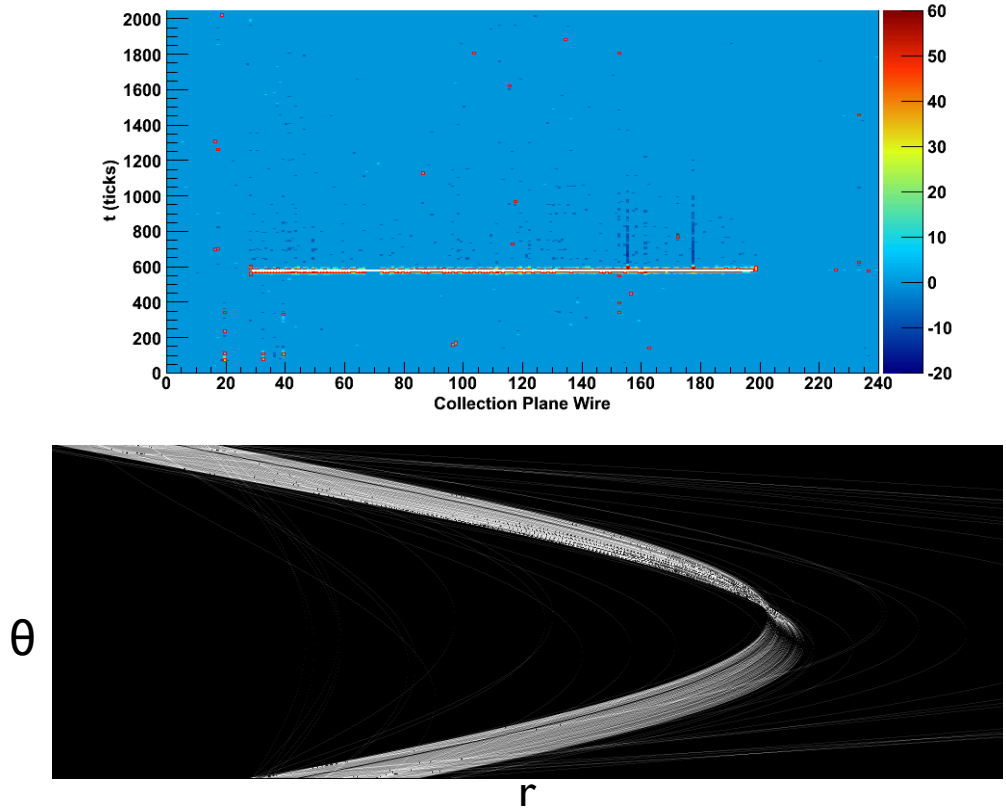

Figure 7.6: (Top) A through-going muon as seen in ArgoNeuT's collection plane with hits shown in red and the Hough line fit to the track in white. (Bottom) A zoomed-in view of the Hough Accumulator for the event. Each curve in the Hough Accumulator corresponds to a hit. In practice, the presumably noise hits that are not associated with the central track/cluster would not be considered in the Hough Accumulator.

imagine, however, that ADC counts, integrated area or some hit fit parameters could be used to weight the Hough Accumulator's curve associated with a hit.

As exemplified in Figure 7.7, the Hough line finder may break up a nearly-line-like track (e.g. a muon) into multiple lines in the case that there is a slight kink, perhaps due to multiple scattering, in the track. This is entirely acceptable and even desirable as long as a downstream reconstruction algorithm joins the linked sub-lines into a "merged-line".

The Hough line finding algorithm currently employed in the software only works in two dimensional (wire,time) space. The algorithm itself is unaware that there are multiple two dimensional views for the event that will be eventually combined into a three dimensional image. A downstream three dimensional track algorithm is necessary to combine the lines on each plane to form a three dimensional cluster/track.

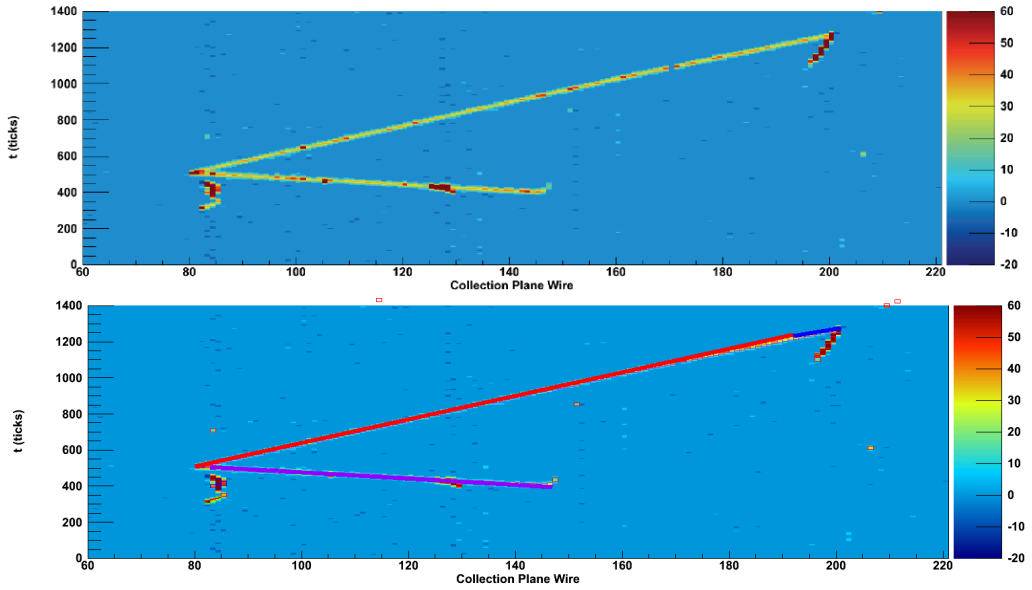

Figure 7.7: (Top) A neutrino candidate in ArgoNeuT as seen on the collection plane. (Bottom) The found and fitted Hough lines overlaid on the neutrino candidate event.

7.4.4 Line-finding efficiency

It is often difficult to quantitatively determine how well an individual algorithm in a reconstruction chain is working. The actual precision/proficiency/efficiency associated with the entire reconstruction chain is the most relevant number when discussing efficiency. However, developing a few quantitative "figures of merit" for tuning an individual algorithm's parameters and structure is important in ensuring that the final numbers are as strong as possible. The following figures of merit have been developed to quantitatively describe the effectiveness of the Hough line finding/fitting algorithm: (1) Distance between a hit and a Hough line, a measure of the goodness-of-fit, (2) number of DBSCAN cluster hits minus the number of Hough line hits in line-like tracks, a measure of efficiency, and (3) the fraction of total DBSCAN cluster hits associated with Hough lines in line-like tracks, a measure of efficiency. In order to quantitatively determine how well the Hough line finding algorithm is working, 3000 muons with 5.0±5.0 GeV/c (uniform distribution) momenta and 0 ± 60^{o} (uniform distribution) angles in the XZ and YZ planes have been simulated in ArgoNeuT.

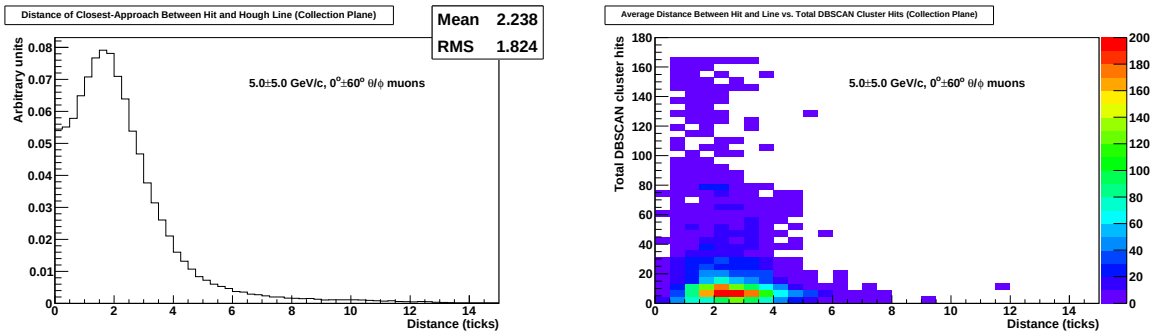

Figure 7.8: (Left) The distance of closest-approach between a hit and a Hough line for a simulated sample of muons at varying angles. (Right) the number of DBSCAN cluster hits versus distance for all simulated muon events in the collection plane.

The large momenta and angle ranges were chosen in order to test the algorithm across many kinematic scenarios.

Figure 7.8 (left) shows the distance of closest approach between a hit and a Hough line for all hits in the 3000 muon events simulated. Beyond about 15 ticks (the actual number changes as it is a function of hit width), a hit can no longer be associated with a Hough line. The mean distance is found to be 2.2 ticks, or approximately 0.7 mm, with the smallest distances coming from the longest tracks as can be seen in Figure 7.8 (right).

The Hough line finding algorithm's input is DBSCAN cluster hits. Figure 7.9 compares the number of hits associated with all DBSCAN clusters to the number of hits associated with all Hough lines in muon events. As muons are largely "line-like", we expect the number of hits associated with DBSCAN clusters and the number of hits associated with line-like objects from the Hough line finder to be approximately equal. Curly, non-line-like delta rays can lead to differences, however. The figure confirms that the Hough line finding algorithm finds muons to be quite line-like, with about 60% of muon events having the same number of hits associated with DBSCAN clusters and Hough lines. The mean hit difference for all events is found to be 1.5 hits while the fractional difference is about 2%, with the difference increasing as the simulated tracks get shorter.

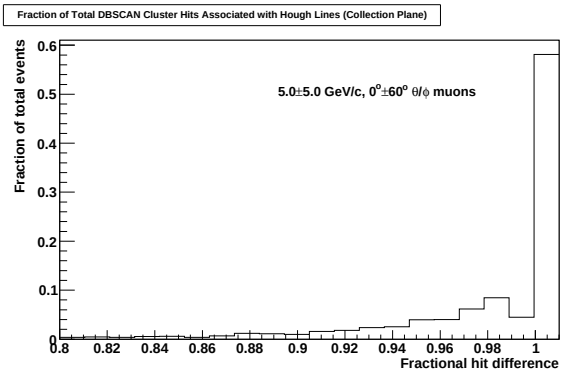

Figure 7.9: The fractional difference between the number of DBSCAN cluster hits and number of hits associated with a Hough line for the simulated muon sample.

The figures of merit discussed above are used to tune the following Hough line finding parameters, in consideration of algorithm speed and line resolution: (1) Maximum number of lines that can be found per cluster, (2) maximum distance of hit from line, in consideration of hit width, and (3) number of r and θ cells in the Hough Accumulator. The number of r and θ cells sets the the resolution of the parameters of a fit line and helps to determine the requirements for breaking a single line into two or more separate lines.

The Hough line finding algorithm is designed to find lines/clusters from hits in an event. It is important to note that the program can be considered as both a cluster finding algorithm and a track fitting algorithm. After finding the line-like clusters, the algorithm returns information about the clusters themselves in terms of slope, intercept, endpoints, as well as each hit that has been associated with the line. The input can be either hits associated with clusters found by the DBSCAN algorithm or hits found directly from a hit finding algorithm after deconvolution and hit finding. That is, the algorithm can search for lines, considering all of the hits in a plane or hits on a cluster-by-cluster basis. The former is perhaps most useful for cluster-finding while the latter is most useful for actual two dimensional track fitting. Running the Hough line finder multiple times before/after other cluster finding algorithms (e.g. DBSCAN) may be useful for efficient cluster finding and track fitting in the future. The Hough line finding algorithm is capable of bridging dead wires if all of the hits in a plane are supplied to it. This capability is vital for the electron lifetime determination which requires long, continuous tracks, an impossibility if

the dead wires are not bridged.

7.5 Three Dimensional Tracking

A pair of two dimensional images of each neutrino event is taken by the ArgoNeuT LArTPC. It is the responsibility of the offline software event reconstruction to transform these images, with knowledge of the wire orientation and electron drift velocity, into a three dimensional image, preferably in terms of an (X,Y,Z) coordinate system. The basic strategy utilized to accomplish this task is to use the common time (drift coordinate) between the set of two dimensional tracks. For example, a single muon which starts at time ∼100 ticks in one plane starts at time ∼100 ticks in the other plane, after accounting for the drift distance between the two planes. The same is true for the endpoints of the two two dimensional tracks. By associating the four two dimensional endpoints, two three dimensional endpoints are created and the rest of the track can be reconstructed fully. It is worth noting that endpoint ambiguities can arise if the tracks are constant in time, a problem that is made more likely in scenarios with multiple overlapping tracks.

7.5.1 Two dimensional line merging

Requiring the Hough line finding algorithm to find the parameters of lines in an image with high resolution in r and θ comes at a cost (other than the processing time cost). With increased resolution, the algorithm is more likely to break a single line-like object into multiple segments of similar slope and proximal endpoints. As two dimensional lines need to be matched in the two views of each plane, the breaking of lines can interfere with three dimensional line formation. This is especially true since the line breaks don't always correspond to a physical process (e.g. multiple scattering) and therefore do not always match in time between the two views. A simple algorithm to merge Hough lines of similar slope and proximal endpoints together is used to create "merged lines" and simplify the downstream three dimensional reconstruction steps. An example of the line merging algorithm at work can be seen in Figure 7.10.

7.5.2 Finding the Interaction Vertex

The two dimensional neutrino interaction vertex is found using the merged lines in each plane view. Identification of the vertex proceeds as follows: the longest two line-like clus-

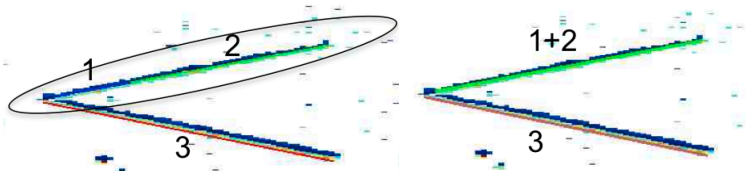

Figure 7.10: An example of the merging of Hough lines in a single ArgoNeuT view of a neutrino event. (Left) Pre-merging, three Hough lines [lines #1 (blue), #2 (green), and #3 (red)] corresponding to two tracks in two dimensions. (Right) Post-merging, two Hough lines corresponding to two tracks in two dimensions. Lines #1 and #2 have been formed into a single, unbroken line.

ters (these can be merged lines or non-merged lines) are identified. Their intersection is considered the two dimensional vertex in that plane view. In the case that there is only a single cluster identified, the most upstream hit is considered the two dimensional vertex. Delta rays can interfere with this simple vertex finding algorithm and there is a protection in place to prevent the point where the delta ray diverges from its "parent" muon from being identified as the interaction vertex. Basically, clusters are identified as delta rays if they have few hits, a similar slope as the longest cluster in the track, and are far away from the longest cluster's start point. After the vertices are identified in each plane, they are matched in terms of a common drift time and the three dimensional vertex is found. The algorithm currently creates only a single vertex for each candidate neutrino event.

7.5.3 Three dimensional tracking

Creation of three dimensional objects in LArTPC reconstruction relies on finding matches in time between two two dimensional objects, one in each plane. A space-point is a three dimensional point in space formed by time-matching a two dimensional object in each plane. In this analysis, space-points and three dimensional tracks are formed using the two dimensional line-like objects provided by the previously described Hough-based algorithm and the line-merging algorithm, in the case that a line-merger has occurred. Both types of line-like objects are considered when creating space-points and tracks. The line-like objects are required to be associated/proximal with the previously found vertex in order to be considered in the three dimensional track formation.

A pair of line-like objects, one in each plane, is matched if both of their sets of endpoints share common drift time coordinates. This common time is defined within a time window tolerance, after accounting for the drift distance between the induction and collection planes.

The association between a wire crossing and a spatial location (given by the subscript P) is illustrated in Figure 7.11. Each set of wire (i_P and c_P are the induction and collection plane wires, respectively) crossings corresponds to a Y_P and Z_P spatial coordinate. The drift time coordinate X_P is arrived at using $X_P = t \cdot v_{\text{drift}}/f$, where t is the drift time after accounting for pre-sampling and the drift time between planes, v_{drift} is the drift velocity given an electric field, and f is the sample frequency. The ArgoNeuT coordinate system is seen in the figure, with positive Z in the beam direction, Y in the positive vertical direction with respect to the ground, and X in the parallel-to-ground direction, increasing as one moves away from the MINOS near detector's coil. The origin of the coordinate system is on the upstream face of ArgoNeuT in Y/Z and at the induction plane in X. The origin is marked in Figure 6.19 (left).

Starting with the two dimensional line with the least number of hits (in either plane), each hit in the plane is matched to a hit or multiple hits in the other plane, in consideration of their common drift coordinate and relative distance, in terms of wire number and time, from the endpoints. The association of hits in terms of wire and time from the two planes forms a three dimensional space-point. That is, all hits from clusters/lines in both planes that occur at the same time and correspond to a wire crossing go into creating a single space-point. The space-points at the edges of each track are considered the three dimensional endpoints of the tracks. After matching lines, a linear fit to each plane's two dimensional line-like object is performed and a three dimensional track is formed in between the terminal space-points of the track.

Associating multiple two dimensional hits between planes that are potentially constant in drift time based on geometry alone (as is done for this analysis) can be problematic. Multiple track trajectories are possible and a one-to-one correspondence between hits on each plane is rare. In the future, three dimensional track reconstruction will be improved with hit association (space-point creation) based on geometry, energy deposition consistency, and continuity requirements. Also, instrumenting three (or more) wire planes (e.g. as in MicroBooNE) can help in breaking some of the degeneracies associated with tracks that are fairly constant in time as well as assist in three dimensional reconstruction in general. Figure 7.12 shows an example of a single short angled track that is constant in drift time. The track features five hits on each plane. Although the three dimensional reconstruction of the track seems straightforward, the association of hits between planes in the creation of space-points/endpoints is riddled with degeneracies. The hit or hits in one plane can

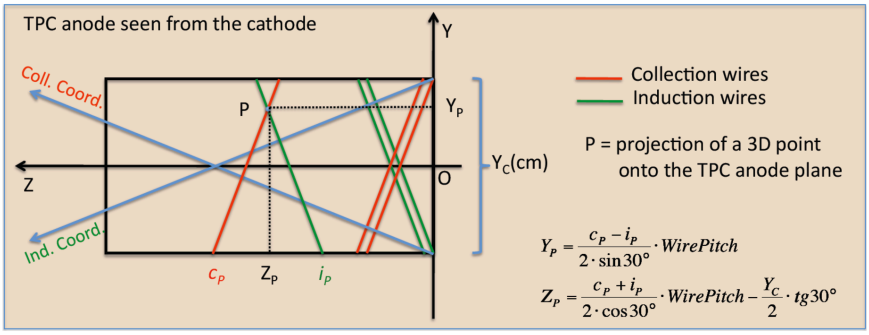

Figure 7.11: The ArgoNeuT reference frame and the association between a wire crossing/time and a three dimensional space-point. i_P and c_p represent the induction and collection wires, respectively, and Y_P/Z_P are the Y and Z space-point coordinates of the track. X is the drift direction and goes into the page. The "$WirePitch$"=4 mm, Y_C =40 cm, and 30° is the angle each wire makes with the beam axis (Z coordinate). The beam is directed from right to left in the drawing.

be associated with any and/or all of the hits on the other plane with each space-point assignment leading to different three dimensional track parameters. There are 120 valid trajectories in this fairly simple example featuring only five hits on each plane. Figure 7.13 shows a valid trajectory for the space-point/track (which happens to be the correct one). Of course, the degeneracy is broken in the case that the track spans a significant range in time. The case of two tracks that are both constant in drift time compounds the issue further. Figure 7.14 demonstrates this case by showing two distinct tracks that appear as one in both plane views. Disentangling the two tracks as well as fitting each individual track correctly is impossible relying on the geometry of the hits alone.

7.6 The ArgoNeuT Reconstruction Software as Applied to Muons Originating Inside the TPC

Now that the full three dimensional reconstruction chain has been described, the effectiveness of the software is presented. This thesis is the first one to use the liquid argon neutrino reconstruction software previously described. The software remains a work in progress and continues to improve. Before testing the reconstruction software on actual and simulated neutrino events, the reconstruction is evaluated with simulated muon events. Approximately 10,000 3 GeV/c muons originating near the center of the TPC Gaussian distributed at [(25,0,45)±(4,4,4)] cm with initial angles 0±25° in the XZ and YZ planes are simulated.

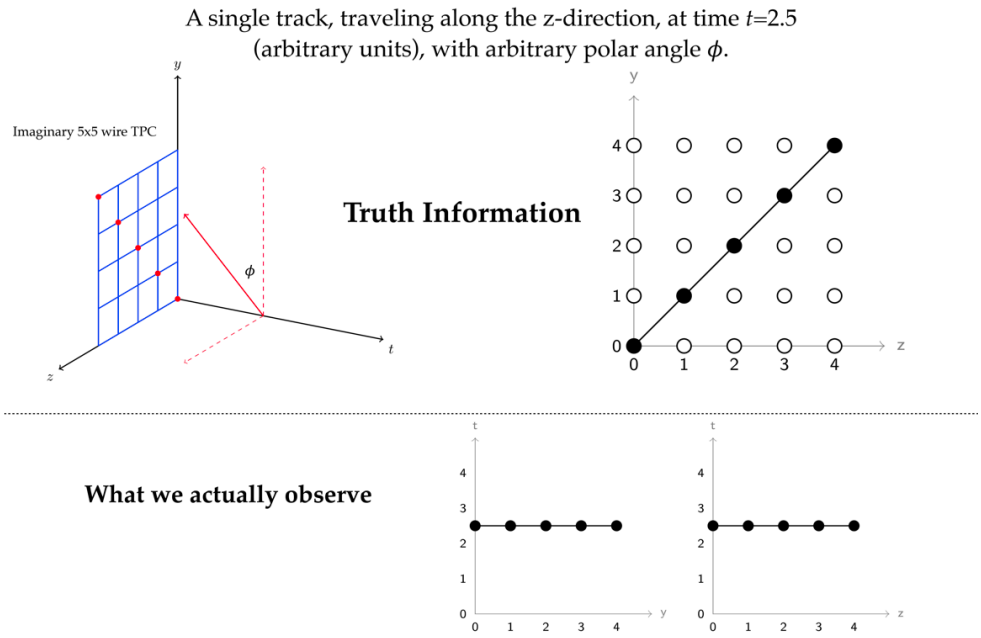

Figure 7.12: (Top) A single track that is constant in drift time as seen in terms of its spatial coordinates. (Bottom) The same track in the (wire,time) views. Matching hits between planes and reconstructing tracks is especially difficult for tracks that are fairly constant in drift time.

The reconstructed and true track angles in the muon simulation are shown in Figure 7.15. The X, Y, and Z vertex reconstructed and true positions are seen in Figure 7.16. Both the angular and vertex distributions present good agreement between the reconstructed and true values. The difference between the reconstructed and true vertex positions can be seen in Figure 7.17. Gaussian fits applied to each distribution show the vertex resolution in the 1-3 mm range, depending on the coordinate in question, for the simulated muons. Note that the vertex resolution in the drift dimension (X) is superior to the wire-based dimensions (Y and Z) as the length corresponding to the sampling time (198 ns, or ≈0.3 mm, given ArgoNeuT's 500 V/cm electric field) is much finer than the 4 mm wire spacing.

The true and reconstructed muon track length inside the TPC, or the distance between track exit and the final reconstructed three dimensional hit, as well as the difference between the two values can be seen in Figure 7.18. A slight offset from the naively expected value of zero difference between the true and reconstructed values exists as the final reconstructed three dimensional space-point is required to be inside the TPC. This requirement is not present in the truth simulation which asks when the particle crosses the threshold

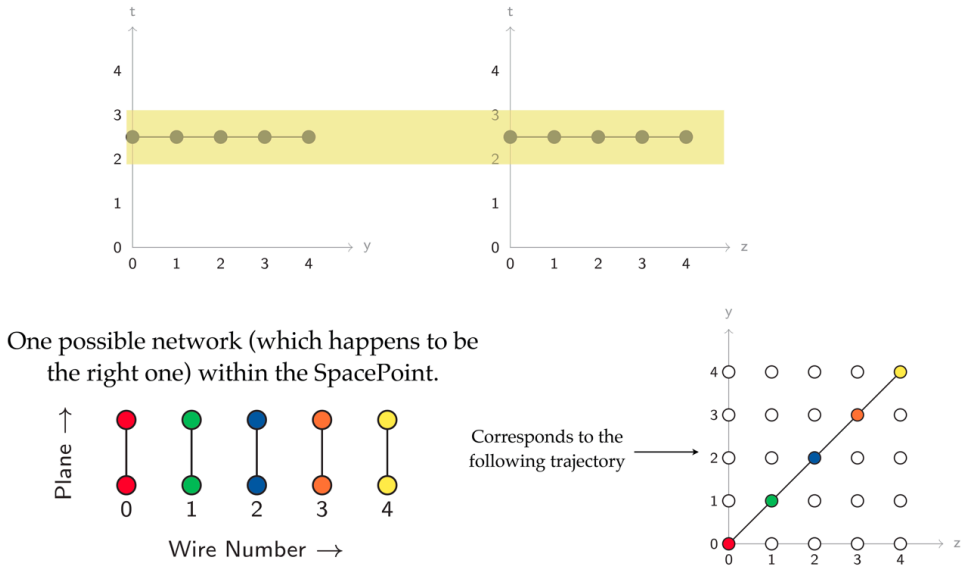

Figure 7.13: Just one of the 120 possible trajectories from the hits in Figure 7.12. The association between hits in the creation of a space-point or space-points is shown.

of the TPC box itself. The true and reconstructed track exit positions can be seen in Figure 7.19. Once again, there is a solid agreement between the reconstructed and true values, a verification of the efficacy of ArgoNeuT's reconstruction software.

7.6.1 MINOS Reconstruction

The analysis described in this thesis requires that a track in ArgoNeuT correspond to and match to a reconstructed muon in MINOS. Recall that the front face of the MINOS near detector is about 1.5 m downstream of ArgoNeuT. The reconstructed tracks in MINOS are provided directly by the MINOS experiment. All tracks with a reconstructed Z vertex of <20 cm from the center of the first MINOS plane are considered candidate tracks for ArgoNeuT-MINOS matching. The actual matching is based on a set of requirements based on the orientation and position of the ArgoNeuT and MINOS tracks relative to one another. The muon momentum measurement as supplied by MINOS is based on energy deposited along the tracks for stopping muons and curvature for non-stopping muons. The definition of "stopping" versus "non-stopping" has been altered from the nominal MINOS definition for ArgoNeuT, with help from the MINERνA collaboration [110]. The definition allows for entering muons to be considered "contained" as long as the muon stops in an instrumented

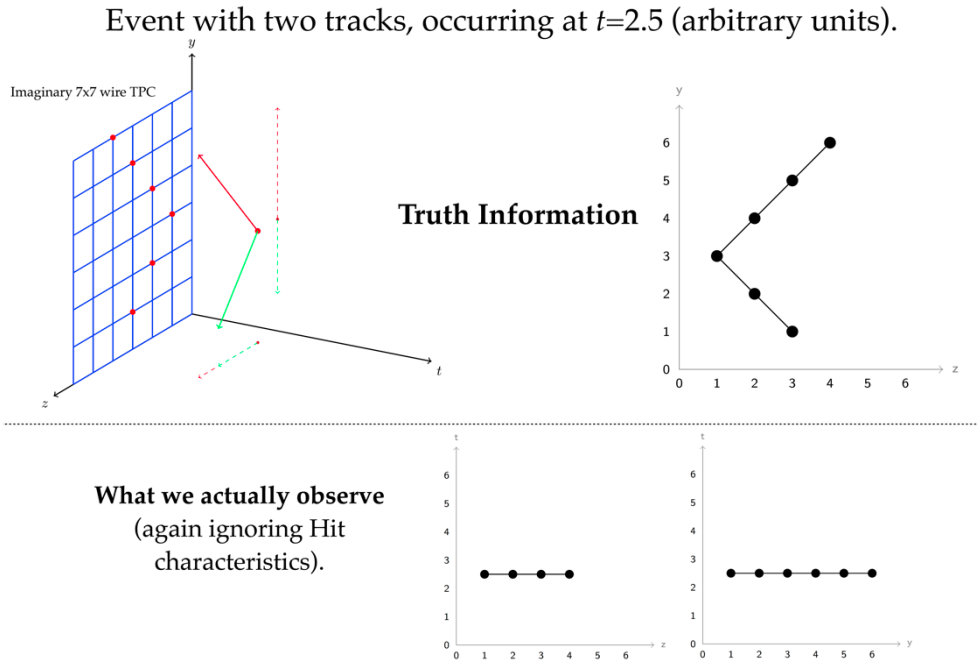

Figure 7.14: A set of two tracks that are constant in drift time as seen in the (wire,time) and (wire,wire) views. Although the two tracks are distinct in three dimensions they appear as a single track/line in both plane views. Such events can fool the reconstruction software into thinking that there is only one track.

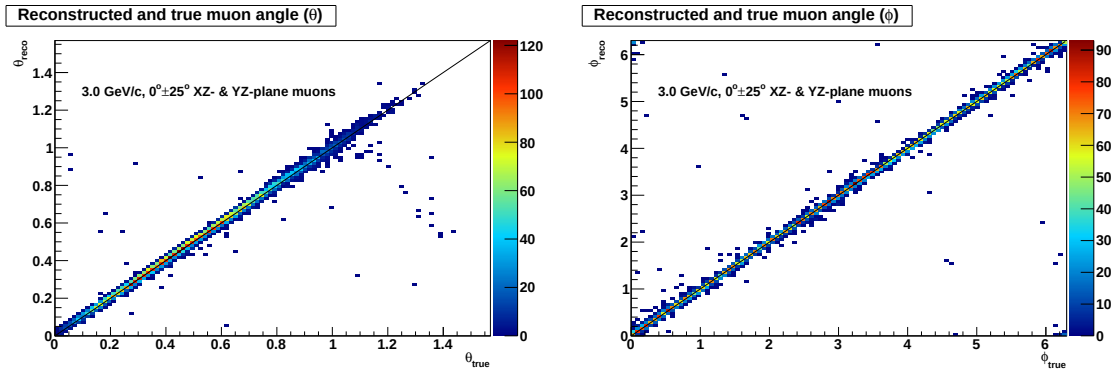

Figure 7.15: The reconstructed and true muon angles in the muon simulation. θ is the angle with respect to the beam axis and ϕ is the azimuthal angle.

region of MINOS. The MINOS reconstructed variables are interpreted by ArgoNeuT and are not necessarily representative of the MINOS experiment, as different cuts, track goodness-of-fit requirements, etc. have been applied.

Schematics of the complete ArgoNeuT simulation and reconstruction chains are shown in Figures 7.20 and 7.21.

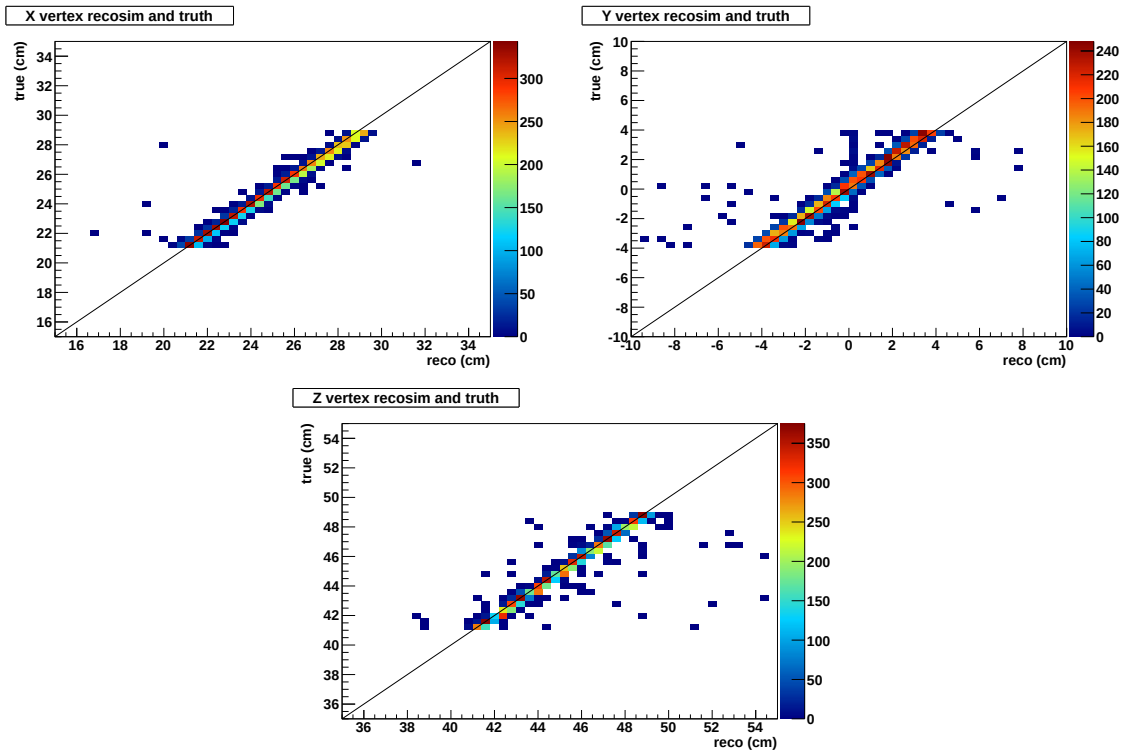

Figure 7.16: The true and reconstructed vertex positions in the muon simulation.

7.7 Electron Lifetime Determination Using Long Tracks

Knowledge of the electron lifetime is vital to the success of a LArTPC-based experiment. Electron drift distances of 2.5 m or more, typical of future LArTPCs [182–186], will require an electron lifetime of >16 ms for <10% charge attenuation over the entire drift length. Although >10 ms lifetimes have been demonstrated [113, 114, 117], attaining this level of purity remains a technical challenge. Knowledge of the electron lifetime is required for energy calibration of signals at different drift distances/times in the case that the lifetime is not infinite. The electron lifetime can be considered immeasurably infinite when the charge collected from a minimum-ionizing track at the cathode is not noticeably different from the charge collected from a minimum-ionizing track at the wire planes, allowing for the effects of noise and diffusion. In consideration of electron lifetime only,

$$Q_{rec} = Q_{true} e^{-t/\tau}, \tag{7.2}$$

with Q_{rec} and Q_{true} the reconstructed and true charge, respectively, and t and τ the drift time and electron lifetime, respectively. As an example, a drift time equal to twice the

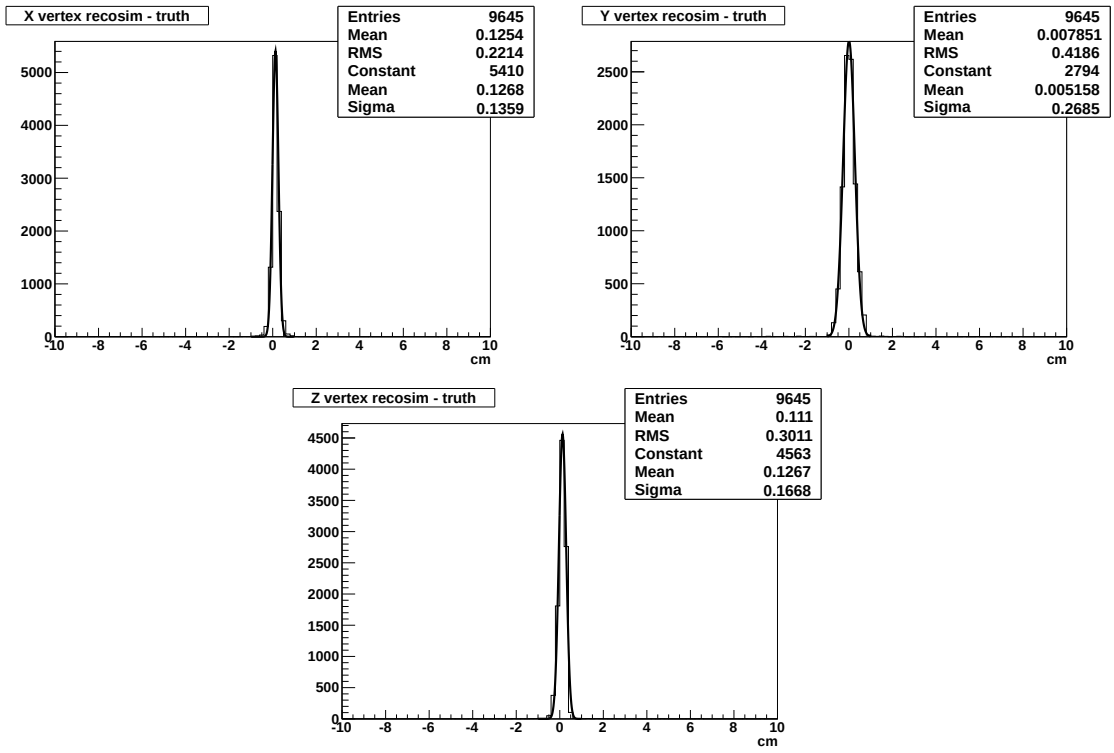

Figure 7.17: The difference between the true and reconstructed vertex positions in the muon simulation.

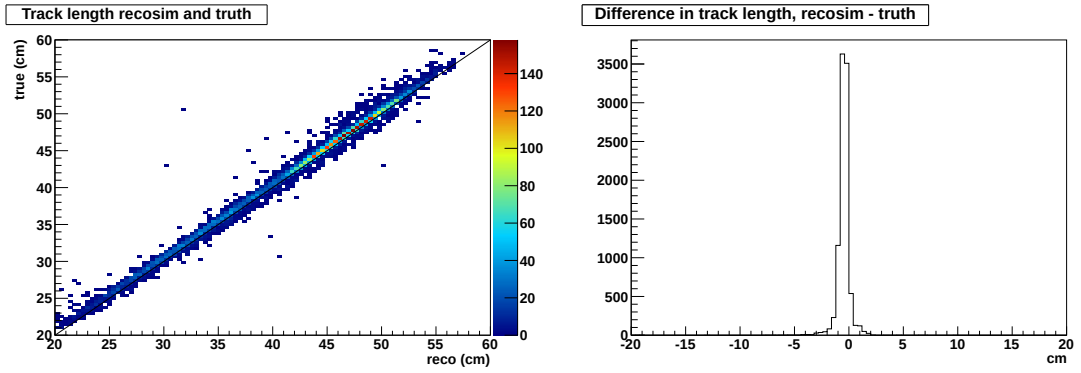

Figure 7.18: The true and reconstructed track length in the muon simulation (left) and their difference (right).

electron lifetime and an electron lifetime uncertainty of 10% leads to a reconstructed charge resolution of 20%.

A purity monitor [115] is nominally used to measure argon purity in a LArTPC. The device is especially useful for on-the-fly purity monitoring and monitoring during the initial liquid argon fill. However, the purity monitor can only measure the lifetime with <10%

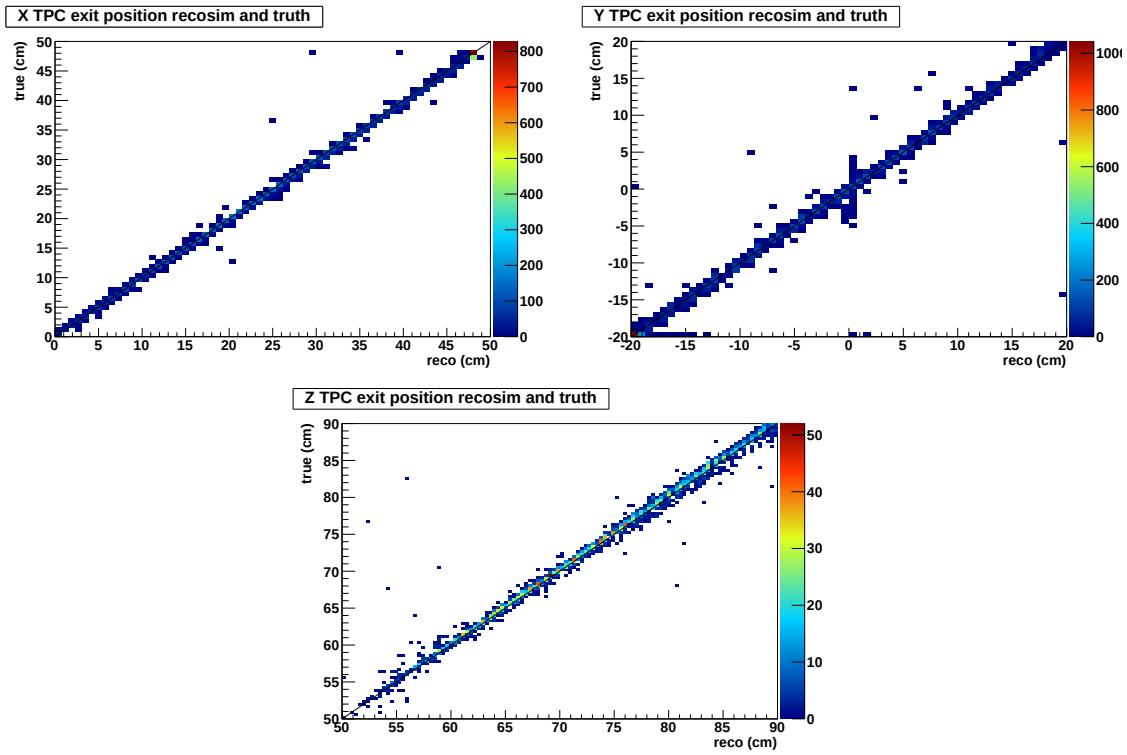

Figure 7.19: The reconstructed and true track exit position in the muon simulation.

precision in the case of non-infinite purity [187]. Furthermore, the purity monitor is unable to measure the electron lifetime if the charge attenuation over the entire drift distance is smaller than its resolution (<10%). That is, the purity monitor cannot tell if the electron lifetime is really infinite or not if the charge attenuation over the drift is <10%. The device is also difficult to employ in consideration of the delicate optical fiber(s) and photocathode(s) required for operation as well as the challenging accessibility issues in the case of a failure. Furthermore, the purity monitor is a potential source of noise and can effect the homogeneity of the TPC's electric field. It is worth noting that Reference [188] presents a novel new to way to measure the purity of liquid argon that circumvents some of the issues discussed.

7.7.1 Using tracks to measure the electron lifetime

Tracks themselves can be used to make an electron lifetime measurement, independent of the purity monitor [189]. This is especially true for a near detector in an accelerator-based experiment that is subject to a high rate of neutrino-induced muons entering through the upstream end of the detector. Although cosmic rays can be used for this purpose, neutrino-

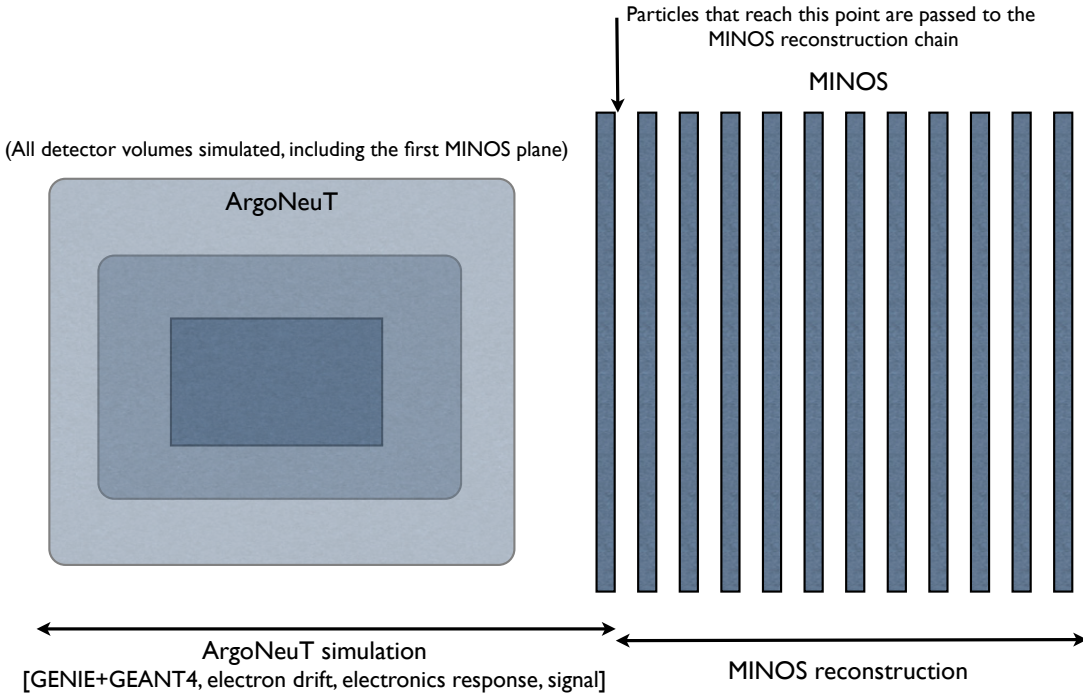

Figure 7.20: The ArgoNeuT simulation chain. The three ArgoNeuT volumes represent the TPC, inner cryostat, and outer cryostat. The drawings are not to scale.

induced muons have a narrow and well-known energy spectrum, $\frac{dE}{dx}$, and directionality suitable for such a measurement. There is also a built-in trigger for these muons, in the form of the accelerator beam-timing signal which is used as the neutrino event trigger for ArgoNeuT. Depending on the through-going muon rate, an electron lifetime measurement using long tracks can have a precision of a few percent or less. The method can also be thought of as an independent cross-check/calibration of the purity monitor's electron lifetime measurement for calorimetric reconstruction and recirculation system operations monitoring.

ArgoNeuT's automated reconstruction software is employed in order to find and characterize long tracks and the hits associated with them. For the purpose of determining the electron lifetime, the procedure is as follows:

- Deconvolution of each event's raw data information.
- Hit finding, to find the hits that are associated with particle tracks in the detector.
- DBSCAN-based cluster finding, to group proximal hits together to form clusters and

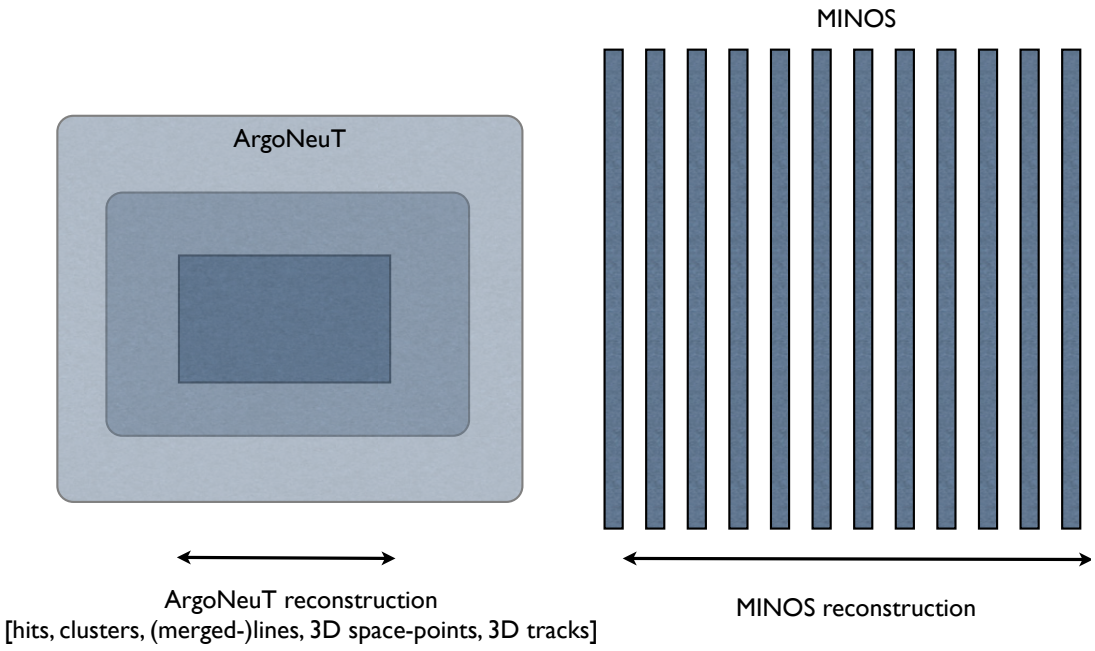

Figure 7.21: The ArgoNeuT reconstruction chain, applied to both the simulation and data. The drawings are not to scale.

to remove noise hits.

- Hough Transform based cluster finding and track fitting, to find and characterize line-like clusters/tracks.

- Hit analysis, to characterize the hits that have been associated with a long, line-like track in order to extract the electron lifetime.

The analysis of the hits belonging to long line-like tracks proceeds as follows. The peak ADC height of every hit associated with a track that spans at least 120 wires is plotted against the hit's drift time. Note that the integrated area of the wire signal's ADC counts can also be used for the measurement and has been found to give similar results as peak height. Figure 7.22 shows a two dimensional scatter plot of signal peak height (ADC counts) versus time sample for a single ArgoNeuT physics sub-run that occurred on 9/27-9/28/2009, spanning ∼26 hours (40,619 beam spills with $<27 \times 10^{12}>$ POT/spill). This sub-run has been chosen as an example for this analysis due to the relatively high beam intensity/consistency during this period, although the electron lifetime extraction is valid

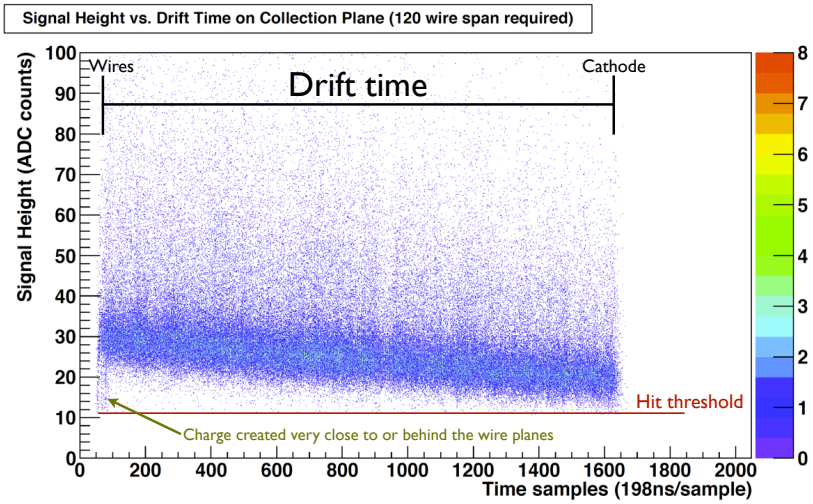

Figure 7.22: A two dimensional scatter plot of signal height versus drift time showing every hit associated with a long track, mostly from through-going muons, on the collection plane in ∼26 hours worth of ArgoNeuT neutrino-mode beam data.

for all sub-runs reported. Recalling that there are 240 wires per ArgoNeuT wire plane, 1513 events featured a track that spanned at least 120 wires in the collection plane, with an average of 161 wires spanned per >120 wire event. There is no other requirement placed on events that enter the plot, other than that they feature a line-like track that spans 120 wires or more. Such tracks could be from neutrino interactions with a vertex inside the detector, cosmic rays entering the detector during the sampling time, or more likely, neutrino-induced tracks, usually muons, entering the upstream side of the detector. The wire-span cut helps to ensure that tracks that enter the sample are largely minimum-ionizing and line-like true muons, ideal for the electron lifetime measurement.

There are a number of interesting features in Figure 7.22. The drift time from the cathode to the wire planes is clearly seen along with the pre- and post-sampling time periods. Note that the pre- and post-sampling regions are devoid of any long, perhaps cosmic-ray induced, tracks. Although cosmic rays enter the pre- and post-sampling periods, the chance of a nearly horizontal (parallel to the ground) cosmic ray induced particle crossing ArgoNeuT is low. A "notch" is visible at short drift times representing charge that has been created very close to or behind the wires. The ADC count threshold of 11 required to be considered a hit in the collection plane can also be seen in this plot. The feature of the plot

that is of most interest to the electron lifetime determination is the downward trend; as the drift time gets larger, the ADC hit signal heights get smaller, indicative of a non-infinite electron lifetime.

The two dimensional scatter plot is broken up into time slices that are eight samples wide and the ADC counts are plotted in a one dimensional histogram for each time slice. The time slice width of 8 ticks was chosen to be as small as possible, to minimize the smearing due to a finite electron lifetime within the time region, while still allowing reasonable statistics to accomplish a decent fit. The one dimensional histograms are fit using a convoluted Landau+Gaussian distribution. The Landau distribution describes the energy loss as the particle traverses matter and the Gaussian distribution describes most everything else: electronic noise, ionization diffusion, the range of particle energies, and track orientation with respect to the wires, among other things [190]. The fit has four parameters: Most Probable Value (MP), the most probable value in the Landau distribution; Width, the Landau distribution's scale parameter; Gaussian sigma (GSigma) of the convoluted Gaussian function; and Area, the area under the convoluted distribution's fit. Figure 7.23 shows a one dimensional histogram of ADC counts for a typical time slice with the fit overlaid. The fit is performed for all 256 time slices from 0 to 2048 time samples. As there are some time slice bins that do not have enough statistics for an acceptable fit and/or feature noisy/outlier hits, all fits with (χ^2/ndf) >1.5 are rejected for the electron lifetime determination. In our example sub-run, the cut dismisses about 5% of the bins.

Plots of MP vs time sample for both the induction and collection planes can be seen in Figure 7.24. An electron lifetime is extracted with an exponential function fit to the MP values for each plane, in a fit range that avoids the detector boundaries. The fit range (from ∼80-1600 samples, about 90% of the drift time) is slightly different for the induction and collection planes as the induction plane is 4 mm closer to the cathode than the collection plane. For our example, the electron lifetime is found to be $771\pm3_{\text{stat}}$ μs on the induction plane and $757\pm3_{\text{stat}}$ μs on the collection plane. The statistical errors come from the fit to MP. Note that the χ^2/ndf for each fit is rather poor due to systematic variations in the MP values for each fit. The variations could be due to coherent noise associated with the actual beam spill systematically affecting signals as a function of drift time. The two independent measurements are combined to arrive at an electron lifetime of $764\pm11_{\text{stat+syst}}$ μs, with a systematic error set equal to the standard deviation of the two points.

The wire-span cut of 120 wires was chosen as it gave the best goodness-of-fit in the

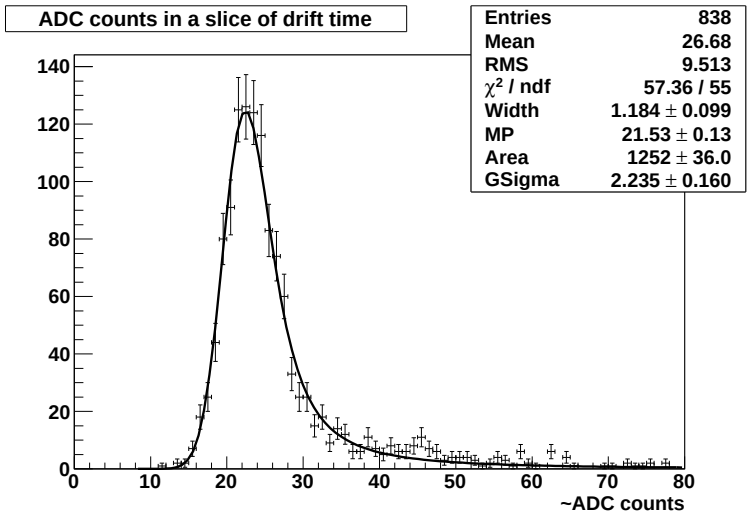

Figure 7.23: A convoluted Landau-Gaussian fit overlaid on all of the signal heights (ADC counts) in an arbitrary time slice from the two dimensional scatter plot of signal height versus drift time on the collection plane. Here, the time slice is 8 time samples wide.

Time slice (ticks)	Electron lifetime (μs)
4	758±3
8	757±3
16	756±3
32	753±3

Table 7.1: The extracted electron lifetime (with statistical-only error) as a function of the chosen time slice.

electron lifetime determination exponential fit. However, the extracted electron lifetime has been found to be largely insensitive to the actual value of the cut (see Figure 7.25). This is expected as the vast majority (>90%) of reconstructed tracks are minimum-ionizing muons, regardless of the number of wires they span. Note that a low wire-span requirement allows more steep-angled tracks to enter the sample. As such tracks have no preferred direction/orientation in the on-axis detector, they do not bias the electron lifetime determination. Also, the electron lifetime measurement is minimally dependent on the time slice width with the extracted lifetime varying by less than one percent with widths of 4, 8, 16, and 32 time samples (see Table 7.1).

Figure 7.26 shows a plot of electron lifetime (with statistical and systematic error) as

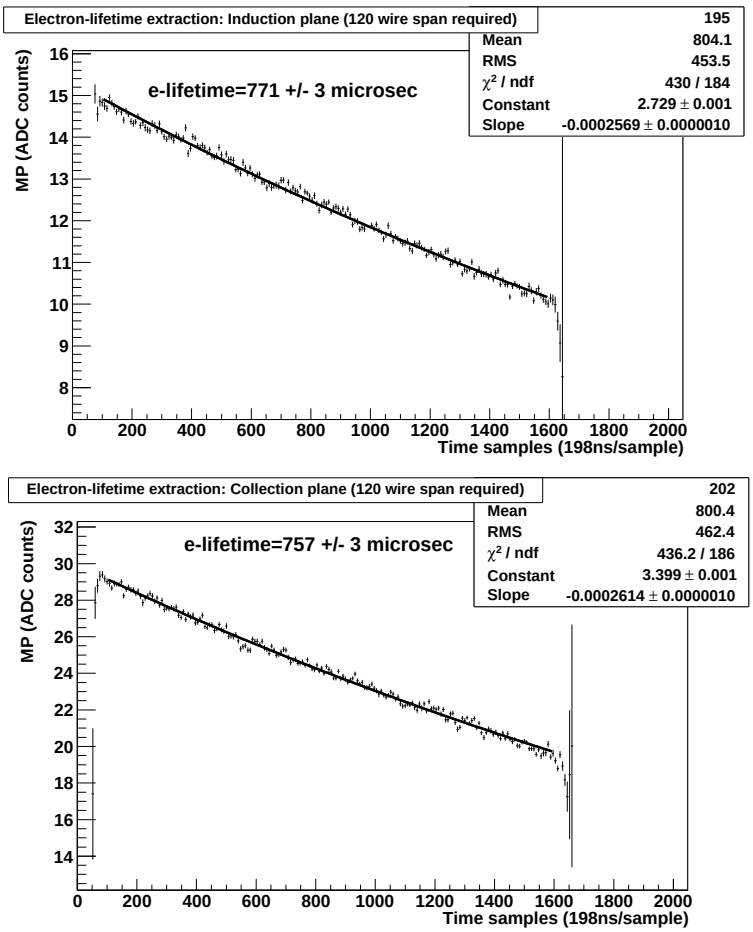

Figure 7.24: The electron lifetime extraction on the induction plane (top) and collection plane (bottom) for a ∼26 hour period ArgoNeuT physics run.

a function of date for ArgoNeuT's neutrino-mode physics run using the method described above (with the measurements from both planes combined). The bin size represents the length of the sub-run and the gaps visible in between some of the sub-run bins are down-times. The data points are observed to be fairly smooth from day-to-day, with the electron lifetime precision for most runs at the ∼2% level. Note that the beam intensity, which the track-based electron lifetime determination is extremely dependent on, steadily increased from the start of the run to the end. Also, a gas purge flow system was activated on 9/22/2009 at 14:40, resulting in a substantial drop in purity easily seen in the plot.

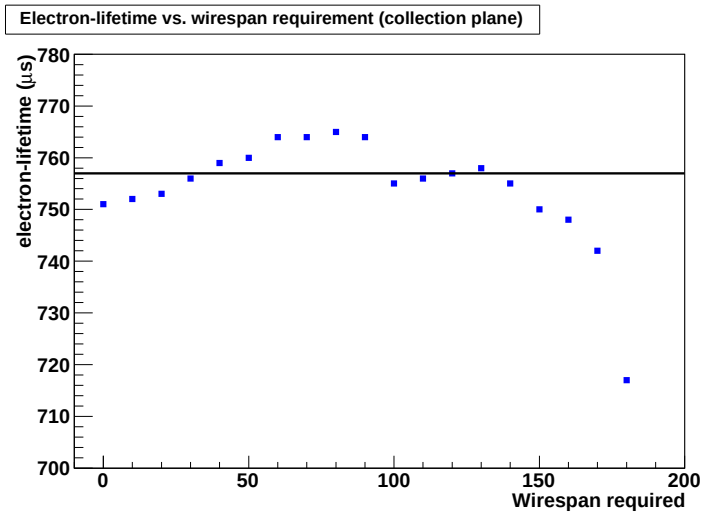

Figure 7.25: The extracted electron lifetime as a function of the wirespan requirement cut. The actual wirespan cut (120 wires) was chosen to give the best fit on the collection plane. The black line indicates the electron lifetime measurement, given the final cuts.

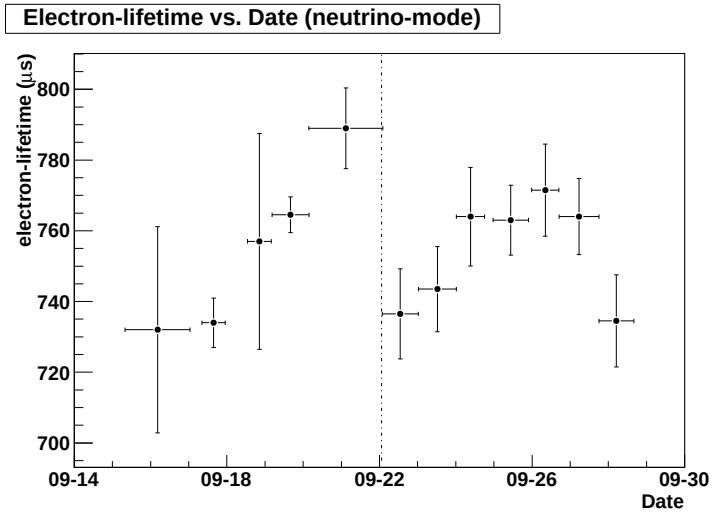

Figure 7.26: The electron lifetime as a function of date for each sub-run in the ArgoNeuT neutrino-mode run period. The dotted line at 9/29/2009 represents a significant change to ArgoNeuT's recirculation system which resulted in a loss of purity.

Part IV

Analysis

8 Charged-Current Muon-Neutrino Analysis

8.1 The CC ν_μ Interaction

This thesis analysis describes the Charged-Current (CC) ν_μ interaction in terms of properties of the outgoing muon. The kinematics of the CC ν_μ interaction ($\nu_\mu N \rightarrow \mu^- X$), where N is the struck nucleon and X is the hadronic final state, can be described quite simply with only a few variables. The leptonic system (ν_μ and μ^-) is given a four-momentum $\mathbf{k}$, the hadronic system is given a four-momentum $\mathbf{p}$, and the exchanged W-boson carries a four-momentum $\mathbf{q}$. Before scattering, the variables are designated with a subscript 1 and after scattering they are given a subscript 2. The incoming neutrino energy, outgoing muon momentum, outgoing muon angle with respect to the initial neutrino direction, and outgoing hadronic energy are given by E_ν, P_μ, θ_μ, and $E_{\rm had}$, respectively. The Bjorken scaling variable x is the fraction of the nucleon momentum that the struck parton carries. For a neutrino moving in the positive Z-direction, the four-momenta before and after scattering in the lab frame are:

$$\begin{aligned} k_1 &= (E_\nu, 0, 0, E_\nu) \\ k_2 &= [E_\mu, P_\mu \sin(\theta_\mu)\cos(\phi_\mu), P_\mu \sin(\phi_\mu)\sin(\theta_\mu), P_\mu \cos(\theta_\mu)] \\ p_1 &= (M, 0, 0, 0) \end{aligned} \tag{8.1}$$

The following invariant variables are often used to describe the interaction:

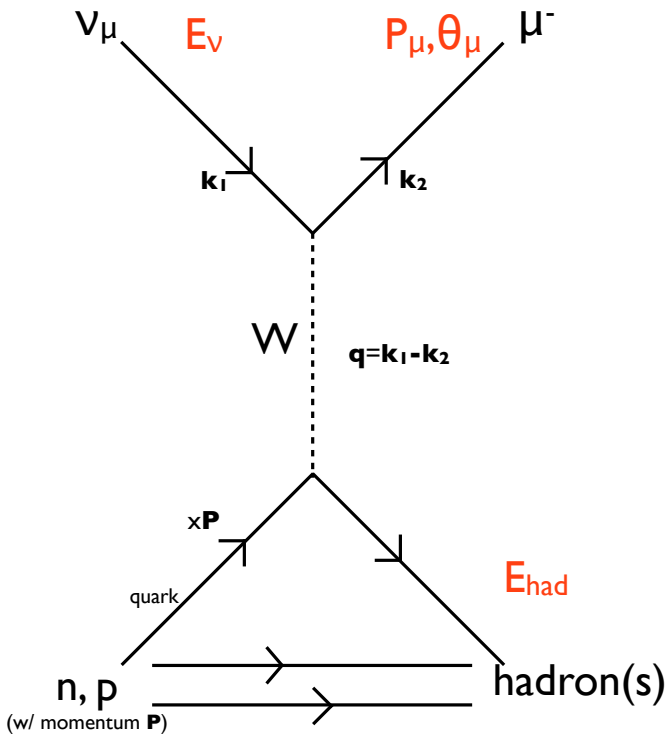

Figure 8.1: The Feynman diagram for the CC ν_μ interaction. The experimental observables are in red.

$4-$mom. transfer squared : $Q^2 = -q^2 = -(k_1 - k_2)^2 = m_\mu^2 + 2E_\nu(E_\mu - p_\mu \cos\theta_\mu)$

Bjorken scaling variable : $x = \dfrac{-q^2}{2p \cdot q} = \dfrac{Q^2}{2M\nu}$

Inelasticity : $y = \dfrac{p \cdot q}{p \cdot k} = \dfrac{E_{\text{had}}}{E_\nu}$

Hadronic invariant mass : $W^2 = (p_2^2) = M^2 + 2M\nu - Q^2$

Center of mass energy : $s = M^2 + 2ME_\nu$

M is the mass of the struck nucleon and ν is the energy transferred to the hadronic system, which is equal to the energy of the hadronic system E_{had} after neglecting the mass of the struck nucleon.

The interaction cross section is given by Fermi's golden rule:

$$d\sigma = d\Gamma \frac{|\mathcal{M}^2|}{\Phi} \tag{8.2}$$

where $\mathcal{M}$ is the matrix element, $d\Gamma$ is the density of final states, and Φ is the flux of the particles through the interaction medium in question. The electroweak Lagrangian contains the charged-current coupling:

$$\mathcal{L}_{CC} = \frac{g}{\sqrt{2}}\Big[\big(\sum_{i=1,2,3} \overline{d}_{i,L}\gamma_\nu u_{i,L} + \bar{l}_{i,L}\gamma_\mu \nu_{i,L}\big)W^{+,\mu} + \big(\sum_{i=1,2,3} \overline{u}_{i,L}\gamma_\mu d_{i,L} + \overline{\nu}_{i,L}\gamma_\mu l_{i,L}\big)W^{-,\mu}\Big], \tag{8.3}$$

with u_i/d_i the up/down quarks and l_i/ν_i the lepton/neutrino of the i generation. Once again, we see the parity non-conservation of the weak interaction as only left-handed couplings (subscript L) exist in the equation above.

The matrix element for the CC interaction is written as:

$$\mathcal{M}_{CC} = \frac{g^2\cos(\theta_C)}{8}[\bar{l}\gamma^\mu(1-\gamma^5)\nu_\mu]\frac{g_{\mu\nu} - \frac{q_\mu q_\nu}{M_W^2}}{q^2 - M_W^2} < X|J^\mu|N >, \tag{8.4}$$

where θ_C is the Cabibbo angle and M_W is the mass of the W boson. This matrix element is composed of a weak leptonic current ($[\bar{l}\gamma^\mu(1-\gamma^5)\nu_\mu]$) and a hadronic current ($< X|J^\mu|N >$). In the case of $q^2 << M_W$ and setting $G_F = \frac{\sqrt{2}g^2}{8M_W^2}$ the matrix element becomes:

$$\mathcal{M}_{CC} = \frac{G_F\cos(\theta_C)}{\sqrt{2}}[\bar{l}\gamma^\mu(1-\gamma^5)\nu_\mu] < X|J^\mu|N > \tag{8.5}$$

Understanding the contributions to the CC-inclusive cross section largely involves parameterizing the hadronic current for each exclusive final state as the leptonic current can be calculated precisely. The three most relevant regimes for GeV-scale CC scattering are quasi-elastic (QE), resonance (RES), and deep inelastic scattering (DIS):

$$\sigma_{CC} = \sigma_{QE} + \sigma_{RES} + \sigma_{DIS} + ... \tag{8.6}$$

Subsequent terms involving coherent neutrino-nucleus scattering, multi-pion production, charm production channels, etc. contribute only a few percent to the total CC cross section at low energies. Although these processes are not discussed here, they are simulated by the GENIE neutrino event generator employed in this analysis.

QE and RES events are generally described as occurring between a neutrino and a single nucleon while DIS interactions represent the interaction of a neutrino with a quark at higher values of Q^2. The transition between nucleon and quark target scattering is a smooth one. The neutrino-quark/nucleon interaction is sensitive to the environment in which the struck

particle inhabits and free and bound nuclear targets exhibit different neutrino scattering properties. The relativistic Fermi gas model describes the effects of Fermi motion, the movement of nucleons inside the nucleus, as well as Pauli suppression, the reduction of cross section due to Pauli blocking effects among nucleons. These issues are discussed at length in Section 6.1.

The Llewellyn-Smith formalism [133] (discussed in Section 6.1.3) provides the differential cross section of QE scattering ($\nu_\mu n \longrightarrow \mu^- p / \overline{\nu}_\mu p \longrightarrow \mu^+ n$) in the lab frame:

$$\frac{d\sigma^{\nu(\overline{\nu})}}{dq^2} = \frac{M^2 G_F^2 \cos^2(\theta_C)}{8\pi E_\nu^2}[A(q^2) \mp B(q^2)\frac{s-u}{M^2} + C(q^2)\frac{(s-u)^2}{M^4}], \tag{8.7}$$

with s, u as the Mandelstam variables and M as the mass of the nucleon. A, B, and C are the various form factors associated with the interaction. Assuming the mass of the lepton to be much smaller than the target nucleon, a safe assumption for all but τ leptons,

$$A(Q^2) = \frac{Q^2}{M^2}\left[(1-\frac{Q^2}{4M^2})F_A^2 - (1-\frac{Q^2}{4M^2})F_1^2 + \frac{Q^2}{4M^2}(1-\frac{Q^2}{4M^2})F_2^2 + 4\frac{Q^2}{4M^2}F_1F_2\right]$$

$$B(Q^2) = \frac{Q^2}{M^2}F_A(F_1 - F_2) \tag{8.8}$$

$$C(Q^2) = \frac{1}{4}(F_A^2 + F_1^2 + \frac{Q^2}{4M^2}F_2^2)$$

The form factor is a measure of the non-point-like structure of the nuclear target. Electric and magnetic scattering both contribute to the form factors of the target neutron/proton. Via the conservation of vector current, the two vector form factors (F_1 and F_2) are parameterized with the vector mass M_V. The axial form factor F_A is parameterized with the axial vector mass M_A. The vector form factors have been measured with high precision in electron elastic scattering experiments over a large kinematic range while the axial form factor can only be measured by neutrino experiments. F_A is usually parameterized by the "dipole" approximation:

$$F_A = 1.23(1 - \frac{q^2}{M_A^2})^{-2} \tag{8.9}$$

where M_A is the axial mass. The form of the equation comes from assuming an exponential electromagnetic charge and magnetic moment distribution of the nucleus [$\rho(r) = \rho(0)e^{-Mr}$]. The contant 1.23 (=F_A, at $q^2 = 0$) has been determined with neutron beta decay.

The differential cross section for CC resonance production [$\nu l \rightarrow l N^*$, $N^* \rightarrow N'\pi$, where N^* is an excited nucleon (resonance)] is:

$$\frac{d\sigma}{dq^2 dW} = \frac{1}{32\pi M E_\nu^2}\frac{1}{2}\sum_{spins}|\mathcal{M}|^2\delta(W^2 - M^2), \tag{8.10}$$

where M is the mass of the resonance (with no width). The width of the resonance Γ is taken into account after replacing the delta-function with the Breit-Wigner form:

$$\delta(W^2 - M^2) \longrightarrow \frac{1}{2\pi}\frac{\Gamma}{(W-M)^2 + \Gamma^2/4} \tag{8.11}$$

The Rein and Sehgal model (discussed in Section 6.1.3 as well) calculates each distinct final state cross section as a superposition of all unique baryon resonances. The resonance production cross section of each final state is calculating using isospin Clebsch-Gordon coefficients with same spin and total momentum resonance states allowed to interfere. The resonant axial vector mass, appearing in the hadronic current's axial form factor, is once again the largest source of uncertainty to the theoretical cross section of resonance production. The resonant axial form factor is usually assumed to have the same "dipole" behavior as Equation 8.9.

The deep inelastic scattering differential cross section in terms of the energy transferred to the hadronic system (ν) is given by:

$$\frac{d\sigma^{\nu(\overline{\nu})}}{d\nu} = A(1 + \frac{B}{A}\frac{\nu}{E} - \frac{C}{A}\frac{\nu^2}{2E^2}), \tag{8.12}$$

with

$$A = \frac{G_F^2 M}{\pi}\int F^2(x)dx$$

$$B = -\frac{G_F^2 M}{\pi}\int (F^2(x) \mp xF_3(x))dx \tag{8.13}$$

$$C = B - \frac{G_F^2 M}{\pi}\int F^2(x)\widetilde{R}dx \ , \ \widetilde{R} = \frac{1+\frac{2Mx}{\nu}}{1+R_L} - \frac{Mx}{\nu} - 1 \ ,$$

where E is the neutrino energy, M is the mass of the proton, G_F is the Fermi weak coupling constant, the F terms are structure functions containing the distribution of quarks and gluons within each nucleon, R_L is the cross section ratio between longitudinal and transverse polarized W bosons, and x is the Bjorken scaling variable. In the definition of B, the plus sign in front of the xF_3 term is for neutrinos and the minus sign is for anti-neutrinos. At high energy (> 10 GeV), where DIS scattering begins to dominate, the cross

section is well understood. The structure functions in the above equation are related to quark parton distribution functions precisely measured by a number of experiments. In the limit of $Q^2 \to \infty$, the structure functions for an isoscalar nucleon are:

$$F^2(x) = x[u(x) + d(x) + 2s(x) + \overline{u}(x) + \overline{d}(x) + 2\overline{c}(x)]$$
$$xF^3(x) = x[u(x) + d(x) + 2s(x) - \overline{u}(x) - \overline{d}(x) - 2\overline{c}(x)] \tag{8.14}$$

with the parton distribution functions for each quark (up, $d$own, $s$trange, and $c$harm) expressed in terms of the Bjorken scaling variable x. Although the DIS cross section is well understood at high-energy/Q^2, the interplay between QE, RES, and DIS at low energy (< 10 GeV) must be treated carefully. The culmination of electron-proton and neutrino nucleon/nucleus data on many different nuclei and across a large kinematic region along with the theoretical models for the various processes described above are required to understand and model neutrino interactions at these energies. The relative contributions from QE, RES, and DIS to the total CC ν_μ cross section are shown in Figure 8.2.

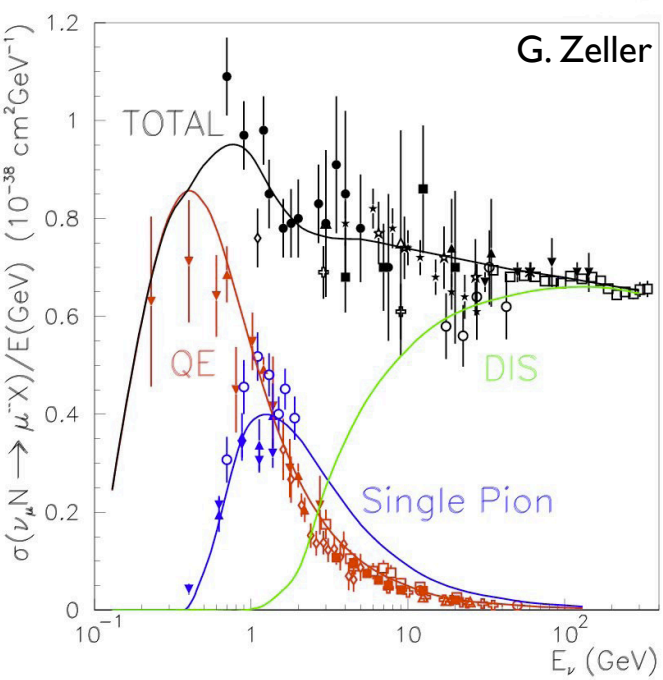

Figure 8.2: The contributions to the total CC ν_μ cross section [164]. "RES", as used in the text, and "Single Pion" are the same thing.

8.2 Why is this Measurement Interesting and Relevant?

The total CC ν_μ cross section as a function of energy [$\sigma(E)$] has been measured by a number of experiments (see Figure 8.3). In the past few years, the cross section has been measured precisely by three different experiments at low energy (<20 GeV), relevant for long (and many short) baseline neutrino oscillation experiments. NOMAD measured the total CC ν_μ cross section [$\sigma(E)$] with a precision of 4% from $2.5 < E_\nu < 10$ GeV and 2.6% from $10 < E_\nu < 40$ GeV [191], MINOS has measured $\sigma(E)$ in the 3-50 GeV energy range with a precision of 2-8% [123], and SciBooNE has measured $\sigma(E)$ in the <3 GeV energy range with a precision of 10-30% [192]. Along with their total cross section measurement, both MINOS and SciBooNE report the rate of events as a function of both outgoing muon angle and momentum/energy–although the differential cross section in terms of these variables is not explicitly reported.

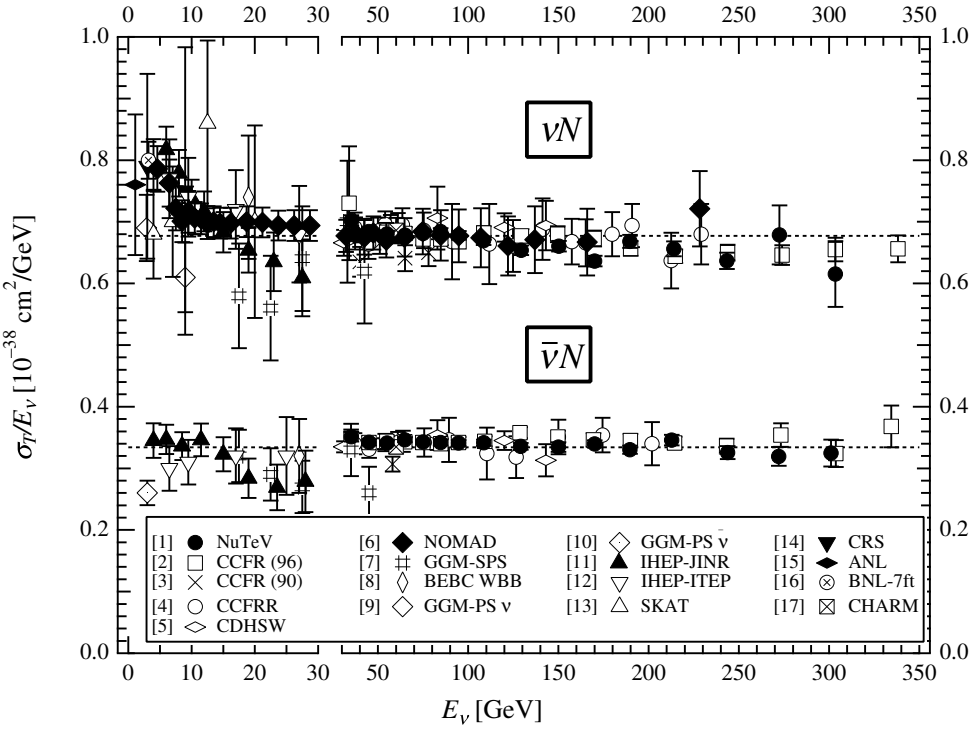

Figure 8.3: The world's CC ν_μ cross section data, from Reference [56].

As previously mentioned, most of the theoretical uncertainty on the neutrino-parton/nucleon/nucleus cross section and differential cross section (in terms of e.g. muon kinematics) comes from

uncertainty on the axial form factor and the axial mass contained in the form factor. These quantities are known to within only about 20-30% in the relevant energy region (0-10 GeV). The MiniBooNE collaboration has recently measured a CCQE cross section and M_A that are significantly higher than theoretical predictions and previous data in the 0.4-2.0 GeV neutrino energy range [137]. The results of this measurement can be seen in Figure 8.4.

The MiniBooNE and NOMAD [193] CCQE cross section measurements disagree under the relativistic Fermi gas model (Reference [134] is commonly used) by up to and exceeding 30%, despite using the same nuclear target (^{12}C). Unexpectedly, the MiniBooNE CCQE cross section measurement, the larger of the two reported cross sections, surpasses the neutrino-on-free-neutron cross section. A neutrino interaction with a bound nucleon is expected to have a smaller cross section than an interaction on a free nucleon due to Pauli blocking and binding energy suppression effects by about 10% for ^{12}C [154]. A possible CCQE multi-nucleon channel in which two correlated same-flavor nucleons are ejected [194] along with the experiments' varying levels of blindness to low energy protons coming out of the vertex or "vertex activity" may be the root of the discrepancy. The channel may be the result of both short range correlations and 2 body currents between bound nucleons within the nucleus. Protons are not considered in the MiniBooNE CCQE measurement and protons with momentum less than ∼300 MeV/c are not reconstructed in the NOMAD analysis. MiniBooNE's complete insensitivity to the proton(s) is advantageous in the sense that the extracted cross section measurements do not rely as much on proton final state interaction modeling uncertainties [137]. However, the experiment is unable to measure a possible multi-nucleon excitation channel. This discrepancy along with the now increasing (and already large) uncertainty on the axial form factor is an example of the need for measurements that do not rely on final state interaction modeling for identification (e.g. a measurement of the CC-inclusive differential or total cross section).

This analysis will focus on the reconstruction of the muon in ν_μ CC-inclusive interactions, with contributions from quasi-elastic, resonant, and deep inelastic scattering. The measurement does not utilize the full capabilities of a LArTPC to describe a neutrino event as it does not employ $\frac{dE}{dx}$ for particle identification. The analysis does not require this– particle identification is largely done by MINOS; if it's reconstructed as a track by MINOS, it is a muon. The small fraction of exceptions to this statement are accounted for in the analysis. Subsequent ArgoNeuT measurements will demonstrate a LArTPC's calorimetric abilities as well as power in describing the vertex activity and non-muon particle properties

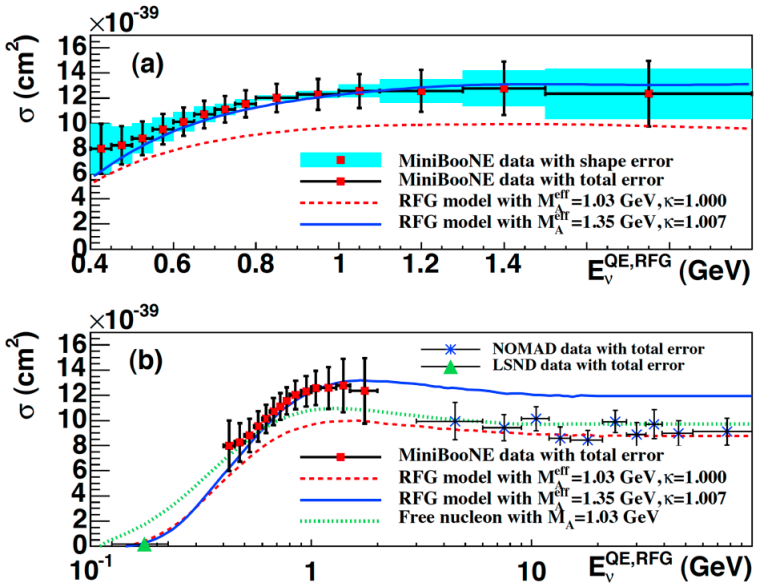

Figure 8.4: The MiniBooNE CCQE ν_μ cross section measurement, from Reference [137]. "RFG" refers to the relativistic Fermi gas model and κ refers to an added degree of freedom in the RFG model, most relevant at low values of Q^2 [136].

for the CC-inclusive event class and exclusive interaction channels.

The oft-reported CC-inclusive $\sigma(E_\nu)$ is limited as it says nothing about muon kinematics. Of course, the utility of $\sigma(E_\nu)$ is in removing near-far detector flux differences as a function of energy in accelerator-based neutrino oscillation experiments searching for oscillation as a function of L/E_ν. The differential cross sections in terms of muon kinematics reported in this thesis can be useful in tuning neutrino event generation models as well as understanding the systematic differences between near and far as a function of muon kinematics. The importance of neutrino cross section knowledge as applied to oscillation physics is discussed at length in References [195] and [196].

The CC-inclusive set of channels provides a "standard candle" for determining the composition of a neutrino beam as it is minimally sensitive to the complicating effects of final state interactions and exclusive channel definitions discussed in Section 6.1. As an example in contrast, the CCQE interaction has been used to normalize the absolute neutrino flux [197], a procedure which is highly model dependent. Furthermore, long baseline neutrino oscillation experiments can use CC-inclusive ν_μ to normalize the neutrino content of the beam, rather than the usual CCQE. Also, the inclusive set of channels can be used in ν_μ disappearance ($\nu_\mu \rightarrow \nu_x$) searches. Taking full advantage of this event class and the increased rate of detection that comes with it is an especially attractive option for future

LArTPC-based oscillation experiments with excellent electron/gamma separation capabilities. This opens up the possibility of a higher energy (>3 GeV) beam with a substantial resonant and deep-inelastic scattering component. Such events can be used in the oscillation searches. Furthermore, a higher energy beam allows the possible observation of multiple oscillation cycles as a function of $\frac{L}{E}$ and significantly increases the event rate since the neutrino interaction cross section generally rises linearly with energy.

Subsequent ArgoNeuT exclusive cross section measurements can also be compared to this inclusive one to perhaps disentangle the effects of final state interactions and nuclear modeling from the actual neutrino-nucleus interaction. As an example of this practice, SciBooNE has taken advantage of the previously mentioned result and measured the CC coherent pion production and neutral-current pion production cross sections using a normalization based on their CC-inclusive measurement [159, 161, 198].

8.3 Measuring a Cross Section

Measuring the ν_μ CC-inclusive cross section entails determining the rate of neutrino interactions which produce a negatively charged muon. Beyond just a single number related to the probability for a ν_μ-induced CC interaction to occur, the rate can be expressed as a function of outgoing particle kinematics and turned into a differential cross section. The cross section measured in this way contains information about the probability for an event to occur as well as the probability for an outgoing particle to have a specific kinematic property. As is common in the literature, the cross section can also be expressed in terms of initial neutrino energy.

Knowledge of the number of targets with which the neutrinos are allowed to interact with inside the fiducial volume (N_{targ}) and the flux of neutrinos through those targets (Φ) allows the measured number of interactions (N_{event}) to be transformed into a cross section, σ:

$$\sigma = \frac{N_{\text{event}}}{\Phi N_{\text{targ}}} \tag{8.15}$$

The number of events is written in terms of initial (I_i) and final state (F_i) variables as:

$$N_{\text{event}} = N_{\text{targ}} \int \frac{\partial^N \sigma(I_1 ... I_M)}{\partial_{F_1} ... \partial_{F_N}} \frac{\partial^M \Phi}{\partial I_1 ... I_M} \mathbf{dIdF} \ , \tag{8.16}$$

where M and N are the number of initial and final state variables, respectively.

The total flux can be written as:

$$\Phi = \int \frac{\partial^M \Phi}{\partial I_1 ... I_M} \mathbf{dI} \tag{8.17}$$

The first integral in Equation 8.16 is made over all (initial state) neutrino energies (I_i=$E_{\nu,i}$) and becomes:

$$N_{\text{event}} = N_{\text{targ}} \Phi \int \left\langle \frac{\partial^N \sigma}{\partial_{F_1} ... \partial_{F_N}} \right\rangle_{\Phi} \mathbf{dF} \tag{8.18}$$

where the integrand is the flux averaged cross section, noticing the subscript-Φ notation. In terms of a single measured variable u in a bin i,

$$N_{\text{event}} = N_{\text{targ}} \Phi \int_{u_{i,low}}^{u_{i,high}} \left\langle \frac{\partial \sigma}{\partial u} \right\rangle_{\Phi} du = N_{\text{targ}} \Phi \left\langle \frac{\partial \sigma}{\partial u} \right\rangle_{\Phi,i} \Delta u_i \tag{8.19}$$

Rearranging provides the equation for the flux averaged differential cross section in terms of an observable final state kinematic variable:

$$\frac{\partial \sigma(u_i)}{\partial u} = \frac{N_{\text{event,i}}}{\Delta u_i N_{\text{targ}} \Phi} \tag{8.20}$$

Experimentally, N_{event} is arrived at after accounting for background and detection efficiency in each bin i:

$$\frac{\partial \sigma(u_i)}{\partial u} = \frac{N_{\text{measured},i} - N_{\text{background},i}}{\Delta u_i \epsilon_i N_{\text{targ}} \Phi} \ , \tag{8.21}$$

where N_{measured} represents the number of signal and background events passing all cuts, $N_{\text{background}}$ is the number of expected background events, and ϵ is the detection efficiency.

The neutrino differential cross section is commonly measured in terms of hadronic energy or muon kinematics (in the case of a CC interaction). This thesis presents a measurement of CC-inclusive ν_μ differential cross sections in muon angle with respect to the neutrino direction (θ_μ) and muon momentum (P_μ) on an argon and isoscalar target. Isoscalar means that there are equal number of neutrons and protons. The variable "θ" refers to the angle with respect to the neutrino direction, unless otherwise specified. This angle is close to but not equal to the angle with respect to the ArgoNeuT and MINOS coordinates systems' Z-axes. The neutrino flux as a function of energy is reported alongside the differential cross section measurements. This is necessary as the differential cross sections reported are a function of the absolute normalization and shape of the neutrino flux.

Ideally, the double differential cross section in terms of both muon angle and muon momentum at the same time (i.e. $\frac{d^2\sigma}{d\theta_\mu dP_\mu}$) would be reported. However, this requires very high statistics in order to populate the two dimensional bins in (θ_μ,P_μ) space. The total cross section as a function of neutrino energy is not reported as the hadronic components of the events are rarely fully reconstructed due to ArgoNeuT's modest size. That is, the neutrino energy determination for most CC-inclusive event types is unattainable by the ArgoNeuT experiment. The differential cross sections in hadronic energy and Q^2 are not reported for the same reason.

8.4 NuMI Flux Calculation and Uncertainty

Along with being relevant for the denominator of Equation 8.21, the flux estimate is employed in the neutrino event simulation previously described. The neutrino interaction and resulting-particle propagation through the detector simulations are required in order to guide analysis sample selection criteria, determine detection efficiency, estimate reconstruction resolution, and predict the expected background contribution to the sample. Furthermore, the simulation acts to confirm the efficacy of the reconstruction software and detector model.

The NuMI flux employed in this analysis was taken in the "low energy" configuration of the beam, with the "...downstream end of the target (placed) 10 cm from the neck of the first focusing horn and the current in the horns is 185 kA, with the polarity set to focus positively charged mesons" [123]. In the 3-50 GeV neutrino energy range, the neutrino flux and statistical, systematic, and normalization uncertainties are taken directly from Reference [123] and are shown in Table 8.1. The flux reported is for the fiducial volume utilized in the MINOS analysis, which comprises the region 0.5-4.0 m into the front face of the MINOS near detector. That is, the flux employed in the ArgoNeuT analysis presented here is at the position corresponding to 2.0-5.5 m downstream of the center of the ArgoNeuT TPC. The negligible flux difference between the center of ArgoNeuT and the reference location of $\sim$1% is ignored.

A brief description of the flux calculation is below, following Reference [123]. The full description of the flux determination is available there.

The NuMI flux shape is determined using a low hadronic energy subset of neutrino events which is then normalized using the precise world average cross section value measured

E_ν bin (GeV)	ν flux (ν/GeV/m^2/10^9 POT)	Error
3-4	8.05×10^4	5.2×10^3
4-5	3.06×10^4	2.4×10^3
5-7	9.07×10^3	5.3×10^2
7-9	5.18×10^3	3.5×10^2
9-12	3.21×10^3	2.2×10^2
12-15	1.94×10^3	1.0×10^2
15-18	1.09×10^3	65
18-22	629	37
22-26	348	20
26-30	200	13
30-36	119	6.8
36-42	72.2	3.9
42-50	51.6	2.8
Total	164588 ν/m^2/10^9 POT	10882 ν/m^2/10^9 POT

Table 8.1: The NuMI flux (from E_ν=3-50 GeV) as measured/calculated by MINOS used in this analysis, from Reference [123]. The total error is not reported in the reference but has been arrived at assuming a positive correlation between bins. The total error is the sum of the error in each energy bin.

above 30 GeV. Equation 8.12 shows that the differential cross section becomes independent of energy with small $\frac{\nu}{E}$. Furthermore, the differential cross section becomes equal to A for neutrino and anti-neutrinos as $\frac{\nu}{E}$ goes to zero. Simply multiplying Equation 8.12 by the flux shape (ϕ) and setting $\nu \to 0$, we arrive at

$$\left.\frac{dN_{\text{event}}}{d\nu}\right|_{\nu\to 0} = A\Phi(E) \tag{8.22}$$

Therefore, the flux in a particular energy range can be reliably determined by counting the number of events that feature a low energy transfer to the hadronic system. The actual shape of the flux as a function of energy [$\phi(E)$] employed in the analysis is determined after applying a correction to take into account the non-zero $\frac{\nu}{E}$ and $\frac{\nu^2}{2E^2}$ terms in Equation 8.12, as well as background and acceptance. The MINOS cross-section-model-dependent low-ν correction factor is <3% at all reported neutrino energies and the uncertainty associated with this correction is included in the flux error estimate. A normalization factor needs to be applied in order to turn the shape of the flux [$\phi(E)$] into an absolutely normalized distribution [$\Phi(E)$]. As the MINOS data extends above 30 GeV and the neutrino cross section in this region (up to 50 GeV, at least) is very well known, the normalization factor comes from the world average on an isoscalar target (for 30-50 GeV) of $(0.675 \pm 0.009) \times$

10^{-38} cm^2/GeV [199–203].

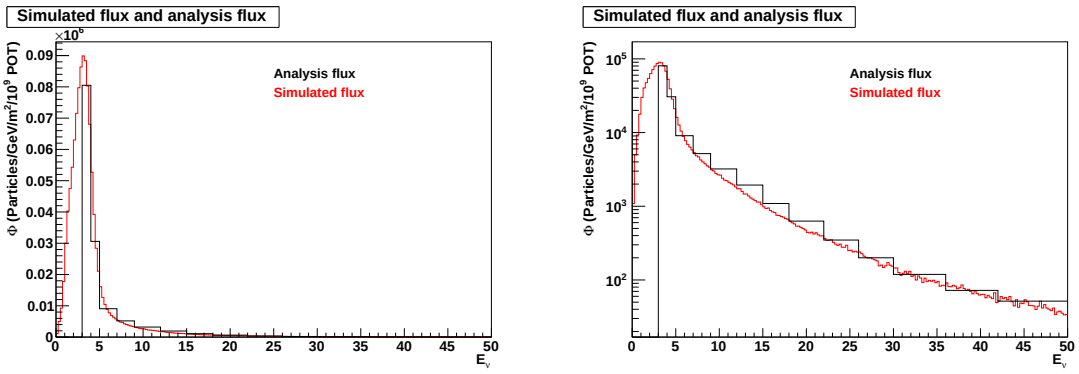

Figure 8.5: The flux employed in the simulation and the flux employed in the analysis with a linear (left) and log (right) y-axis scale. The simulation and analysis fluxes are the same from 0-3 GeV.

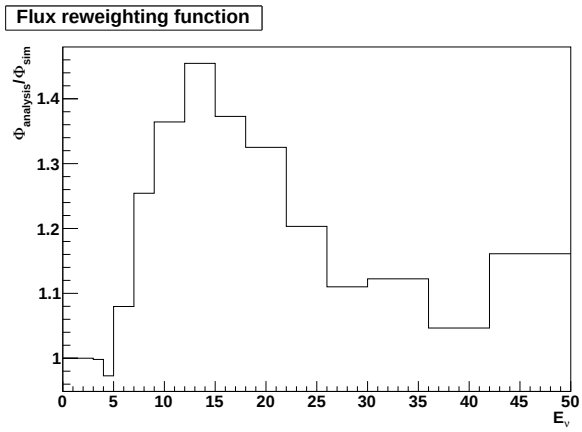

Figure 8.6: The flux re-weighting function, or analysis flux divided by simulated flux.

A NuMI flux determination that is independent of the MINOS measured cross sections at the ArgoNeuT (MINOS near detector) location is not published for the 0-3 GeV energy region. The MINOS collaboration has kindly provided a set of high statistics flux ntuples for the ArgoNeuT location for all relevant energies of the NuMI beam [204]. The flux in this form is used in the ArgoNeuT Monte Carlo simulation. There are a few minor advantages to employing the flux ntuple for the simulation of the entire neutrino energy range, rather than a simple flux histogram displaying neutrino flux versus neutrino energy. The ntuple accounts for the flux window, radial/longitudinal dependence of the beam, and keeps track of the neutrino daughter's parent meson kinematics for cross-checking purposes.

A flux re-weighting procedure is applied after the simulation completes in order to

utilize the quoted "analysis" flux in the measurement rather than the simulated flux for the 3-50 GeV energy range. The reweighting procedure changes the shape and absolute normalization of the neutrino flux as a function of energy only. The directionality and radial dependence of the beam information for the ArgoNeuT location is kept intact. The simulated flux with its shape and absolute normalization is employed for the analysis in the 0-3 GeV range. The simulated and analysis flux are both shown in Figure 8.5 and the flux re-weighting function (analysis flux divided by simulated flux) is shown in Figure 8.6. The integrated flux from 0-3 GeV is reported in Table 8.2 and the integrated flux from 0-50 GeV is reported in Table 8.3.

The integrated flux needed in the denominator of Equation 8.21 is arrived at after taking into account the variable width flux bins in Table 8.1. The integrated flux is

$$\int_{0\ \mathrm{GeV}}^{50\ \mathrm{GeV}} \frac{\partial \Phi}{\partial E_\nu} dE_\nu = (2.91 \pm 0.46) \times 10^5\ \nu/\mathrm{m}^2/10^9\mathrm{POT} \tag{8.23}$$

The error on the integrated flux from 0-50 GeV comes from adding the errors on the 0-3 GeV and 3-50 GeV flux bins in quadrature. The flux predictions from the two bins are considered uncorrelated. From 0-50 GeV, the total fractional error on the integrated flux comes out to 15.7%.

E_ν (GeV)	ν flux ($\nu/\mathrm{m}^2/10^9$ POT)	Error
0-1	8.3×10^3	†
1-2	4.3×10^4	
2-3	7.5×10^4	

Table 8.2: The NuMI flux (from E_ν=0-3 GeV) used in this analysis, as simulated and provided by MINOS [204]. †The error on the flux from 0-3 GeV is 35% [205].

E_ν (GeV)	ν flux ($\nu/\mathrm{m}^2/10^9$ POT)	Error
0-50	2.91×10^5	4.55×10^4

Table 8.3: The NuMI flux (from E_ν=0-50 GeV) used in this analysis.

8.5 Protons on Target and Number of Targets in the Fiducial Volume

The number of POT and number of targets in the fiducial volume are required for an absolutely normalized differential cross section measurement. These terms apply to the denominator in Equation 8.21.

8.5.1 Protons on target

The Fermilab accelerator division's NuMI variable "trtgtd" is employed for the POT counting measurement and represents the number of protons at the beamline monitor closest to the target. Table 8.4 show the collected POT for each ArgoNeuT neutrino-mode run in the latter half of September 2009. The first column shows the POT collected by ArgoNeuT and the second column shows the POT collected by both ArgoNeuT and MINOS at the same time. This column represents the sample employed in the analysis. ArgoNeuT collected a total of 9.5×10^{18} POT in neutrino-mode, with 8.5×10^{18} POT of those used in this analysis. Each $\sim$10 μs spill delivered about 2.2×10^{13} POT on average.

Run	ArgoNeuT POT ($\times10^{12}$)	ArgoNeuT w/ MINOS POT ($\times10^{12}$)
609	171731	131738
616	4158	3466
618	174703	115391
621	431618	313362
622	164384	153024
626	72653	68081
627	368162	367771
628	812124	799550
629	842734	834926
631	835814	831349
632	21990	14738
633	799426	797072
634	483704	168028
635	695477	674362
639	14560	14486
640	179501	178921
642	4760	4760
644	743349	739174
648	810250	806269
649	1096490	913972
650	755194	588401
Total	9482782 (9.5×10^{18} POT)	8518841 (8.5×10^{18} POT)

Table 8.4: The protons on target taken by ArgoNeuT in the central column and taken by both ArgoNeuT and MINOS concurrently in the rightmost column.

8.5.2 Number of targets in the fiducial volume

The number of argon atom targets in the fiducial volume [$(41 \times 32 \times 80)$ cm^3] is calculated simply with

$$(41 \times 32 \times 80)\ \text{cm}^3 \times \frac{1.399\ \text{g}}{\text{cm}^3} \times \frac{1\ \text{mol Ar}}{39.948\ \text{g}} \times \frac{6.022\text{E}23\ \text{atoms}}{\text{mol}} = 2.21\text{E}27\ \text{atoms Ar} \quad (8.24)$$

That is, the variable "N_{targ}" in Equation 8.21 is equal to 2.21×10^{27} atoms/nuclei of argon.

8.6 Matching Muons from ArgoNeuT to MINOS

The ArgoNeuT experiment employs the MINOS near detector in order to fully reconstruct CC ν_μ-induced muons. For this to be accomplished successfully, an ArgoNeuT track needs to be matched with a reconstructed muon in MINOS. A number of matching and mismatching scenarios exist, each affecting the differential cross section measurements to varying degrees. The scenarios and the result of each possibility are described below.

- A match occurs between a single ArgoNeuT track and a single MINOS track. Result: the matched ArgoNeuT-MINOS track is identified as a muon and the event enters the matched sample.

- A match does not occur. Result: the ArgoNeuT event does not enter the matched sample.

- A match occurs between multiple ArgoNeuT tracks and a single MINOS track. Result: the ArgoNeuT track that best aligns with the MINOS track is matched. "Best" alignment is defined based on $\Delta r / \cos\theta$ where r is the radial difference between the ArgoNeuT track projected onto MINOS and the MINOS reconstructed vertex and θ is the angle between the ArgoNeuT track and the MINOS track. The ArgoNeuT-MINOS track is identified as a muon and the event enters the matched sample.

- A match occurs between a single ArgoNeuT track and multiple MINOS tracks. Result: the MINOS track that best aligns with the ArgoNeuT track is matched. The ArgoNeuT-MINOS track is identified as a muon and the event enters the matched sample.

- A match occurs between multiple ArgoNeuT tracks and multiple MINOS tracks. Result: the ArgoNeuT-MINOS track combination that best aligns is chosen as the matched track combination. The ArgoNeuT-MINOS track is identified as a muon and the event enters the matched sample.

Mismatches and non-matches are accounted for in the measurement resolution, reconstruction probability, and background estimates. The scenarios with multiply matched tracks are rare. Schematics of the various matching scenarios and outcomes can be seen in Figures 8.7 and 8.8.

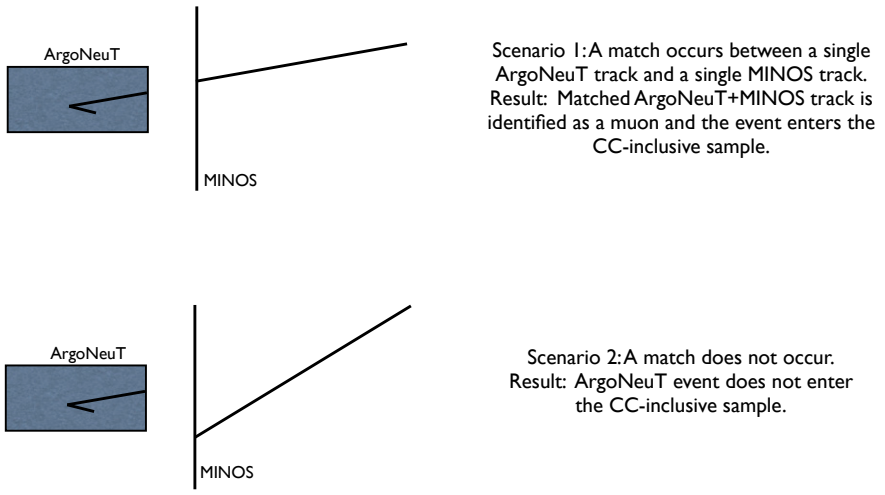

Figure 8.7: The scenarios and outcomes for simple cases of track matching between ArgoNeuT and MINOS.

8.7 Setting the Cuts

Most physics analyses require analysis sample selection criteria (cuts) in order to reduce the expected background contamination of the signal-like sample. Cuts are chosen based on the usually different characteristics of signal and background events. While such cuts inherently reduce signal efficiency, a strong cut removes a disproportionate number of background events as compared to signal.

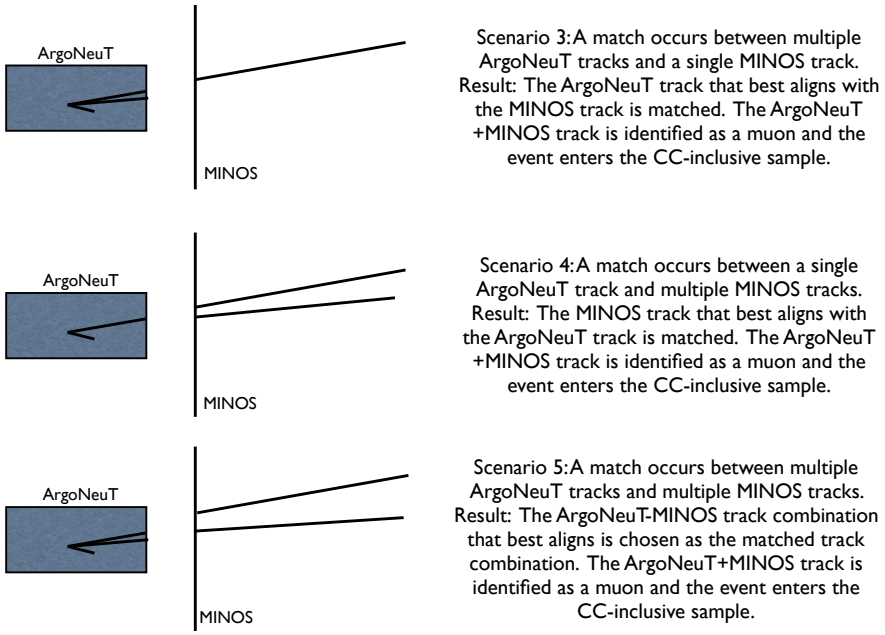

Figure 8.8: The scenarios and outcomes for multiply matched tracks between ArgoNeuT and MINOS.

The CC ν_μ differential cross section analysis presented here features very simple and straightforward cuts. This analysis requires only an outgoing negatively charged muon, and no other exclusive final states. Therefore, there is almost no dependence on the cross section and final state interaction models employed by the GENIE neutrino event generator, a common source of systematic error in characterizing exclusive final states and measuring exclusive cross sections. The cuts discussed below have been set with the intent of minimizing background while maintaining high efficiency and statistics.

There are three main selection criteria:

- Require that the reconstructed neutrino interaction vertex as well as the reconstructed start position of the muon track are inside of the fiducial volume. Although these two variables are the same in reality, track reconstruction allows them to be slightly different.

- Require that a track reconstructed in ArgoNeuT is "well matched" to a track in MINOS.

- Require that the matched MINOS track is reconstructed and negatively charged.

8.7.1 Setting the fiducial volume

The driving factors in setting the fiducial volume cuts are 1) avoiding the possibility of incorrectly identifying a through-going muon as a neutrino-induced muon, 2) avoiding electric field non-uniformities near the edges of the rectangular-box TPC, and 3) maintaining a large event sample.

As the neutrino interaction vertex is determined using two dimensional information and the starting position of the reconstructed muon is determined using three dimensional information, the identified interaction vertex and muon start position are not necessarily the same. In this analysis, the reconstruction software only considers particle tracks that are proximal to an identified neutrino interaction vertex. This requirement makes sure that the muon is associated with the vertex, although the start position of the muon and vertex need not be the exact same reconstructed three dimensional point. In order to fully minimize the possibility of a through-going muon being reconstructed as an originating-in-ArgoNeuT neutrino-induced muon, both the muon start position and the neutrino interaction vertex are required to be inside of the fiducial volume in order to enter the sample.

The reconstructed neutrino interaction vertex versus true vertex distributions for each X/Y/Z coordinate in simulation are shown in Figure 8.9. In the figure and those that follow, the truth information comes from the GENIE neutrino event generator while "recosim" refers to the reconstruction applied to the complete neutrino event simulated with the GENIE- and GEANT4-based software. The background muon simulation is treated separately and discussed in Section 8.10. All events that pass reconstruction and MINOS matching cuts, discussed later, enter these plots. A Gaussian fit is applied to each reconstructed vertex minus true vertex difference distribution in order to provide an idea of the vertex resolution. Recall that the wire spacing is 4 mm (relevant for the Y and Z coordinates) and the sampling time corresponds to 0.3 mm (relevant for the X coordinate). As can be seen, the fits are poor with significant non-Gaussian tails apparent, especially for the Y and Z coordinates. These tails usually represent a minor failure of the reconstruction software, often stemming from issues related to the creation of space-points for tracks that are fairly constant in time. This is evidenced by the fact that long tails are not present for the X-coordinate which is not as sensitive to misreconstructed space-points. A hit in one plane view can be incorrectly matched to a similarly-timed hit or hits in the other plane view. This has been discussed previously (see Section 7.5.3). The three dimensional

reconstruction and vertex finding algorithms (and hence vertex/track resolution, among other things) will be improved in future versions of the ArgoNeuT software. Even with room for software improvements, the vertex resolution is clearly at the sub-cm level for all coordinates and is around 3 mm for the drift coordinate.

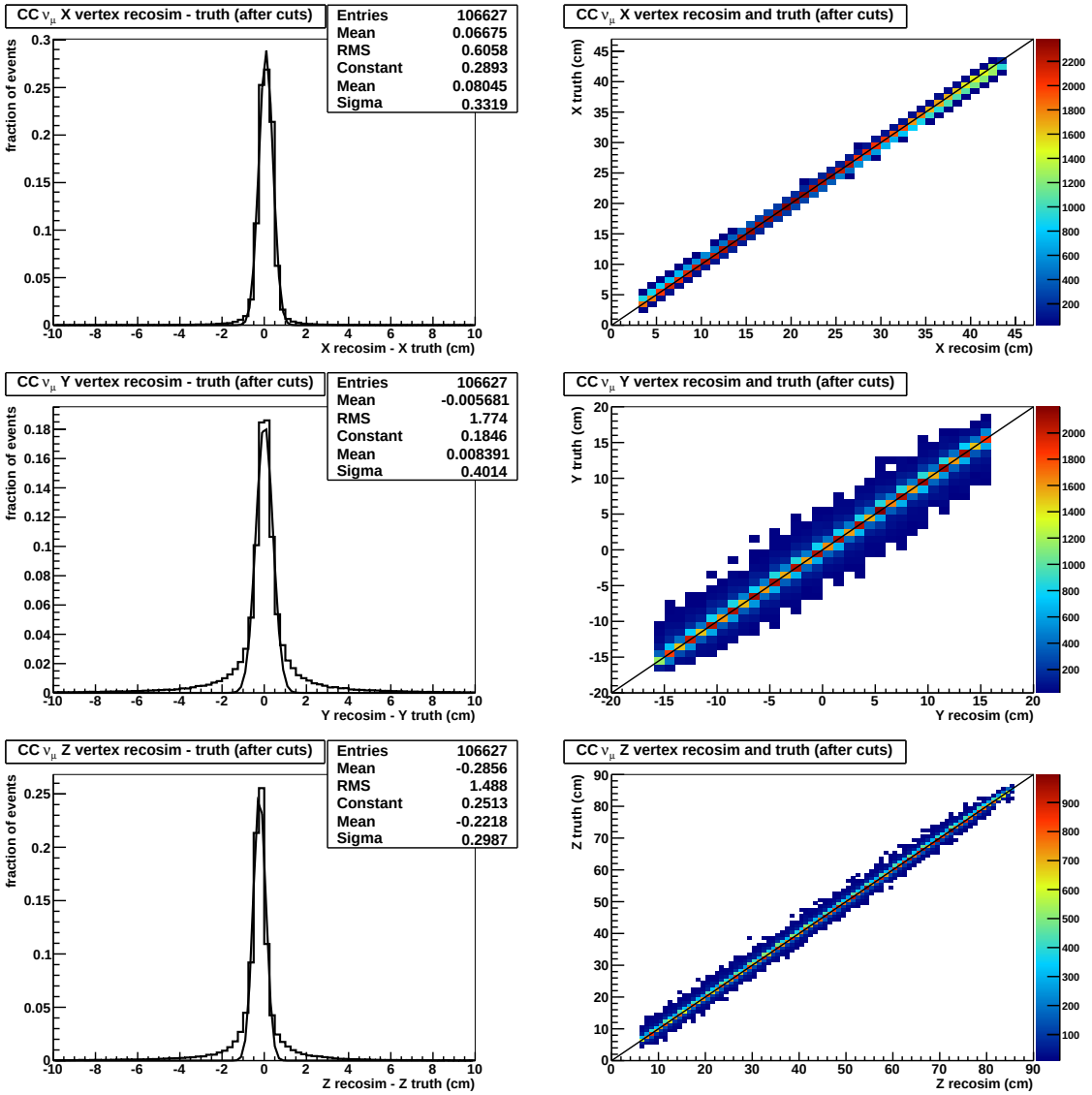

Figure 8.9: The X, Y, and Z vertex coordinates for events that pass all cuts, comparing the true value to the reconstructed value in simulation.

A nominal fiducial volume cut distance of 4 cm from each field cage boundary (i.e. the Y and Z boundaries only) is employed in order to avoid electric field non-uniformities near the edges of the TPC. Figure 5.18 (right) is an instructive example of the non-uniform electric

field lines close to the edges of a field cage. The example features the field lines within the ArgoNeuT purity monitor but is very loosely demonstrative of the TPC's field lines as well. The additional fiducial volume cuts employed in this analysis have largely been determined empirically. Simply plotting a distribution of reconstructed neutrino-candidate vertices in the fiducial volume from the background simulation or in data allows one to readily identify those potential background particles that did not originate inside of the ArgoNeuT detector. An example of this procedure is provided below. There is an additional distance of 2 cm subtracted from the fiducial volume for the upstream Z edge of the detector in order to strengthen the prevention of through-going muons from entering the sample. This extra cut is really only necessary for the upstream Z edge as through-going muons mainly enter the TPC in this way. A plot showing the vertex distribution of events in the Z dimension after relaxing the nominal upstream Z fiducial volume cut by 3 cm is shown in Figure 8.10. Clearly, through-going muons are entering the sample with this relaxed cut as evidenced by the anomalously high number of events at low-Z. The muons enter the sample via a slight, few-cm scale misreconstruction of their upstream-Z vertex and muon start position. The upstream-Z fiducial cut is set in order to avoid this problematic region. Note that through-going muons were not simulated in the creation of the reconstructed simulation ("recosim") histograms but are simulated later for the data analysis background estimate and subtraction. That is, "recosim" represents the expected contribution from neutrino events only, with no simulated contribution from through-going muons.

The X boundaries (cathode and wire planes) are less susceptible to electric field non-uniformities as these electrodes span the entire YZ range of the TPC (see Figures 5.12 and 5.13). A conservative fiducial volume cut of 3 cm is set for the X boundaries, recalling that the beam window is 10 μs (corresponding to $\sim$1.5 cm of drift in the X direction). The effect of increasing and decreasing the fiducial volume on the extracted differential cross sections is discussed later as a possible source of systematic error.

The vertex distributions for data events that pass all cuts are shown in Figures 8.11 and 8.12. The normalization of the plots in Figure 8.12 is indicative of the number of CC ν_μ events expected with simulation in the ArgoNeuT fiducial volume, given cuts and the analysis exposure. Note that the aspect ratios are incorrect in both histograms of Figure 8.11. The range of each axis represents the active volume of the TPC and the fiducial cuts can clearly be seen in the figures. The histograms reveal a fairly uniform distribution of events in the fiducial volume. Once again, "recosim" represents the expected contribution

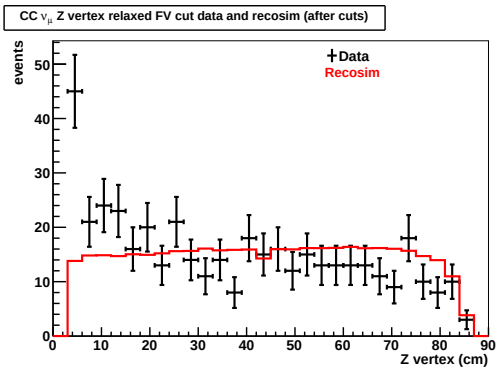

Figure 8.10: The distribution of vertices for all data events that pass the relaxed cuts in the Z dimension. The Z fiducial volume cut is relaxed by 3 cm from its nominal value. Clearly, there are through-going muons entering the upstream end of the TPC in this scenario. Note that "Recosim", the reconstructed neutrino event simulation distribution, does not feature the simulation of through-going muons. The simulation of these particles is treated separately and discussed later.

from neutrino events only in Figure 8.12. Note that there has been no background subtraction applied to the data distributions and the errors reported are statistical only. The background is expected to make up about 4-5% of the sample, as discussed in Section 8.10.

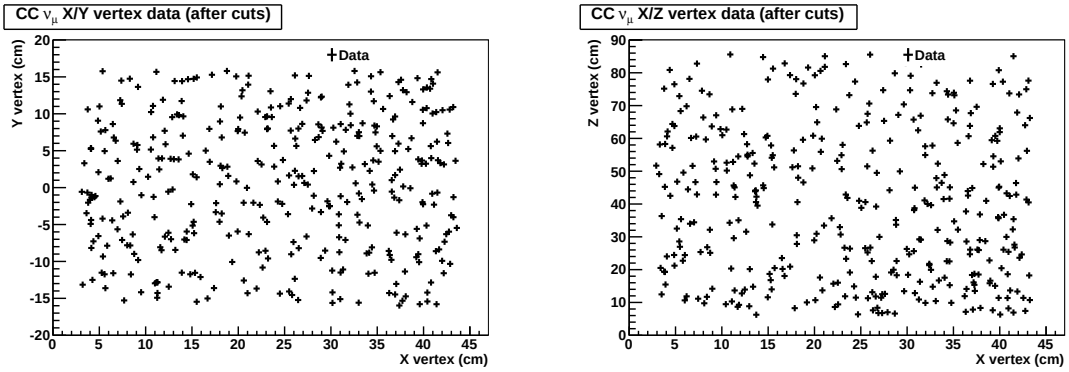

Figure 8.11: The distribution of vertices for all data events that pass cuts in the X/Y (left) and X/Z (right) two dimensional views.

8.7.2 Matching requirements

There are two levels of matching requirements for associating an ArgoNeuT track to a MINOS track. The first, low-level reconstruction requirements associate an ArgoNeuT track to a candidate MINOS track very loosely. Section 8.6 outlines the various matching scenarios and outcomes for cases of (e.g.) multiply matched tracks. These stipulations consider MINOS tracks with a vertex in the upstream-most 20 cm of the detector and

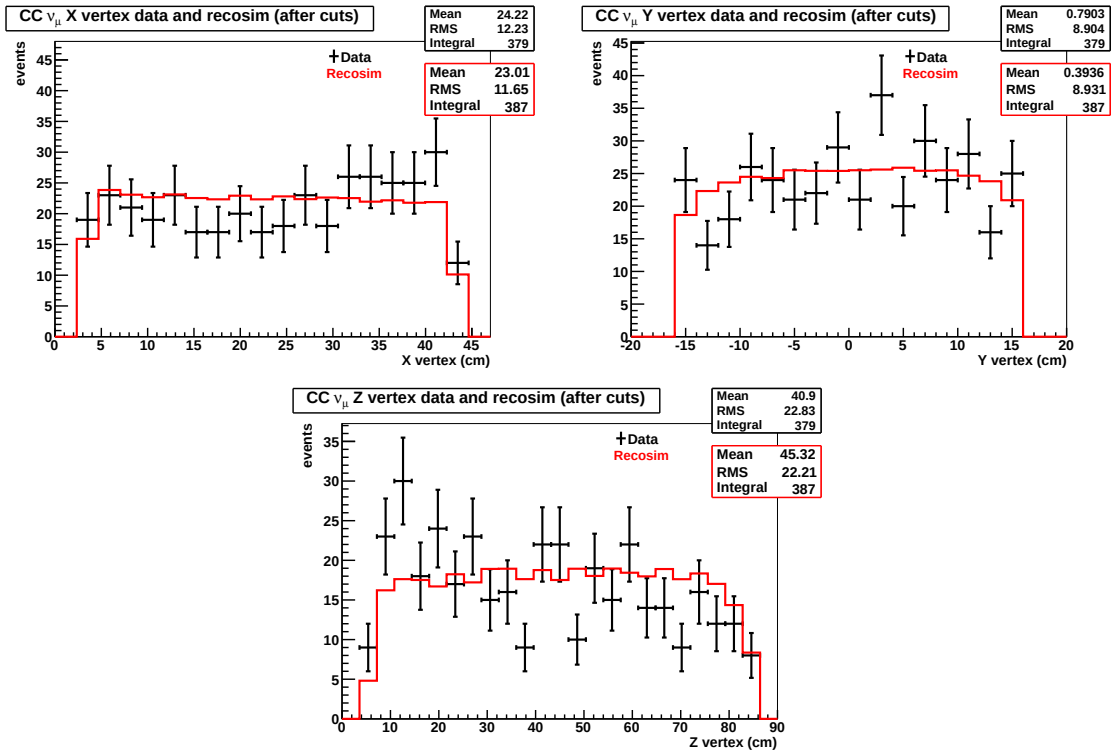

Figure 8.12: The distribution of vertices for all data events that pass cuts in each dimension. The vertices reconstructed in simulation (recosim) and data are shown. No background subtraction has been applied to the data and the errors are statistical only.

require that the ArgoNeuT projected track onto the MINOS vertex Z-position be <35 cm from the MINOS track's vertex in the radial direction. An ArgoNeuT track is considered to have left the TPC if its endpoint is within 5 cm of a boundary. This loose requirement insures that tracks featuring slightly misreconstructed endpoints are considered in matching with MINOS tracks. A strict requirement is not necessary as the number of neutral-current events matched to muon-like tracks in MINOS is 1-2% of the expected signal after all cuts. All ArgoNeuT tracks that leave the TPC are projected onto MINOS and considered when attempting a match. These low-level matching requirements are considered reconstruction steps rather than a "cut". The high-level requirements for matching an ArgoNeuT track with a MINOS track are considered cuts as through-going muons reconstructed by MINOS, unrelated to the originating-in-ArgoNeuT CC ν_μ muon, represent a potential background for the analysis described here. These backgrounds are discussed in Section 8.10.

The matching requirements have been set based on the Monte Carlo expectation for the radial/angular differences between the projected ArgoNeuT track and the candidate MINOS

matched track. The definition of "best match" for events featuring multiple candidate matches is based on $\Delta r / \cos\theta$ between the projected ArgoNeuT track and the MINOS track/vertex. The cuts are set in order to reduce the chance of an ArgoNeuT track match to a spurious MINOS track. The angle between the ArgoNeuT track at its TPC exit position and the MINOS track is required to be less than 0.4 rad ($\sim$23°) and the difference between the projected-onto-MINOS ArgoNeuT track's radial position and the reconstructed MINOS track vertex is required to be less than 27 cm.

Figure 8.13 shows the differences between the projected ArgoNeuT track and the matched MINOS track in terms of angle and radial distance. The r and θ cuts imposed are clearly seen in the figures. These high-level cuts reduce the total CC ν_μ reconstruction probability by 2% compared to using no cuts beyond the low-level reconstruction requirements while increasing the signal purity substantially by removing the potential for mismatches. The spread in r and θ has contributions from the vertex/angular resolution of reconstructed MINOS tracks along with the exit position/angular resolution of ArgoNeuT tracks as well as physics (e.g. multiple Coulomb scattering). Note that there has been no background subtraction applied to the data plots and the errors reported are statistical only. A slight shift of 1° between simulation and data is apparent in the ArgoNeuT-MINOS angular difference plot. This discrepancy is most likely due to a slight coordinate-system mismatch between ArgoNeuT and MINOS, perhaps arising from a small rotation of the ArgoNeuT detector in installation. The effect has a <0.5% effect on the final differential cross section results, arrived at after adjusting the angular cut by $\pm 1°$ and recalculating the cross sections. The effect is small since the ArgoNeuT-MINOS matching requirements are quite loose, as exemplified in Figure 8.13.

Figure 8.14 shows the radial coordinate vertex for MINOS tracks that have been matched in simulation and data in the ArgoNeuT coordinate system. The coordinates reported correspond to the ArgoNeuT coordinate system, with the center of the TPC at $(\mathrm{X}, \mathrm{Y}, \mathrm{Z}) = (23.5, 0, 45)$. The X and Y distances between the projected ArgoNeuT track and the reconstructed MINOS track match are shown in Figure 8.15. Both data and reconstructed simulation are shown in the plots with statistical errors reported and no background subtraction to the data. Simulation and data are seen to agree to within about 1 cm. The X distribution is seen to be more narrow than the Y distribution in simulation and data as the X drift-time-based coordinate information in ArgoNeuT is more reliable and precise than the Y and Z wire-based coordinate information, as discussed previously.

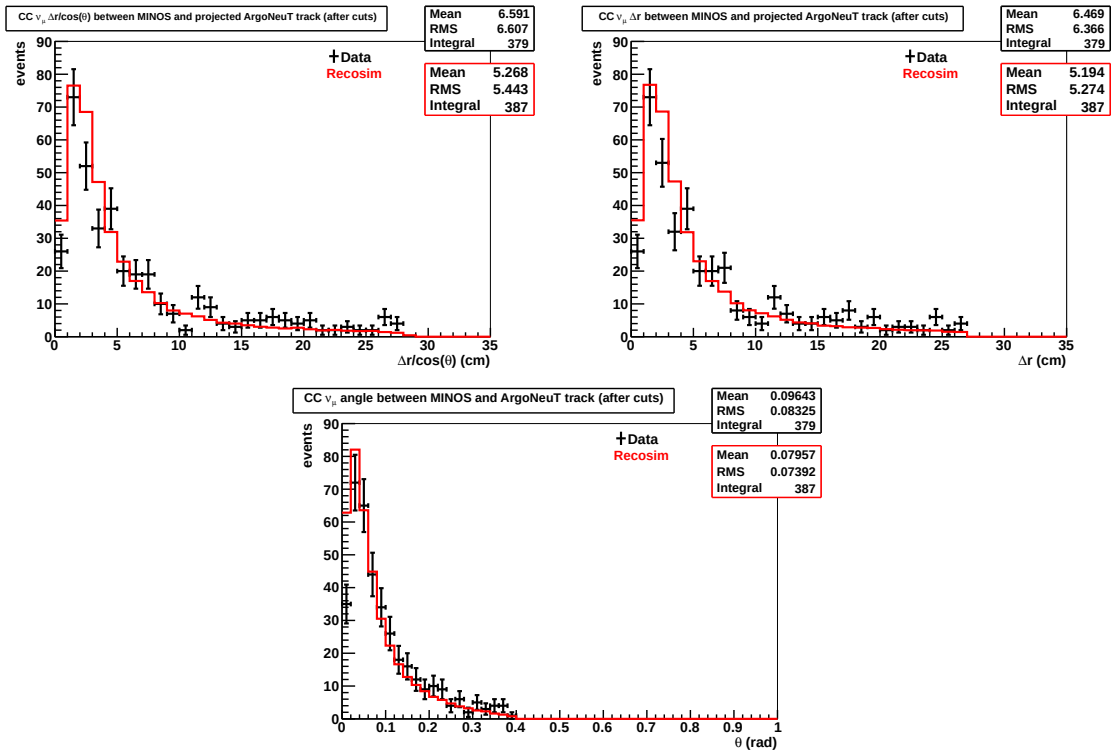

Figure 8.13: In terms of angle and radial position, the difference between the projected ArgoNeuT track and the MINOS track for matched events passing all cuts. No background subtraction has been applied to the data and the errors are statistical only.

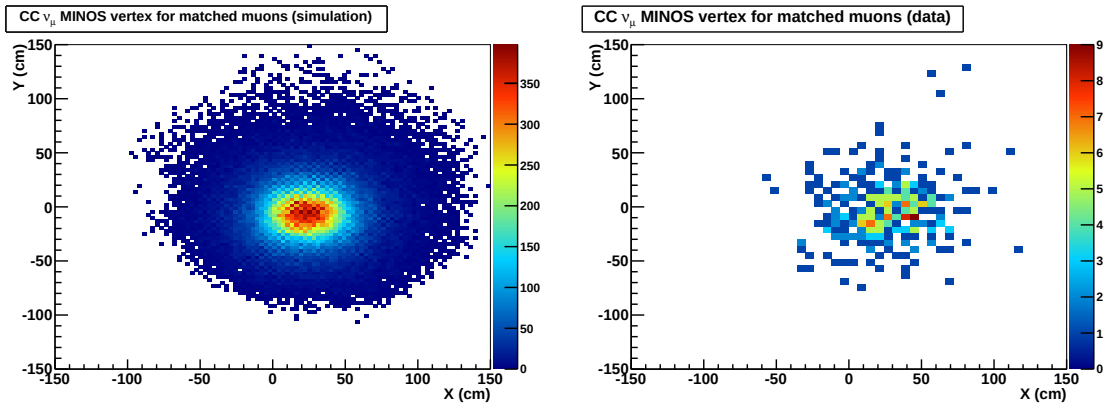

Figure 8.14: The MINOS radial coordinate vertex for all events passing cuts in simulation (left) and data (right).

The differences between the angular components of the matched ArgoNeuT and MINOS tracks are shown in Figure 8.16. Once again, the X angle distribution is more narrow than the Y and Z distributions for the reasons discussed above. A simulation-data disagreement of about 1° is especially apparent in the $\Delta\theta_x$ distribution. As discussed previously, the effect

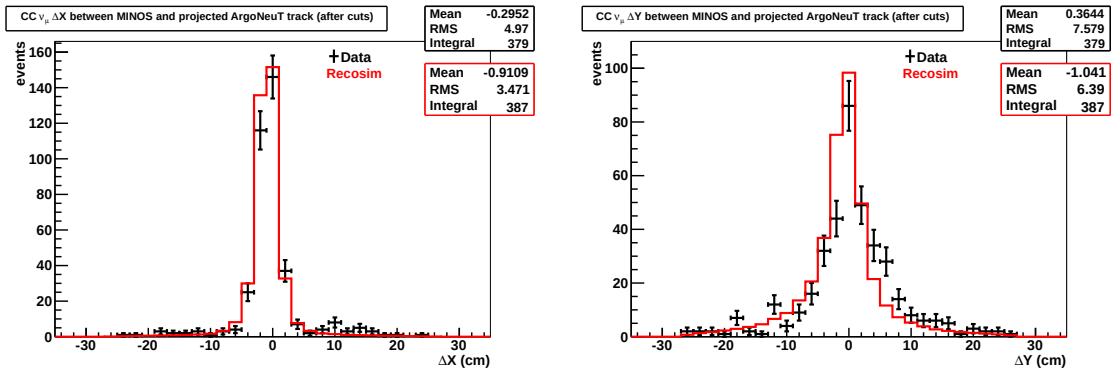

Figure 8.15: The distance in X (left) and Y (right) between the projected ArgoNeuT track and reconstructed MINOS track for matched events passing all cuts in data and (reconstructed) simulation. No background subtraction has been applied to the data and the errors are statistical only.

on the final result is minimal. Overall, the data and reconstructed simulation distributions (with statistical-only errors and without the 4-5% background subtraction) match to within about 1°.

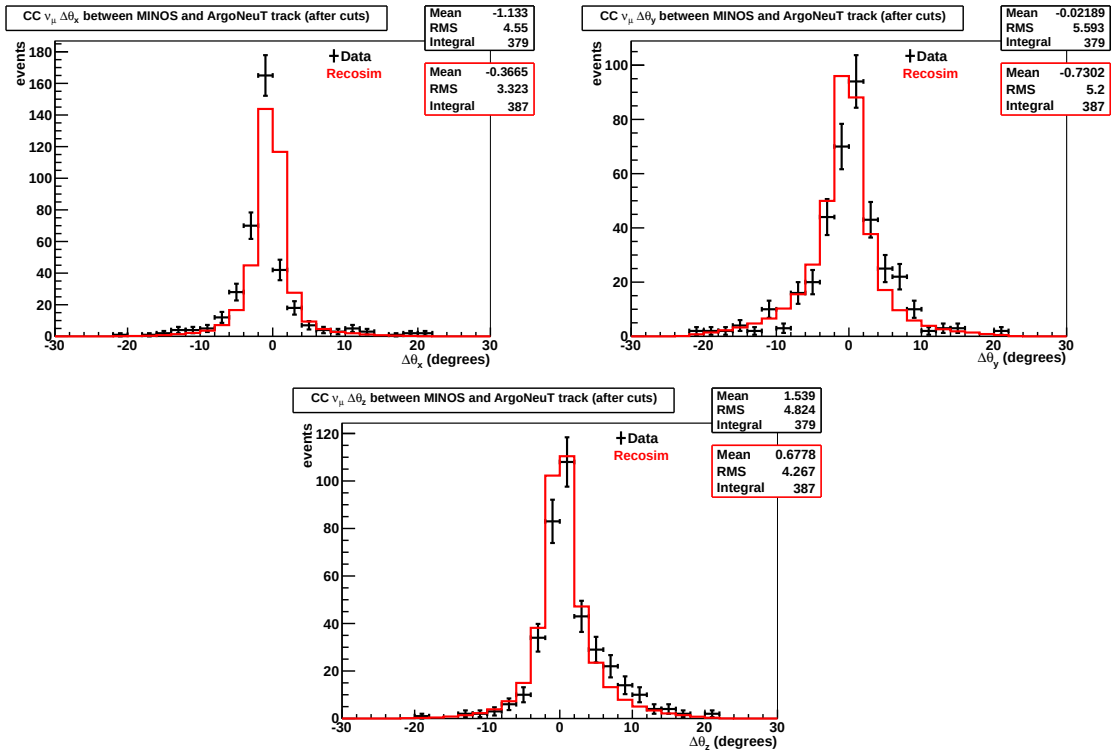

Figure 8.16: The angles between the exiting ArgoNeuT track and MINOS track for matched events passing all cuts. No background subtraction has been applied to the data and the errors are statistical only.

8.7.3 MINOS reconstruction requirements

A track in MINOS is considered as a potential match to a CC ν_μ track in ArgoNeuT as long as it is reconstructed. In order to enter the final after-cuts sample, however, the track is required to be reconstructed as negatively charged (corresponding to a μ^-). This cut takes place after the match has occurred. That is, both negatively and positively charged tracks are considered equally when attempting a track match. Also, the definition of "best" match in the case of multiply matched tracks is not dependent on the reconstructed charge of the track.

Notably, there are no MINOS track reconstruction goodness-of-fit requirements imposed. Also, the charge (q) cut merely requires that the track needs to have a reconstructed $\frac{q}{p}$ less than zero. A stricter cut (e.g. $\frac{q}{p}$<-0.3) was considered for this analysis but was not established. Notably, the MINOS-based cuts employed are not representative of those used by MINOS in their analyses.

The MINOS reconstruction cuts serve to single out the reconstructed track in question as a negatively charged muon. The effect of these cuts can be seen in Figure 8.17. The plots show the true neutrino energy distributions for the most relevant classes of neutrino interaction, normalized to the number of events expected given the analysis exposure. Before the cuts, the neutral-current and wrong-sign ($\overline{\nu}$) sample represents about 1/4 of the total. After cuts, the neutral-current and wrong-sign sample becomes negligible (2.2%) as there is no negatively charged muon to reconstruct by MINOS in such interactions. Note that all of the reconstruction cuts are applied in the plots displaying "after cuts" distributions, not just the MINOS reconstruction ones. A summary of the cuts and reconstruction requirements used in this analysis is presented in Table 8.5.

Fiducial volume requirements	3 cm $<$ X $<$ 44 cm (3 cm from boundaries) -16 cm $<$ Y $<$ 16 cm (4 cm from boundaries) 6 cm $<$ Z $<$ 86 cm [6(4) cm from up(down)stream boundary]
Matching requirements	$\theta <$ 0.4 rad $\Delta r <$ 27 cm
MINOS requirement	q $<$ 0

Table 8.5: The cuts imposed in the CC ν_μ analysis. Δr and θ refer to the radial difference between the projected ArgoNeuT track and the vertex of the MINOS track and the angle between the two tracks, respectively. q is the reconstructed charge of the track according to MINOS.

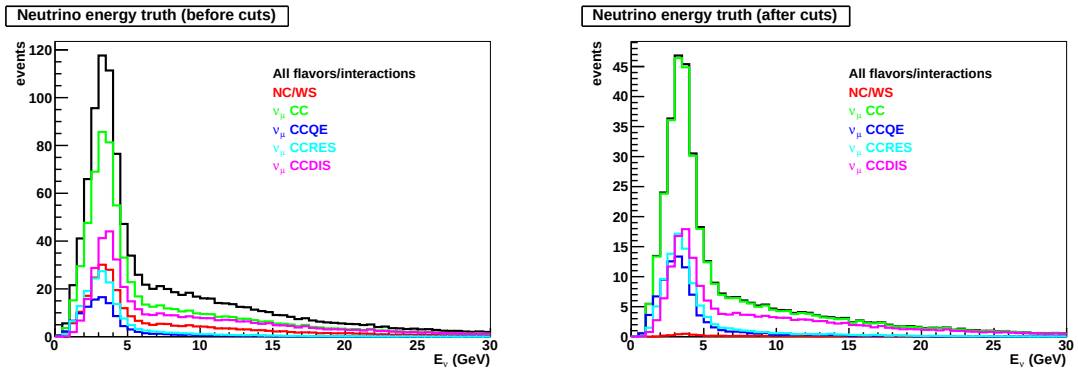

Figure 8.17: The true neutrino energy distribution before (left) and after (right) cuts according to Monte Carlo simulation. Note that the neutral-current (NC) and wrong sign (WS) background becomes negligible after applying the cuts as an ArgoNeuT-MINOS match is highly unlikely for a neutral-current event and MINOS rarely misreconstructs particle charge. "Wrong sign" refers to $\overline{\nu}_\mu$.

8.8 Efficiency

A measure of the probability to reconstruct a CC ν_μ event is necessary in order to turn the observed rate into the true rate required for a cross section measurement. The Monte Carlo event generation and detector model is necessary for this procedure. Detection efficiency and acceptance effects are considered together when discussing reconstruction probability. The efficiency on a per-bin basis is given by the simple equation:

$$\epsilon_i = \frac{\#\text{ of truly CC } \nu_\mu \text{ events reconstructed in FV after cuts}}{\#\text{ of MC-generated CC } \nu_\mu \text{ events in FV}} \ , \tag{8.25}$$

where "FV" stands for fiducial volume. The efficiency distribution is formed using true bins rather than reconstructed measurement bins in θ_μ/P_μ. That is, a bin i refers to the true, according to the Monte Carlo, value of the variable in question. The efficiency is assumed to be largely unaffected by the underlying neutrino physics of the event. In a scenario in which some aspect of the neutrino event generation is problematic or biased, for example, the numerator and denominator in the above equation will both see a similar effect and ultimately cancel.

Simulated neutrino events are generated outside of the fiducial volume of the TPC as well as inside. Events that are generated outside can enter the numerator in the above equation if the event vertex is misreconstructed and found to be inside the fiducial volume. Likewise, events that originate inside the fiducial volume can be reconstructed as being outside and reduce the numerator. Of course, the neutrino events generated outside

the fiducial volume have the same properties as those generated inside. Since the Monte Carlo generator accounts for both of the inside⇔outside scenarios in setting the numerator, the efficiency equation remains applicable in turning the per-bin measured rate into the efficiency-corrected true rate.

There are many components that contribute to a non-100% CC ν_μ reconstruction probability:

- Failing to consider a CC ν_μ as a candidate event.
- Failing to reconstruct a CC ν_μ muon due to ArgoNeuT vertex and/or track reconstruction inefficiencies.
- Failing to match a CC ν_μ muon to a MINOS track.
- A CC ν_μ event's muon does not enter or is not reconstructed by MINOS.

The CC ν_μ total reconstruction probability distributions as a function of outgoing muon angle (θ_μ) and momentum (P_μ) are shown in Figure 8.18. CC ν_μ events can fail to be reconstructed in ArgoNeuT for multiple reasons. A failure can occur in the case that the neutrino interaction vertex is not found. Such failures can transpire if the true vertex is confused with a delta ray's break from a parent muon or if the tracks in the event have a very small extent inside of the TPC. Also, an event with a true vertex in the fiducial volume can fail to enter the sample if either the vertex or the muon start position is reconstructed to be outside of the fiducial volume. Aside from the chance of this occurring due to intrinsic vertex position resolution and/or the possibility of a misreconstruction, the endpoint of a backwards traveling track can incorrectly be identified as the vertex. Such a misidentification can render the reconstructed vertex outside of the fiducial volume. Without considering the start position of the muon, a neutrino interaction vertex is found approximately 95% of the time for CC ν_μ interactions originating inside of the ArgoNeuT fiducial volume.

A CC ν_μ event's muon can also fail to be reconstructed or reconstruct poorly in the ArgoNeuT software. Failures can occur at any step in the reconstruction chain: hit finding, clustering (noise removal), line-finding and merging, and three dimensional track formation. Each reconstruction step depends on the previous step in order to succeed. At present, there is no feedback loop or mechanism in place in order to correct for a single step's

failure. The majority of failures are due to the three dimensional reconstruction steps which include space-point creation and track fitting. The two dimensional reconstruction steps are considered quite robust. Associating multiple two dimensional hits between planes that are potentially constant in drift time based on geometry alone, as is done here, can be problematic. Multiple track trajectories are possible and a one-to-one correspondence between hits on each plane is rare. Associating a single hit in one plane to multiple hits in another plane with a common time for three dimensional reconstruction is difficult. In the future, reconstruction will be improved with hit association and three dimensional track formation based on geometry, energy deposition consistency, and continuity. Also, instrumenting three or more wire planes, as in MicroBooNE, can help in breaking some of the degeneracies associated with tracks that are fairly constant in time as well as assist in three dimensional reconstruction in general.

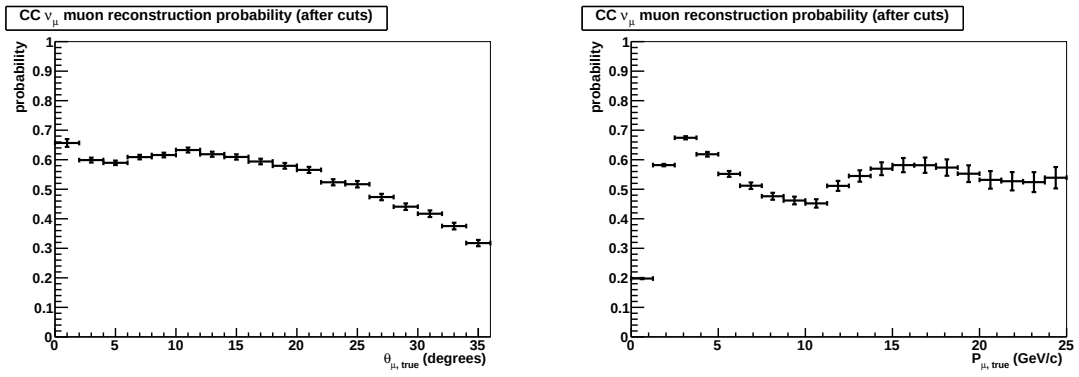

Figure 8.18: The total CC ν_μ reconstruction probability for events originating in the ArgoNeuT fiducial volume in terms of the true/simulated outgoing muon angle (left) and momentum (right).

CC ν_μ events with a muon that is not matched between ArgoNeuT and MINOS do not enter the final sample. A failed match can occur due to a reconstruction failure by either ArgoNeuT or MINOS. Furthermore, muons that stop in between ArgoNeuT and MINOS as well as muons that fail to enter the active region(s) of MINOS are not reconstructed. An attempt to deconstruct the reconstruction probability has been made. While Figure 8.18 shows the total CC ν_μ reconstruction probability, Figure 8.19 shows the reconstruction probability as a function of outgoing muon θ_μ and P_μ for CC ν_μ events featuring a negatively charged particle reconstructed by MINOS. This probability is referred to as the "ArgoNeuT+matching reconstruction probability" and is only relevant in the attempt to deconstruct the total reconstruction probability. The total reconstruction probability is

the only efficiency that is actually used in this analysis. The ArgoNeuT+matching reconstruction probability is not completely independent of MINOS as the matching efficiency is conditional upon MINOS vertex/angular resolutions. Also, the ArgoNeuT+matching reconstruction probability receives contributions from events featuring a negatively charged non-muon particle in MINOS. The ArgoNeuT-specific reconstruction probability is further reduced due to the fiducial volume cuts employed in this analysis. Events close to the edge of the detector but still inside the fiducial volume may only travel a few centimeters before leaving the active volume. These events are less likely to be reconstructed than more extended events featuring a longer track or tracks and negatively affect the probability of reconstruction.

The definitions of "Total reconstruction probability" and "ArgoNeuT+matching reconstruction probability" are given below.

$$\text{Total reco. probability} = \frac{\text{\# of completely reconstructed CC } \nu_\mu \text{ events in FV}}{\text{\# of CC } \nu_\mu \text{ events in FV}} \tag{8.26}$$

$$\text{ArgoNeuT + matching reco. probability} = \frac{\text{\# of completely reconstructed CC } \nu_\mu \text{ events in FV}}{\text{\# of CC } \nu_\mu \text{ events in FV with a q<0 particle reconstructed by MINOS}} \tag{8.27}$$

Note that these definitions place no restrictions on the kinematics of the outgoing muon. That is, all muon angles and momenta are considered when reporting the reconstruction probability numbers. The reconstruction probability in terms of muon angle drops as the angle of the muon increases. This behavior includes effects from 1) acceptance, the decreasing likelihood of the muon to be reconstructed in MINOS as the angle with respect to the beam axis increases, 2) high angle muons, which are more likely to have low momentum and never reach MINOS, and 3) ArgoNeuT's track reconstruction generally improving as the muon angle gets smaller.

The muon reconstruction probability behavior as a function of muon angle with respect to the initial neutrino has a number of noteworthy features. As stated previously, the reconstruction probability generally increases as the angle gets smaller. However, the probability is seen to decrease by a few percent going down from about 12°. This is a result of the space-point creation issue for tracks that are fairly constant in time. The probability is seen to increase again as the muon becomes parallel to the initial neutrino direction.

This effect can be explained by the downward angle of the neutrino beam with respect to ArgoNeuT/MINOS of $\sim 3^{\circ}$ compounded with the space-point issue.

The reconstruction probability in terms of the muon momentum behavior also has a number of interesting features. The reconstruction probability increases as the muon gains momentum and becomes more likely to enter and be reconstructed by MINOS until it peaks in the heart of the QE/RES regime at about 3 GeV/c (see Figure 8.2 for reference). The reconstruction probability is then seen to decrease as DIS takes over and track multiplicity increases, leading to possible reconstruction issues, usually involving three dimensional track matching, in ArgoNeuT. Then, the reconstruction probability is seen to increase with P_{μ} >10 GeV/c as the DIS muons straighten out and the possibility of a match with MINOS increases.

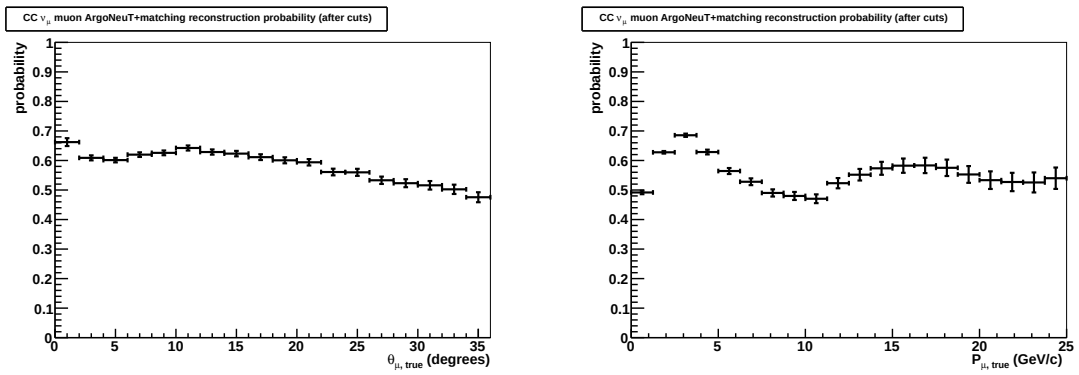

Figure 8.19: The outgoing muon angle (left) and momentum (right) ArgoNeuT+matching reconstruction probability for a CC ν_{μ} event originating in the ArgoNeuT fiducial volume. The "ArgoNeuT+matching reconstruction probability" is defined as the probability for a CC ν_{μ} event which leads to a negatively charged particle reconstructed by MINOS to enter the final sample.

Tables 8.6 and 8.7 show the reconstruction probabilities broken up in terms of event class. The probability for a CC ν_{μ} event originating inside the ArgoNeuT fiducial volume to be fully reconstructed, pass cuts, and enter the final sample is 49.5%. The probability for a QE ν_{μ} event, the simplest event topology in general, to enter the sample is 75.3%. The probability for a CC ν_{μ} event originating inside the ArgoNeuT fiducial volume–with a negatively charged particle reconstructed by MINOS–to be fully reconstructed, pass cuts, and enter the final sample is 59.4%. The ArgoNeuT reconstruction probabilities are seen to increase as the event topology becomes less complicated. The most complicated event topology in general, DIS, has an ArgoNeuT+matching reconstruction probability of 50.0% while the RES and QE probabilities are 67.1%, and 83.3%, respectively, as the events

become less and less convoluted and multiplicity decreases.

	Total reconstruction probability
ν_μ CC	49.5%
ν_μ CCQE	75.3%
ν_μ CCRES	57.5%
ν_μ CCDIS	40.4%

Table 8.6: The total reconstruction probability for the most relevant neutrino interaction channels. The total probability includes contributions from ArgoNeuT reconstruction, MINOS reconstruction, ArgoNeuT-MINOS track matching, angular acceptance, and energy acceptance.

	ArgoNeuT+matching reconstruction probability
ν_μ CC	59.4%
ν_μ CCQE	83.3%
ν_μ CCRES	67.1%
ν_μ CCDIS	50.0%

Table 8.7: The probability for an event originating in the ArgoNeuT fiducial volume which leads to a negatively charged particle reconstructed by MINOS to enter the final sample.

8.9 Measurement Resolution

Understanding the measurement resolution is necessary in order to estimate the systematic errors associated with finding the differential cross sections. Comparing Monte Carlo truth and reconstructed values of a number of variables also assists in determining the efficacy of the reconstruction and the validity of the simulation. An observed systematic disagreement between a true and reconstructed value can also help in determining if an unfolding procedure is necessary.

There are two relevant angles for the muon reconstruction in this analysis: the initial muon angle in the TPC at the neutrino interaction vertex and the initial reconstructed muon angle in MINOS. The initial in-ArgoNeuT reconstructed muon angle with respect to the transverse coordinate axes versus true distributions is shown in Figure 8.20. Just like in the case of the radial distributions of the projected ArgoNeuT track on the MINOS face as compared to the MINOS vertex, as well as the angular differences (see Figures 8.15 and 8.16), the X distribution is seen to be more narrow than the Y distribution. Note that these angles are with respect to the ArgoNeuT/MINOS coordinate system, rather than

with the initial neutrino direction. The downward angle of the neutrino beam with respect to the ArgoNeuT orientation and coordinate system is apparent in the two dimensional θ_y distribution. The neutrino beam is oriented downward (in the negative Y direction in the ArgoNeuT/MINOS coordinate systems) by about 3 degrees so that it can successfully reach the MINOS far detector in Minnesota. This slight offset is taken into account when reporting θ_μ, the angle of the outgoing muon with respect to the initial neutrino direction.

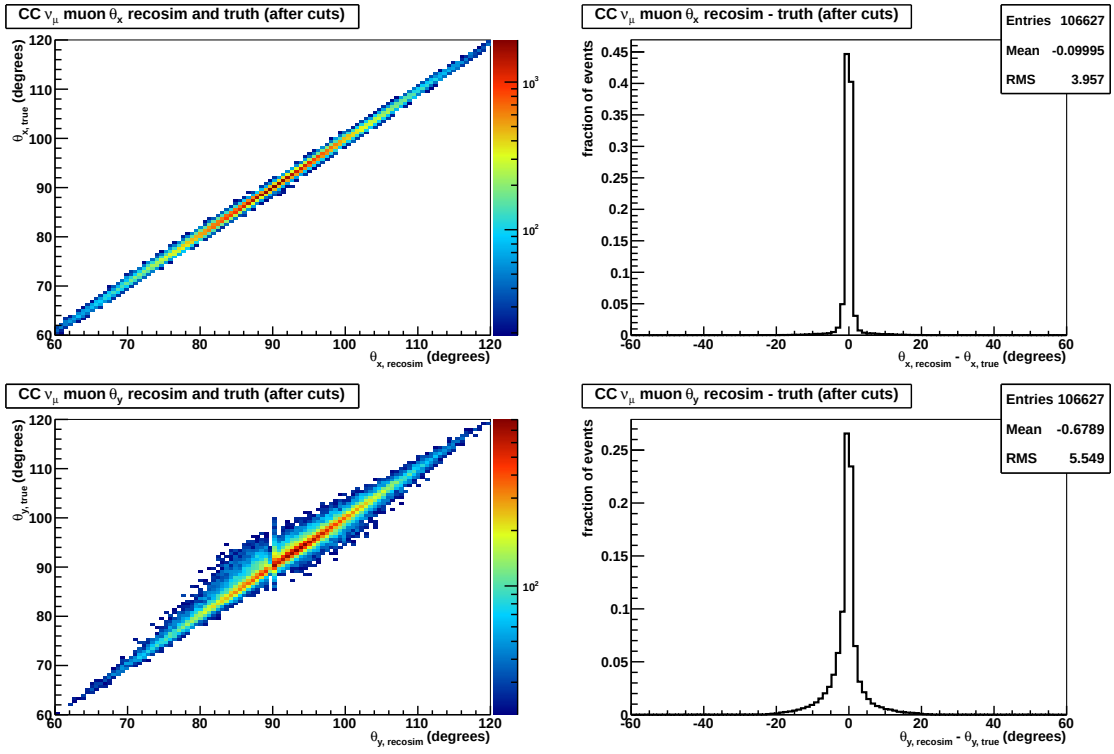

Figure 8.20: The reconstructed-by-ArgoNeuT muon angles with respect to the X (top) and Y (bottom) axes as compared to the true values at the interaction vertex for events that pass all cuts.

The three dimensional track fitter returns the position of the initial in-ArgoNeuT muon and the muon as it leaves the TPC. The initial and exiting muon angles are equal to each other in reconstruction. The truth-level distribution of the angle between the initial and exiting muon track for simulated CC ν_μ events is shown in Figure 8.21. The average difference between the two angles is less than one degree, largely coming from the muon multiple Coulomb scattering as it travels through the liquid argon medium.

Muon momentum reconstruction is accomplished using the MINOS near detector. In the case that a muon stops in MINOS, the energy deposited along its track is tabulated and used for the momentum measurement. In the case that the muon does not stop in MINOS, the

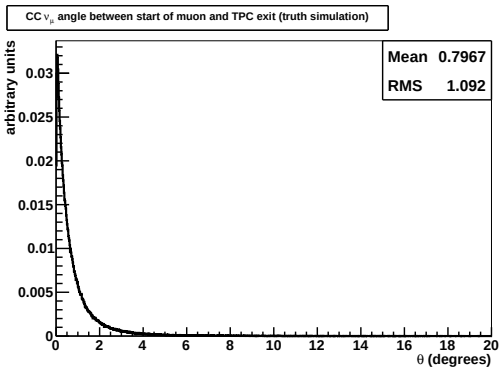

Figure 8.21: The angle between the initial muon track and the track as it exits the TPC in the truth simulation.

track curvature in the magnetic field is employed to make the momentum determination. Of course, the momentum as determined by MINOS is usually an underestimate of the initial, in-ArgoNeuT muon momentum. The muon loses energy as it travels through the ArgoNeuT TPC, a few centimeters of stainless steel in the form of the inner and outer ArgoNeuT cryostats as well as the ArgoNeuT bathtub, and the first (few) plane(s) of MINOS. The muon's lost energy (<200 MeV>) is accounted for using the Geant4-based detector simulation previously described. After matching an ArgoNeuT CC ν_μ-induced muon to a MINOS track in simulation, the distance between the creation point and MINOS vertex is recorded and the average energy loss of the muon in that distance is tabulated. For data and reconstructed simulation, the appropriate energy is added on to the MINOS-reconstructed muon energy for the initial muon momentum reconstruction, given a measured track distance traveled. A two dimensional histogram showing the distance traveled in between creation and the MINOS vertex as a function of energy lost for CC ν_μ-induced negatively charged muons is shown in Figure 8.22 (left). A Gaussian fit to the energy distribution inside each distance bin is applied. The mean and standard deviation of the fit inside each bin are shown in Figure 8.22 (right). A linear fit is applied to the points and the parameters of the line are used to determine the average energy loss of a particle that travels a known distance for the initial muon momentum determination. The distance between the reconstructed interaction vertex in ArgoNeuT and the reconstructed vertex in MINOS, given the reconstructed track parameters, sets the distance used in the determination. The efficacy of this method in accounting for the outside-of-MINOS energy loss can be seen in Figure 8.23. Before the correction, the initial muon momentum is underestimated by

an average of about 200 MeV, considering all tracks, vertices, and orientations. After the correction is applied, the reconstructed muon momentum is seen to match the true momentum well.

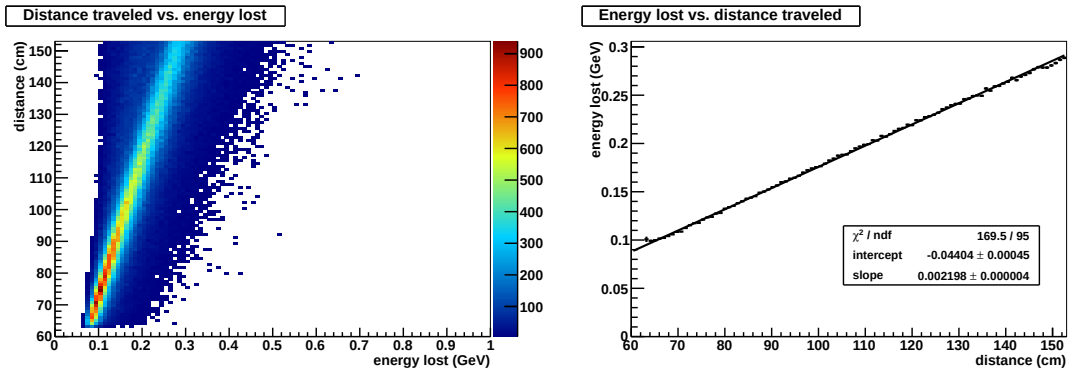

Figure 8.22: The energy lost by a negatively charged muon before it reaches MINOS. (Left) The distance between the muon origin and the point at which it reaches the back of the MINOS first plane as a function of energy lost. (Right) The mean energy lost in each distance bin. The linear relationship between distance and energy lost is extracted and used to account for the unmeasured energy loss of the muon in the determination of the initial muon momentum.

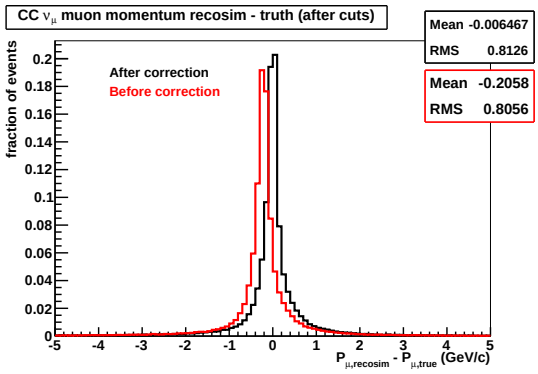

Figure 8.23: The difference between the true and reconstructed muon momentum for all muons that enter the final sample. The distributions before and after the outside-of-MINOS energy lost correction are shown.

This analysis calls for differential cross section measurements in terms of outgoing muon momentum and angle with respect to the initial neutrino direction. Two dimensional histograms showing the reconstructed and true muon angle in simulation can be seen in Figure 8.24. The vertical coordinate is representative of the relative number of events in each bin expected in arbitrary units. The reconstruction and truth distributions are seen to agree well in the measurement range reported here (0-36°). A set of similar plots for the muon momentum can be seen in Figure 8.25 spanning the measurement range of 0-25 GeV/c.

The muon momentum correction discussed above has been applied to the reconstructed momentum reported in the plots. The distributions are also seen to be largely symmetric around the reconstruction-equals-truth line. Based on the strong reconstruction and truth simulation agreement and symmetry in all measured θ_μ/P_μ bins, no unfolding procedure is applied to the measurements. This is discussed in more detail in Section 8.11.

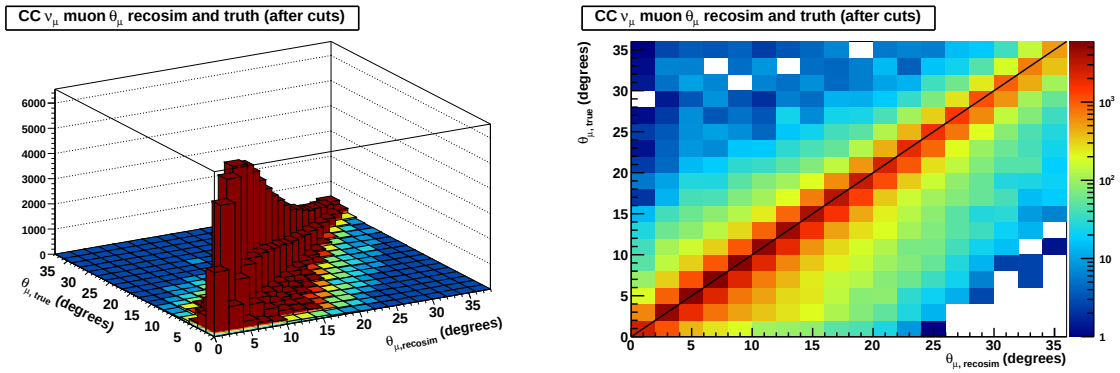

Figure 8.24: The reconstructed initial muon angle with respect to the initial neutrino direction, as compared to the true value at the interaction vertex for events that pass all cuts.

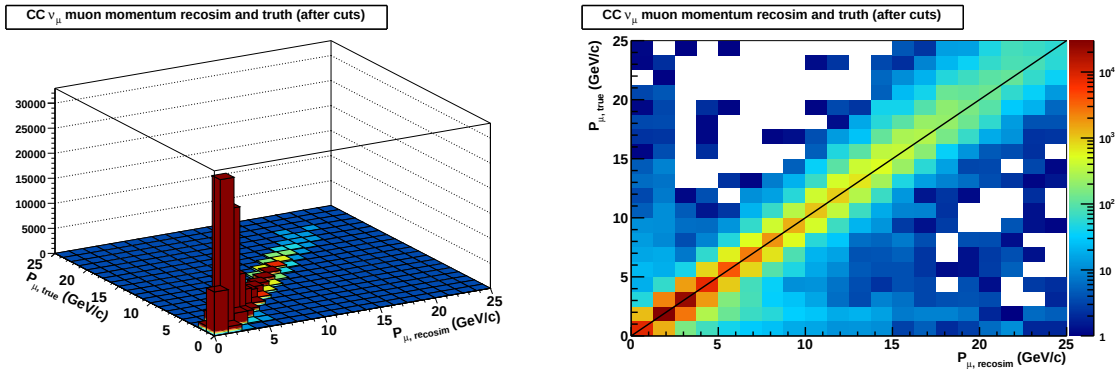

Figure 8.25: The reconstructed initial muon momentum as compared to the true value for events that pass all cuts. Note that the muon momentum as reconstructed by MINOS is corrected by a factor to take into account the particle's energy loss in ArgoNeuT and between ArgoNeuT and MINOS in order to arrive at the reported reconstructed momentum.

An example of the difference between the measured value of muon angle and the true value in a single true value bin is shown in Figure 8.26 (left). The fractional difference ($\frac{\text{reco}-\text{true}}{\text{true}}$ or $\frac{\Delta\theta_\mu}{\theta_{\mu,\text{true}}}$) for the $\theta_\mu = 28 - 30^\circ$ bin is shown along with a Gaussian fit to the distribution. The standard deviation extracted from the fit is considered the fractional measurement resolution in the bin and is utilized in the estimate of systematic error associated with the measurement scale discussed later. The angular resolution extracted from this

bin is seen to be 1.6°. A similar example appears for the muon momentum in Figure 8.26 (right). Just like in the case of muon angle, an estimate of the momentum resolution comes from a Gaussian fit to the fractional difference ($\frac{\text{reco}-\text{true}}{\text{true}}$ or $\frac{\Delta P_\mu}{P_{\mu,\text{true}}}$) distribution. In the case of the example $P_\mu = 10.0 - 11.25$ GeV/c bin, the momentum resolution is seen to be 7.4%. Three dimensional histograms showing $\frac{\text{reco}-\text{true}}{\text{true}}$ in terms of θ_μ/P_μ as a function of the true value of the variable are shown in Figures 8.27 and 8.28 for θ_μ and P_μ, respectively. The vertical coordinate is representative of the relative number of events in each bin expected in arbitrary units.

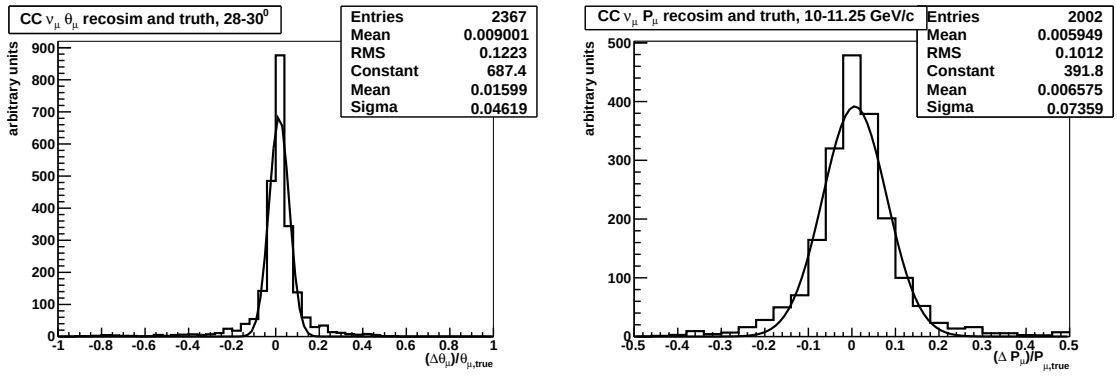

Figure 8.26: (Left) The fractional difference between the true and reconstructed muon angle for measurements in the 28-30° bin, as an example. The angular resolution corresponds to 1.6°. (Right) The fractional difference in momentum between the true and reconstructed muon for measurements in the 10.0-11.25 GeV/c bin, as an example. The momentum resolution corresponds to 7.4%.

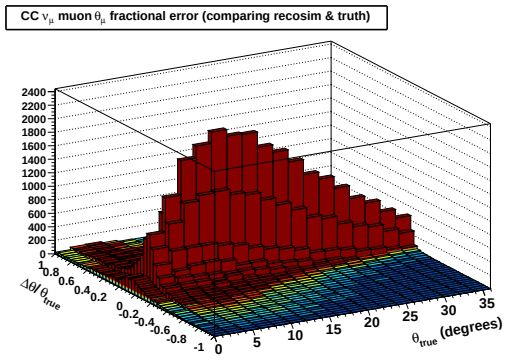

Figure 8.27: The difference in reconstructed and true value of θ_μ as a function of the true θ_μ.

As discussed above, the fractional error on the angle and momentum measurements is found with the distributions of the difference between the reconstructed and true values for each (θ_μ/P_μ) bin. A two-sided Gaussian is fit to the one dimensional distribution of

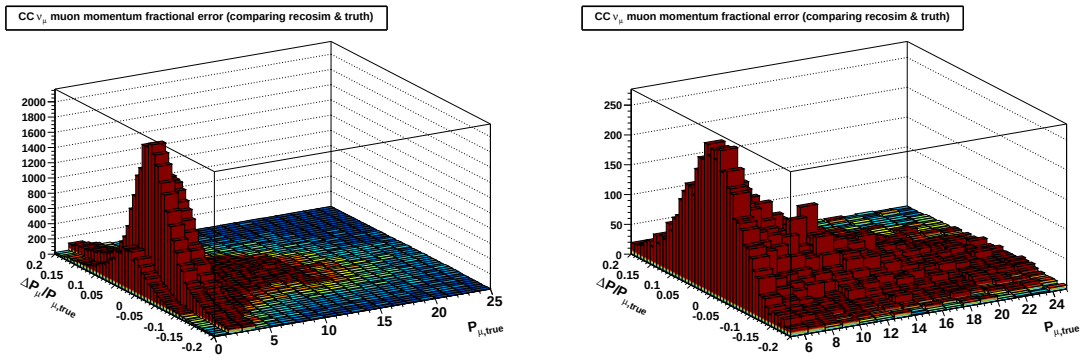

Figure 8.28: The difference between the reconstructed and true value of P_μ as a function of the true P_μ. Two plots are shown spanning slightly different ranges in order to elucidate the distributions at all values of P_μ.

$\frac{\text{reco}-\text{true}}{\text{true}}$, where the variable in question is either θ_μ or P_μ. The one sigma result of the fit is considered the fractional error of the measurement and is denoted as $\delta[\frac{\text{reco}-\text{true}}{\text{true}}]$. The results are shown in Figure 8.29. The outgoing muon angular resolution across most of the measurement range is about 1.5°. The momentum resolution is 5-10% for most of the measurement range. The momentum resolution is seen to largely improve as the momenta get smaller since such muons are more likely to stop in MINOS than their higher momentum counterparts. Recall that the momentum determination for stopped muons is more precise than the curvature-based reconstruction procedure applied for those that leave MINOS. The momentum resolution reported here should not be quoted as the actual MINOS muon momentum resolution. The definition of "track containment", used to decide the method by which the muon momentum is determined, has been altered from the nominal MINOS definition. Also, the unmeasured energy lost factor as well as the fact that these muons originate inside ArgoNeuT (rather than the MINOS fiducial volume) alter the just-MINOS muon momentum resolution. Note that the ∼5% error bars close to the edge of the P_μ distribution are negligible compared to the statistical uncertainty on those bins associated with data–although the errors are taken into account when quoting the final differential cross section measurement uncertainties.

8.10 Background

There are a number of backgrounds that can mimic a CC ν_μ event and enter the final, after cuts sample. For reference and as discussed in Section 8.12.6, 379 events pass all cuts in the

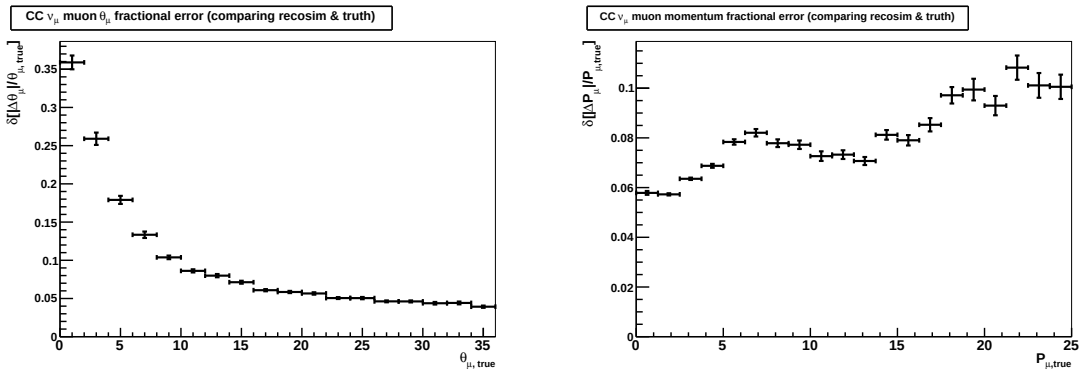

Figure 8.29: The fractional error in the CC ν_μ muon angle (left) and momentum (right) measurement bins. The values come from the standard deviation of a Gaussian fit to the one dimensional $\frac{\text{reco}-\text{true}}{\text{true}}$ distribution in each true bin.

analysis presented. The following scenarios can lead to an incorrect CC ν_μ identification:

- A pion from a neutral-current event originating in ArgoNeuT can lead to a track reconstructed as a negatively charged particle in MINOS.
- The charge of a wrong-sign ($\overline{\nu}_\mu$) neutrino event's muon originating in ArgoNeuT can be misreconstructed as negatively charged in MINOS.
- A neutral-current neutrino-induced track originating in ArgoNeuT can be matched with an unrelated through-going muon track in MINOS.
- A through-going muon that enters ArgoNeuT and is subsequently reconstructed by and matched to MINOS can be misreconstructed as having an interaction vertex inside of the ArgoNeuT fiducial volume.

8.10.1 Neutral-current and wrong sign contamination

A particle track from a neutral-current event in ArgoNeuT that is reconstructed as negatively charged in MINOS can potentially enter the CC ν_μ signal sample. A similar but slightly different scenario, with the background featuring a neutral-current event in ArgoNeuT matched to an unrelated muon in MINOS, is discussed in Section 8.10.2. The expected background contamination due to neutral-current and wrong sign events given the analyzed ArgoNeuT exposure can be seen in Figure 8.30. The neutrino event generator, detector model, Geant4-based simulation, and ArgoNeuT-MINOS reconstruction has been used to predict this background. As has been shown previously (see Figure 8.17), the

matching and MINOS reconstruction requirement cuts imposed almost completely eliminate the neutral-current and wrong sign contamination. About 8 neutral-current and wrong-sign events are expected to pass all cuts, making up about 2% of the expected final sample. As can be seen in the right side of the figure, the background contribution is dominated by low-momentum tracks. This makes sense as neutral-current-induced pions usually have much lower energy than their charged-current-induced muon counterparts.

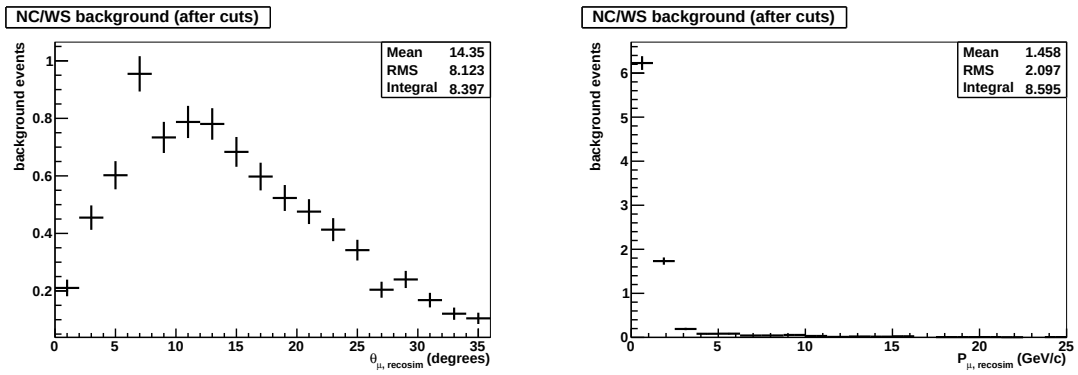

Figure 8.30: The expected number of neutral-current (NC) and wrong-sign (WS) background events that pass all selection criteria and enter the signal sample.

8.10.2 Mismatches

A track from a neutral-current event that is matched to an unrelated through-going muon can potentially enter the CC ν_μ signal sample. This is most likely to occur with a neutral-current-induced pion matched to a coincident through-going muon reconstructed by MINOS. The expected mismatch background for the analyzed ArgoNeuT neutrino-mode exposure is shown in Figure 8.31. About 4 such events are expected in the final analysis sample, contributing about 1% to the total. Notice that the reconstructed muon momentum is higher and is more evenly distributed across the bins than the distribution shown in Figure 8.30 as the MINOS-reconstructed tracks in this case are muons.

A number of scenarios exist in which a mismatch occurs between tracks in ArgoNeuT and MINOS. A CC ν_μ non-muon track can be matched to the correct muon track in MINOS. Similarly, a CC ν_μ-induced muon can be matched to the incorrect track in MINOS. The incorrect track can be any number of particles that reconstruct as negatively charged, including through-going muons and neutrino-induced pions. In the case that the event originating in ArgoNeuT was a CC ν_μ event, the event is not considered a background–

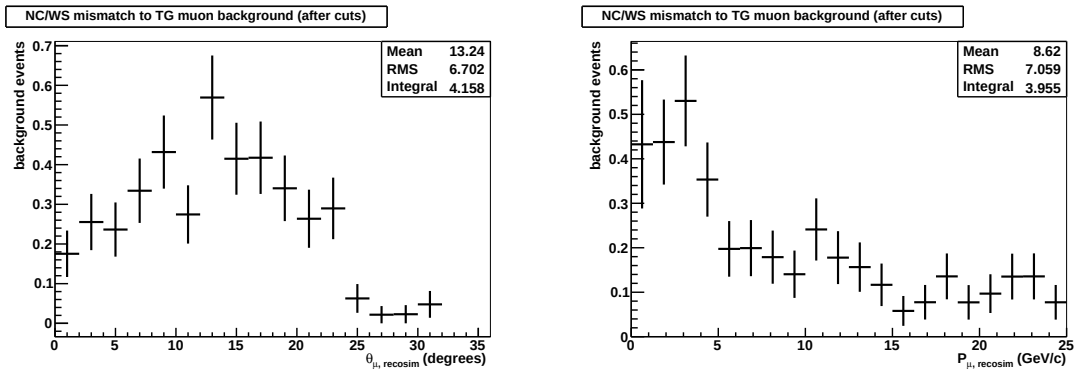

Figure 8.31: The expected number of neutral-current (NC) and wrong-sign (WS) background events matched to through-going muons in MINOS that pass all selection criteria and enter the signal sample.

although the mismatch usually negatively affects the θ_μ/P_μ measurement resolution. Such mismatched events are accounted for in the measurement resolution estimates. The muon angle and momentum distributions for CC ν_μ events that are matched to an unrelated through-going muon in MINOS are shown in Figure 8.32. The distributions have been normalized to the number of such events that are expected given the ArgoNeuT neutrino-mode exposure. About 4 mismatched (but non-background) events are expected in the final analysis sample and only negligibly contribute to the θ_μ/P_μ measurement resolution.

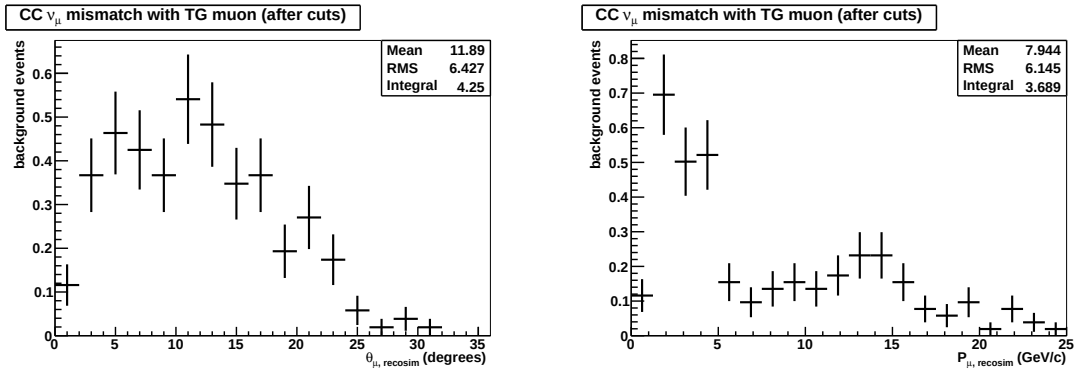

Figure 8.32: The expected number of CC ν_μ events that are matched to an unrelated muon in MINOS. These events are not considered a background because they are CC ν_μ events. However, they do affect the muon angle and momentum measurement resolutions.

8.10.3 Through-going muons

The through-going muon simulation, based on the measured rate and distribution of muons collected by MINOS during the physics run (discussed in Section 6.4), is employed in or-

der to determine the expected number of through-going muons that are reconstructed by ArgoNeuT and MINOS and enter the sample. The simulated through-going muons that enter the TPC, ionize argon atoms, and eventually induce signals on the simulated wires are reconstructed by ArgoNeuT and passed to the MINOS reconstruction software. That is, the simulated through-going muons are allowed to enter the Monte Carlo sample in order to obtain an estimate of this background contamination. The expected number of through-going muons that actually pass through ArgoNeuT is arrived at after correcting the MINOS reconstructed muon rate for the MINOS-specific reconstruction probability in bins of muon angle and momentum separately. This is necessary as the flux of through-going muons from ArgoNeuT is based on the MINOS data after reconstruction. This efficiency correction is distinct from the "total reconstruction probability" (efficiency) correction that is applied to the data after background subtraction. The expected through-going muon contamination in the signal sample is shown in Figure 8.33. The statistics are rather low for this background estimate as the prediction is based on an *in-situ* measurement. Oversampling from the collected through-going muon data was avoided. There are about 5 through-going muon events expected to be reconstructed as CC ν_μ events by ArgoNeuT-MINOS in the final analysis sample, contributing about 1% to the total.

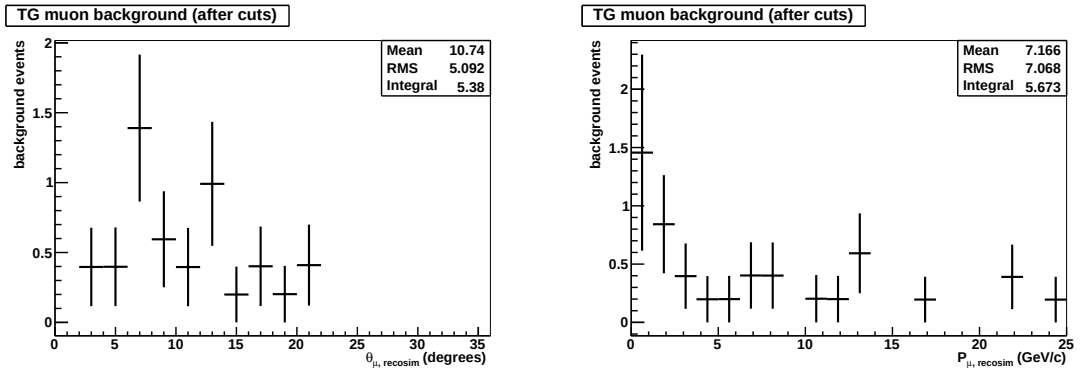

Figure 8.33: The expected number of through-going (TG) muon background events that pass all selection criteria and enter the signal sample.

8.10.4 Background summary

After all of the cuts are applied to the signal candidates, the total CC ν_μ sample (379 events) is 95.5% pure. Purity is defined simply as:

$$\text{Signal (CC } \nu_\mu\text{) purity} = \frac{\text{\# of true CC } \nu_\mu \text{ events that pass all cuts}}{\text{\# of events that pass all cuts}} \tag{8.28}$$

Approximately 2.2% of the sample is composed of neutral-current/wrong sign events. Through-going muon background makes up 1.4% of the sample and the remaining 1.0% of background events come from true neutral-current events in ArgoNeuT that have been incorrectly matched to through-going muons in MINOS. The probability for a CC ν_μ event that originates in the fiducial volume to be reconstructed by ArgoNeuT and MINOS and enter the signal sample after all cuts is 49.5%, as discussed in Section 8.8. This number is a combination of inefficiencies due to acceptance, ArgoNeuT vertex and track reconstruction, and MINOS track reconstruction. Inefficiencies due to acceptance include muons that lose all their energy before reaching MINOS and muons that do not enter the active region of MINOS due to (e.g.) a high angle. The purity, reconstruction probability, and background contributions are summarized in Table 8.8.

Signal (CC ν_μ) reconstruction probability	49.5%
Signal (CC ν_μ) purity	95.4%
NC/WS background contamination	2.2%
TG muon background contamination	1.4%
NC match w/ TG muon background contamination	1.0%

Table 8.8: The reconstruction probability and purity of the CC ν_μ sample along with the expected level of background contamination from various sources. The background estimate reported in this table is made before the parameterization of the background, although the differences are negligible.

The effect of several reconstruction cuts on the total reconstruction probability and the background contamination can be seen in Table 8.9. The muon start position fiducial volume cut, MINOS-based negatively charged particle reconstruction, and high-level ArgoneuT-MINOS track matching requirements are studied. The combination of these three cuts brings the total signal purity from 77.6% to 95.4%. The requirement that the muon start position be inside the fiducial volume is seen to reduce the through-going muon contamination of the signal by a factor of 3 as the extra requirement assists in determining whether the event originated inside ArgoNeuT or not. The requirement that the track in question be reconstructed as negatively charged by MINOS reduces the wrong-sign contri-

bution to the sample by a factor of 4-5 and the high-level MINOS matching requirements increase signal purity by 2.8%. The three cuts combined bring the signal reconstruction probability from 58.4% to 49.5%.

	no cuts	μ	μ+q	μ+q+M
Signal (CC ν_μ) reconstruction probability	58.4%	53.7%	51.2%	49.5%
Signal purity	77.6%	81.8%	92.6%	95.4%
NC/WS contamination	12.8%	13.2%	2.8%	2.2%
TG muon contamination	6.8%	2.3%	2.0%	1.4%
NC match w/ TG muon contamination	2.7%	2.6%	2.6%	1.0%

Table 8.9: The effect of each cut on the signal efficiency/purity and background. "μ" refers to the requirement that the muon start position be inside the fiducial volume, "q" refers to the requirement that the track be reconstructed as negatively charged by MINOS, and "M" refers to the "high-level" ArgoNeuT-MINOS track matching requirements.

The total number of background events expected in bins of outgoing muon angle and momentum from all contributions and their parameterizations are shown in Figure 8.34. A parameterization is employed for the to-be-subtracted background estimate. There is a significant level of statistical error in the background expectation as a fraction of the estimate is based on a statistics-limited *in-situ* measurement. The parameterization works to largely remove the effects of statistical fluctuations in the relevant measurement bins. As the expected background level is so small (4.5%) compared to signal, the differential cross section results are minimally sensitive to the lack of statistics that seed the parameterized background prediction. About 18 background events are expected to have entered the signal-like sample. The distribution of background events in θ_μ is parameterized using a three parameter Landau fit (discussed in Section 7.7.1). The distribution of background events in P_μ is parameterized using a three parameter shifted power fit of the form $a(x - c)^b$. The background histograms corresponding to the parameterizations with one sigma fit errors are shown in Figure 8.35. The fits have been produced with each bin given equal weight. These parameterization-based background histograms are subtracted directly from the raw signal histograms in order to arrive at the background-corrected rates. The reconstruction probability (efficiency) correction is applied after background subtraction as in Equation 8.21.

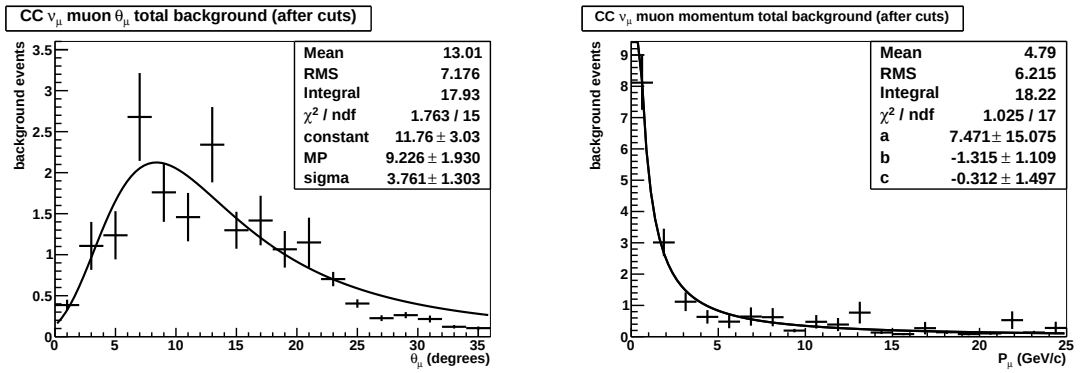

Figure 8.34: The total background expected. There are contributions from through-going muons, NC/WS events, and NC events that are matched to through-going muons in MINOS.

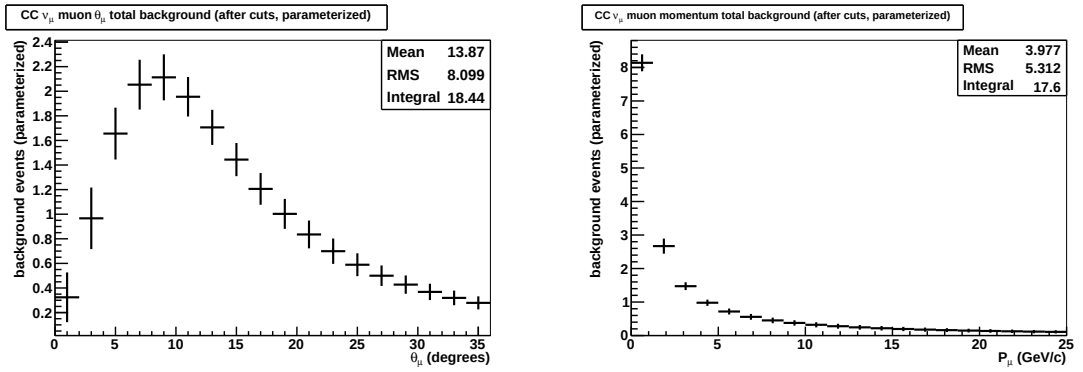

Figure 8.35: The parameterized total background. These distributions are subtracted from the raw rate to arrive at the background-corrected rate.

8.11 Unfolding

In an attempt to turn a reconstructed variable's distribution into the underlying true distribution, unfolding techniques are often used. Unfolding is meant to remove the effects of limited detection resolution, detection/reconstruction biases, and acceptance in order to uncover the underlying physics and more directly compare a particular measurement to others. The influence of each of these issues can be studied with the simulation and reconstruction of Monte Carlo events under the assumption that the Monte Carlo model of the detector and detector response are accurate.

The previously shown true versus reconstructed θ_μ/P_μ distributions (Figures 8.24 and 8.25) are measures of the departure between true and reconstructed measurement bins and the effect of detection/reconstruction biases. These two dimensional distributions are simply turned into Monte Carlo bin migration matrices by normalizing each true row to

one. Each element of the normalized matrix is then equal to the probability that a true value represented by bin i will have a reconstructed value corresponding to bin j. A bin migration matrix acts to turn the true distribution into the reconstructed distribution via:

$$R_j = \sum_i B_{ji} T_i \ , \tag{8.29}$$

where R is the distribution of reconstructed bins, B is the bin migration matrix, and T is the distribution of truth bins. Unfolding is meant to uncover the truth distribution, given a reconstructed distribution and an unfolding matrix. The presumed truth distribution can be arrived at with:

$$P_i = \sum_j M_{ij}(O_i - S_i) \ , \tag{8.30}$$

where P_i is the presumed truth distribution, O_i is the observed distribution, S_i is the spurious/background distribution, and M_{ij} is the unfolding matrix. Performing the inverse of the bin migration matrix, B_{ji}^{-1}, seems like a good choice for M_{ij} and recovering the distribution of true values. Despite being simple to construct and unbiased towards the Monte Carlo truth distribution, this technique is known to have problems and is especially sensitive to statistical fluctuations [206].

A number of well behaved methods of unfolding exist. The Bayesian-based unfolding method is discussed here [206, 207]. Bayes' theorem is given by:

$$P(A|B) = \frac{P(B|A)P(A)}{P(B)} \ , \tag{8.31}$$

where $P(A|B)$ is the probability of a true value A being measured as B and $P(A)$ is the probability of A to occur. The bin migration matrix discussed above represents the probability that a true value represented by bin i will have a measured value corresponding to bin j and can be related to Bayes' theorem with

$$P(B_j|A_i) = \frac{P(A_i|B_j)P(B_i)}{\sum_k P(A_i|B_k)P(B_k)} \tag{8.32}$$

Instead of asking about the measurement expectation given a true result, we can ask: What is the probability that a given/prior measured value came from a true value? This is accomplished by replacing A with B and setting the appropriate indices in the equation above. Rather than normalizing each true row in the truth versus reconstructed distribution

to one as in the construction of the bin migration matrix, we normalize each reconstructed column to one and call the resulting matrix M_{ij} as it satisfies Equation 8.30. The former is independent of the truth distribution and the latter is dependent on (and biased towards) the truth distribution. M_{ij} gives the probability that a measured value represented by bin j came from a true value corresponding to bin i. This matrix is sensitive to the shape of the purported true distribution in each reconstructed bin column. That is, the contributions from each reconstructed bin in setting the eventually reported measurement value are dependent on the underlying true distribution.

Unfolding matrices (based on Figures 8.24 and 8.25) for the outgoing muon angle and momentum are shown in Figure 8.36. Acting to turn the measured signal and predicted background into a distribution that is closer to the underlying true distribution, the matrices can be inserted into the differential cross section equation via:

$$\frac{\partial\sigma(u_i)}{\partial u} = \frac{\sum_j M_{ij}(N_{\text{measured},j} - N_{\text{background},j})}{\Delta u_i \epsilon_i N_{\text{targ}} \Phi} \tag{8.33}$$

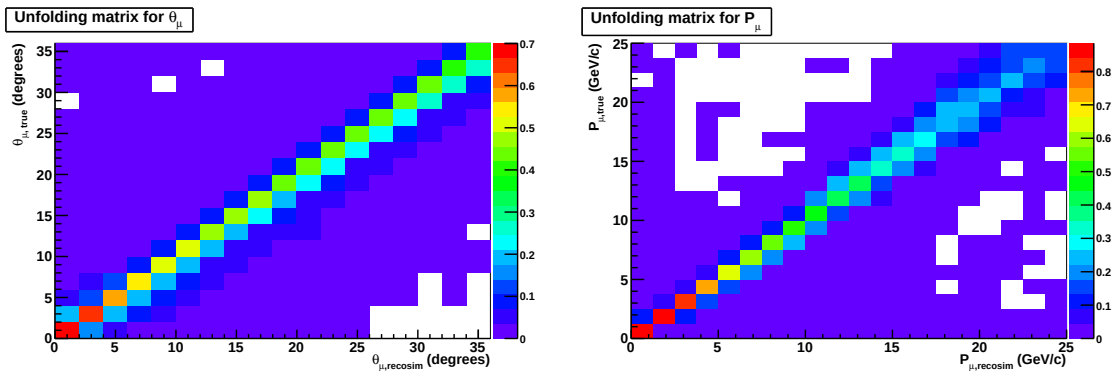

Figure 8.36: The unfolding matrices for the outgoing muon angle and momentum.

The pre- and post-unfolding outgoing muon angle and momentum distributions are shown in Figure 8.37. No efficiency correction has been applied and the data are background subtracted before the unfolding procedure takes place as in Equation 8.33. Although the unfolding has a negligible effect on the P_μ distribution and high-values of θ_μ, the procedure is observed to enhance the weights of the bins in low-θ_μ. However, the statistical errors in this region are large. In fact, the pre-unfolded and post-unfolded statistical errors overlap in every θ_μ/P_μ bin reported.

In spite of this discussion, unfolding is not performed for the analysis presented here, except as a measure of the systematic error due to the measurement scale and resolution as

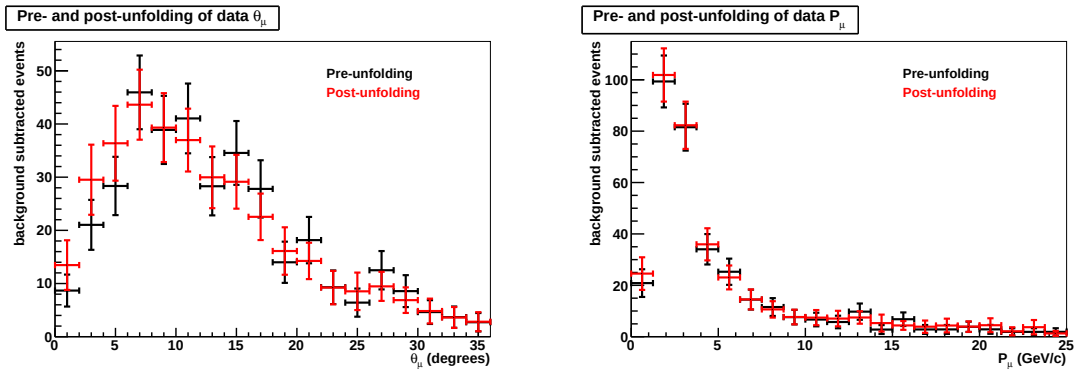

Figure 8.37: The pre- and post-unfolding outgoing muon angle and momentum distributions. Statistical-only error bars are shown.

discussed later. Aside from a number of disadvantages to unfolding, as discussed below, the large statistical error bars present in this measurement largely mask any possible advantages of unfolding.

The unfolding procedure enhances the smoothness of the measured distribution. Post-unfolding, each reported measurement bin is a culmination of the weights of neighboring reconstructed bins in the case that the resolution is not much smaller than the bin width and the reconstruction/detection bias is small, as is the case here. That is, the weights of adjacent bins on either side of a central bin each contribute to the weight of this central bin, usually reducing the difference in amplitude between adjacent bins. An example of this is provided in Figure 8.37 (left). The pre-unfolded $\theta_\mu = 6 - 8^\circ$ bin is seen to be $>1\sigma$ above each of its nearest neighbors. As resolution effects lead to these neighbors contributing to the central bin according to the unfolding matrix, the post-unfolded central value of the bin decreases significantly and the distribution becomes more smooth. This smoothness enhancement is an apparent downsizing of the statistical errors in the distribution. The effect can make error bars difficult to interpret, especially in the case of statistics-dominated uncertainty, as is the case for the measurements reported here.

Aside from being inherently biased towards the inferred true Monte Carlo distribution, a lack of Monte Carlo statistics in the off-diagonal terms of the unfolding matrix can enhance the measurement error. These issues along with the simple statement that these measurements' comparatively large error bars dampen any possible unfolding advantages allow us to proceed without unfolding. Subsequent ArgoNeuT measurements that are less dominated by statistical error may find an unfolding procedure advantageous and worthwhile.

8.12 Error Analysis

The sources of statistical and systematic error in the CC ν_μ differential cross section measurement in outgoing muon angle and momentum are discussed below. The analysis presented is largely statistics-limited for most measurement bins. However, there are a number of sources of systematic errors that have been taken into account. These are described below.

8.12.1 Flux

The error associated with the integrated flux from 3-50 GeV is taken directly from Reference [123]. The errors in each reported energy bin are considered correlated and the total error on the integrated flux is the sum of the error in each energy bin of Table 8.1, after accounting for the variable bin width. The true correlation between the errors is of little consequence as the flux error in the 0-3 GeV region dominates the 0-50 GeV flux uncertainty. The fractional error on the integrated flux from 3-50 GeV is 6.6%. The Monte Carlo prediction for the flux in the 0-3 GeV region at the ArgoNeuT location as well as its estimated fractional error of 35% are supplied by MINOS [205]. After adding the flux errors in the two energy bins in quadrature, the total fractional error in the full 0-50 GeV region is 15.6%. The two bins are considered uncorrelated as the 0-3 GeV bin relies solely on the Monte Carlo prediction, based on a beamline model and parent meson production, while the 3-50 GeV flux prediction comes from the "low-ν" method discussed above with a slight dependence on measured cross section.

8.12.2 Number of targets in the fiducial volume

The size of the ArgoNeuT TPC's active volume is 47x40x90 cm^3, where the active volume refers to the liquid argon enclosed by the walls of the TPC, the cathode, and the shield plane. The Y and Z active volume dimensions are measured with an uncertainty of 1 mm. The length of the X dimension considered in the analysis (e.g. for setting the fiducial volume) is measured in units of time. The electron drift velocity, measured at 1.56$\pm$0.03 mm/μs, along with the measured X dimension length of 47 cm (with measurement uncertainty 1 mm) go into setting the final X dimension uncertainty of $\sim$1 cm. Combining the uncertainties in all dimensions, we arrive at the uncertainty on the number of targets of 2.2%. The fractional uncertainty on the active volume is assumed to be the same as the fiducial volume. The

uncertainties associated with the density of liquid argon, Avogadro's constant, and the molecular weight of argon are considered negligible.

8.12.3 Measurement scale

The fractional errors on the θ_μ/P_μ determination in each measurement bin are provided in Figure 8.29. An estimate of the systematic error due to measurement resolution is arrived at by applying the unfolding technique discussed above with these fractional errors as an input. Recall that the unfolding matrix M_{ij} gives the probability that a measured value came from a true value, based on an underlying inferred truth distribution of the variable in question. That is, the unfolding matrix sets the likelihood of a migration from the postulated true value of a variable to the reconstructed value. We consider the case of a shifting scale in finding the systematic error associated with measurement resolution. A new true versus reconstructed bin migration matrix with each reconstructed column normalized to one is created after altering the reconstructed values in each bin by minus one sigma, where sigma comes from the measurement resolution estimate found and displayed in Figure 8.29. In the case that the shift causes the new reconstructed value to take on an unphysical meaning, the weight is assigned to the physical bin adjacent to the unphysical bin in question. For example, if the shift takes a reconstructed P_μ to a value less than zero, the shifted event is assigned to the 0-1.25 GeV/c bin. A new unfolding matrix is formed with these modified values. The same procedure is applied after altering the reconstructed values in each bin by plus one sigma. The unfolding matrices for each $\pm 1\sigma$ case are shown in Figure 8.38 for the outgoing muon angle and Figure 8.39 for the outgoing muon momentum. The central value unfolding matrices have been shown previously in Figure 8.36. The unfolded background corrected rate is then calculated for the three cases, where the third case utilizes the unaltered unfolding matrix and is considered the central value of the measurement for the purposes of determining the measurement scale systematic error. The effect of the measurement scale adjustments can be seen in Figure 8.40. The systematic uncertainty on the differential cross section due to the measurement scale is set equal to the largest fractional deviation from the central value, due to either the one sigma increase or one sigma decrease, in each θ_μ/P_μ bin. That is, the largest fractional increase or decrease from the central value is conservatively set equal to the systematic uncertainty on a per-bin basis.

Although the unfolding procedure is not employed to set the central values of the actual

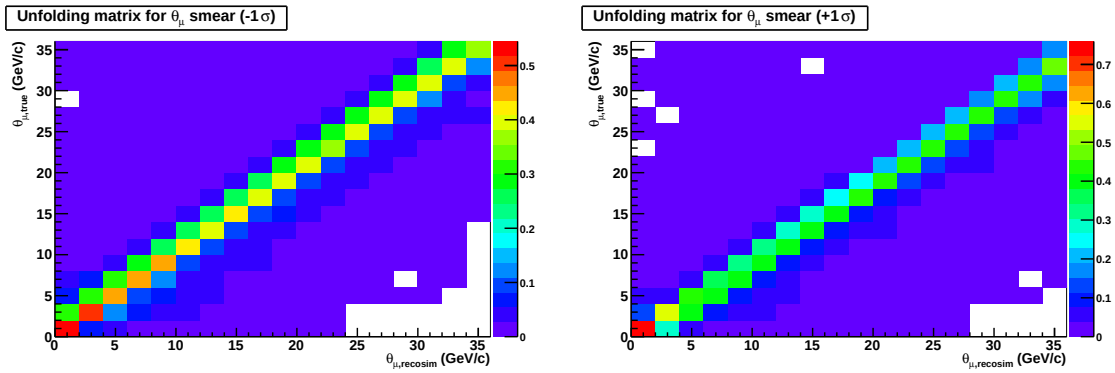

Figure 8.38: The θ_μ unfolding matrices for setting the measurement resolution systematic uncertainty. The matrices have been created after altering the reconstructed values in each bin by minus one sigma (left) and plus one sigma (right), where sigma comes from the measurement resolution reported in Figure 8.29.

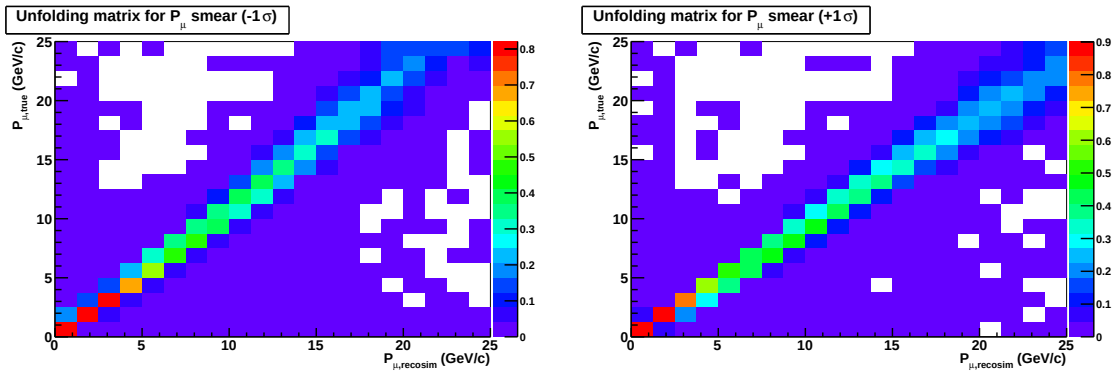

Figure 8.39: The P_μ unfolding matrices for setting the measurement resolution systematic uncertainty. The matrices have been created after altering the reconstructed values in each bin by minus one sigma (left) and plus one sigma (right), where sigma comes from the measurement resolution reported in Figure 8.29.

differential cross section measurements, the procedure has been used as an estimate of the measurement scale error. Only the fractional deviation from a measurement's central value as determined by the unfolding method is used, however. The process for setting the error is less dependent on the inferred true distribution as it only considers the relative deviation from a central value. The central value of the true distribution could change without affecting the extracted error estimates.

As an alternative to the procedure described above, one can recalculate the differential cross section after adjusting the values of the Monte Carlo reconstructed θ_μ/P_μ by $\pm 1\sigma$, where sigma once again comes from the measurement resolution as determined above. This procedure is similar to the unfolding-based one described but is naively unaware that a

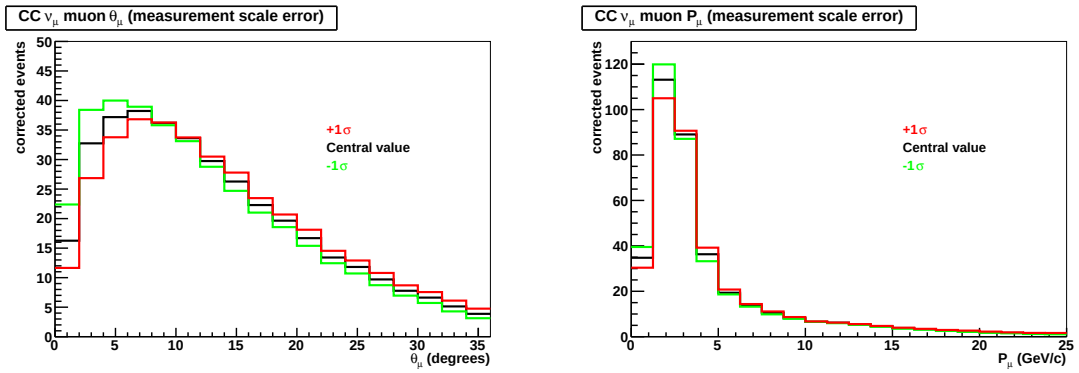

Figure 8.40: The effect of adjusting the muon angle/momentum by plus and minus one sigma from the central value, where sigma comes from the measurement resolution on a per-bin basis. The central value represents the unfolded background subtracted distribution of reconstructed Monte Carlo events. The systematic error associated with the measurement scale is conservatively taken as the largest fractional deviation from the central value in each bin.

true value can distribute itself across multiple reconstructed bins. Determining the effect of a sliding measurement scale with unfolding takes into account this extra information. Instead of just pushing a reconstructed value from one bin to another according to the previously determined measurement resolution, the unfolding method uses this resolution to redistribute the entire set of reconstructed bins that correspond to a single true bin. This is employed as a more accurate method of finding the systematic error due to the measurement scale, although the two methods provide similar results.

Variations due to the measurement scale shift are especially apparent in the bins at the edge of each plot (the θ_μ=0-2° bin and the P_μ=0-1.25 GeV/c bins) as these bins only receive contributions from one direction when adjusting the measurement scale. That is, the weights of bins adjacent to the physical bounds of each plot are significantly affected. Bins within the steep slope regions of each distribution are also subject to significant measurement scale alterations. The effect is pronounced in the 0-8° region of the muon angle plot where the weight in each bin is rapidly increasing. Such bins receive largely varying contributions from their neighbors with each plus or minus one sigma shift. This is in contrast to a flat distribution with adjacent bins being filled with the same weights. The shape of a flat distribution would be largely unaffected by a change in measurement scale.

8.12.4 POT counting

The POT counting error is estimated at 1% [208].

8.12.5 Fiducial volume cuts

As described in Section 8.12.5, the background prediction is sensitive to the fiducial volume cuts. The systematic error associated with these cuts is found by calculating the reconstructed Monte Carlo simulation rate on a per-bin basis three times in terms of θ_μ/P_μ; once with the nominal fiducial volume, once with the fiducial volume increased by 1.0 cm on all sides, and once with the fiducial volume decreased by 1.0 cm on all sides. The value of 1.0 cm was chosen as it is loosely and conservatively representative of the reconstruction software's vertex resolution as seen in Figure 8.9. Note once again that the neutrino interaction vertex as well as the muon start position are required to be inside of the fiducial volume. The systematic uncertainty on the differential cross section due to the fiducial volume cuts is conservatively set equal to the largest fractional deviation from the central value, due to either the 1.0 cm increase or 1.0 cm decrease on all sides of the fiducial volume, in each θ_μ/P_μ bin. The effects of the fiducial volume adjustments can be seen in Figure 8.41. The corrected number of events reported in the plot for each distribution is the expectation for the nominal fiducial volume. That is, the fiducial volume decrease (increase) does not feature less (more) events than the fiducial volume increase as the appropriate volume normalization correction has been applied.

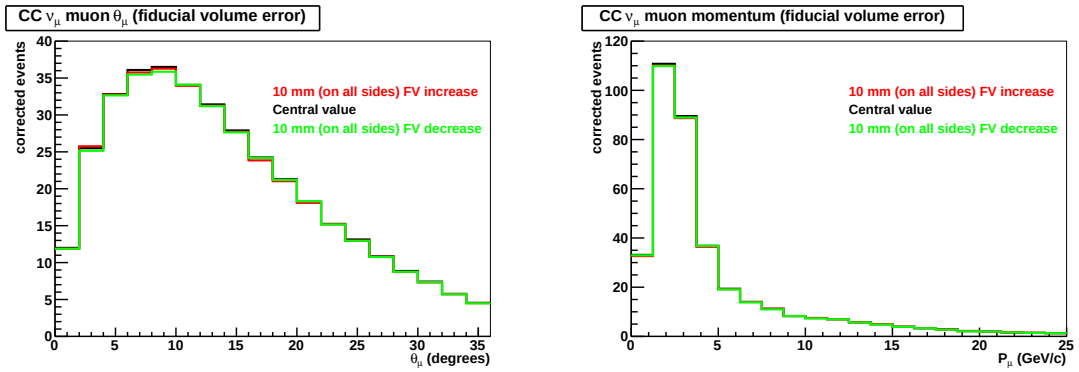

Figure 8.41: The effect of adjusting the fiducial volume by plus and minus one 1 cm on all sides. The increase or decrease occurs all at once. The central value represents the background subtracted distribution of reconstructed Monte Carlo events. The systematic error associated with the fiducial volume cut is taken as the largest fractional deviation from the central value in each bin.

8.12.6 Statistics

There are 379 ArgoNeuT events that pass all cuts. There are 373 events that fall in the $0° < \theta_\mu < 36°$ measurement range and 362 events in the $0.0 < P_\mu < 25.0$ GeV/c range.

The number of bins reported is 18 for θ_μ and 20 for P_μ. The bin width choice allows every bin reported to have $\geq$2 events, before the efficiency correction is applied. There are no momentum contraints/requirements placed on events that enter the θ_μ plot and no angle constraints/requirements placed on events that enter the P_μ plot.

The statistical error associated with the Monte Carlo signal event generation is considered negligible but is accounted for in this error analysis. Also, the errors on the simulated background generation and the background parameterization fits are included.

8.12.7 Error summary

The contributions to the uncertainty in each bin of muon angle/momentum can be seen in Figures 8.42 and 8.43. The one sigma fractional errors are reported as well as the total error (after the efficiency correction and background subtraction) on the corrected number of events. These measurements are statistics-limited in most of the bins reported. The measurement scale error contributes significantly to the uncertainty, however, especially for the bins at the edge of each plot and where the slope of the distribution is rapidly changing, as discussed above. The uncertainty on the flux is another leading error, with all other sources contributing negligible amounts.

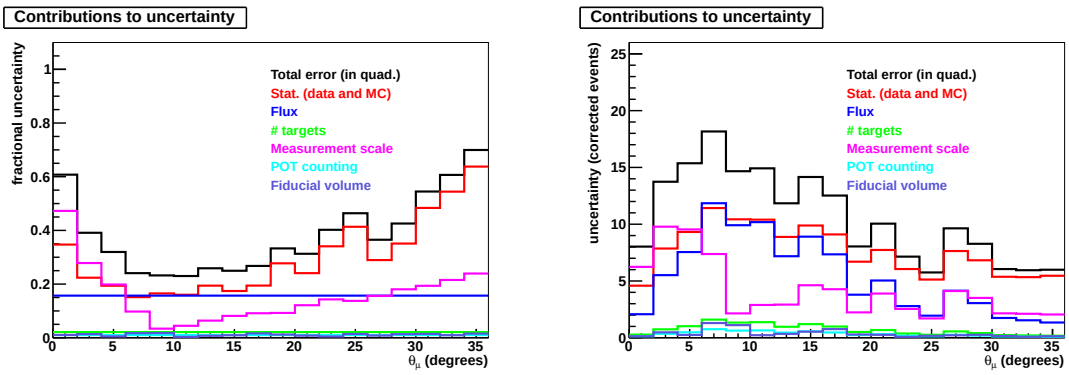

Figure 8.42: Contributions to the muon angle measurement uncertainty. The fractional errors are reported on the left and the contributions in terms of the efficiency and background corrected number of events are reported on the right.

8.13 Results

The outgoing muon angle and momentum distributions of events passing all cuts before the background and reconstruction probability corrections are applied (with statistical-only

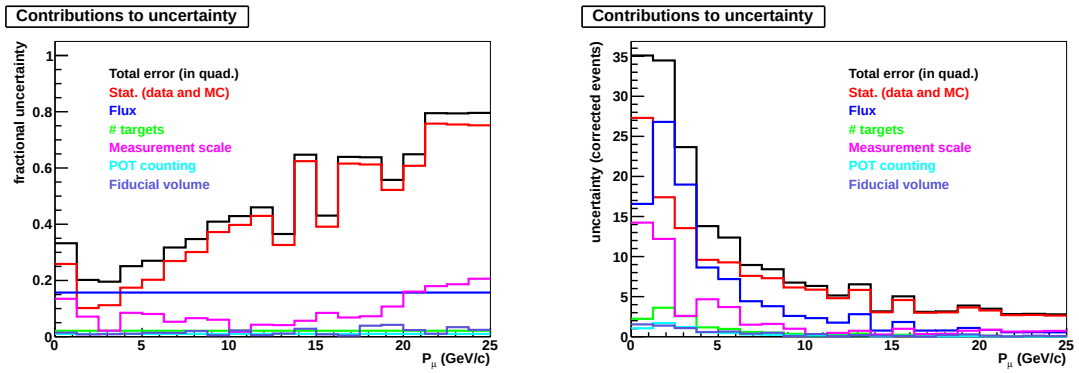

Figure 8.43: Contributions to the muon momentum measurement uncertainty. The fractional errors are reported on the left and the contributions in terms of the efficiency and background corrected number of events are reported on the right.

error bars) are shown in Figure 8.44. These plots present the raw collected rate of events as well as the raw collected shape of the angle/momentum distributions.

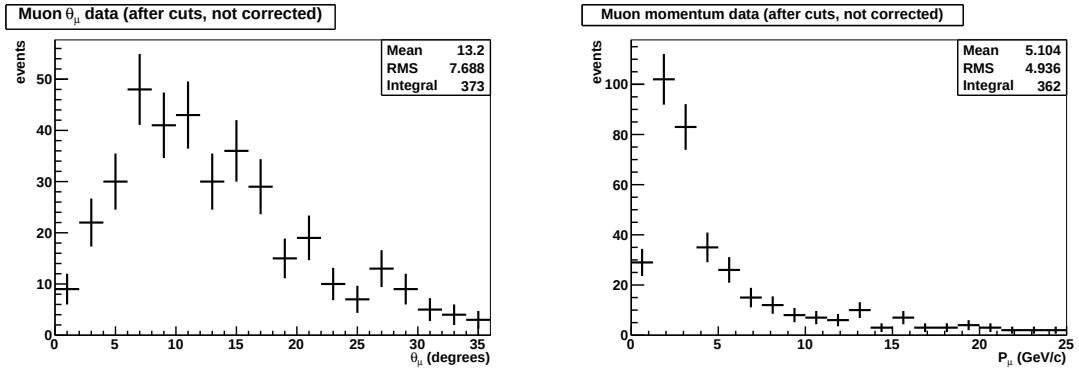

Figure 8.44: The number of events that pass all cuts. No background subtraction or efficiency correction has been applied. The error bars are statistical only.

The outgoing muon angle and momentum event sample distributions after the application of the background subtraction and reconstruction probability correction are shown in Figure 8.45. The error bars represent the statistical and systematic error contributions in each bin. Although a rate is being reported in the figure, the systematic error contributions from the flux, POT, and number of targets in the fiducial volume, used in arriving at the actual differential cross sections, are included in this plot for reference. The GENIE neutrino event generator's expectation for each distribution is also shown, along with the neutrino channel composition that makes up the total CC ν_μ prediction. Note that this Monte Carlo expectation is the raw information that comes out of the Monte Carlo; it is

the "true" distribution, rather than the "recosim" (reconstructed simulation) distribution.

The Monte Carlo expectation naively represents the sum of the world's neutrino cross section data and model knowledge. The GENIE expectation is reported alone, rather than along with other neutrino generator predictions, for simplicity. As stated previously, the NOMAD, MINOS, and SciBooNE CC ν_μ results [123, 191, 192] do not feature explicitly stated differential cross sections in muon kinematics. SciBooNE and MINOS report the rate of CC ν_μ interactions in terms of outgoing muon angle with respect to the incoming neutrino and muon momentum. However, a shape-only comparison with SciBooNE is made difficult as the result reported by them is specific to the Booster Neutrino Beam flux at the SciBooNE location and the 0.25-3.0 GeV energy range. The MINOS result covers the energy range 3-50 GeV with the same flux used in this measurement. However, as the extra 0-3 GeV energy bin employed in this analysis contributes about 43% to the total 0-50 GeV flux according to the MINOS-supplied Monte Carlo prediction, a direct comparison with the shape-only MINOS muon rates is difficult.

The integrated neutrino flux and POT exposure along with the number of targets in the ArgoNeuT fiducial volume are used to turn corrected rate into differential cross section using Equation 8.21. The differential cross sections in outgoing muon angle and momentum from CC ν_μ events on an argon target corresponding to the flux in Tables 8.1 and 8.2 are reported in Figures 8.46 and 8.47, respectively. The shape of these distributions is identical to those in Figure 8.45.

The differential cross sections for CC ν_μ interactions on argon are reported along with the differential cross sections on an isoscalar (equal number of protons and neutrons) target. The latter is useful for more simply comparing these results to other measurements with different nuclei. Recalling that stable argon has 18 protons and 22 neutrons, the correction factor for turning the argon target measurement into an isoscalar one is arrived at after weighting each GENIE simulated CC ν_μ interaction based on its nucleon target. An interaction featuring a neutron target is given a weight of (18/20) and an interaction with a proton target is given a weight of (22/20). The outgoing muon angle/momentum isoscalar correction factor can be seen in Figure 8.48, reported in the relevant bins for this measurement. A linear fit is applied to each distribution and the fit results are used for the argon-to-isoscalar correction. The functionality of the angle correction in each θ_μ bin is corr. $= \frac{-.00023 \cdot \theta_\mu}{\text{degree}} + 0.962$ and the functionality of the momentum correction in each P_μ bin is corr. $= \frac{-.000014 \cdot P_\mu}{\text{GeV/c}} + 0.958$. The effect on the interaction rate (or CC ν_μ cross section,

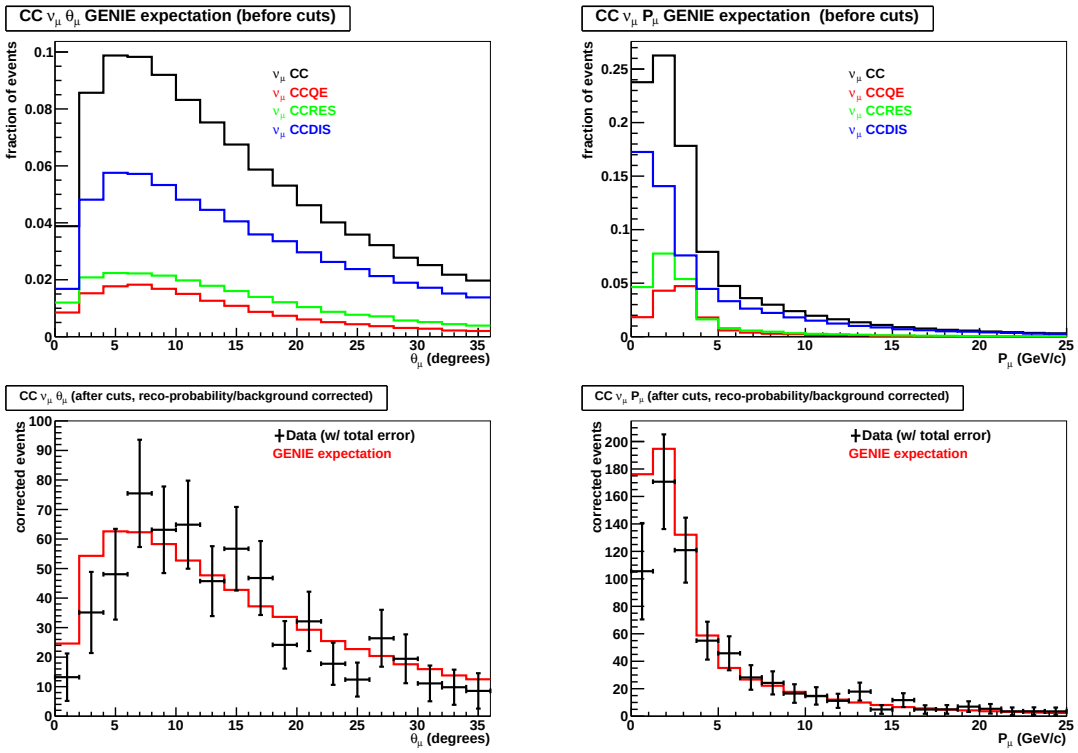

Figure 8.45: (Top) The Monte Carlo expectation for the composition of the outgoing muon angle and momentum distributions for CC ν_μ events in terms of neutrino interaction type. (Bottom) The total reconstruction probability and background/efficiency corrected event rate as a function of the measured variables. The data (with statistical and systematic errors) and Monte Carlo expectation are shown. The Monte Carlo statistical errors are too small to be seen.

equivalently) as a function of neutrino energy can be seen in Figure 8.49. The correction factor applied is model-dependent as it employs the GENIE neutrino event generator's cross sections. A model independent method for isoscalar correction only seems possible for an experiment that measures every single exclusive cross section individually.

The on-argon differential cross sections are reported "per argon nucleus". "Per nucleon" is also common in the literature, especially for the case of an isoscalar target. For simplicity, the isoscalar differential cross sections are reported in "per nucleon".

The differential cross section measurements are explicitly reported in Tables 8.10 and 8.11 for argon and in Tables 8.12 and 8.13 for an isoscalar target. The differential cross section data and Monte Carlo expectation are seen to agree well for almost all of the measurement θ_μ/P_μ bins reported. A small deficit of data compared to the expectation is seen for θ_μ less than 6° and P_μ less than 3.75 GeV/c. More data are needed in order to confirm this behavior.

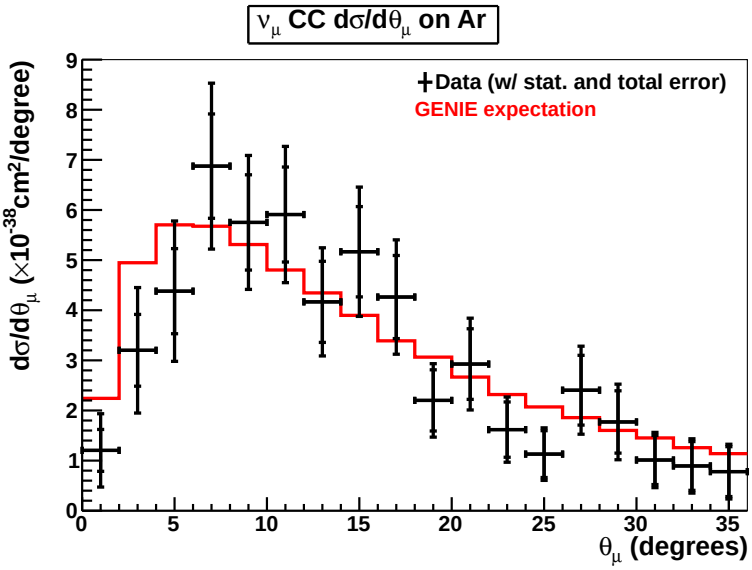

Figure 8.46: The CC ν_μ differential cross section in muon angle on an argon target. The differential cross sections are reported "per argon nucleus". Total and statistical-only error bars are shown.

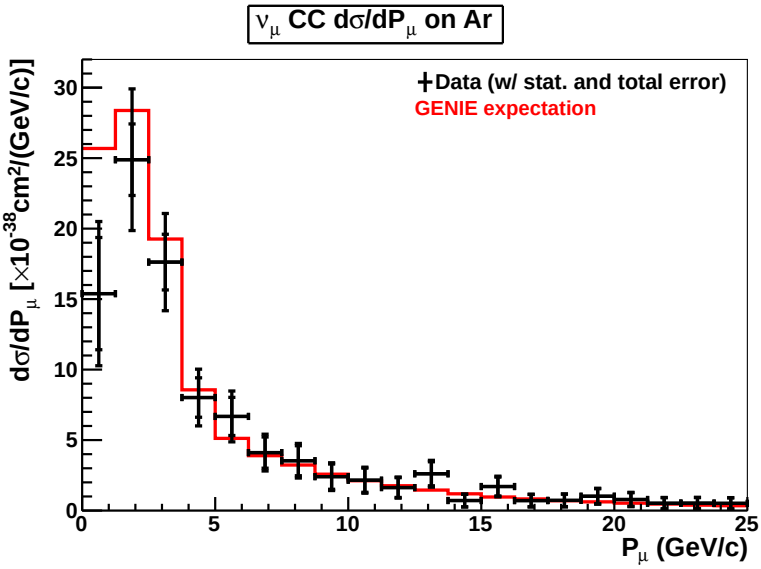

Figure 8.47: The CC ν_μ differential cross section in muon momentum on an argon target. The differential cross sections are reported "per argon nucleus". Total and statistical-only error bars are shown.

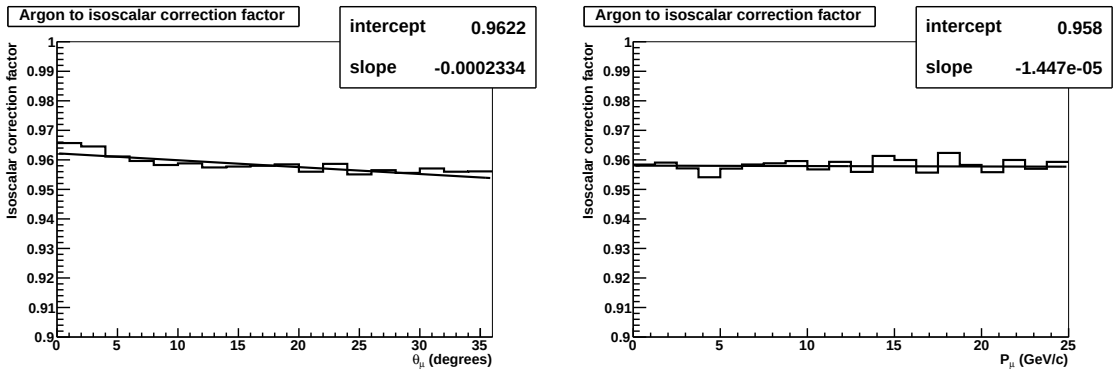

Figure 8.48: The argon to isoscalar conversion correction factor for CC ν_μ interactions in terms of θ_μ (left) and P_μ (right).

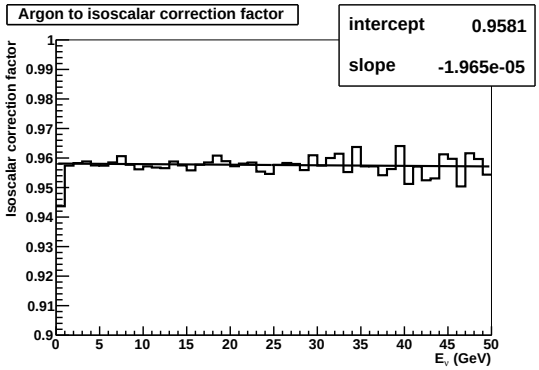

Figure 8.49: The argon to isoscalar conversion correction factor for CC ν_μ interactions in terms of E_ν).

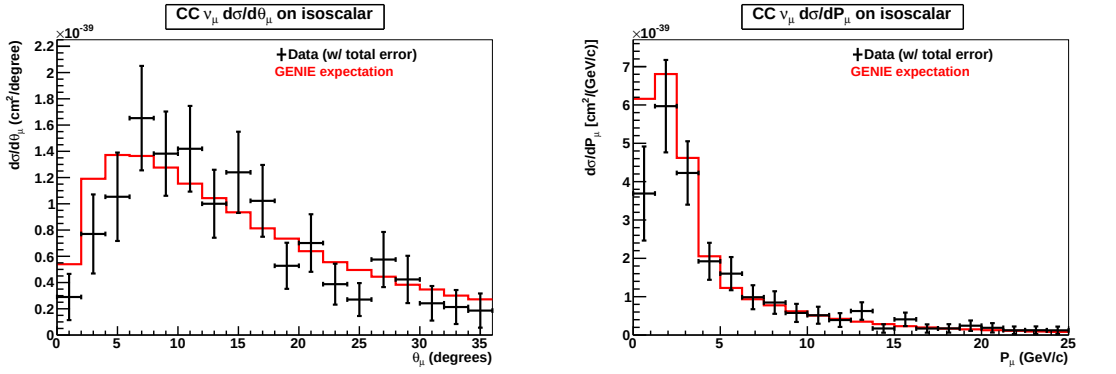

Figure 8.50: The CC ν_μ differential cross section in muon angle (left) and momentum (right) on an isoscalar target. The differential cross sections are reported "per isoscalar nucleon".

Measurement bin (on Ar nucleus) $[\theta_\mu]$ (degrees)	$d\sigma/d\theta_\mu$ $(\frac{10^{-38}\text{cm}^2}{\text{degree}})$	error $(\frac{10^{-38}\text{cm}^2}{\text{degree}})$
0-2	1.21	0.73
2-4	3.20	1.25
4-6	4.38	1.40
6-8	6.87	1.66
8-10	5.75	1.34
10-12	5.91	1.36
12-14	4.17	1.08
14-16	5.17	1.29
16-18	4.26	1.14
18-20	2.20	0.73
20-22	2.93	0.92
22-24	1.62	0.65
24-26	1.13	0.52
26-28	2.40	0.88
28-30	1.77	0.75
30-32	1.01	0.55
32-34	0.89	0.54
34-36	0.78	0.55

Table 8.10: The CC ν_μ differential cross sections per argon nucleus in muon angle. The errors reported include statistical and systematic uncertainties.

Measurement bin (on Ar nucleus) $[P_\mu]$ (GeV/c)	$d\sigma/dP_\mu$ $(\frac{10^{-38}\text{cm}^2}{\text{GeV/c}})$	error $(\frac{10^{-38}\text{cm}^2}{\text{GeV/c}})$
0.00-1.25	15.39	5.12
1.25-2.50	24.89	5.02
2.50-3.75	17.62	3.45
3.75-5.00	8.02	2.01
5.00-6.25	6.68	1.80
6.25-7.50	4.11	1.30
7.50-8.75	3.53	1.23
8.75-10.00	2.41	0.98
10.00-11.25	2.15	0.92
11.25-12.50	1.63	0.75
12.50-13.75	2.61	0.95
13.75-15.00	0.71	0.46
15.00-16.25	1.71	0.73
16.25-17.50	0.71	0.45
17.50-18.75	0.72	0.46
18.75-20.00	1.02	0.57
20.00-21.25	0.78	0.51
21.25-22.50	0.52	0.41
22.50-23.75	0.52	0.42
23.75-25.00	0.51	0.41

Table 8.11: The CC ν_μ differential cross sections per argon nucleus in muon momentum. The errors reported include statistical and systematic uncertainties.

Measurement bin (on isoscalar nucleon) $[\theta_\mu]$ (degrees)	$d\sigma/d\theta_\mu$ $(\frac{10^{-40}\text{cm}^2}{\text{degree}})$	error $(\frac{10^{-40}\text{cm}^2}{\text{degree}})$
0-2	2.90	1.76
2-4	7.70	3.01
4-6	10.54	3.37
6-8	16.53	3.98
8-10	13.82	3.21
10-12	14.19	3.26
12-14	10.00	2.59
14-16	12.40	3.10
16-18	10.22	2.74
18-20	5.28	1.76
20-22	7.01	2.19
22-24	3.88	1.56
24-26	2.70	1.25
26-28	5.75	2.10
28-30	4.24	1.80
30-32	2.42	1.32
32-34	2.13	1.29
34-36	1.86	1.30

Table 8.12: The CC ν_μ differential cross sections per isoscalar nucleon in muon angle. The errors reported include statistical and systematic uncertainties.

Measurement bin (on isoscalar nucleon) $[P_\mu]$ (GeV/c)	$d\sigma/dP_\mu$ $(\frac{10^{-40}\text{cm}^2}{\text{GeV/c}})$	error $(\frac{10^{-40}\text{cm}^2}{\text{GeV/c}})$
0.00-1.25	36.90	12.27
1.25-2.50	59.68	12.05
2.50-3.75	42.26	8.27
3.75-5.00	19.23	4.82
5.00-6.25	16.01	4.32
6.25-7.50	9.86	3.13
7.50-8.75	8.48	2.94
8.75-10.00	5.77	2.36
10.00-11.25	5.16	2.21
11.25-12.50	3.91	1.80
12.50-13.75	6.26	2.29
13.75-15.00	1.71	1.10
15.00-16.25	4.09	1.76
16.25-17.50	1.70	1.08
17.50-18.75	1.73	1.10
18.75-20.00	2.44	1.36
20.00-21.25	1.88	1.22
21.25-22.50	1.24	0.99
22.50-23.75	1.25	1.00
23.75-25.00	1.23	0.98

Table 8.13: The CC ν_μ differential cross sections per isoscalar nucleon in muon momentum. The errors reported include statistical and systematic uncertainties.

8.14 Concluding remarks

The outgoing muon angle and momentum CC ν_μ differential cross sections on an argon and isoscalar target as measured by the ArgoNeuT experiment in the NuMI beamline at Fermilab have been presented. These are the first CC-inclusive differential cross section measurements on argon ever reported. This analysis has utilized the first two-weeks of the ArgoNeuT physics run, comprising the entirety of the neutrino-mode data taking and corresponding to 8.5×10^{18} POT. Approximately 1.25×10^{20} POT were taken in anti-neutrino mode over the latter part of the five-and-a-half month physics run in late 2009-early 2010. Along with future CC $\overline{\nu}_\mu$ inclusive and exclusive measurements foreseen with this data, the anti-neutrino-mode's neutrino "contamination" can be studied as well. This sample can be used to improve the large statistical errors reported in this analysis, although the anti-neutrino mode neutrino flux uncertainties and anti-neutrino "background" will also need to be taken into account in that case. Furthermore, the ratio between CC ν_μ and CC $\overline{\nu}_\mu$ in terms of many kinematic variables can be analyzed.

There is much room for improvement in terms of in-ArgoNeuT reconstruction for future analyses. The reconstruction probability, matching probability, and measurement resolution can all be augmented. Each step of the automated reconstruction is under continual development. A special focus is being placed on improving three dimensional reconstruction and incorporating calorimetric information to assist in the process. Along with reconstruction improvements in general, subsequent analyses will demonstrate the full power of LArTPCs with $\frac{dE}{dx}$-based particle identification and vertex activity characterization.

These measurements are among the first physics results with a LArTPC and are the first with a LArTPC in a low energy neutrino beam. This thesis also represents the first analysis that utilizes the from-scratch automated LArTPC reconstruction framework created by the "LArSoft" group [209] and the first physics analysis with the ArgoNeuT experiment. The results have elucidated the behavior of the outgoing muon in charged-current muon-neutrino interactions and can be used to tune neutrino event generators, reduce the systematics involved in a long baseline oscillation experiment's near-far comparison, and inform the theory of neutrino-nucleus interactions.

Although the total cross section as a function of energy for inclusive and exclusive interaction channels has been extensively reported, differential cross section measurements in terms of the outgoing muon kinematics are sparse. The charged-current interaction,

comprising the sum total of charged-current exclusive channels, is not subject to the modeling uncertainties associated with final state interactions and exclusive channel definition ambiguity in event identification. Furthermore, measurements independent of any sort of neutrino interaction and nuclear model are needed in order to further understand issues such as the uncertain axial-vector form factors of the nucleon and the behavior of nucleons within the nucleus.

These results provide a standard candle for future exclusive channel cross section measurements with ArgoNeuT and other experiments. Although the differential cross section measurements are specific to the NuMI flux reported here, such information can be utilized across a large range of relevant neutrino energies and muon kinematics and may be especially useful for those experiments that share and have shared the NuMI low energy flux such as MINERνA, MINOS, and PEANUT [210]. Long baseline neutrino oscillation experiments, searching for non-zero θ_{13}, CP-violation in the lepton sector, and trying to measure the orientation of the mass hierarchy, among other things, can use this measurement to improve the systematic error estimate arising from flux/target differences between near and far detectors. Realistically, this can be accomplished through the tuning of the charged-current interaction and outgoing particle kinematics models at NuMI energies and then applying the tuned model(s) to the appropriate neutrino flux.

Bibliography

[1] E. Fermi, *Z. Physik* **88** 161 (1934).

[2] C.L. Cowan Jr., F. Reines, F.B. Harrison, H.W. Kruse and A.D. McGuire, *Science* **124** 103 (1956).

[3] C.L. Cowan Jr. *et al.*, *Science* **124** 3212 (1956).

[4] T.D. Lee and C.N. Yang, *Phys. Rev.* **104** 254 (1956).

[5] C.S. Wu *et al.*, *Phys. Rev.* **105** 1413 (1957).

[6] M. Goldhaber, L. Grodzins and A.W. Sunyar, *Phys. Rev.* **109** 1015 (1958).

[7] E.C.G. Sudarshan and R.E. Marshak, *Phys. Rev.* **109** 1860 (1958).

[8] G. Danby *et al.*, *Phys. Rev. Lett.* **9** 36 (1962).

[9] M.L. Perl *et al.*, *Phys. Rev. Lett.* **35** 22 (1975).

[10] K. Kodama *et al.* [DONUT Collaboration], *Phys. Lett. B* **504** 218 (2001).

[11] F.J. Hasert *et al.* [Gargamelle Neutrino Collaboration], *Phys. Lett. B* **46** 138 (1973).

[12] S.L. Glashow, *Nucl. Phys.* **22** 579 (1961).

[13] S. Weinberg, *Phys. Rev. Lett.* **19** 1264 (1967).

[14] A. Salam, *Phys. Rev. Lett.* **19** 1264 (1967).

[15] G. Arnison *et al.* [UA1 Collaboration], *Phys. Lett. B* **122** 103 (1983).

[16] G. Arnison *et al.* [UA1 Collaboration], *Phys. Lett. B* **126** 398 (1983).

[17] B. Pontecorvo, *Sov. Phys. JETP* **6** 429 (1957).

[18] Z. Maki, M. Nakagawa, and S. Sakata, *Prog. Theor. Phys.* **28** 870 (1962).

[19] W.M. Yao *et al.* [Particle Data Group Collaboration], *J. Phys. G* **33** 264 (2006).

[20] M. Fukugita and T. Yanagida, *Phys. Lett. B* **174** 45 (1986).

[21] G. 't Hooft, *Phys. Rev. Lett.* **37** 8 (1976).

[22] V. Kuzmin, V. Rubakov, and M. Shaposhnikov, *Phys. Lett. B* **155** 36 (1985).

[23] S.P. Mikheev and A. Yu. Smirnov, *Sov. J. Nucl. Phys.* **42** 913 (1985).

[24] L. Wolfenstein, *Phys. Rev. D* **17** 2369 (1978).

[25] E. Majorana, *Nuovo Cim.* **14** 171 (1937).

[26] M. Gell-Mann, P. Ramond and R. Slansky, *Supergravity, ed. by D. Freedman et al.* (North Holland 1979).

[27] T. Yanagida, *Prog. Theor. Phys.* **64** 1103 (1980).

[28] R. Mohapatra and G. Senjanovic, *Phys. Rev. Lett.* **44** 912 (1979).

[29] J. Bahcall, *Neutrino Astrophysics* (Cambridge: Cambridge University Press 1989).

[30] B. Cleveland *et al.*, *Astrophysical Journal* **496** 505 (1998).

[31] J.N. Abdurashitov *et al.* [SAGE Collaboration], *Phys. Rev. C* **80** 015807 (2009).

[32] W. Hampel *et al.* [GALLEX Collaboration], *Phys. Lett. B* **447** 127 (1999).

[33] Y. Fukuda *et al.*, *Phys. Rev. Lett.* **77** 1683 (1996).

[34] K. Hirata *et al.*, *Phys. Rev. Lett.* **63** 16 (1989).

[35] K. Hirata *et al.*, *Phys. Lett. B* **416** 205 (1988).

[36] Q.R. Ahmad *et al.* [SNO Collaboration], *Phys. Rev. Lett.* **89** 011301 (2002).

[37] Y. Fukuda *et al.*, *Phys. Rev. Lett.* **81** 6 (1998).

[38] Y. Ashie *et al.* [Super-Kamiokande Collaboration], *Phys. Rev. Lett.* **93** 101801 (2004).

[39] K. Abe *et al.* [Super-Kamiokande Collaboration], *Phys. Rev. Lett.* **97** 171801 (2006).

[40] S. Abe *et al.* [KamLAND Collaboration], *Phys. Rev. Lett.* **100** 221803 (2008).

[41] E. Lisi, A. Marrone, and D. Montanino, *Phys. Rev. Lett.* **85** 1166 (2000).

[42] G. Fogli, E. Lisi, A. Marrone, and D. Montanino, *Phys. Rev. D* **67** 093006 (2003).

[43] V. Barger, J. Learned, S. Pakvase, and T. Weiler, *Phys. Rev. Lett.* **82** 2640 (1999).

[44] V. Barger *et al.*, *Phys. Lett. B* **462** 109 (1999).

[45] M.H. Ahn *et al.* [K2K Collaboration], *Phys. Rev. D* **74** 072003 (2006).

[46] P. Adamson *et al.* [MINOS Collaboration], *Phys. Rev. Lett.* **101** 131802 (2008).

[47] P. Adamson *et al.* [MINOS Collaboration], *Phys. Rev. Lett.* **107** 021801 (2011).

[48] P. Adamson *et al.* [MINOS Collaboration], *Phys. Rev. D* **82** 051102 (2010).

[49] P. Adamson *et al.* [MINOS Collaboration] "Improved search for muon-neutrino to electron-neutrino oscillations in MINOS (2011)", `arXiv:1108.0015`.

[50] N. Agafonova *et al.* [OPERA Collaboration], *Phys. Lett. B* **691** 138 (2010).

[51] A. Aguilar *et al.* [LSND Collaboration], *Phys. Rev. D* **64** 112007 (2001).

[52] G.S. Abrams *et al.*, *Phys. Rev. Lett.* **63** 2173 (1989).

[53] D. Decamp *et al.* [ALEPH Collaboration], *Phys. Lett. B* **231** 519 (1989).

[54] A.A. Aguilar-Arevalo *et al.* [MiniBooNE Collaboration], *Phys. Rev. Lett.* **98** 231801 (2007).

[55] A.A. Aguilar-Arevalo *et al.* [MiniBooNE Collaboration], *Phys. Rev. Lett.* **105** 181801 (2010).

[56] K. Nakamura *et al.* [Particle Data Group Collaboration], *J. Phys. G* **37** 075021 (2010).

[57] V.M. Lobashev *et al.*, *Phys. Lett. B* **460** 227 (1999).

[58] C. Kraus *et al.*, *Eur. Phys. Jour.* **40** 447 (2005).

[59] K. Abe *et al.* [T2K Collaboration] "The T2K Experiment (2011)", `arXiv:1106.1238`.

[60] D. Beavis, A. Carroll, I. Chiang *et al.* "Proposal of BNL AGS E-889", (1995).

[61] K. Abe *et al.* [T2K Collaboration] "Indication of Electron Neutrino Appearance from an Accelerator-produced Off-axis Muon Neutrino Beam (2011)", `arXiv:1106.2822`.

[62] [Daya Bay Collaboration] "A Precision Measurement of the Neutrino Mixing Angle θ_{13} using Reactor Antineutrinos at Daya Bay (2007)", `arXiv:hep-ex/0701029`.

[63] RENO Collaboration "http://neutrino.snu.ac.kr/RENO/".

[64] M. Apollonio *et al.*, *Eur. Phys. Jour. C* **27** 331 (2003).

[65] M. Ardellier *et al.* [Double CHOOZ Collaboration] "A search for the neutrino mixing angle θ_{13} (2006)", `arXiv:hep-ex/0606025`.

[66] D. Ayres *et al.* "Letter of Intent to build an Off-axis Detector to study numu to nue oscillations with the NuMI Neutrino Beam (2002)", `arXiv:hep-ex/0210005`.

[67] E. Aprile *et al.* [XENON100 Collaboration] "Dark Matter Results from 100 Live Days of XENON100 Data (2011)", `arXiv:astro-ph/1104.2549`.

[68] O. Bunemann and J.A. Harvey, *Can. J. Res.* **27** 191 (1949).

[69] A. Martinez de la Ossa "Study of accelerator neutrino interactions in a liquid argon TPC", *Ph.D. Thesis. University of Granada* (2007).

[70] J. Birks, *Proc. Phys. Soc. A* **64** 874 (1951).

[71] P. Cennini *et al.*, *Nucl. Instr. & Meth. A* **345** 230 (1994).

[72] A. Badertscher *et al.*, *New J. Phys.* **7** 63 (2005).

[73] A. Ankowski *et al.*, *Eur. Phys. Jour. C* **48** 667 (2006).

[74] R. Kalman, *Trans. ASME D J. Basic Eng.* **82** 35 (1960).

[75] A.A. Aguilar-Arevalo *et al.* [MiniBooNE Collaboration], *Phys. Rev. Lett.* **102** 101802 (2009).

[76] M. Maltoni and T. Schwetz, *Phys. Rev. D* **76** 093005 (2007).

[77] S. Goswami and W. Rodejohann, *JHEP* **10** 73 (2007).

[78] H. Pas, S. Pakvasa, and T.J. Weiler, *Phys. Rev. D* **72** 095017 (2005).

[79] C. Giunti and M. Laveder, *Phys. Rev. D* **77** 093002 (2008).

[80] T. Katori, A. Kostelecky and R. Tayloe, *Phys. Rev. D* **74** 105009 (2006).

[81] A. de Gouvea and Y. Grossman, *Phys. Rev. D* **74** 093008 (2006).

[82] J. Harvey, C. Hill, and R. Hill, *Phys. Rev. Lett.* **99** 261601 (2007).

[83] X.Q. Li *et al.*, *Eur. Phys. Jour. C* **56** 97 (2008).

[84] C. Giunti and M. Laveder, *Phys. Rev. D* **82** 093016 (2010).

[85] G. Mention *et al.* "The Reactor Anti-Neutrino Anomaly (2011)", `arXiv:hep-ex/1101.2755`.

[86] J.M. Conrad and M.H. Shaevitz "Limits on Electron Neutrino Disappearance from the KARMEN and LSND Electron Neutrino - Carbon Cross Section Data (2011)", `arXiv:1106.5552`.

[87] L.B. Auerbach *et al.* [LSND Collaboration], *Phys. Rev. C* **64** 065501 (2001).

[88] B.E. Bodmann *et al.* [KARMEN Collaboration], *Phys. Lett. B* **332** 251 (1994).

[89] S. Amerio *et al.*, *Nucl. Instr. & Meth. A* **527** 329 (2004).

[90] C. Rubbia *et al.* [ICARUS Collaboration] "Underground operation of the ICARUS T600 LAr-TPC: first results (2011)", `arXiv:hep-ex/1106.0975`.

[91] C. Rubbia "DOUBLE-LAr: sterile neutrinos at the CERN-PS?", *Presentation at the Workshop on New Opportunities in the Physics Landscape at CERN* (2009).

[92] B. Baibussinov *et al.* "A New search for anomalous neutrino oscillations at the CERN-P", `arXiv:hep-ex/0909.0355`.

[93] H. Nishino *et al.* [Super-K Collaboration], *Phys. Rev. Lett.* **102** 141801 (2009).

[94] A. Bueno and others, *JHEP* **0704** 041 (2007).

[95] A. Ereditato and A. Rubbia, *Nucl. Phys. Proc. Suppl.* **154** 163 (2006).

[96] A. Rubbia, *Nucl. Phys. Proc. Suppl.* **91** 223 (2001).

[97] J. Conrad, A. de Gouvea, S. Shalgar, and J. Spitz, *Phys. Rev. D* **82** 093012 (2010).

[98] K. Hirata *et al.* [Kamiokande-II], *Phys. Rev. Lett.* **58** 1490 (1987).

[99] R.M. Bionta *et al.*, *Phys. Rev. Lett.* **58** 1494 (1987).

[100] E.N. Alekseev *et al.*, *Phys. Lett. B* **205** 209 (1988).

[101] I. Gil-Botella and A. Rubbia, *JCAP* **08** 001 (2004).

[102] A. Bueno, I. Gil-Botella, and A. Rubbia "Supernova Neutrino Detection in a liquid Argon TPC (2003)", `arXiv:hep-ph/0307222`.

[103] A. Cocco, A. Ereditato, G. Fiorillo, G. Mangano, and V. Pettorino, *JCAP* **0412** 002 (2004).

[104] A. Abramov *et al.*, *Nucl. Instr. & Meth. A* **485** 209 (2002).

[105] J. Spitz (under the supervision of E.D. Zimmerman) "T2K Beam Monte Carlo Study", *Undergraduate thesis, Department of Physics, University of Colorado at Boulder* (2006).

[106] [T2K Collaboration] "Letter Of Intent, Neutrino Oscillation Experiment at JHF", (2003).

[107] Z. Pavlovich, MINOS collaboration, *Private Communication* .

[108] M. Soderberg, for the ArgoNeuT Collaboration "ArgoNeuT: A Liquid Argon Time Projection Chamber Test in the NuMI Beamline (2009)", `arXiv:physics.ins-det/0910.3433`.

[109] D.G. Michael *et al.* [MINOS Collaboration], *Nucl. Instr. & Meth. A* **596** 190 (2008).

[110] D. Drakoulakos *et al.* [MINERνA Collaboration] "Proposal to perform a high-statistics neutrino scattering experiment using a fine-grained detector in the NuMI beam (2004)", `arXiv:hep-ex/0405002`.

[111] R. Andrews *et al.*, *Nucl. Instr. & Meth. A* **608** 251 (2009).

[112] W. Walkowiak, *Nucl. Instr. & Meth. A* **288** 449 (2000).

[113] B. Baibussinov *et al.*, *Journal of Instrumentation* **5** 3005 (2010).

[114] A. Curioni *et al.*, *Nucl. Instr. & Meth. A* **605** 306 (2009).

[115] P. Cennini *et al.*, *Nucl. Instr. & Meth. A* **333** 567 (1993).

[116] P. Benetti *et al.*, *Nucl. Instr. & Meth. A* **332** 395 (1993).

[117] F. Arneodo *et al.*, *Phys. Rev. D* **74** 112001 (2006).

[118] Engelhard Corporation, MSDS for Cu-0226 S 14 x 28 (2002).

[119] G. Carugno *et al.*, *Nucl. Instr. & Meth. A* **292** 580 (1990).

[120] PolyMicro Technologies Inc., #FVP600660710UVMI.

[121] G. Bakale *et al.*, *Journal of Physical Chemistry* **80** 23 (1976).

[122] D. Edmunds "http://www.pa.msu.edu/∼edmunds/LArTPC".

[123] P. Adamson *et al.* [MINOS Collaboration], *Phys. Rev. D* **77** 072002 (2008).

[124] D.G. Michael *et al.* [MINOS Collaboration], *Phys. Rev. Lett.* **97** 191801 (2006).

[125] C. Andreopoulos *et al.*, *Nucl. Instrum. Meth. A* **614** 87 (2010).

[126] C. Andreopoulos, *Private Communication* .

[127] A. Ankowski and J. Sobczyk, *Phys. Rev. C* **74** 054316 (2006).

[128] F. Cavanna and O. Palamara, *Nucl. Phys. B Proc. Suppl.* **112** 183 (2002).

[129] Y. Hayato, *Acta Phys. Polon. B* **40** 2477 (2009).

[130] H. Gallagher, *Nucl. Phys. Proc. Suppl.* **159** 229 (2006).

[131] A. Rubbia "NUX neutrino generator", *Presentation at NuINT 2001* (2001).

[132] A.A. Aguilar-Arevalo *et al.* [MiniBooNE Collaboration], *Nucl. Instr. & Meth. A* **599** 28 (2009).

[133] C.H. Llewellyn Smith, *Phys. Rep. C* **70** 068202 (1972).

[134] R. Smith and E. Moniz, *Nucl. Phys. B* **43** 605 (1972).

[135] M. Ahn *et al.*, *Phys. Rev. Lett.* **90** 041801 (2003).

[136] A.A. Aguilar-Arevalo *et al.* [MiniBooNE Collaboration], *Phys. Rev. Lett.* **100** 032301 (2008).

[137] A.A. Aguilar-Arevalo *et al.* [MiniBooNE Collaboration], *Phys. Rev. D* **81** 092005 (2010).

[138] P. Bosted, *Phys. Rev. C* **51** 409 (1990).

[139] H. Budd, A. Bodek, and J. Arrington "Modeling Quasi-elastic Form Factors for Electron and Neutrino Scattering (2003)", `arXiv:hep-ex/0308005`.

[140] R. Bradford, H. Budd, A. Bodek, and J. Arrington "A New Parameterization of the Nucleon Elastic Form Factors (2006)", `arXiv:hep-ex/0602017`.

[141] L. Ahrens *et al.*, *Phys. Rev. D* **35** 785 (1987).

[142] A.A. Aguilar-Arevalo *et al.* [MiniBooNE Collaboration], *Phys. Rev. D.* **82** 092005 (2010).

[143] A.A. Aguilar-Arevalo *et al.* [MiniBooNE Collaboration], *Phys. Rev. D.* **81** 013005 (2010).

[144] A.A. Aguilar-Arevalo *et al.* [MiniBooNE Collaboration], *Phys. Rev. D.* **83** 052009 (2011).

[145] A.A. Aguilar-Arevalo *et al.* [MiniBooNE Collaboration], *Phys. Rev. Lett.* **103** 081801 (2009).

[146] A.A. Aguilar-Arevalo *et al.* [MiniBooNE Collaboration], *Phys. Rev. D.* **83** 052007 (2011).

[147] D. Rein and L. Sehgal, *Annals Phys.* **133** 79 (1981).

[148] M. K. R.P. Feynman and F. Ravndal, *Phys. Rev. D* **3** 2706 (1971).

[149] A. Bodek and U. Yang, *Nucl. Phys. Proc. Suppl.* **112** 70 (2002).

[150] A. Bodek, I. Park, and U. Yang, *Nucl. Phys. Proc. Suppl.* **139** 113 (2005).

[151] L. Whitlow *et al.*, *Phys. Lett. B* **250** (1990).

[152] N. Schmitz, *Neutrino 1988 proceedings* (1988).

[153] PYTHIA-6/JETSET, *http://home.thep.lu.se/∼torbjorn/Pythia.html* .

[154] D. Casper, *Nucl. Phys. Proc. Suppl.* **112** 161 (2002).

[155] D. Rein and L. Sehgal, *Nucl. Phys. B* **223** 29 (1983).

[156] L. M. Sehgal, *AIP Conf. Proc.* **967** 166 (2007).

[157] A.A. Aguilar-Arevalo *et al.* [MiniBooNE Collaboration], *Phys. Lett. B* **664** 41 (2008).

[158] G. Zeller "Low energy ν cross sections", *Presentation at Neutrino 2008* (2008).

[159] Y. Kurimoto *et al.* [SciBooNE Collaboration], *Phys. Rev. D* **81** 033004 (2010).

[160] M. Hasegawa *et al.* [K2K Collaboration], *Phys. Rev. lett.* **95** 252301 (2005).

[161] K. Hiraide *et al.* [SciBooNE Collaboration], *Phys. Rev. D* **78** 112004 (2008).

[162] R. Ransome *et al.*, *Phys. Rev. C* **45** 509 (1992).

[163] R. Ransome, *Nucl. Phys. Proc. Suppl.* **139** 208 (2005).

[164] G. Zeller, *Private Communication* .

[165] V. Flaminio, W. Moorehead, D. Morrison, and N. Rovoire, *CERN-HERA-83-01, CERN-HERA-83-02, CERN-HERA-84-01* (1983-1984).

[166] V. Ammosov, *Presentation at NuInt 2001* (2001).

[167] S. Dytman and H. Gallagher, *INTRANUKE documentation GENIE-PUB/2007/003.3* (2007).

[168] D. Ashery *et al.*, *Phys. Rev. C* **2173** 23 (1981).

[169] I. Navon *et al.*, *Phys. Rev. C* **28** 2548 (1983).

[170] A. Carroll *et al.*, *Phys. Rev. C* **14** 635 (1976).

[171] A. Clough *et al.*, *Nucl. Phys. B* **76** 15 (1974).

[172] W. Bauhoff, *At. Data and Nucl. Data Tab.* **35** 429 (1986).

[173] D. Cochran *et al.*, *Phys. Rev. D* **6** 3085 (1972).

[174] G. Hoffmann *et al.*, *Phys. Lett. B* **79** 376 (1978).

[175] T. Bowles *et al.*, *Phys. Rev. C* **23** 439 (1981).

[176] D. Marlow *et al.*, *Phys. Rev. C* **30** 1662 (1984).

[177] S. Mashnik, K. Gudima, A. Sierk, M. Baznat, and N. Mokhov, *LANL Report LA-UR-05-7321* (2005).

[178] S. Mashnik, A. Sierk, K. Gudima, and M. Baznat, *J. Phys. Conf. Ser.* **41** 340 (2006).

[179] J. Finn *et al.*, *Nucl. Phys. A* **274** 28 (1976).

[180] M. Ester, H.-P. Kriegel, J. Sander, and X. Xu "A density-based algorithm for discovering clusters in large spatial databases with noise", *Proc. 2nd Int. Conf. on Knowledge Discovery and Data Mining* 226 (1996).

[181] P. Hough "Machine analysis of bubble chamber pictures", *Proc. Int. Conf. on High Energy Accelerators and Instrumentation* (1959).

[182] H. Chen *et al.* [MicroBooNE Collaboration] "A Proposal for a New Experiment Using the Booster and NuMI Neutrino Beamlines : MicroBooNE", *FERMILAB-PROPOSAL-0974* (2007).

[183] A. Rubbia "Experiments For CP-Violation: A Giant Liquid Argon Scintillation, Cerenkov And Charge Imaging Experiment? (2004)", `arXiv:hep-ph/0402110`.

[184] L. Bartoszek *et al.* "FLARE, Fermilab Liquid Argon Experiments (2004)", `arXiv:hep-ex/0408121`.

[185] D. Cline *et al.*, *Nucl. Instr. & Meth. A* **503** 136 (2003).

[186] B. Baibussinov *et al.*, *Astroparticle Physics* **29** 174 (2008).

[187] A. Bettini *et al.*, *Nucl. Instr. & Meth. A* **305** 177 (1991).

[188] B. Rossi *et al.*, *Journal of Instrumentation* **4** 7011 (2009).

[189] S. Amoruso *et al.*, *Nucl. Instr. & Meth. A* **516** 68 (2004).

[190] F. Arneodo *et al.*, *Nucl. Instr. & Meth. A* **498** 292 (2003).

[191] Q. Wu *et al.* [NOMAD Collaboration], *Phys. Lett. B* **660** 19 (2008).

[192] Y. Nakajima *et al.* [SciBooNE Collaboration], *Phys. Rev. D* **83** 012005 (2011).

[193] V. Lyubushkin *et al.*, *Eur. Phys. Jour. C* **63** 355 (2009).

[194] M. Martini, M. Ericson, G. Chanfray, and J. Marteau, *Phys. Rev. C* **80** 065501 (2009).

[195] Y. Itow, *Nucl. Phys. Proc. Suppl.* **112** 3 (2002).

[196] D. Harris *et al.* [MINERνA Collaboration] "Neutrino Scattering Uncertainties and their Role in Long Baseline Oscillation Experiments (2004)", `arXiv:hep-ex/0410005`.

[197] N. Baker *et al.*, *Phys. Rev. D* **25** 617 (1982).

[198] Y. Kurimoto *et al.* [SciBooNE Collaboration], *Phys. Rev. D* **81** 111102 (2010).

[199] P. Auchinloss *et al.*, *Z. Phys. C* **48** 411 (1990).

[200] D. Macfarlane *et al.*, *Z. Phys. C* **26** 1 (1984).

[201] P. Berge *et al.*, *Z. Phys. C* **35** 443 (1987).

[202] J. Morfin *et al.*, *Phys. Lett. B* **104** 235 (1981).

[203] J. Morfin *et al.*, *Z. Phys. C* **2** 187 (1979).

[204] R. Hatcher, MINOS collaboration, *Private Communication* .

[205] A. Weber, MINOS collaboration, *Private Communication* .

[206] G. Cowan *Statistical Data Analysis.* Oxford Science Publications 1998.

[207] G. D'Agostini, *Nucl. Instr. & Meth. A* **362** 487 (1995).

[208] A. McGowan "Observation of a Deficit in NuMI Neutrino-induced Rock and Non-fudical Muons in the MINOS Far Detector and Measurement of Neutrino Oscillation Parameters", *Ph.D. Thesis. University of Minnesota* (2003).

[209] https://cdcvs.fnal.gov/redmine/projects/larsoftsvn.

[210] S. Aoki *et al.*, *New J. Phys.* **12** 113028 (2010).